NUREG/CR-6460
ORNL/TM-13207

CSNI Project for Fracture Analyses of Large-Scale International Reference Experiments (FALSIRE II)

Prepared by
B. R. Bass, C. E. Pugh, J. Keeney, ORNL
H. Schulz, J. Sievers, GAR

Oak Ridge National Laboratory
Gesellschaft für Anlagen-und Reaktorsicherheit

Prepared for
U.S. Nuclear Regulatory Commission

AVAILABILITY NOTICE

Availability of Reference Materials Cited in NRC Publications

Most documents cited in NRC publications will be available from one of the following sources:

1. The NRC Public Document Room, 2120 L Street, NW., Lower Level, Washington, DC 20555-0001

2. The Superintendent of Documents, U.S. Government Printing Office, P. O. Box 37082, Washington, DC 20402-9328

3. The National Technical Information Service, Springfield, VA 22161-0002

Although the listing that follows represents the majority of documents cited in NRC publications, it is not intended to be exhaustive.

Referenced documents available for inspection and copying for a fee from the NRC Public Document Room include NRC correspondence and internal NRC memoranda; NRC bulletins, circulars, information notices, inspection and investigation notices; licensee event reports; vendor reports and correspondence; Commission papers; and applicant and licensee documents and correspondence.

The following documents in the NUREG series are available for purchase from the Government Printing Office: formal NRC staff and contractor reports, NRC-sponsored conference proceedings, international agreement reports, grantee reports, and NRC booklets and brochures. Also available are regulatory guides, NRC regulations in the *Code of Federal Regulations*, and *Nuclear Regulatory Commission Issuances*.

Documents available from the National Technical Information Service include NUREG-series reports and technical reports prepared by other Federal agencies and reports prepared by the Atomic Energy Commission, forerunner agency to the Nuclear Regulatory Commission.

Documents available from public and special technical libraries include all open literature items, such as books, journal articles, and transactions. *Federal Register* notices, Federal and State legislation, and congressional reports can usually be obtained from these libraries.

Documents such as theses, dissertations, foreign reports and translations, and non-NRC conference proceedings are available for purchase from the organization sponsoring the publication cited.

Single copies of NRC draft reports are available free, to the extent of supply, upon written request to the Office of Administration, Distribution and Mail Services Section, U.S. Nuclear Regulatory Commission, Washington, DC 20555-0001.

Copies of industry codes and standards used in a substantive manner in the NRC regulatory process are maintained at the NRC Library, Two White Flint North, 11545 Rockville Pike, Rockville, MD 20852-2738, for use by the public. Codes and standards are usually copyrighted and may be purchased from the originating organization or, if they are American National Standards, from the American National Standards Institute, 1430 Broadway, New York, NY 10018-3308.

DISCLAIMER NOTICE

NUREG/CR–6460
ORNL/TM–13207

CSNI Project for Fracture Analyses of Large-Scale International Reference Experiments (FALSIRE II)

Manuscript Completed: April 1996
Date Published: November 1996

Prepared by
B. R. Bass, C. E. Pugh, J. Keeney, ORNL
H. Schulz, J. Sievers, GAR

Oak Ridge National Laboratory
Oak Ridge, TN 37831–6285

Gesellschaft für Anlagen-und Reaktorsicherheit
Department of Component Integrity (GRS)
Koln, Germany

M. Vassilaros, NRC Project Manager

Prepared for
Division of Engineering Technology
Office of Nuclear Regulatory Research
U.S. Nuclear Regulatory Commission
Washington, DC 20555–0001
NRC Job Code W6631

DISCLAIMER

Abstract

A summary of Phase II of the Project for Fracture Analysis of Large-Scale International Reference Experiments (FALSIRE) is presented. Project FALSIRE was created by the Fracture Assessment Group (FAG) of the Organization for Economic Cooperation and Development/Nuclear Energy Agency's (OECD/NEA's) Committee on the Safety of Nuclear Installations (CSNI) Principal Working Group No. 3 (PWG-3). The CSNI/FAG was formed to evaluate fracture prediction capabilities currently used in safety assessments of nuclear components. Members were from laboratories and research organizations in Western Europe, Japan, and the United States. The CSNI/FAG initiated an international project (FALSIRE I) in 1988 to assess various fracture methodologies through interpretive analyses of six large-scale fracture experiments. These experiments were conducted by research organizations in Europe, Japan, and the United States. Following the successful completion of FALSIRE I in 1992, several participating organizations indicated a desire to proceed with further evaluation of fracture analysis methods in a Phase II program. FALSIRE II included seven reference cleavage fracture experiments that focused primarily on behavior of relatively shallow cracks in the transition temperature region. Included were experiments for which cracks showed either unstable extension or two stages of extension (e.g., stable crack extension followed by unstable extension) under transient thermal and mechanical loadings. Also, crack initiation was investigated in connection with clad surfaces and with biaxial loading conditions. Procedural steps for FALSIRE II essentially followed the format used for FALSIRE I. The CSNI/FAG prepared comprehensive problem statements for each of the reference experiments, including supporting information and available analysis results. The statements provided the basis for evaluations that were performed by an international group of analysts using a variety of techniques. A FALSIRE II Workshop was held November 8–10, 1994, in Atlanta, Georgia, which focused on analyses of the reference fracture experiments. More than 30 participants representing 22 organizations from 12 countries took part in the workshop. Final results for 45 analyses of the reference experiments were received from the participating analysts. For each experiment, analysis results provided estimates of variables that included temperature, crack-mouth-opening displacement, stress, strain, and applied K and J values. The data were sent electronically to the Organizing Committee, who assembled the results into a comparative data base using a special-purpose computer program. A comparative assessment and discussion of the analysis results are presented in the report. Generally, structural responses of the test specimens were predicted with tolerable scatter bands; these represent a marked improvement over the results achieved in the initial phase (FALSIRE I). The analyses revealed that the loss-of-constraint effects observed in specific cases require a second (or dual) fracture parameter to be introduced into the fracture model to characterize crack-tip conditions. Additional toughness data obtained from a range of specimen geometries and constraint conditions are required to validate these dual-parameter cleavage fracture methodologies. Finally, proposals for future work in the context of cooperative international analytical projects similar to FALSIRE are provided.

Contents

List of Figures

List of Tables

Executive Summary

This report summarizes the recently completed Phase II of the Project for Fracture Analysis of Large-Scale International Reference Experiments (FALSIRE). Project FALSIRE was created by the Fracture Assessment Group (FAG) of the Organization for Economic Cooperation and Development/Nuclear Energy Agency's (OECD/NEA's) Committee on the Safety of Nuclear Installations (CSNI) Principal Working Group No. 3 (PWG-3). The CSNI/FAG was formed in 1988 for the purpose of evaluating fracture prediction capabilities used in safety assessments of nuclear reactor components. Members of the CSNI/FAG are from laboratories and research organizations in Western Europe, Japan, and the United States. To meet its obligations, the CSNI/FAG initiated an international project (FALSIRE I) in 1988 to assess various fracture methodologies through interpretive analyses of selected large-scale fracture experiments. On behalf of the CSNI/FAG, the Oak Ridge National Laboratory (ORNL) in the United States (U.S.A.) and the Gesellschaft für Anlagen-und Reaktorsicherheit (GRS) in Köln, Germany, had responsibility for organizational arrangements related to FALSIRE I.

In FALSIRE I, six reference thermal-shock experiments were selected for detailed analysis and interpretation by the CSNI/FAG. Generally, these experiments examined various aspects of fracture initiation and ductile crack growth in reactor pressure vessel (RPV) steels under pressurized-thermal-shock (PTS) loading conditions. Thirty-seven participants representing 19 organizations provided a total of 39 analyses of the experiments using a variety of structural and fracture mechanics techniques. A 3-day workshop was held in Boston, Massachusetts, during May 1990, at which all participating analysts examined these evaluations in detail.

A final report was prepared on FALSIRE I, which highlighted conclusions and recommendations derived from interpretations of the comparative fracture assessments. These assessments confirmed the importance of adequately modeling structural behavior of the test specimens before performing fracture mechanics evaluations. Applications of various single-parameter fracture methodologies were found to be partially successful in some cases, but not in others. Some analyses were performed from a safety assessment perspective to achieve a conservative prediction; the results tended to show significant deviation from experimental data and best-estimate analyses. Proposals for follow-on work in the context of a FALSIRE II project were included in the report.

It was proposed that the follow-on FALSIRE II project should emphasize experiments that focus on behavior of relatively shallow cracks subjected to combined thermal and mechanical loading in the transition temperature region. If possible, experiments for cracks showing two stages of extension (e.g., stable crack extension followed by unstable extension) should be included. Investigations of crack initiation and extension in connection with clad surfaces were also proposed. In 1993, these criteria were utilized by the CSNI/FAG to select a new set of experiments for the FALSIRE II project.

The experiments utilized in FALSIRE II examined various aspects of the cleavage fracture process in RPV steels for a wide range of materials, crack geometries, and constraint and loading conditions. PTS loading transients were applied in three of the experiments by internally pressurizing a heated vessel containing a sharp crack and thermally shocking it with a coolant on the inner surface (NKS-5 and -6, from Materialprüfungsanstalt, Stuttgart, Germany) or outer surface (PTS-I/6, from Central Research Institute of Structural Materials, Russia, VTT Manufacturing Technology and IVO International Ltd., Finland). In the spinning cylinder experiment (SC-4, from AEA Technology, United Kingdom), a thick cylinder with two deep cracks on the inner surface was thermally shocked with a water spray while simultaneously spinning the cylinder about its axis in a specially constructed rig. Clad beams (DD2 and DSR3, from Electricité de France) subjected to uniform temperature and unaxial four-point bending were used to investigate initiation of shallow underclad cracks in the base material. The influence of out-of-plane biaxial loading on cleavage fracture toughness of shallow cracks in the transition temperature region was studied using a biaxially loaded cruciform beam (BB-4, from Oak Ridge National Laboratory, U.S.A.). Data provided in the CSNI/FAG problem statements for these experiments included pretest material characterization, geometric parameters, loading histories, instrumentation, and measured results for temperatures, strains, crack-mouth-opening displacements (CMODs), and crack extension histories.

More than 30 participants representing 22 organizations from 12 countries performed a total of 45 analyses of the 7 reference fracture experiments in FALSIRE II. These organizations took part in the FALSIRE II Workshop held during November 1994, in Atlanta, Georgia, to assess these analyses and the relevant fracture methodologies. The analysis techniques employed by the participants focused

primarily on finite-element methods; these techniques were combined with single- or dual-parameter constraint methodologies for fracture mechanics assessments. A list of Special Requirements (SRs) was prepared for each reference experiment and distributed to participating analysts in advance of the workshop. The SRs comprise a set of quantities that characterize the thermal/structural behavior of the test specimens and the fracture behavior of the cracks. Prior to the workshop, participants provided the Organizing Committee (OC) with analytical results for the parameters included in the SRs. For each of the experiments, these parameters included temperature, CMOD, strains, stresses, crack loading in terms of J-integral and stress intensity factor, as well as various constraint parameters. Also, conditions of crack initiation were identified in the experiments, and where possible, computed values of parameters were compared with measured data. The analysis results and measured data have been compiled into an electronic data base. For each experiment, the results are available in 40 to 50 comparative plots generated from the data base using a special-purpose evaluation program.

The report provides an overview of the comparative assessments, which are based predominantly on the fracture mechanics results compiled from discussions of each reference experiment at the FALSIRE II Workshop and from the analysis results data base. A comprehensive selection of comparative plots from the data base serves as the focal point for discussion of these assessments. Analyses provided by organizations participating in FALSIRE II are identified by an alphanumeric code to preserve the public anonymity of the contributors.

Some conclusions drawn from the FALSIRE II Workshop and from an evaluation of the analysis results data base follow:

- The temperature distributions in the specimens loaded by thermal shock generally were approximated with high accuracy and small scatter bands. Discrepancies appeared only for limited time periods during the transients and could be traced to different assumptions concerning the heat transfer coefficients.

- Structural response (i.e., CMOD, strains, etc.) of the test specimens was predicted reasonably well from best-estimate analyses. This outcome represents a significant change compared with some of the results achieved in FALSIRE I. In part, the change reflects a more widespread recognition that the assumptions adopted to ensure failure avoidance in safety assessments are inappropriate when attempting to predict actual failure.

- Discrepancies that appeared in the structural calculations could usually be traced to the assumed material models and to approximations of material properties (i.e., stress-strain data).

- Calculations of fracture parameters such as J or K_I and the parameter CMOD generally showed small scatter bands. Discrepancies could be traced to the differences between elastic and elastoplastic approaches or assumptions concerning material properties.

- The K_I vs temperature diagram combined with material data curves describing fracture toughness vs temperature were determined to be useful for fracture assessments of crack behavior. Crack initiation could be predicted from a single fracture parameter (K_I, J, etc.), reasonably well in tests where initiation was not significantly affected by constraint effects.

- When constraint effects become significant, a single parameter is not sufficient to characterize crack-tip conditions, and a second parameter must be introduced into the fracture model. Candidate constraint parameters employed by the participating analysts include Q-stress, stress triaxiality h, local approach of cleavage fracture, and a strain-based function of the plastic-zone width in the crack plane. In the SC-4 experiment, constraint effects were quantified using the Q-stress and, to a more limited degree, the triaxiality parameter h. In PTS-I/6 and NKS-5, the parameter h showed indications of loss-of-constraint, while the Q-stress was not evaluated. Finally, in BB-4, a shallow-crack effect was demonstrated by the computed Q-stress, which indicated a loss-of-constraint associated with the departure of in-plane stresses from reference small-scale yielding conditions.

- The Q-stress and other stress-based constraint methodologies have been applied successfully to correlate constraint conditions for in-plane (or uniaxial) loading conditions. However, prior studies have determined that stress-based constraint methodologies (such as the Q-stress) are not sensitive to changes in constraint conditions due to changes in out-of-plane biaxial loading. The plastic zone width was employed successfully to correlate changes in constraint conditions for shallow cracks subjected to changes in out-of-plane biaxial loading ratios. Further investigations are necessary to clarify whether one parameter can be recommended or a set of parameters should be computed to assess constraint effects.

- Additional toughness data measured in the transition temperature region using a range of specimen geometries and constraint conditions are required to validate the predictive capabilities of cleavage fracture methodologies that incorporate constraint effects.

- Simulations of crack growth and crack arrest events (e.g., in NKS-6) showed large uncertainties among the applied fracture methods.
- Additional data concerning the HAZ fracture toughness are necessary for further refinement of analyses of shallow subclad flaws.
- Almost all participants elected to use the finite-element method in addressing the problems of FALSIRE II. This represents a marked change from FALSIRE I, which included applications of a number of different estimation schemes. The detailed information that participants were asked to provide from the analyses in FALSIRE II encouraged the use of finite-element methods over estimation schemes (see the Special Requirements given in the appendix). It should not be inferred from the outcome of FALSIRE II that detailed finite-element analyses are always the preferred or necessary technique for structural integrity assessments.

A proposal for future work in the context of a cooperative international analytical project similar to FALSIRE is provided in the report. An RPV Benchmark Analysis Project is being planned for the benefit of organizations concerned with evaluation of fracture methodologies used in RPV integrity assessments. This project is motivated in part by the strong interest expressed by participants in Phases I and II of FALSIRE to proceed with further evaluations of fracture mechanics analysis methods. The RPV Benchmark Analysis Project will focus on a Western-type four-loop RPV with cladding on the inner surface. Primary emphasis of the project will be the behavior of relatively shallow cracks (underclad and through-clad) at different locations in the vessel when subjected to PTS-type loading. Effects of cladding and constraint on cleavage fracture will be studied.

A detailed analysis matrix will be defined for the vessel that includes selected cases of transient thermomechanical loading associated with postulated loss-of-coolant accidents. Different assumptions will be made concerning the thermally shocked regions on the inner surface of the vessel. The number of cooling strips under the inlet nozzles will be varied, as well as the width of the cooled strips, so that comparisons can be made with the loading case due to axisymmetric cooling. Additional tasks will be proposed that can be addressed using thermohydraulic analysis techniques.

The schedule for the RPV Benchmark Analysis Project calls for the OC to commence distribution of problem statements in 1996. Analysts participating in the Benchmark Project will be requested to submit analysis results to the OC by mid-1997 in preparation for a workshop scheduled for Fall 1997 in the Eastern United States. A final report will be issued after completion of the workshop.

Acknowledgment

Gratitude is expressed to the U. S. Nuclear Regulatory Commission and the German Minister for Education, Science, Research, and Technology (BMBF) for sponsoring our work in support of FALSIRE. Furthermore, the authors thank each participant listed in Table 1.6 for cooperation in supplying the experimental data and performing the analytical work.

1 Introduction

This report summarizes the recently completed Phase II of the Project for Fracture Analysis of Large-Scale International Reference Experiments (FALSIRE II). Project FALSIRE was organized for the purpose of evaluating fracture prediction capabilities used in the nuclear industry through applications to selected international fracture experiments. Chapter 1 provides a review of the organization of Project FALSIRE, which has completed two phases of comparative fracture assessments of large-scale experiments. Detailed descriptions of the conditions and results for each of the fracture experiments studied in FALSIRE II are given in Chap. 2. A comprehensive assessment and discussion of the analysis results for each of the experiments is presented in Chap. 3. Based on this assessment, some conclusions concerning the predictive capabilities of fracture methodologies employed by the participants in FALSIRE II are given in Chap. 4. Finally, proposals for future work in the context of cooperative international analytical projects similar to Project FALSIRE are provided in Chap. 5.

Gesellschaft für Anlagen-und Reaktorsicherheit (GRS), Köln, Germany, and Oak Ridge National Laboratory (ORNL), United States, have responsibility for organizational arrangements related to Project FALSIRE and for preparation of this document.

1.1 Organization of Project FALSIRE

Project FALSIRE is sponsored by the Fracture Assessment Group (FAG) of the Organization for Economic Cooperation and Development/Nuclear Energy Agency's (OECD/NEA's) Committee on the Safety of Nuclear Installations (CSNI) Principal Working Group No. 3 (PWG-3). Motivation for the project was derived from recognition by the CSNI/PWG-3 that inconsistencies were being revealed in predictive capabilities of a variety of fracture assessment methods. As a consequence, the CSNI/FAG was formed in 1988 to evaluate fracture prediction capabilities currently used in safety assessments of nuclear components. Members were from laboratories and research organizations in Western Europe, Japan, and the United States.

To meet its obligations, the CSNI/FAG planned an international project to assess various fracture methodologies through interpretive analyses of selected large-scale fracture experiments. A survey of large-scale experiments and related analyses was given at the first meeting of the group in May 1988 at Stuttgart, Germany. Priority was given to thermal-shock experiments to include combinations of mechanical and thermal loads. Reference experiments were selected for detailed analysis and interpretation by the CSNI/FAG at their second meeting in August 1989 at Monterey, California. (The reference experiments and testing organizations are given in Table 1.1; detailed descriptions of the experiments are given in Refs. 1 and 2.) Before the 1989 Monterey meeting, the CSNI/FAG established a common format for comprehensive statements of these experiments, including supporting information and available analysis results. These statements formed the basis for evaluations of the experiments that were performed by an international group of analysts using a variety of structural and fracture mechanics techniques. Based on the CSNI/FAG problem statements, 37 participants representing 19 organizations performed a total of 39 analyses of the experiments. A 3-day workshop was held in Boston, Massachusetts, during May 1990, at which all participating analysts examined these evaluations in detail.

Table 1.1 Large-scale fracture experiments analyzed in Phase I of CSNI/FAG Project FALSIRE

Experiment[a]	Organization	Testing country
NKS-3	Materialprüfungsanstalt (MPA), Universität Stuttgart	Germany
NKS-4	MPA, Universität Stuttgart	Germany
PTSE-2A	ORNL	U.S.A.
PTSE-2B	ORNL	U.S.A.
SC-I	AEA Technology, Risley	U.K.
SC-II	AEA Technology, Risley	U.K.
Step B PTS	Japan Power and Engineering Inspection Corporation (JAPEIC)	Japan

[a]Descriptions of the experiments and comparative FALSIRE assessments are given in Refs. 1 and 2.

Using results from the workshop, ORNL and GRS jointly completed a final report on Phase I of Project FALSIRE that was published as a NUREG report[1] and a GRS report.[2] Generally, results presented in the report highlight the importance of adequately modeling structural behavior of specimens before performing fracture mechanics evaluations. Applications of the various single-parameter fracture methodologies were found to be partially successful in some cases, but not in others. Based on these assessments, some conclusions concerning predictive capabilities of selected ductile fracture methodologies, as applied to reactor pressure vessels (RPVs) subjected to pressurized-thermal-shock (PTS) loading, were given, and

recommendations for future development of fracture methodologies were made. Finally, proposals for follow-on work in the context of a Phase II of Project FALSIRE were included in the report.

1.2 FALSIRE II

Following completion of Phase I of Project FALSIRE, several participating organizations indicated a desire to proceed with further evaluation of fracture mechanics analysis methods in a Phase II program. Stimulated by somewhat unfavorable results from analyses of the PTSE-2 experiment in Phase I, it was proposed in Refs. 1 and 2 that FALSIRE II should emphasize experiments that focus on behavior in the transition temperature region of relatively shallow cracks subjected to combined thermal and mechanical loading. If possible, experiments for cracks showing two stages of extension (e.g., stable crack extension followed by unstable extension) should be included. Investigations of crack extension in connection with clad surfaces should also be included. In response to these recommendations, the Organizing Committee (OC) of CSNI/FAG formulated an action plan for a Phase II program that was based on the schedule of events given in Table 1.2. (The OC consists of H. Schulz, Chairman of CSNI/FAG, J. Sievers, and R. Bass).

1.2.1 Reference Experiments

In 1992, a proposal was made to CSNI/PWG-3 by the chairman of CSNI/FAG to initiate planning for FALSIRE II. After obtaining approval from CSNI/PWG-3, the OC of CSNI/FAG contacted informally several international organizations to request preliminary information on a new set of candidate experiments for possible use in FALSIRE II. These organizations are listed in Table 1.3 along with the candidate experiments that were subsequently proposed by each organization. (A description of the experiments is given in Chap. 2 of this report.) A summary of the test objectives for each of the experiments proposed for FALSIRE II is given in Table 1.4. Relevant features of each experiment are given in Table 1.5.

During May 1993, each of the organizations in Table 1.3 provided detailed information on the candidate experiments

Table 1.2 Schedule of events for Phase II CSNI/FAG Project FALSIRE

November 1993	OC distributes problem statements and participant response form
February 1994	Participants submit response forms to OC
April 1994	OC distributes 1-page reminder concerning submission of structural analysis results from participants
May 1994	Participants submit summaries of structural analysis results to OC
May 1994	OC meets to review (1) progress in Phase II and (2) structural analysis results submitted by participants
June 1994	Participants submit summaries of fracture mechanics assessment to OC
August 1994	OC completes development of evaluation programs FEDIT/FPLOT
October 1994	OC compiles analysis results submitted electronically by participating analysts
November 8–10, 1994	OC hosts Phase II FALSIRE Workshop for participating analysts in Atlanta, Georgia
March 1995	Participants submit additional data and analysis results to OC (action items)
May 1995	OC meets to review progress in preparation of final report and to discuss future work of CSNI/FAG
February 1996	OC submits draft final report for reviews
March 1996	OC completes final report
Spring 1996	OC submits final report to CSNI/PWG-3
Spring 1996	Publication of final reports—ORNL/NRC (NUREG); GRS/CSNI

Table 1.3 Large-scale reference fracture experiments selected for FALSIRE II

Experiment	Organization	Testing country
Thick cylinder, thermal/ centrifugal load (SC-4)	AEA Technology, Risley	U.K.
Thick cylinder, thermal/pressure load (PTS-I/6)	Central Research Institute of Structural Materials (Prometey)[a] Technical Research Center of Finland (VTT)[b]	Russia Finland
Clad beam, isothermal/uniaxial bend load (DD2, DSR3)	Electricité de France (EdF)	France
Thick cylinder, thermal/pressure/ tension load (NKS-5, NKS-6)	MPA, Universität Stuttgart	Germany
Cruciform beam, isothermal/ biaxial bend load (BB-4)	ORNL	U.S.A.

[a]Organization performing test.
[b]Organization performing analysis.

Table 1.4 Summary of test objectives of large-scale experiments used in FALSIRE II

Experiment (place)	Objective
SC-4 (AEA Technology, U.K.)	Investigate transition fracture behavior for surface cracks in thick-section steel specimen under thermal-shock loading conditions
PTS-I/6 (Prometey, Russia)	Investigate crack initiation and arrest of a shallow-surface crack in a bimaterial thick-section steel specimen under PTS loading conditions
DD2, DSR3 (EdF, France)	Investigate cleavage initiation of shallow underclad cracks in clad beams subjected to four-point bending
NKS-5 (MPA, Germany)	Investigate unstable crack propagation in transition region of two symmetrically placed surface cracks in thick-section steel specimen under PTS loading conditions
NKS-6 (MPA, Germany)	Investigate unstable crack propagation and arrest of fully circumferential crack in low-toughness vessel material in thick-section steel specimen under PTS loading conditions
BB-4 (ORNL, U.S.A.)	Investigate influence of biaxial loading on cleavage fracture toughness of shallow cracks using biaxially loaded cruciform beam

to the OC of CSNI/FAG using the special problem statement format developed by the CSNI/FAG during Phase I of FALSIRE; a sample problem statement is included in Appendix A of Refs. 1 and 2. The format of the problem statement consists of 16 pages of questions that are intended to provide information on a full range of topics, including the following:

1. general information, including the cognizant contact for the organization performing the experiment;
2. testing facility;
3. specimen geometry;
4. material, physical, and fracture properties;
5. loading conditions;
6. instrumentation;
7. test data and experimental results;
8. available analysis results; and
9. comparison of experimental and analysis results.

The preliminary draft problem statements provided by the testing organizations listed in Table 1.3 were examined in considerable detail by the OC for clarity, completeness, and compatibility with FALSIRE II objectives. The OC elected to accept all of the experiments in Table 1.3 for

Table 1.5 Summary of FALSIRE II reference experiments

Experiment (place)	Material toughness[a] A_V^{us}/T_{50J}	Loading[b,c]	Crack, specimen geometry[d]	Crack growth
SC-4 (AEA, U.K.)	>90 J/100°C	Thermal shock $T_o = 305°C/T_c = 7°C$	Two cracks (1 and 2) partly axial (max a/t = 0.2 and 0.3) at the inner surface of a cylinder (R_i = 500 mm, T = 200 mm)	Crack 1: cleavage[e] 0–71 mm Crack 2: cleavage[e] 0–32 mm
PTS 1/6 (Prometey, Russia)	Base material 120 J/110°C Weld material 120 J/40°C	Thermal shock $T_o = 280°C/T_c = 15°C$ Internal pressure (transient)	Partly axial crack (max a/t = 0.25) at the outer surface of a cylinder vessel (R_i = 340 mm, t = 150 mm)	Cleavage 0–90 mm and arrest in base material; cleavage 0–13 mm and arrest in weld material
DD2, DSR3 (EdF, France)	Not yet available	Four-point bending at $T_o = -170°C$	Semielliptical underclad crack (max a/t = 0.04; 0.11) in a cladded four-point bending specimen (cross section 120 × 145 mm)	Cleavage without crack arrest
NKS-5 (MPA, Germany)	Base material 90 J/140°C Weld material 220 J/–60°C	Thermal shock $T_o = 230°C/T_c = 18°C$ Axial tension Internal pressure (constant)	Two cracks partly circumferential (max a/t = 0.135) at the inner surface of a cylinder (R_i = t = 200 mm)	Cleavage in base material; depth 13-mm circumferential 220°; arrest at base metal/weld metal interface
NKS-6 (MPA, Germany)	Base material[f] 30 J Weld material 220 J/–60°C	Thermal shock $T_o = 280°C/T_c = 20°C$ Axial tension Internal pressure	Circumferential crack (a/t = 0.185) at the inner surface of a cylinder (R_i = t = 200 mm)	Cleavage 20 mm in base material; ductile extension 41 mm; arrest at base metal/weld metal interface
BB-4 (ORNL, U.S.A.)	L-T orientation 330 J/–40°C T-L orientation 245 J/–40°C	Biaxial bending (ratio 0.6:1) at $T_o = -45°C$	Straight-through crack (a/t = 0.1) in a cruciform-shaped specimen (cross section 91 × 111 mm)	Cleavage initiation preceded by 0.08-mm ductile tearing

[a] A_V^{us} = Charpy V-notch upper shelf energy.
[b] T_o = initial crack-tip temperature/test temperature.
[c] T_c = cooling water temperature.
[d] R_i = internal radius,
t = wall/specimen thickness,
a = crack depth.
[e] Predominantly in axial direction.
[f] Maximum Charpy energy lower than 50 J.

FALSIRE II, contingent upon certain modifications to the statements being completed satisfactorily. The final version of these problem statements provided the basis for evaluations performed by the analysts participating in FALSIRE II.

To publicize FALSIRE II internationally, the OC prepared a two-page, call-for-participation announcement that was distributed to the participants of Phase I, to the American Society for Mechanical Engineers (ASME) Pressure Vessel and Piping Conference in July 1993, and to the 12th International Conference on Structural Mechanics in Reactor Technology (SMiRT) in August 1993. The announcement described the objectives and schedule for FALSIRE II and included a form to allow prospective participants to declare their intentions to the OC by return mail.

1.2.2 FALSIRE II Workshop

Subsequent procedural steps for FALSIRE II essentially followed the format used for FALSIRE I. The completed problem statements for each reference experiment were distributed to participating analysts beginning in November 1993. Participants were requested to provide summaries of structural analysis results to the OC in April 1994. A total of 26 preliminary analyses prepared by an international group of analysts participating in FALSIRE II were submitted to the OC on special documentation forms. The submitted results were reviewed and assessed by the OC during scheduled May 1994 working sessions held at GRS. The primary purpose of this evaluation was to ensure that proper modeling of structural response was being achieved by analysts prior to performing fracture assessments of the reference experiments.

Documentation describing final results from fracture mechanics assessments of the reference experiments was requested from the participants starting at the end of June 1994. Analysts were asked to transmit their results electronically to GRS, where a special-purpose computer program was developed to organize the analyses into a comparative data base. This data base also includes selected portions of the measured data generated in the six reference experiments. Summaries were generated from the data base for use in the FALSIRE II Workshop.

The FALSIRE II Workshop was held November 8–10, 1994, at the Terrace Garden Hotel in Atlanta, Georgia. More than 30 participants representing 22 organizations from 12 countries took part in the workshop that focused on analyses of the reference fracture experiments; the organizations participating in the workshop are given in Table 1.6. Final results for 45 analyses of the reference experiments were received by the OC from the participating analysts (see Chap. 3). A major objective of the workshop was for participating analysts to achieve an understanding of the comparative relationships among the analytical results, that is, why various analyses may agree or disagree with one another or with the available measured data. To facilitate achieving this objective, the OC adopted a workshop format that incorporates several notable features.

Table 1.6 Organizations participating in the FALSIRE II Workshop in Atlanta during November 1994

Organization	Country
AEA Technology	U.K.
Bhabha Atomic Research Center (BARC)	India
Commissariat á l'Energie Atomic (CEA) Centre d'Etudes Nuclearies de Saclay	France
Engineering Center of Nuclear Equipment Strength, Reliability & Lifetime (ECS)	Russia
EdF	France
FMC Corporation	U.S.A.
Framatome	France
Fraunhofer Institut für Werkstoffmechanik (IWM)	Germany
GRS	Germany
Institute for Problems of Strength (IPS)	Ukraine
Kurchatov Institute	Russia
Nuclear Electric (NE)	U.K.
Onsala Inqenjorsbyra	Sweden
ORNL	U.S.A.
Paul Scherrer Institut (PSI)	Switzerland
Central Research Institute of Structural Mechanics (Prometey)	Russia
Staatliche MPA Universität Stuttgart	Germany
VTT	Finland
Siemens (KWU)	Germany
University of Maryland	U.S.A.
University of Pisa	Italy
University of Tokyo	Japan

Prior to the workshop, participants were provided with comparative summaries of each of the reference experiments for which they had submitted a solution. These summaries were transmitted by fax in October 1994 to provide analysts with an opportunity to prepare responses to particular issues raised by the comparisons in advance of the workshop. Also, participants were requested to perform a quality assurance check of their results depicted in the summaries prepared by GRS and to quickly inform the OC of any discrepancies. The comparative summaries were based on analysis results received by the OC at GRS through October 9, 1994; the contents were defined by the

Special Requirements (SRs) forms prepared for each reference experiment by the OC and provided to the participants. Comparative summaries of all analysis results submitted for the reference experiments were also made available to participating analysts upon their arrival at the workshop in Atlanta.

The format of the workshop sessions in Atlanta focused on discussions dedicated to each of the six reference experiments over a period of ~ 2 1/2 days. For each experiment, a panel was assembled that included (1) all of the analysts contributing solutions to that experiment and (2) a representative of the institution that performed the experiment. Discussion of each experiment was initiated with a presentation from the institutional representative describing the details of the experiment, including objectives, experimental setup, instrumentation, loading conditions, test results, measured data, etc. This was immediately followed by a brief review of the SRs and the comparative summaries compiled by the OC from the submitted analyses; the purpose was to highlight significant features of the comparisons. The latter presentation was made by the OC member responsible for compilation of the analytical summaries for the experiments (J. Sievers). Next, each of the individual panelists was asked to participate in the discussion by addressing factors that potentially influenced the outcome of the analytical assessments. Comments and questions concerning the analyses and experimental results were also welcomed at this point from workshop participants not on the panel. A major objective of this discussion was to develop a consensus among the participants regarding the effectiveness of the various fracture methodologies used to assess the reference experiment. A designated secretary drawn from the participants (S. McAllister) was responsible for drafting a brief summary of the conclusions derived from discussions of the analytical assessment.

The final session of the workshop was moderated by the CSNI/FAG chairman (H. Schulz). Summaries of the results and conclusions developed from discussions of each reference experiment were distributed to participants to provide a basis for a general assessment of the FALSIRE II analysis results. A discussion of future goals and plans for the CSNI/FAG also took place at that time.

1.2.3 Workshop Action Items

At the FALSIRE II Workshop, an extensive list of action items was compiled for each of the reference experiments to resolve outstanding issues raised in discussions of the experimental and analytical results. After the workshop was concluded, the OC prepared and distributed detailed requests for supplemental information and analysis results to be provided by the testing organizations and the participating analysts. Ten organizations provided a response to the requests from the OC. The data received from these organizations were reviewed by the OC and incorporated into the FALSIRE II data base compiled for the reference experiments. Also, evaluations were made concerning the impact of these data on completion of the list of action items drafted during the workshop. The majority of these action items were addressed in the responses received from the participants and have been included in the final assessment of the analysis results.

References

1. B. R. Bass, C. E. Pugh, J. Keeney-Walker, H. Schulz, and J. Sievers, Martin Marietta Energy Systems, Inc., Oak Ridge Natl. Lab., *CSNI Project for Fracture Analysis of Large-Scale International Reference Experiments (Project FALSIRE)*, USNRC Report NUREG/CR-5997 (ORNL/TM-12307), June 1993.*

2. J. Sievers, H. Schulz, B. R. Bass, C. E. Pugh, and J. Keeney-Walker, *CSNI Project for Fracture Analysis of Large-Scale International Reference Experiments (Phase I)*, GRS-108, NEA/CSNI/R (94) 12, Gesellschaft für Anlagen-und Reaktorsicherheit, Köln, Germany, April 1994.

*Available for purchase from National Technical Information Service, Springfield, VA 22161.

2 Description of FALSIRE II Reference Experiments

This chapter provides a summary of each reference experiment selected for FALSIRE II and characterized in Tables 1.3–1.5. These summaries are intended to provide available information on specimen geometry, test material, loading conditions, experimental results, and selected bibliographic references for each experiment. Information on the experiments is based on problem statements and supporting documents provided to the OC by the cognizant organizations. The experimental results were accepted from these organizations without qualifying the data. Because a consistent set of data was not available for all reference experiments, information from the above-mentioned categories was not uniformly available at the same level of detail for all experiments. Thus, emphasis on certain features varies among the individual summaries.

The objectives of the experiments were to evaluate fracture analysis methods, as well as to demonstrate special effects, such as the influence of biaxial loading on fracture toughness. Generally, the problems modeled by the reference experiments should contribute to understanding the behavior of postulated cracks in RPVs within the transition temperature region in the case of overcooling accidents. Note that the materials, loadings, and specimen/crack geometries used in these experiments were designed to obtain the desired results in the presence of financial and technical limitations.

2.1 Spinning Cylinder Experiment (SC-4)

The Spinning Cylinder (SC) project[1] at AEA Technology, Risley, United Kingdom, is concerned with investigation of fracture behavior in thick-walled test specimens under severe thermal-shock and simulated pressure loading conditions. A special test rig was constructed at Risley to produce the appropriate loading conditions. The general arrangement of the SC thermal-shock apparatus is shown in Fig. 2.1, where the central feature is an 8-ton cylindrical test specimen (1.3-m-long, 1.4-m OD, 200-mm wall thickness as shown in Fig. 2.2) suspended by a flexible shaft

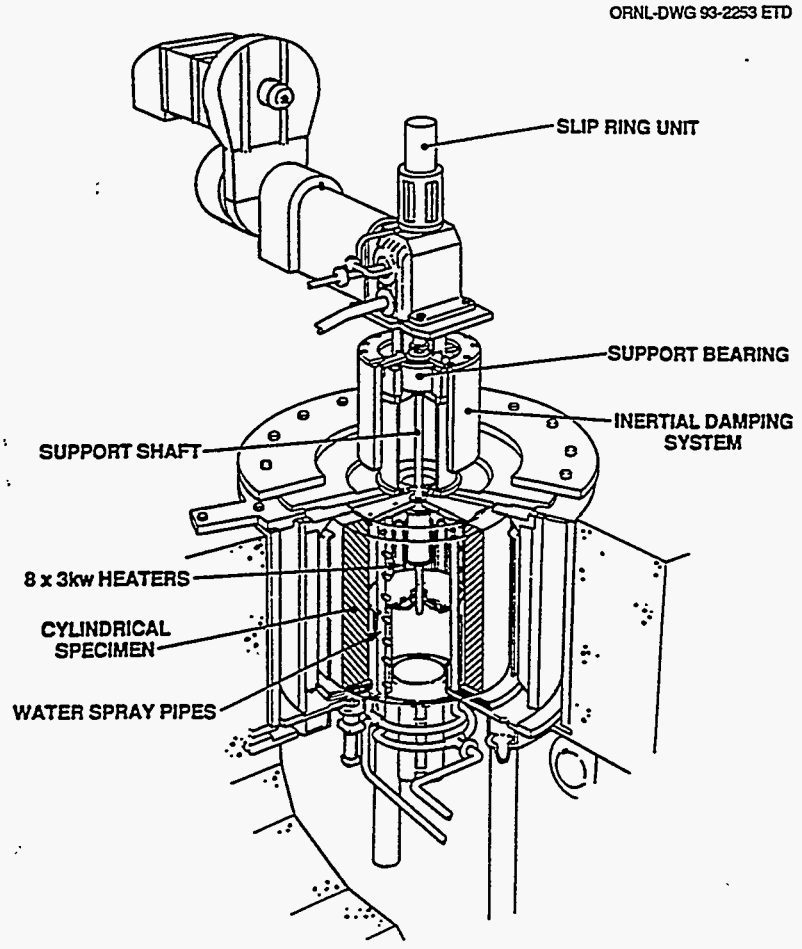

Figure 2.1 Experimental facility at AEA-Risley for performing thermal-shock tests with spinning cylinders

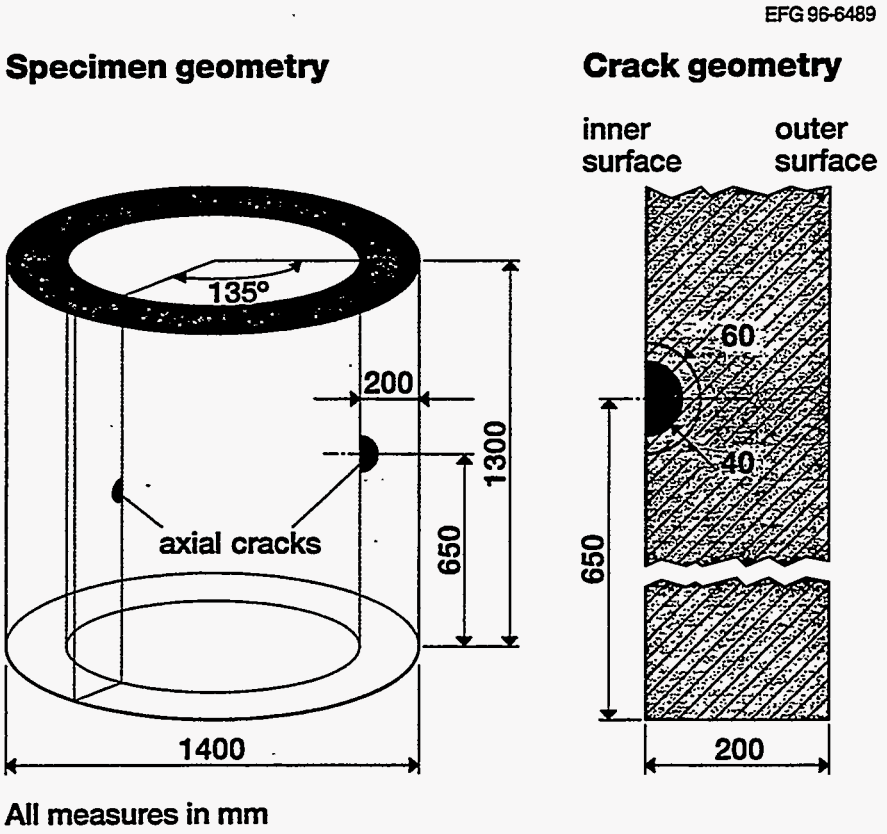

Figure 2.2 Test cylinder and crack geometry for SC-4 experiment (AEA-Risley, U.K.)

from a single pivoted bearing so that it is free to rotate about the vertical axis. The driving power is provided by a 375-kW dc motor that is capable of a maximum design speed of about 3500 rpm at the rotor. A damping device (not shown) is attached to the bearing pivot to stabilize the rotor against aerodynamically induced precessional motion. Eight 3-kW heaters mounted vertically within the cylinder enclosure provide the necessary heat to raise the specimen to the required test temperature of ~300°C. Pressure loading can be simulated by rotating the cylinder about its own axis; the generated hoop stress distribution resembles that in a large-diameter pressurized vessel. A stationary water spray system within the cylinder provides the mechanism for thermally shocking the rotating inner surface (Fig. 2.3). According to researchers at Risley, the design ensures uniformity of cooling and very high heat transfer coefficients at moderate speeds.

A series of large-scale experiments has been conducted in the Risley SC facility. The first three were concerned with fully ductile upper-shelf fracture; as indicated in Table 1.1, two of these experiments were used in Phase I of Project FALSIRE. The fourth spinning cylinder experiment (SC-4) was an investigation into transition fracture behavior under contained yield in a thick-section, low-alloy steel structure subjected to severe thermal shock.[1] The stated objectives of SC-4 and the associated fracture analysis and material characterization programs were

- to determine the toughness near the inner surface of a thermally shocked thick-walled specimen in which the material yields near the quenched surface,
- to compare the measured toughness with the transition toughness curve determined from standard test specimens,
- to evaluate the methods used in the assessment of part-penetration defects under severe thermal-shock conditions when the elastically calculated peak stresses exceed yield, and
- to provide information concerning the arrest of a cleavage fracture.

2.1.1 Specimen Geometry

Figure 2.2 depicts the test specimen containing two semicircular defects at the inner surface, which were oriented in an axial plane, located halfway along the length of the cylinder and separated by 135°; both were fatigue precracked. Two sizes of defect (40- and 60-mm radii) were produced to maximize the likelihood of achieving the test objectives.

EFG 96-6490

Thermal and mechanical loading

rotation velocity:
ω = 530 rpm at T = 305°C

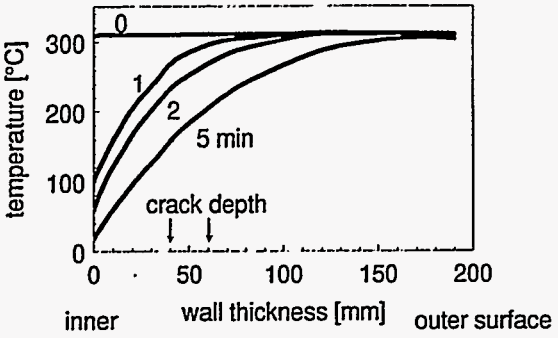

Material characterization (A 508 class 3)

yield stress $R_{p0,2}$ [MPa]	543 (20°C) 521 (290°C)
charpy energy for upper shelf [J]	> 90
$T_{50\,J}$ [°C]	100

Figure 2.3 Loading and test material data for SC-4 specimen

2.1.2 Material Properties

The SC-4 test was performed on a specimen extracted from a single large steel forging with the chemical composition of A 508 Class 3 steel that was given a nonstandard heat treatment to provide suitable mechanical properties for test purposes. A summary of the chemical analysis and the thermal heat treatment is given in Table 2.1. The 200-mm-thick forging consisted of two cylinders separated by a centrally located test ring and bounded top and bottom by additional test rings (Fig. 2.4). The test rings were parted from the cylinders after forging and heat treatment were completed. Values of physical properties obtained from analysis of the test rings are given in Table 2.2. Four tensile tests were performed on circumferentially oriented test specimens, two at 20°C according to BS 18 and two at 290°C according to BS 3688. In all cases, specimens of 22.5-mm diameter and 127-mm gage length were used. Values for all four tests are given in Table 2.3. No significant effects of either axial or circumferential forging

Table 2.1 Chemical analysis and thermal heat treatment of SC-4 test material

Chemical analysis (%)							
C	Si	Mn	S	P	Cr	Mo	Ni
0.23	0.23	1.32	0.011	0.012	0.08	0.5	0.73

Heat treatment	
Austenize	6 h at 950°C
Quench	Water quench from 950°C
Temper	8 h at 580°C ± 10°C

EFG 96-6491

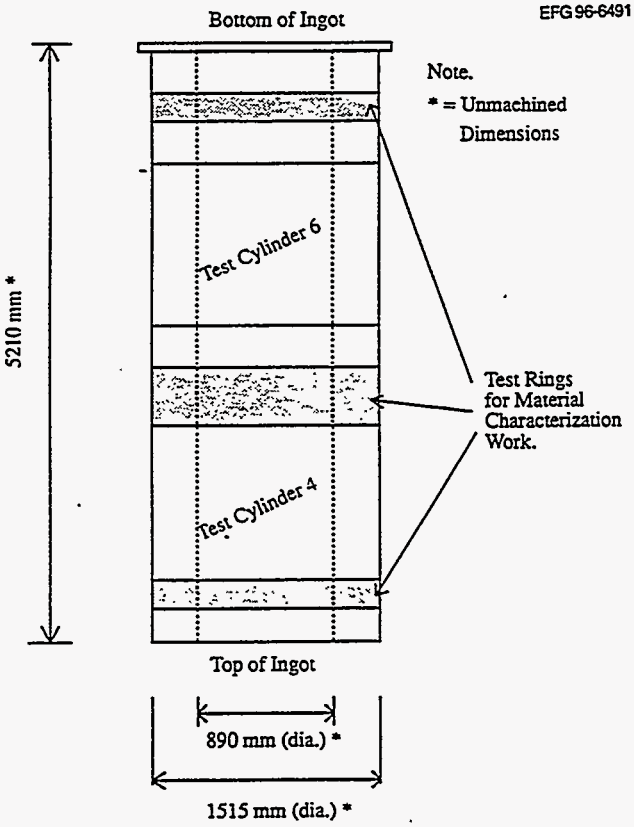

Figure 2.4 Position of test cylinder SC-4 and material characterization test rings within overall forging

position were reported with respect to engineering tensile properties. The true stress/true plastic strain properties across the temperature range of 20 to 350°C were also

Table 2.2 Physical properties of SC-4 specimen material

Heat convection coefficient h, W/m^2 K	$3{,}000 < h < 5{,}000$ $5{,}000 < h < 20{,}000$ $20{,}000 < h < 5{,}000$	for t = 0 to 2 min for t = 2 to 3 min for t > 3 min
Thermal conductivity λ, W/m K	$38.6 - 2.2 \times 10^{-2}\,T + 1.67 \times 10^{-5}\,T^2$ where temperature, T (°C)	
Specific heat capacity c_p, kJ/kg K	$4.1 \times 10^{-4}\,T + 0.432$ where temperature, T (°C)	
Density ρ, kg/m^3	7787 at 290°C	
Coefficient of thermal expansion α, 1/K	Instantaneous: $(11.46 + 0.0105T) \times 10^{-6}$ Mean (20 – T): $(11.59 + 5.161 \times 10^{-3}\,T) \times 10^{-6}$ where temperature, T (°C)	

Table 2.3 Engineering tensile properties for SC-4 specimen

Specimen location	Temperature (°C)	0.2% Proof stress (MPa)	Ultimate tensile stress (MPa)	Elongation (%)	Reduction of area (%)
Forging top 0° position	20	543	685	21	56
Forging bottom 180° position	20	553	695	20	52
Forging top 0° position	290	521	660	18	51
Forging bottom 180° position	290	521	660	17	51

Note: E-modulus (MPa) = 212.35×10^3 at 0°C and 189.10×10^3 at 350°C.
Poisson ratio = 0.28.

considered necessary for analysis of the SC-4 test. In view of the similarities in steel chemistry and heat treatment conditions between test cylinder SC-4 and cylinders SC-2 and SC-3, the true stress/true plastic strain data previously generated for the latter cylinders were used for SC-4. Engineering stress/strain and true stress/strain data from the SC-2 and SC-3 characterization programs are given in Table 2.4.

Standard Charpy V-notch (CVN) impact tests were performed on specimens extracted in the circumferential-radial (C-R) orientation from locations adjacent to those of the tensile specimens. A total of 30 tests were performed, with 15 specimens being extracted, each from the top and bottom of the forging. Results of all 30 tests are presented in Fig. 2.5. The results show the absence of systematic influence of either axial or circumferential location on impact toughness properties and indicate a brittle/ductile transition for the forging. The test temperature corresponding to an impact energy level of 68 J (i.e., T_{68J}) is in excess of 100°C. [According to the ASME Boiler and Pressure Vessel Code, RT_{NDT} is the higher of the nil ductility temperature (NDT) from drop-weight tests and $T_{68J} - 33$°C.]

All fracture toughness specimens were extracted from the test rings in the C-R orientation . Three sizes of compact specimens were fabricated and tested: 10 mm thick, 35 mm thick, and 75 mm thick. A total of 45 specimens of 10-mm thickness were extracted from a test ring adjacent to the SC-4 cylinder. Of these, 30 were fabricated with the notch positioned on the 0° datum line, and 15 specimens had the notch on a line 225° around the circumference from the 0° line (see Fig. 2.6). Specimens on the 0° datum line were taken from two positions within the thickness of the forging wall; these two positions (15 specimens each) corresponded to the surface (i.e., first 10-mm thickness) and the mid-thickness of the finished cylinder. Specimens located 225° away from the datum line were all positioned at the surface location.

Table 2.4 Engineering and true stress–true strain values for test rings of SC-4 cylinder forging

JU21/JU3 (20°C)				JU22/JU4 (20°C)			
Strain	Stress (MPa)	True strain	True stress (MPa)	Strain	Stress (MPa)	True strain	True stress (MPa)
JU21				**JU22**			
0.0002	67.0	0.0003	67.0	0.0002	50.9	0.0002	50.9
0.0006	129.4	0.0006	129.5	0.0005	115.3	0.0005	115.3
0.0009	191.1	0.0009	191.3	0.0008	177.3	0.0008	177.4
0.0012	252.0	0.0012	252.3	0.0011	237.8	0.0011	238.1
0.0015	311.7	0.0015	312.2	0.0014	297.9	0.0014	298.3
0.0018	371.8	0.0018	372.5	0.0017	358.8	0.0017	359.4
JU3				**JU4**			
0.0024	503.1	0.0024	504.3	0.0021	455.3	0.0021	456.3
0.0033	546.0	0.0033	547.8	0.0030	548.3	0.0030	550.0
0.0041	551.4	0.0041	553.6	0.0038	552.9	0.0038	555.0
0.0049	557.1	0.0049	559.8	0.0045	558.7	0.0046	561.4
0.0070	586.8	0.0070	590.9	0.0082	598.8	0.0082	603.7
0.0138	615.7	0.0137	624.1	0.0150	620.5	0.0149	629.8
0.0202	637.4	0.0200	650.3	0.0217	642.2	0.0215	656.2
0.0261	657.8	0.0258	675.0	0.0281	662.0	0.0277	681.4
0.0325	675.3	0.0320	697.3	0.0349	674.9	0.0343	698.5
0.0389	687.2	0.0382	714.0	0.0417	686.9	0.0408	715.5
0.0453	698.0	0.0443	729.6	0.0480	699.2	0.0469	732.8
0.9521	707.7	0.0508	744.6	0.0552	706.9	0.0537	746.0
0.0584	715.6	0.0658	757.5	0.0624	713.3	0.0605	757.8
0.0652	720.1	0.0632	767.0	0.0696	715.6	0.0672	765.4
0.0728	724.4	0.0703	777.1	0.0771	719.7	0.0743	775.3
0.0800	724.6	0.0769	782.5	0.0847	719.1	0.0813	780.0
0.0871	728.3	0.0835	791.7	0.0926	719.7	0.0886	786.4
0.0947	728.7	0.0905	797.7				

Table 2.4 (continued)

JU5 (150°C)[a]				JU24/JU6 (150°C)			
Strain	Stress (MPa)	True strain	True stress (MPa)	Strain	Stress (MPa)	True strain	True stress (MPa)
JU5				**JU24**			
0.0024	456.4	0.0024	457.5	0.0003	59.4	0.0003	59.4
0.0033	503.1	0.0033	504.8	0.0006	115.6	0.0006	115.7
0.0041	514.6	0.0041	516.7	0.0009	173.5	0.0009	173.6
0.0049	523.1	0.0049	525.6	0.0012	231.7	0.0012	232.0
0.0082	552.9	0.0081	557.4	0.0015	286.0	0.0015	286.5
0.0142	581.7	0.0141	590.0	0.0018	338.9	0.0018	339.5
0.0205	602.3	0.0203	614.7				
0.0265	618.8	0.0262	635.2	**JU6**			
0.0325	639.3	0.0320	660.1				
0.0389	650.5	0.0382	675.8	0.0024	466.5	0.0024	467.6
0.0453	662.7	0.0443	692.7	0.0033	504.2	0.0033	505.0
0.0516	670.7	0.0504	705.3	0.0041	617.7	0.0041	519.8
0.0584	675.0	0.0568	714.5	0.0049	526.6	0.0049	529.2
0.0652	680.4	0.0632	724.8	0.0101	558.0	0.0101	563.6
0.0720	684.6	0.0695	733.9	0.0167	576.7	0.0166	586.3
0.0791	688.7	0.0762	743.3	0.0229	603.1	0.0227	617.0
0.0859	689.7	0.0824	748.9	0.0291	619.9	0.0287	638.9
0.0935	694.0	0.0894	758.9	0.0357	632.4	0.0351	655.0
0.1007	688.7	0.0959	758.1	0.0423	646.2	0.0415	673.6
				0.0485	656.1	0.0474	687.9
				0.0551	665.8	0.0537	702.5
				0.0621	674.2	0.0603	716.1
				0.0692	678.4	0.0669	725.3
				0.0766	681.1	0.0738	733.3
				0.0836	685.3	0.0803	742.6
				0.0910	687.5	0.0871	750.1
				0.0989	686.7	0.0943	754.6
				0.1051	690.3	0.0999	762.8

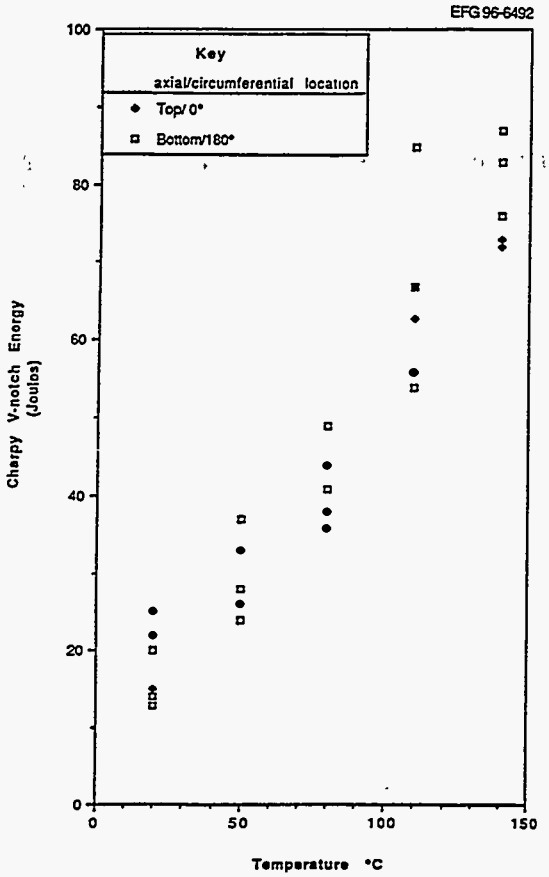

Figure 2.5 Effect of axial and circumferential position on Charpy V-notch toughness in SC-4 specimen

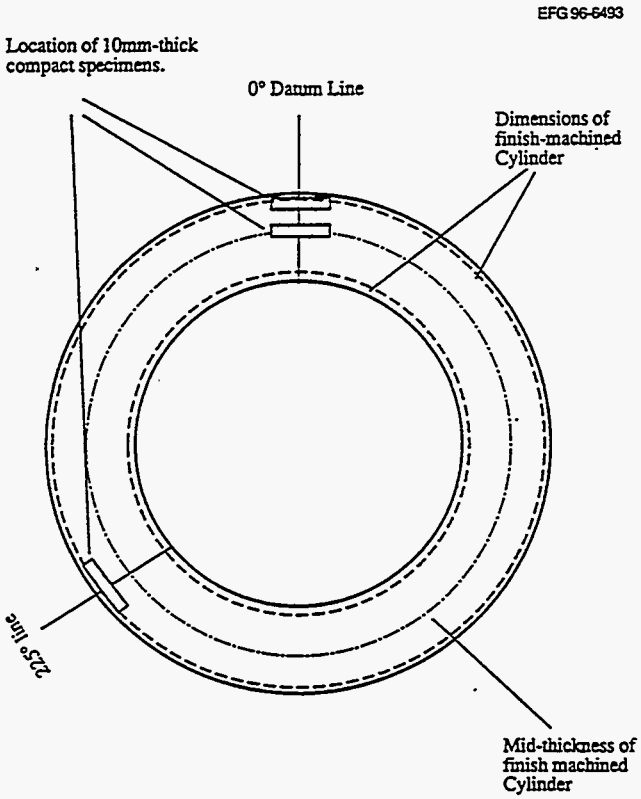

Figure 2.6 Schematic diagram showing location of 10-mm thick compact specimens within the material characterization test ring of SC-4 material

Description

Specimen fatigue precracking was performed at ambient temperature according to the American Society of Testing and Materials (ASTM) E399-81 standard. The 10- and 35-mm-thick specimens were tested in the plane-sided condition, while the 75-mm-thick specimens were 20% side-grooved after fatigue precracking. All tests were performed using displacement control within the temperature range 0 to 100°C and at loading rates in accordance with the ASTM standard.

For the 10-mm-thick specimens, fracture toughness at the point of cleavage fracture, or at the point of specimen unloading if fracture did not occur, was calculated from J and converted to K_J using the plane-strain relation. Results of all 10-mm-thick compact tension (CT) specimen tests are presented in Table 2.5 and Fig. 2.7. Except for three cases, fracture toughness values for the 35- and 75-mm-thick CT specimens were determined using the same procedures. Results of all 35- and 75-mm-thick specimen tests are given in Table 2.6 and depicted with corresponding data from the 10-mm-thick specimens in Fig. 2.8. These results do not indicate any significant effects of specimen thickness, circumferential location, or wall-thickness location on fracture toughness behavior in the brittle/ductile transition region.

Table 2.5 Transition region fracture toughness test data from 10-mm compact specimens of SC-4 material

Circumferential Position and Location Relative to the Finish-Machined Cylinder Wall Thickness	Sample No	Temp °C	Δa(ix) mm	K_J MPa√m	Cleavage (Yes or No)
0° position cylinder surface wall thickness location	KM2	0	0.01	64	Yes
	KM14	0	0.01	67	Yes
	KM8	23	0.01	87	Yes
	KM1	23	0.01	51	Yes
	KM13	40	0.02	81	Yes
	KM3	40	0.02	88	Yes
	KM6	60	0.02	93	Yes
	KM5	60	0.03	86	Yes
	KM10	70	0.03	111	Yes
	KM12	70	0.04	124	Yes
	KM9	100	0.68	193	No
	KM4	100	0.76	214	No
	KM11	100	0.99	233	Yes
	KM7	110	1.28	254	No
	KM15	110	1.70	238	No
0° position cylinder mid wall-thickness location	KM16	22	0.03	75	Yes
	KM23	22	0.03	69	Yes
	KM25	40	0.02	89	Yes
	KM27	40	0.02	87	Yes
	KM20	50	0.06	73	Yes
	KM17	60	0.02	76	Yes
	KM24	60	0.02	79	Yes
	KM21	70	0.03	106	Yes
	KM26	70	0.05	100	Yes
	KM30	80	0.04	173	Yes
	KM22	80	0.09	118	Yes
	KM28	90	0.04	129	Yes
	KM19	90	0.05	133	Yes
	KM29	110	0.90	267	No
	KM18	110	0.96	208	No
225° position cylinder surface wall-thickness location	KM40	0	0.02	45	Yes
	KM32	0	0.03	47	Yes
	KM37	10	0.03	48	Yes
	KM45	10	0.04	71	Yes
	KM35	30	0.03	55	Yes
	KM42	30	0.09	66	Yes
	KM31	50	0.02	70	Yes
	KM38	50	0.02	70	Yes
	KM41	70	0.02	84	Yes
	KM33	70	0.04	103	Yes
	KM39	70	0.04	115	Yes
	KM43	90	0.75	193	Yes
	KM36	90	0.97	186	No
	KM44	110	0.06	267	No
	KM34	110	0.06	197	No

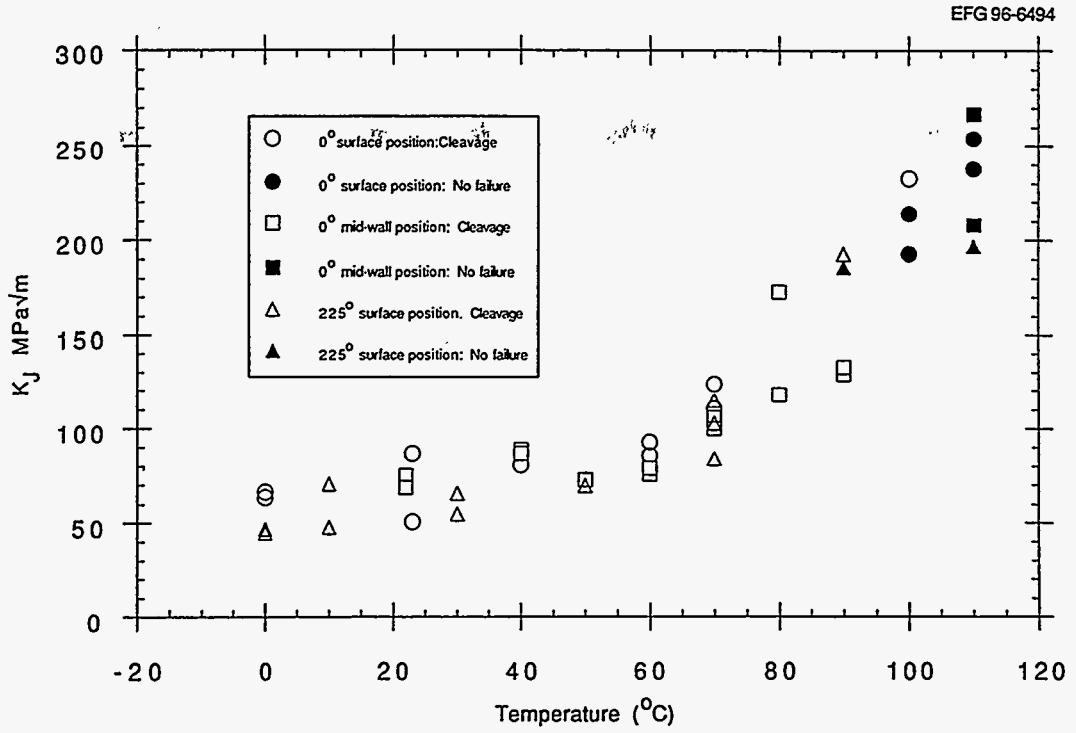

Figure 2.7 Effect of specimen location on fracture toughness properties of 10-mm-thick CT specimen of SC-4 material

Table 2.6 Fracture-toughness transition data for 35- and 75-mm-thick compact specimens of SC-4 material

Specimen identity/location in forging	Test temperature (°C)	Δa (mm)	J (MJm^{-2})	K_I (MPa$\sqrt{m}$)[a]	Comments
		0% SG 35-mm CS			
J4/Top (0°)[b]	20	0.07	-	66.3	K from load (not J)
J6/Top (0°)	20	0.03		65.4	K from load (not J)
J2/Bottom (180°)	60	0.01	0.042	96.4	
J5/Top (0°)	60	0.05	0.049	103.3	
J1/Bottom (180°)[b]	100	0.33	0.188	203.0	
J3/Bottom (180°)	100	0.41	0.107	152.7	
		20% SG 75-mm CS			
K6/Top (0°)	60	0.04		92.2	K from load (not J)
K4/Top (0°)	100	0.03	0.143	177.3	
K5/Top (0°)[c]	150	21.6	0.625	370.6	No failure

Note: All specimens taken from midwall thickness location.
[a]K_J values all calculated using a Young's Modulus = 2.0×10^5 MPa.
[b]Uneven fatigue crack fronts on these specimens due to poor machined notch.
[c]Massive amount of growth on this specimen means that the absolute value of J quoted is of limited value.

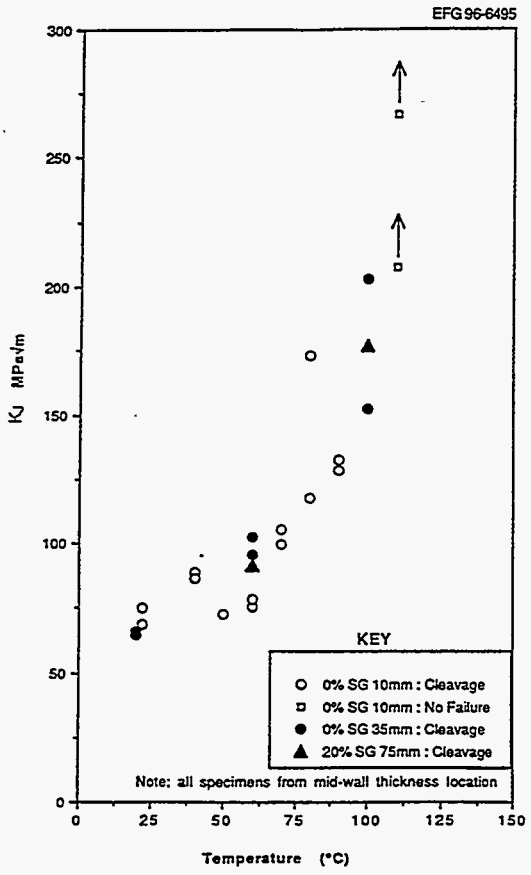

Figure 2.8 Effect of specimen size on fracture toughness transition properties of SC-4 material

2.1.3 Instrumentation

Most of the instrumentation related to the test was mounted directly on the rotating specimen and thus required the deployment of cabling through hollow rotating components such as the support shaft, drive coupling, and gearbox. Signals were extracted via a 100-way slip ring unit mounted directly above the gearbox. All instrumentation signals were routed through the data logging system, which processed and recorded them at scanning periods variable on demand down to 3 s. The arrangement of the crack measuring instrumentation for SC-4 can be seen in Fig. 2.9. Four active alternating current potential drop (ACPD) measurement stations were mounted on the inner surface of the specimen, one at each end of the two defects. In addition, two reference stations were included in the uncracked region. Current and voltage probes were located on a transverse line through the tip of the fatigue precrack with separations of 10 and 5 mm, respectively. Two ACPD instruments were used to achieve a minimum scan period of ~5 s. Twelve strain gages (weldable type) were situated on the cylinder as shown in Figs. 2.9 and 2.10. Thermocouples were deployed to measure the cylinder temperature variations axially, circumferentially, and through the thickness (see Figs. 2.9 and 2.11). Cylinder speed was measured by three independent devices. The primary speed indication was an analogue tachometer, which also provided the control signal for the motor servo system. The backup systems were two digital counters, that is, one electromagnetic and the other optical.

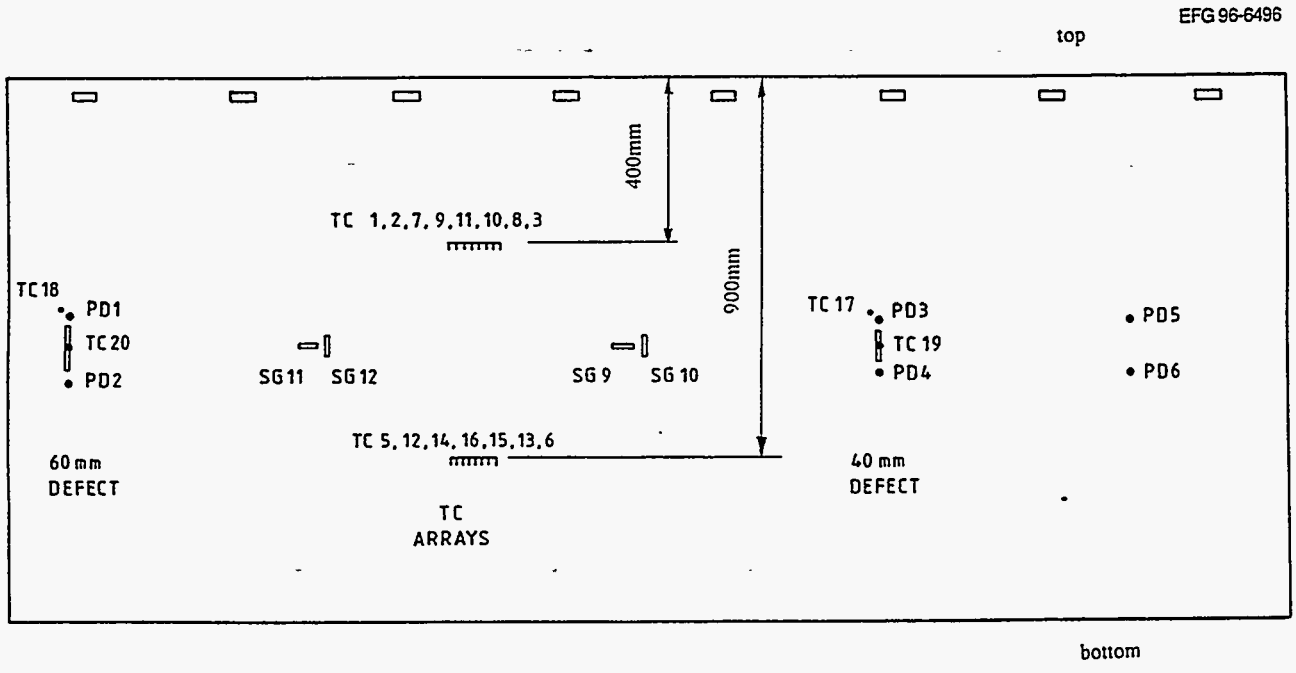

Figure 2.9 Location of instrumentation in bore of SC-4 cylinder specimen

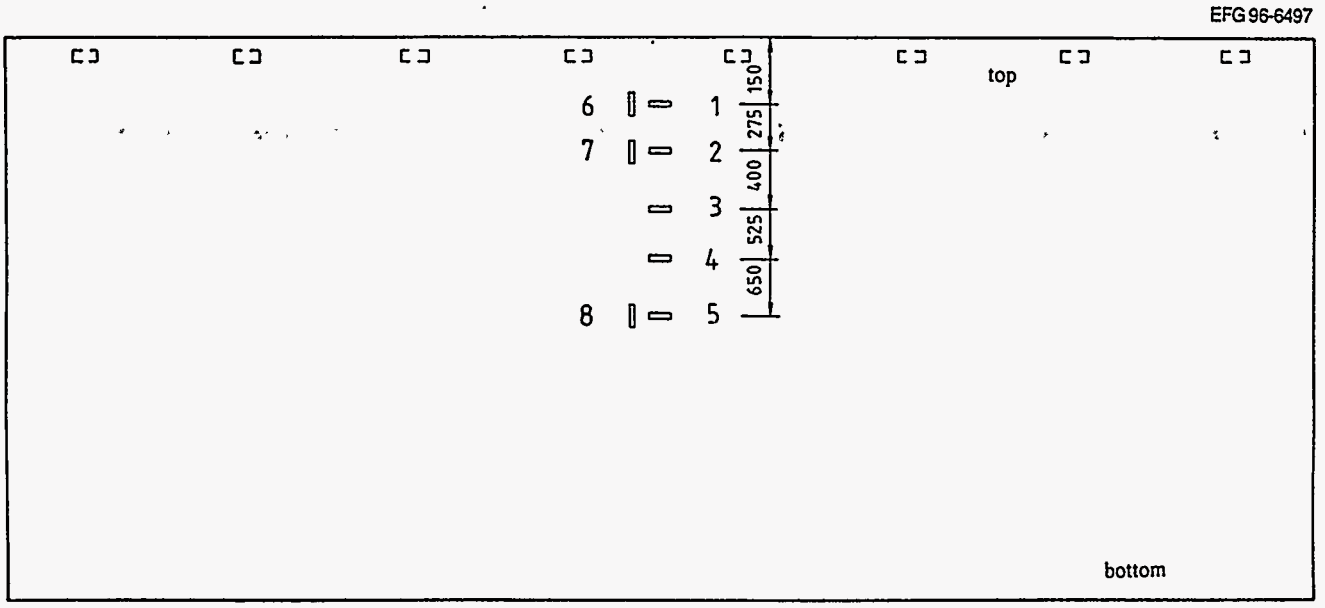

Figure 2.10 Location of back-face strain gages on SC-4 cylinder specimen

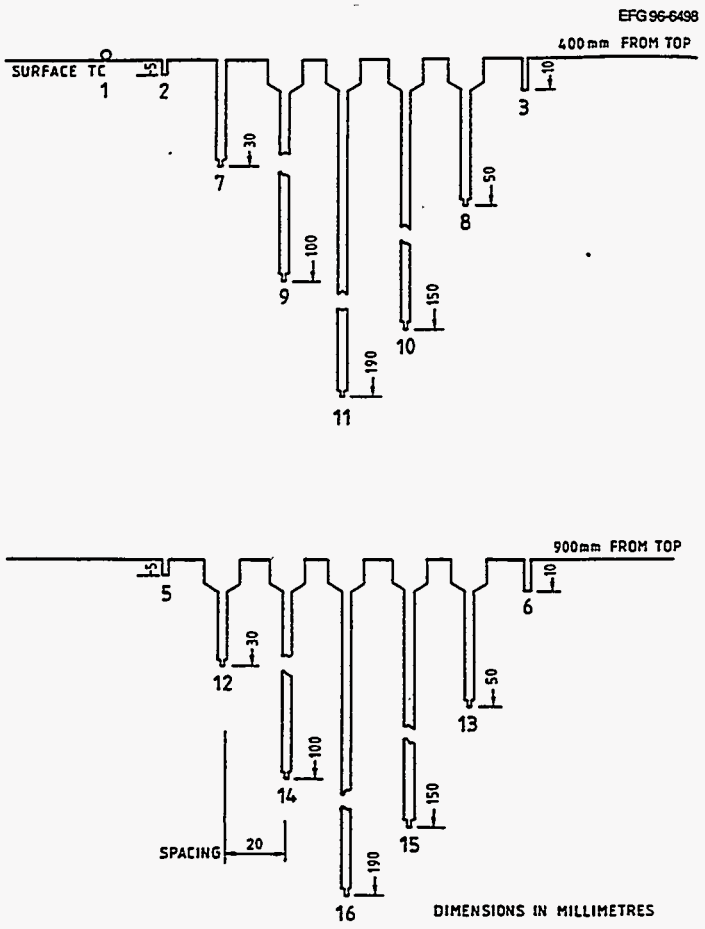

Figure 2.11 Thermocouple arrays employed in SC-4 cylinder specimen

2.1.4 Experimental Results

The SC-4 test was initiated by stabilizing the cylinder at a mean temperature of 305°C. The test was conducted at a low rotational speed (530 rpm), and the thermal shock was generated by water spray cooling (~7°C) the inner surface of the preheated cylinder (see Fig. 2.3). The initial flow rate of the cooling water was ~60 gal/min, which produced an effective heat transfer coefficient in the range $3000 < h < 5000$ W/m^2 K. After 2 min at the initial flow rate, in the absence of indications of crack growth, the cooling water flow rate was increased to 290 gal/min, producing an effective heat transfer coefficient in excess of 20 kW/m^2 K. The temperature data recorded at selected thermocouples, shown in Figs. 2.9 and 2.11, as a function of transient time are shown in Fig. 2.12. Crack-tip temperatures were initially consistent with upper-shelf fracture behavior. During the test, crack-tip temperatures near the inner surface fell through the brittle/ductile transition regime.

Data collected during the test provided indications of crack growth at each end of the 40-mm defect. Subsequent destructive examination confirmed this result and revealed growth at the ends of the 60-mm defect, which had not been detected using the ACPD method. The fracture surfaces were similar in several respects (see Fig. 2.13): first, the cracks grew in an axial direction, and no growth from the deepest point of either defect was produced; second, the aspect ratios of the arrested cracks were approximately the same, with a 6:1 length-to-depth ratio; and third, a thin (2- to 5-mm) ligament of material extended to, or very close to, the point of intersection of the crack with the inner surface of the cylinder. The presence of this unexpected ligament indicated that the cleavage initiation site was some distance below the surface. It also explained the failure of the ACPD method to detect growth of the 60-mm defect where the ligament was thickest. Additional information on the experimental results for the SC-4 experiment is available in Ref. 1.

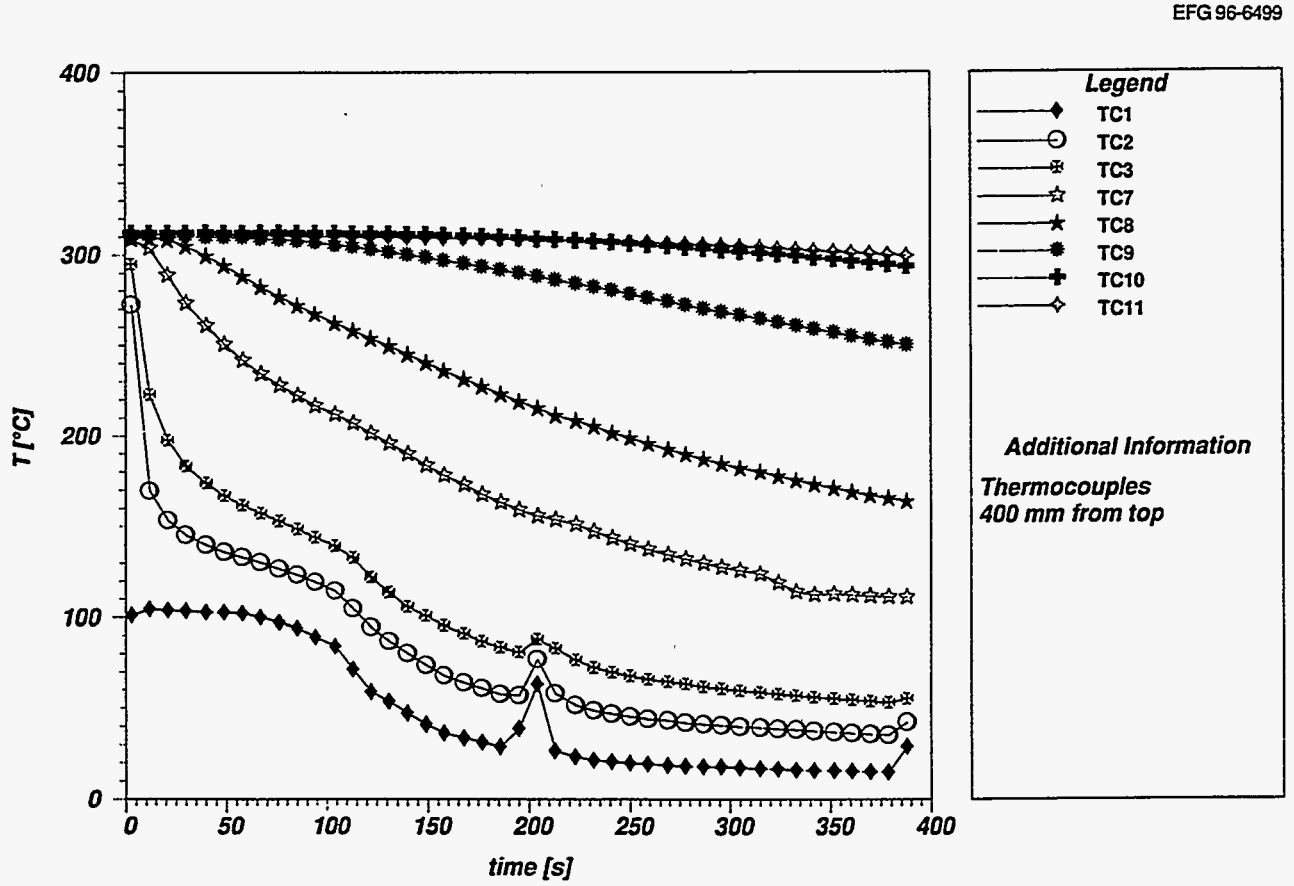

Figure 2.12 Temperature vs time data recorded at selected thermocouple locations during SC-4 experiment

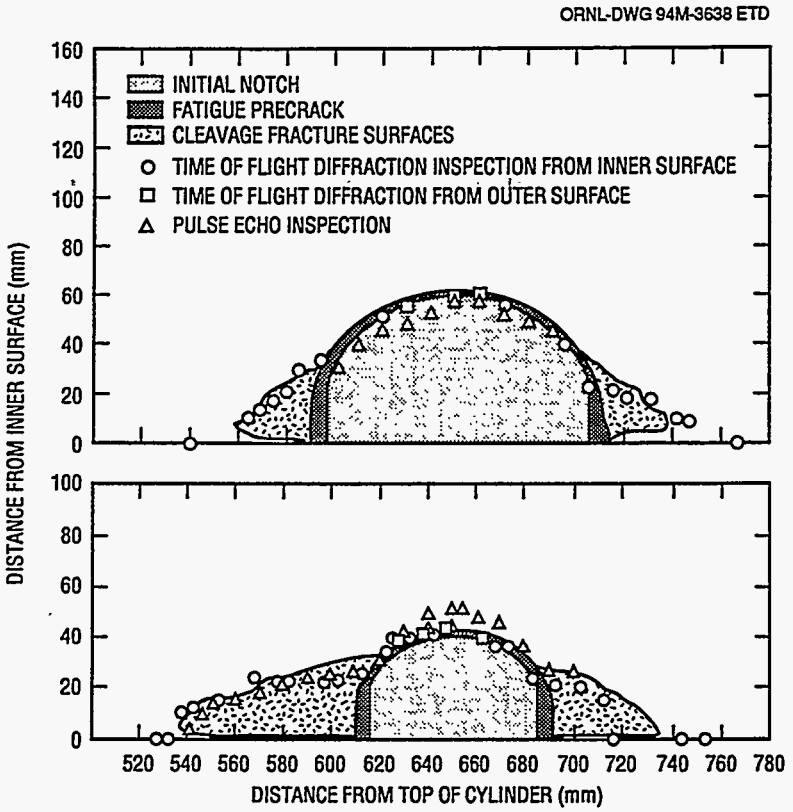

Figure 2.13 Comparison of fracture surfaces and ultrasonic profiles for the two defects in the SC-4 cylinder: (*a*) 60-mm crack depth and (*b*) 40-mm crack depth

2.2 Sixth CRISM "Prometey" PTS Experiment (PTS-I/6)

PTS experiments are being performed at the Central Research Institute of Structural Materials (CRISM "Prometey") St. Petersburg, Russia, for the purpose of investigating the behavior of surface flaws under pressurized-water reactor overcooling accident conditions.[2] The joint pressure vessel integrity research program was initiated in 1990 through the efforts of three participating organizations. The participants are the Prometey Institute; the IVO International Ltd. (IVO IN), Finland; and the Technical Research Center of Finland (VTT). The main objective of the research program is to increase the reliability of safety analysis methodologies applied to VVER-440 reactor vessels. This is achieved by providing materials property data for VVER-440 pressure vessel steels and by producing experimental data of crack behavior under PTS loading conditions for validation of fracture assessment methodologies.

The research program is divided into four parts: pressure vessel tests, material characterization, computational fracture analyses, and evaluation of analysis methodologies. The testing program is being conducted on two model pressure vessels containing artificial axial flaws. A special heat treatment is applied to the vessels prior to the tests to simulate toughness conditions in an RPV near end of life. The CRISM "Prometey" is responsible for manufacture of the vessels, the heat treatment, and performance of the PTS tests. The IVO IN has responsibility for experimental measurements during the tests, while VTT is responsible for material characterization and pretest and posttest analyses. All participants contribute to the pretest planning and the formulation of final conclusions.

Seven PTS experiments were performed with the same model pressure vessel using five different flaw geometries. The test facility constructed at Prometey to conduct the PTS experiments is depicted in Fig. 2.14. The vessel geometry for the PTS-I/6 experiment is depicted in Fig. 2.15. The pressure vessel is first heated to ~280°C using heating resistors. Concurrently, the vessel is pressurized internally by water and steam generated inside the vessel due to heating (i.e., a closed system). The heating resistors are lifted from the vessel just prior to initiation of the thermal shock. The vessel is then subjected to a sudden flow of tap water at ~15°C around the outside surface (Fig. 2.16). The coolant flow is effective the first 200 s because of the capacity of the cooling water tanks. After that time, the flow rate gradually decreases to zero.

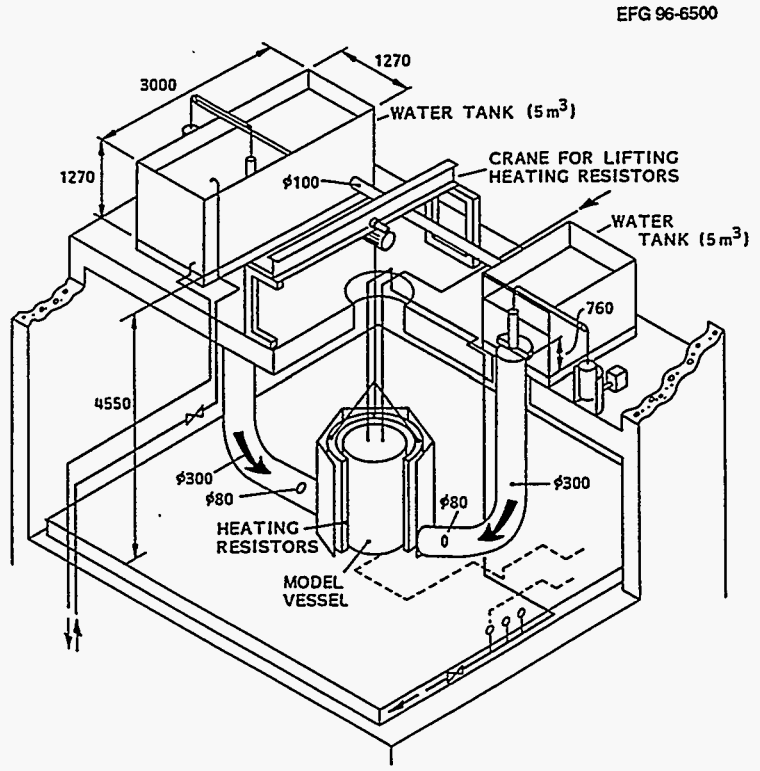

Figure 2.14 Test facility used to conduct the PTS-I/6 experiment (Prometey Institute, Russia)

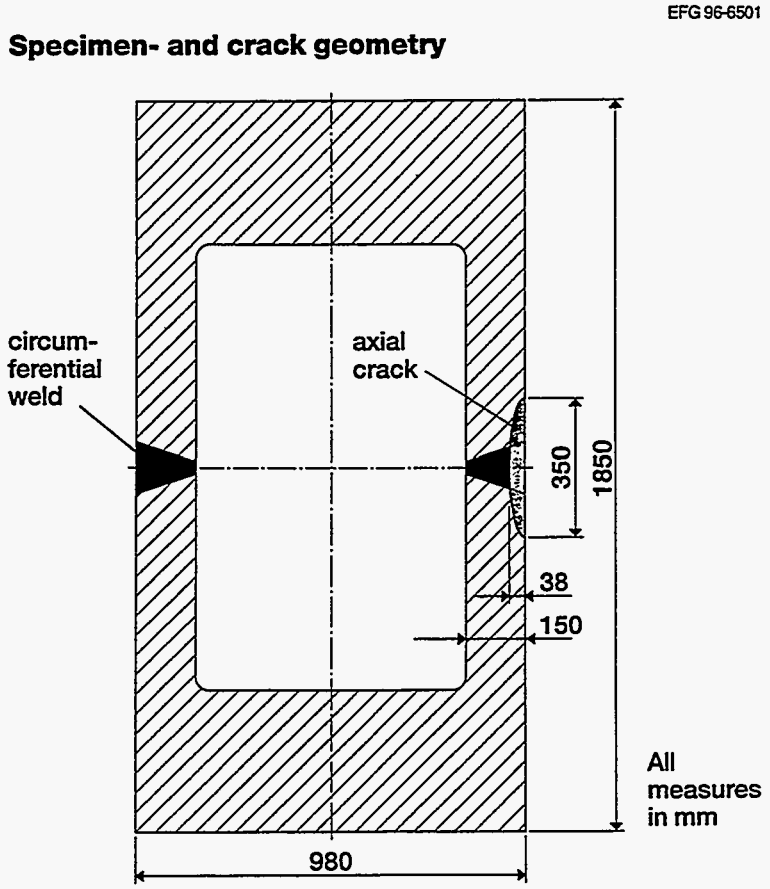

Figure 2.15 Specimen and crack geometry used in PTS-I/6 experiment

Thermal and mechanical loading

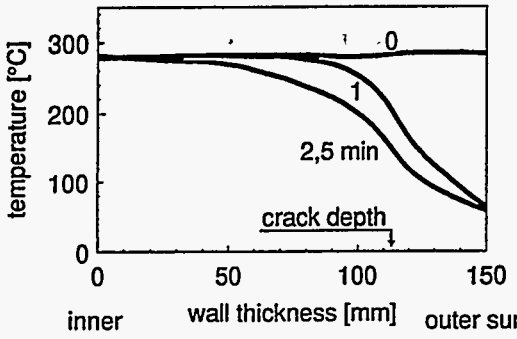

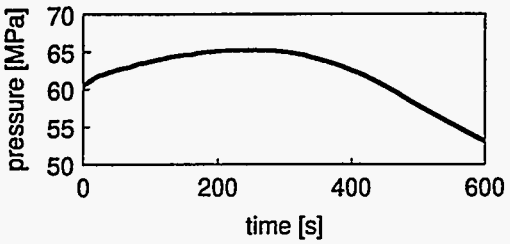

Material characterization

	base material (15X2MFA)	weld material (Sv-10XMFT)
yield stress $R_{p0,2}$ [MPa]	1037 (20°C) 874 (300°C)	624 (20°C) 542 (300°C)
charpy energy for upper shelf [J]	120	120
$T_{50\,J}$ [°C]	110	40

Figure 2.16 Loading and test material data for PTS-I/6 specimen

2.2.1 Specimen Geometry

The primary objective of the sixth experiment was to produce crack initiation and arrest under PTS loading, as well as VVER-440 material property data. The vessel contained a circumferential weldment at the midlength of the vessel (Fig. 2.15). The width of the weld was determined by etching to be 160 mm at the outside surface and 50 mm at the inside surface. The weld was produced in a machined cavity, so that it did not extend completely through the wall thickness. An axial outside surface flaw was located at the midlength of the vessel partly in weld and base material. A sharp precrack was made by a special welding technique. The crack welding data and parameters are given in Table 2.7. The initial crack geometry, presented in Fig. 2.15, is a near semiellipse (a = 38 mm and 2c = 350 mm).

Table 2.7 Welding data and parameters for crack preparation in PTS-I/6 cylinder (manual metals are welding)

Electrode	Fox Dur 500 3.25 mm
Chemical composition	0.4% C, 1.2% Si, 1.2% Mn, 2.8% Cr
Current and velocity	215 A dc, 12 cm/min

2.2.2 Material Properties

The material used in fabricating the model vessel is VVER-440-type RPV steel 15Kh2MFA. In Table 2.8 the chemical composition of the base and weld material is presented. The circumferential weld in the vessel was made by the submerged arc welding technique using weld wire Sv-10KhMFT and flux AN-42. The vessel was subjected to heat treatment to simulate the radiation embrittlement of the VVER-440-type steel. According to the Prometey Institute, the heat-treatment parameters were given as follows: annealing at 1000°C, holding 4 h, cooling in oil, tempering at 620°C for 10 h, and cooling in air. A more detailed history of the thermal treatment of the vessel is presented in Table 2.9.

Table 2.8 Chemical composition of the base and the weld material in PTS-I/6 cylinder

	Chemical composition (%)									
Part	C	Si	Mn	Cr	Mo	V	Ni	S	P	Cu
Base	0.16	0.35	0.45	2.65	0.62	0.29	0.23	0.006	0.010	0.12
Weld	0.03	0.44	0.96	1.62	0.47	0.20	0.05	0.010	0.012	0.06

Table 2.9 Manufacture and heat treatment history of the PTS-I/6 test vessel provided by Prometey

Phase	Temperature (°C)	Rate (°C/h)
Forging (→ structure; length 2.8 m, outside diameter 1020 mm, round hole, wall thickness 300 mm)	≥ 600	-
Post-forging heat treatment	600...650 (1...2h)	-
Cooling	625 → 250...300	80
Keeping	250...300 (5h)	-
Warming	300 → 940	80
Normalizing heat treatment	920...960 (3h)	-
Cooling	940 → 745	80
Heat treatment	730...760 (9,5h)	-
Cooling in oven, cooling in air	745 → 400, 400 → 20	20, n.a.
Warming	20 → 400 → 1000	<80
Austenizing heat treatment	1000 (5h)	-
Cooling in oil (hardening)	1000 → 20	
Warming	20 → 660	80
Tempering heat treatment	660 (5h)	-
Cooling in oven	660 → 300	20
Cooling in air	300 → 20	
Machining to right dimensions		
Warming	20 → 1000	
Austenizing heat treatment	1000 (8h)	-
Cooling in oil (hardening)	1000 → 20	
Warming	20 → 610	80
Tempering heat treatment	610 (6h)	-
Cooling in oven	610 → 300	20
Keeping	300	-
Cooling in air	300 → 20	
Cutting of the vessel into two pieces and welding (circumferential weld)	150	-
Warming	20 → 610	80
Post-weld tempering heat treatment	610 (6h)	-
Cooling	610 → 300	20
Cooling in air	300 → 20	
Crack manufacture		

Physical properties for the model vessel materials are given in Table 2.10. Material characterization specimens were taken from the vessel according to the cutting plan given in Fig. 2.17. The CVN samples for standard and instrumented impact tests, tensile test bars, side-grooved CT25 specimens, and crack arrest test specimens were first manufactured from both the base and the weld material in C-R orientation. Later, when toughness variation depending on the location of the point of interest in the vessel was observed, precracked (CVN_{pc}) and standard (CVN) Charpy-size specimens were manufactured for additional static fracture toughness and instrumented impact tests. All the specimens were cut in the C-R orientation. Table 2.11 provides a summary of the characterization tests that were performed. Mechanical properties determined from the tensile tests are summarized in Table 2.12. The multilinear engineering stress-strain curves are tabulated in Table 2.13 and plotted in Fig. 2.18.

The conventional impact testing for base and weld materials was carried out according to the standard SFS-EN 10045-1. In addition, tests using the VTT instrumented impact tester were made. It was found that the base material was tougher near the vessel outside surface. Thus, additional tests were made with samples cut from the same depth (50 mm) as the CT25 specimens. Figure 2.19 presents the test results. Unfortunately, it was later apparent that toughness of the base material varied depending on the location in the vessel circumference and length. Thus, the impact toughness values presented here for the base material are not relevant to the behavior of the crack (samples were taken far from the crack).

Based on the fracture toughness test results, "master curves" describing the temperature dependence of fracture toughness and arrest toughness were determined.

Table 2.10 Physical properties of PTS-I/6 vessel material

Heat convection coefficient h:								
T, °C	40	80	90	95	100	105	110	300
h, kW/m^2 K	2.5	3.3	6.0	8.0	15.0	20.0	30.0	40.0
Thermal conductivity[a] λ			37 (Constant)					
Specific heat capacity[a] c_p:								
T, °C	20	150	300	400				
λ, W/m K	0.476	0.485	0.497	0.497				
Density ρ, kg/m^3			7800					
Coefficient of thermal expansion[a] α:								
T, °C	20	150	300	400				
α, $1/K \times 10^6$	11.7	12.15	12.7	12.7				

[a]For both base and weld material.

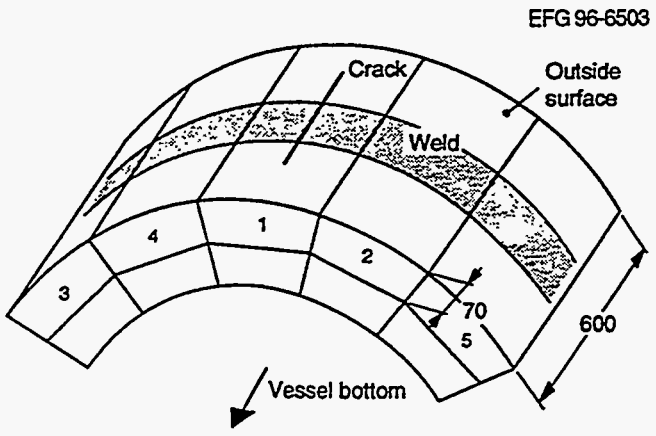

Figure 2.17 Pieces (1–5) taken from PTS-I/6 vessel for material characterization

Table 2.11 Material characterization test matrix for the PTS-I/6 test vessel

Purpose	Description of test	Sample	Number of tests
Impact energy vs temperature transition curves	Impact	CVN 10 mm	12^{B} 12^{W}
	Instrumented impact	CVN 10 mm	25^{B}
Stress-strain curves	Tension:		
	Room temperature	ϕ 10-mm tension sample	3^{B} 3^{W}
	Elevated temperature	Special tension sample (ϕ 10 mm)	6^{B} 6^{W}
Fracture toughness vs temperature transition curves	Fracture toughness and resistance	CT25 (25-mm) side-grooved	17^{B} 16^{W}
	Fracture toughness	CVN_{pc} (CVN 10-mm prefatigued)	40^{B}
Crack arrest toughness transition curves	Crack arrest	Large sample	8^{B}
	Instrumented impact	CVN 10 mm	14^{B}

Note: ^{B}Base material; ^{W}Weld material.

Table 2.12 Average engineering values from tension tests of PTS-I/6 vessel material

	Temperature (°C)			
Vessel material	20	150	300	400
$R_{0.2}$ base material[a]	1037	946	874	
$R_{0.2}$ weld material[a]	624	578	542	
R_M base material[b]	1132	1063	1011	
R_M weld material[b]	705	661	627	
A_5 base material[c]	15.5	15.3	15.5	
A_5 weld material[c]	18.7	18.7	17.2	
E base material	206,437	184,638	188,519	180,000[d]
E weld material	204,032	209,315	178,140	170,000[d]
Poisson ratio	0.3	0.3	0.3	0.3

[a] $R_{0.2}$ is stress at strain 0.2% (MPa).
[b] R_M is ultimate strength (MPa).
[c] A_5 is elongation at fracture (%).
[d] Approximated values.

Table 2.13 Stress-strain values for base and weld material of PTS-I/6 vessel material

BASE MATERIAL, 20 C

STRAIN (m/m)	STRESS (MPa)
0.000000E+00	0.000000E+00
0.307600E-02	0.635000E+03
0.372000E-02	0.762000E+03
0.416000E-02	0.826000E+03
0.471200E-02	0.889000E+03
0.555200E-02	0.953000E+03
0.720000E-02	0.101700E+04
0.870000E-02	0.104800E+04
0.136000E-01	0.108000E+04
0.568000E-01	0.136200E+04
0.100000E+00	0.164400E+04

BASE MATERIAL, 150 C

STRAIN (m/m)	STRESS (MPa)
0.000000E+00	0.000000E+00
0.345000E-02	0.637000E+03
0.380000E-02	0.701000E+03
0.425000E-02	0.765000E+03
0.480000E-02	0.829000E+03
0.575000E-02	0.892000E+03
0.642500E-02	0.924000E+03
0.750000E-02	0.956000E+03
0.970000E-02	0.988000E+03
0.168000E-01	0.102000E+04
0.100000E+00	0.139500E+04

BASE MATERIAL, 300 C

STRAIN (m/m)	STRESS (MPa)
0.000000E+00	0.000000E+00
0.270000E-02	0.509000E+03
0.312500E-02	0.573000E+03
0.355000E-02	0.637000E+03
0.410000E-02	0.700000E+03
0.475000E-02	0.764000E+03
0.565000E-02	0.828000E+03
0.725000E-02	0.891000E+03
0.892500E-02	0.923000E+03
0.121250E-01	0.955000E+03
0.100000E+00	0.135100E+04

BASE MATERIAL, 400 C

STRAIN (m/m)	STRESS (MPa)
0.000000E+00	0.000000E+00
0.255000E-02	0.459000E+03
0.312500E-02	0.523000E+03
0.355000E-02	0.587000E+03
0.410000E-02	0.650000E+03
0.475000E-02	0.714000E+03
0.565000E-02	0.778000E+03
0.725000E-02	0.841000E+03
0.892500E-02	0.873000E+03
0.121250E-01	0.915000E+03
0.100000E+00	0.130100E+04

WELD MATERIAL, 20 C

STRAIN (m/m)	STRESS (MPa)
0.000000E+00	0.000000E+00
0.248000E-02	0.506000E+03
0.264000E-02	0.537000E+03
0.288000E-02	0.569000E+03
0.336000E-02	0.600000E+03
0.416000E-02	0.619000E+03
0.680000E-02	0.623000E+03
0.944000E-02	0.626000E+03
0.547200E-01	0.686000E+03
0.100000E+00	0.746000E+03

WELD MATERIAL, 150 C

STRAIN (m/m)	STRESS (MPa)
0.000000E+00	0.000000E+00
0.182500E-02	0.382000E+03
0.222500E-02	0.446000E+03
0.272500E-02	0.510000E+03
0.310000E-02	0.542000E+03
0.350000E-02	0.561000E+03
0.492500E-02	0.574000E+03
0.837500E-02	0.586000E+03
0.541880E-01	0.647000E+03
0.100000E+00	0.707000E+03

WELD MATERIAL, 300 C

STRAIN (m/m)	STRESS (MPa)
0.000000E+00	0.000000E+00
0.215000E-02	0.383000E+03
0.257500E-02	0.447000E+03
0.287500E-02	0.479000E+03
0.350000E-02	0.511000E+03
0.390000E-02	0.524000E+03
0.472500E-02	0.537000E+03
0.625000E-02	0.550000E+03
0.882500E-02	0.562000E+03
0.100000E+00	0.683000E+03

WELD MATERIAL, 400 C

STRAIN (m/m)	STRESS (MPa)
0.000000E+00	0.000000E+00
0.195880E-02	0.333000E+03
0.257500E-02	0.397000E+03
0.287500E-02	0.429000E+03
0.350000E-02	0.461000E+03
0.390000E-02	0.474000E+03
0.472500E-02	0.487000E+03
0.625000E-02	0.500000E+03
0.882500E-02	0.512000E+03
0.100000E+00	0.633000E+03

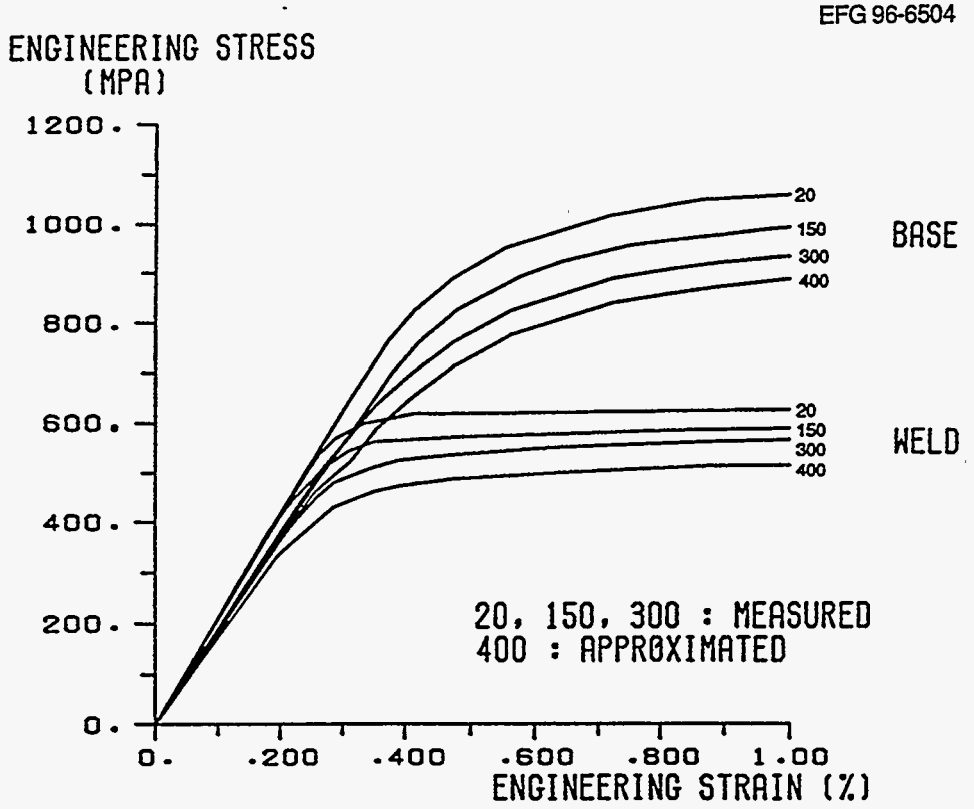

Figure 2.18 Engineering stress-strain curves used in analyses of PTS-I/6 experiment

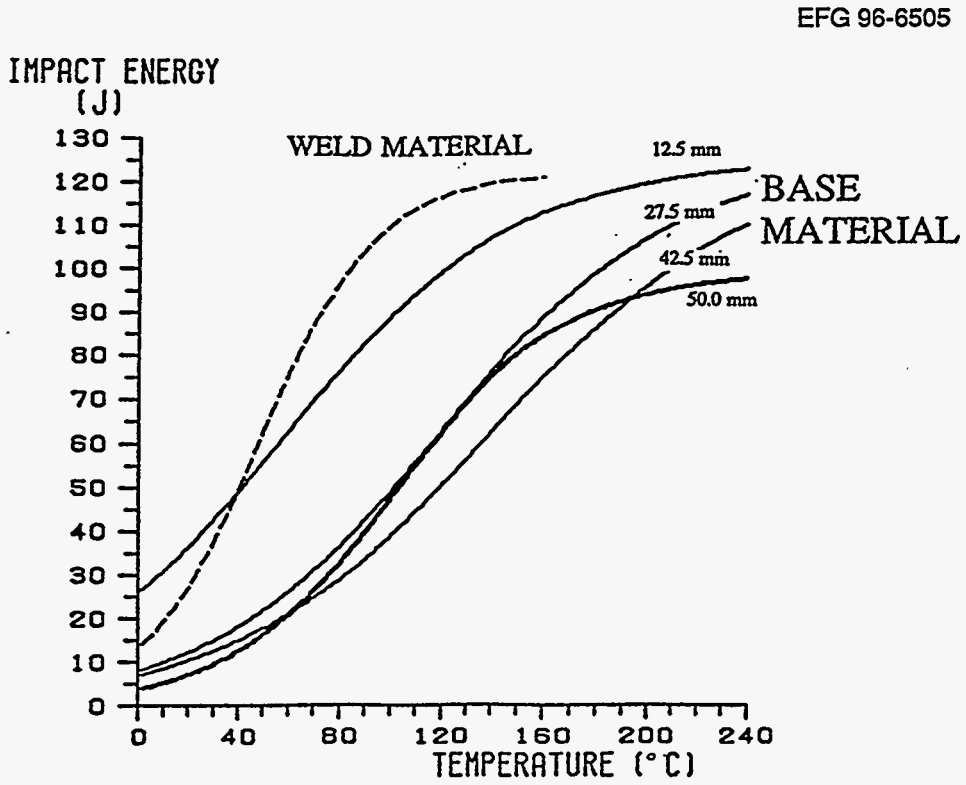

Figure 2.19 Charpy impact energy vs temperature data generated from PTS-I/6 material characterization. The curves show results for the base material (B) determined by using samples cut at different depths (mm) from the vessel outside surface. Only one curve was constructed for the weld material.

The curves corresponding to the failure probability of 50% and the specimen thickness of 25 mm (statistical size correction included) are of the form[3]

$$K = 30 + 70\, e^{0.019(T-T_o)} \qquad (2.1)$$

The transition temperature T_o of base material is 131°C in the deeper part of the crack. The transition temperature T_o of weld material is 64°C. These master curves are described further in Fig. 2.20 and Table 2.14.

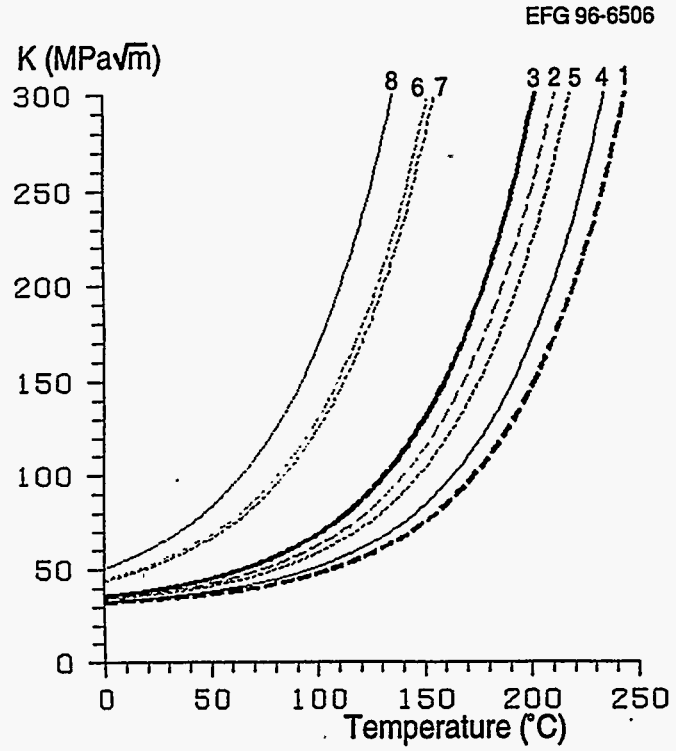

Figure 2.20 Measured fracture toughness vs temperature data and corresponding transition curves generated from PTS-I/6 material characterization. The fracture toughness and crack arrest toughness transition curves for the base and weld material corresponding to the failure probability of 50% and specimen thickness of 25 mm (statistical size correction included). The number of each curve refers to Table 2.14.

Table 2.14 Transition temperature T_o for the base material [(Eq. (2.1)]

Determined curve	Samples	T_o (°C)	Number of curve
Crack arrest toughness (in the vicinity of flaw 3)	CVN	173[a]	1
Crack arrest toughness (thick end)	Large arrest	140	2
Fracture toughness (in the vicinity of flaw 3)	CVN_{pc}	131[a]	3
Fracture toughness	CT25	163	4
Fracture toughness	CVN_{pc}/CT25[b]	147	5
Fracture toughness	CVN_{pc}/CVN[c]	81	6
Fracture toughness	CVN_{pc}/K_{Ia}[d]	84	7
Fracture toughness, weld material	CT25	64[a]	8

[a]Relevant values to be used in fracture assessment.
[b]Samples manufactured from tested CT25 specimens.
[c]Samples manufactured from tested CVN specimens.
[d]Samples manufactured from tested K_{Ia} specimens.

2.2.3 Instrumentation

The temperatures were measured on the outside and inside surfaces of the vessel using thermocouples. The strains were measured at selected points on the outside surface using weldable strain gages. In addition, the crack-mouth-opening displacement (CMOD) and pressure were measured. Note that all the transducers were set to zero after pressurization and just before the beginning of the thermal transient. The number and locations of the instrumentation are summarized in Fig. 2.21.

2.2.4 Experimental Results

The pressure vessel was first heated to a test temperature of ~280°C using the heating resistors. At the same time, the vessel was pressurized by water and steam generated inside

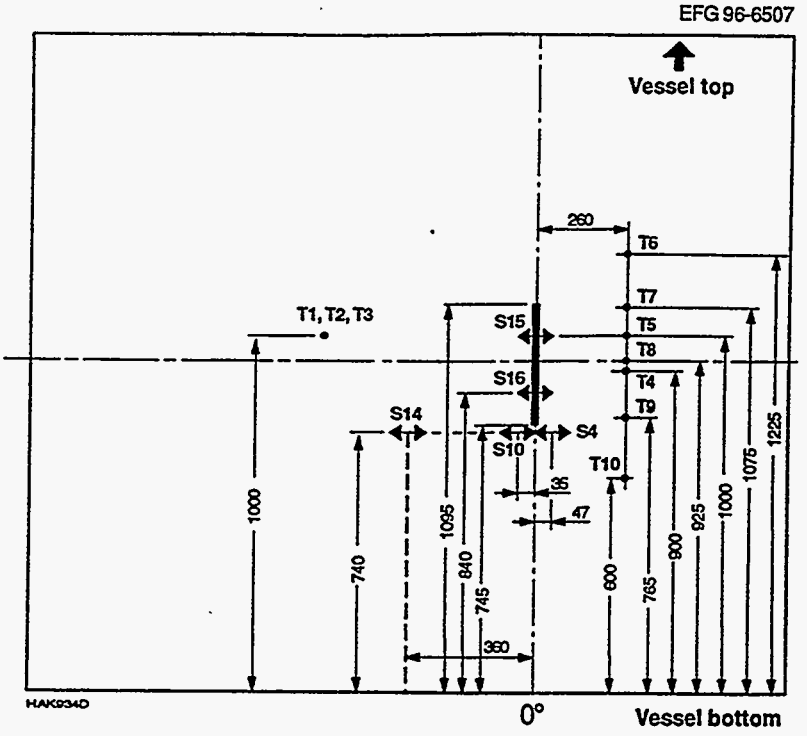

Transducer	Distance from the vessel bottom (mm)	Distance from the crack line along the vessel outside surface (mm)	Depth from the vessel outside surface (mm)
T1 temperature	1000		25
T2 temperature	1000		50
T3 temperature	1000		75
T4 temperature	900		98
T5 temperature	1000		0
T6 temperature	1225		0
T7 temperature	1075		0
T8 temperature	925		0
T9 temperature	765		0
T10 temperature	600		0
S15 CMOD	1000		0
S16 CMOD	840		
S14 strain	740	360	
S4 strain	740	47	
S10 strain	740	35	

Figure 2.21 Locations of thermocouple (T) and strain-gage (S) transducers in PTS-I/6 vessel

the vessel to an initial pressure of 60 MPa (see Fig. 2.16). The initial temperature distribution was approximated to be linear along the vessel length:

$$T = 0.126 * X + 160.0894 \ (°C) \ , \qquad (2.2)$$

in which the coordinate value X = 0 corresponds to the vessel bottom, and X = 1850 mm to the vessel top. During the heatup phase, steam is generated inside the vessel because of the high temperature. To avoid overpressurization, this steam is allowed to flow out of the vessel. The fact that the vessel is not full of water results in nonuniform heat transfer on the inside surface of the vessel along the vessel length. Also, the vessel stands with one end on the floor. According to Prometey, these two factors contributed to a nonuniform initial temperature distribution in the vessel. In addition, the ends of the vessel were closed and free to move axially.

The initial temperature distribution was assumed to be rotationally symmetric based on temperature measurements done by Prometey during similar PTS tests. On the basis of measured initial temperatures during the test, the variation through the wall was below 10°C. Thus, the initial temperature was approximated to be constant through the wall.

Just before the thermal shock was initiated, the heating resistors were raised. The vessel was then subjected to a sudden flow of 15°C tap water around the outer surface. Owing to the capacity of cooling water tanks, the coolant flow is effective for only the first 200 s, after which the flow rate gradually decreases to zero. The measured surface strains and CMODs are given in Figs. 2.22 and 2.23, respectively. The time of crack propagation was determined on the basis of the CMOD measurements.

Cleavage fracture initiation was achieved in the transition temperature region of the base material. The final configuration of the arrested crack is shown in Fig. 2.24. The amount of crack growth determined from visual examination of the fracture surface was asymetric with respect to the initial configuration of the flaw, that is, brittle fracture in the base metal and essentially no crack extension in the weld metal. Furthermore, no crack extension occurred near the surface of the vessel.

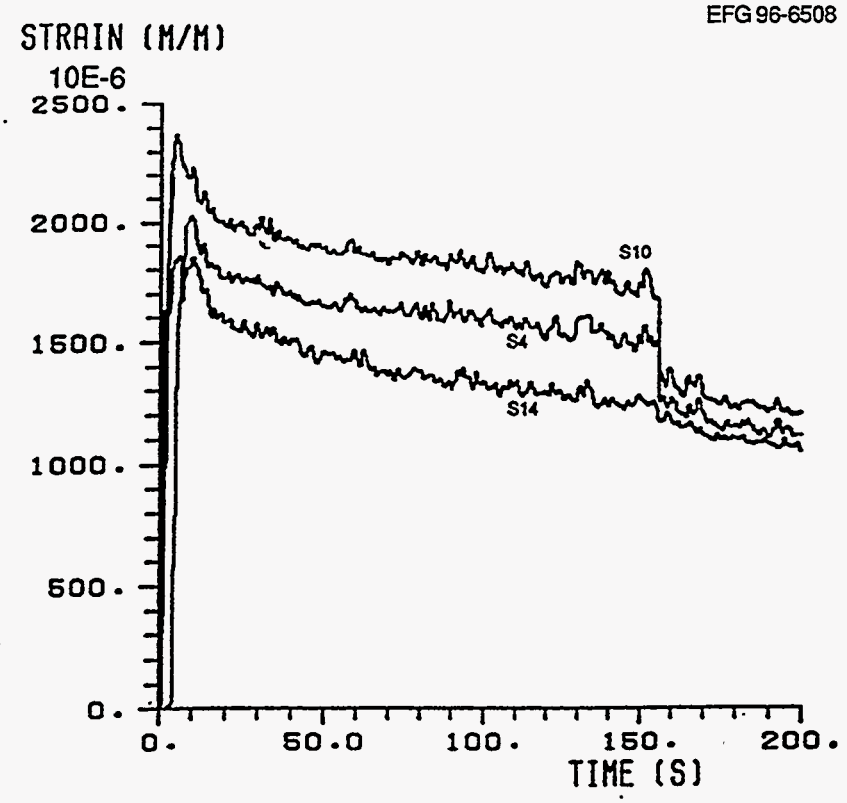

Figure 2.22 Strain vs time data measured at three transducer locations in PTS-I/6 experiment

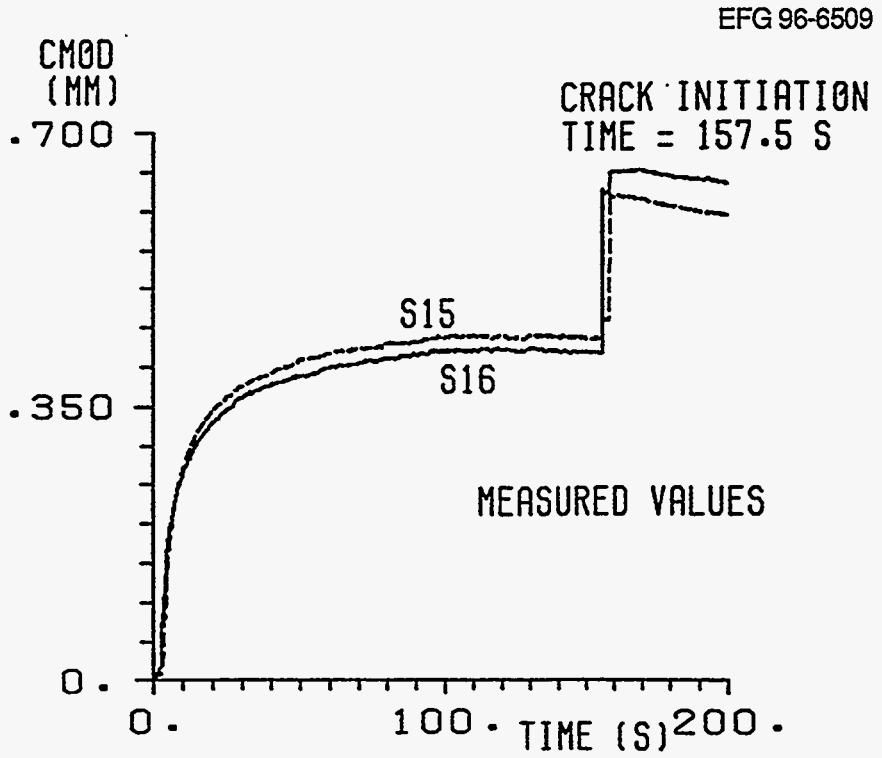

Figure 2.23 CMOD vs time data measured at two locations in PTS-I/6 experiment

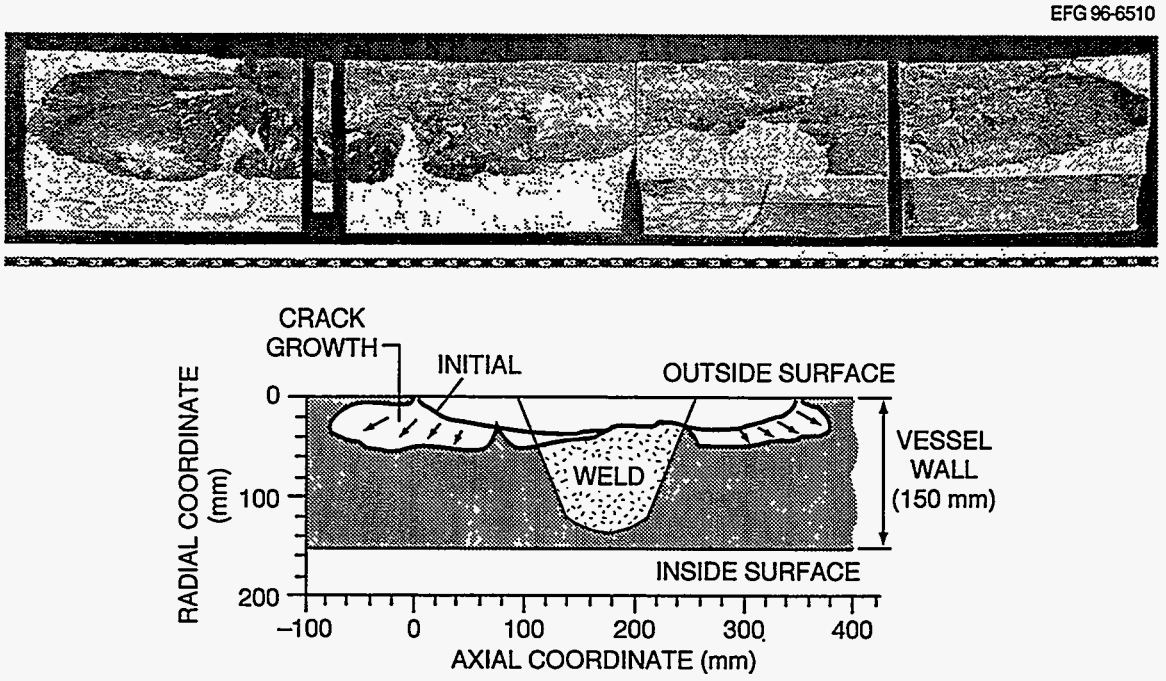

Figure 2.24 Initial and final crack configurations in PTS-I/6 experiment determined from visual inspection of fracture surface

2.3 NKS PTS Experiments

Large-scale experiments[4] were conducted on thick-section cylindrical specimens under PTS loading at MPA–Stuttgart to investigate crack growth and crack arrest behavior of primary circuit RPV materials. The material characteristics varied from high- to low-toughness material with a high NDT temperature to simulate end-of-life (EOL) or beyond EOL state. All tests started from simulated in-service conditions and were cooled down to room temperature.

The PTS testing program at MPA–Stuttgart utilizes a thick-walled, hollow cylinder (Fig. 2.25) that is welded at both ends to the grips of a 100-MN tensile testing machine. In addition to an axial tensile load, the specimens are loaded by internal pressure (pressurized water up to 30 MPa and 300°C). The thermal-shock cooling is achieved by spraying cold water evenly over the inner surface of the cylindrical specimen (Fig. 2.26).

2.3.1 NKS-5

The objectives of the NKS-5 test were to attain unstable crack initiation in the transition region of a weld material and extension of two symmetrically placed surface cracks up to a tough external ring. The material properties of vessel material should be represented by the properties of weld material. The purpose of the tough external ring was to simulate the toughness increase in a real irradiated vessel from the inner to the outer surface.

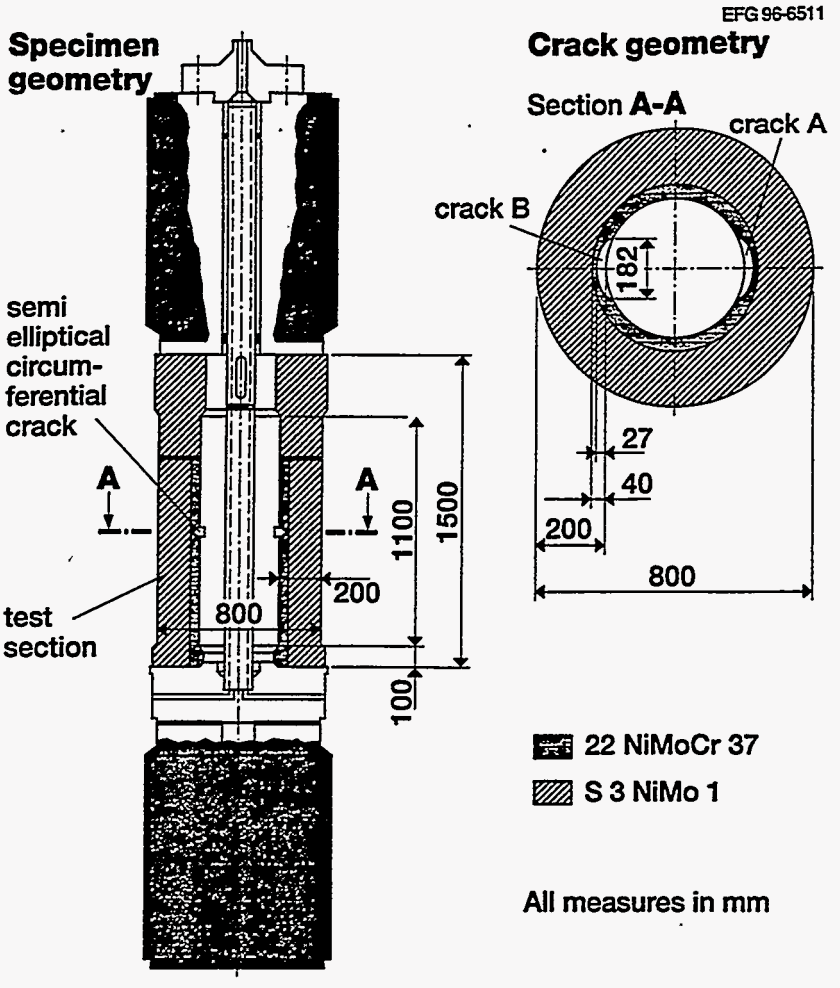

Figure 2.25 Geometry of composite NKS-5 specimen with symmetric cracks on inner surface (MPA-Stuttgart, Germany)

EFG 96-6512

Thermal and mechanical loading

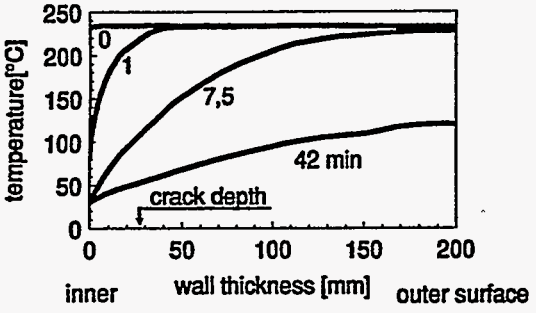

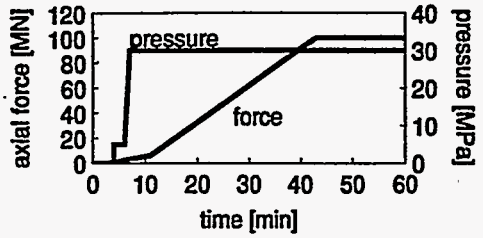

Material characterization

	base material (22 NiMoCr 37)	weld material (S3 NiMo 1)
yield stress $R_{p0,2}$ [MPa]	441 (20°C) 434 (220°C)	469 (20°C) 428 (220°C)
charpy energy for upper shelf [J]	90	220
$T_{50\,J}$ [°C]	140	-60

Figure 2.26 Loading and test material data for NKS-5 specimen

2.3.1.1 Specimen Geometry

The geometry of the composite NKS-5 specimen with symmetric cracks on the inner surface is depicted in Fig. 2.25. Two prefatigued semielliptical cracks (denoted A and B) with the circumferential angle of 52° and each with a maximum crack depth of 27 mm were installed in an axial plane of the specimen. The cylindrical specimen was composed of a low-toughness basic material (22 NiMoCr 37) with a shape-welded high-toughness external ring of 160-mm thickness made of S3 NiMo 1.

2.3.1.2 Material and Fracture Properties

The chemical composition of the base (22 NiMoCr 37) material used in the NKS-5 specimen is given in Table 2.15. Temperature-dependent tensile data for both the base and weld (S3 NiMo 1) materials are given in Table 2.16. Physical properties of thermal conductivity, heat capacity, density, and heat transfer coefficient on the inner surface are summarized in Table 2.17. Data describing CVN impact energy vs temperature are given for the base and weld materials in Figs. 2.27 and 2.28, respectively. The Charpy upper-shelf energy was 90 and 220 J for the base and weld materials, respectively; the corresponding RT_{NDT} values were determined to be 122 and –30°C, respectively. For the base material, J_R curves were generated at three temperatures using 20% side-grooved CT-25 specimens. These data are provided for temperatures of 160, 200, and 240°C in Figs. 2.29–2.31, respectively.

2.3.1.3 Instrumentation

The temperatures through the wall thickness were measured with thermocouples inserted into boreholes. Additional thermocouples, together with strain gages, were applied on the internal and external surfaces of the specimen. According to MPA, the thermocouple positions allowed an even temperature distribution both in the circumferential and longitudinal direction. The CMODs were recorded with clip gages positioned at selected points along both the A and B cracks on the inner surface. The measurement positions in the NKS-5 specimen for axial and circumferential strains, temperature, and CMOD are given in Figs. 2.32 and 2.33.

Table 2.15 Chemical composition of the base (22 NiMoCr 37) material in the NKS-5 specimen

	Chemical composition (%)										
Base material	C	Si	Mn	P	S	Cr	Mo	Ni	Al	V	Cu
NKS-5 (22 NiMoCr 37)	0.28	0.27	0.63	0.021	0.016	0.47	0.22	0.78	0.05	0.26	0.007

Table 2.16 Temperature-dependent tensile data for base and weld (S3 NiMo 1) materials of the NKS-5 specimen

Temperature (°C)	Young's modulus (MPa)	Yield strength $R_{p0.2}$ (MPa)	Ultimate strength R_m (MPa)	A_5 (%)	Z (%)	Ramberg Osgood parameter	
						α	n
Base material: 22 NiMoCr 37							
20	210,000	441	679	18.4	45	0.45820	8.66850
120	202,400	403	619	17.3	45	0.29823	9.63920
160	180,000	436	523	22.4	70.5	1.83870	14.06400
220	197,000	434	547	15.5	46.5	0.34950	17.21700
280	199,800	433	697	13.7	31	0.20930	9.14720
320	189,000	391	639	14.0	29	0.16887	9.46930
Weld material: S3 NiMo 1							
20	202,400	469	617	29.2	70.5		
120	204,000	492	569	27.0	72.5		
160	202,400	446	530	25.7	71		
220	199,900	428	534	24.0	71.5		
280	189,500	434	573	23.4	69.5		
320	192,000	427	583	31.2	70.5		

Table 2.17 Physical properties of thermal conductivity, heat capacity, density, and heat transfer coefficient on the inner surface of the NKS-5 specimen material

Initial temperature: 223°C
Conductivity: 45 W/m K
Density: 7800 kg/m^3
Capacity: 550 J/kg K

Time (s)	Heat transfer coefficient [kW/(m^2 K)]	Time (s)	Cooling temperature (C°)
0	0.0	0	189
30	3.0	20	65
60	4.0	270	65
90	2.5	360	28
120	2.3	3900	28
150	1.8		
210	1.5		
240	3.0		
300	2.0		
450	10.0		
3900	6.0		

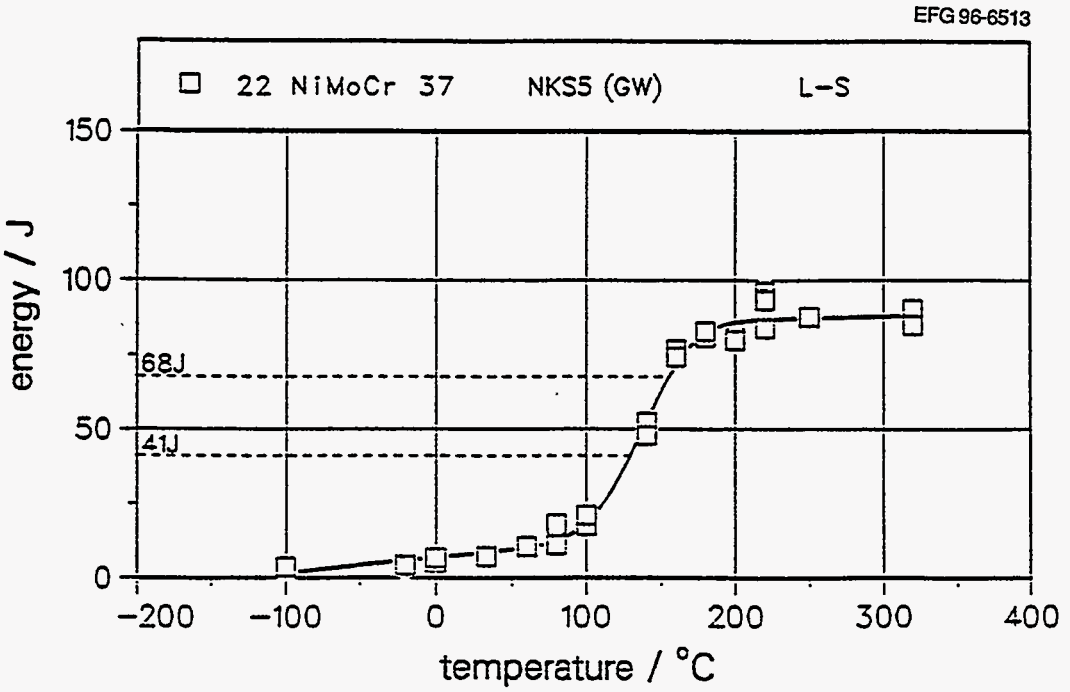

Figure 2.27 Charpy impact energy vs temperature for base material of NKS-5 test specimen

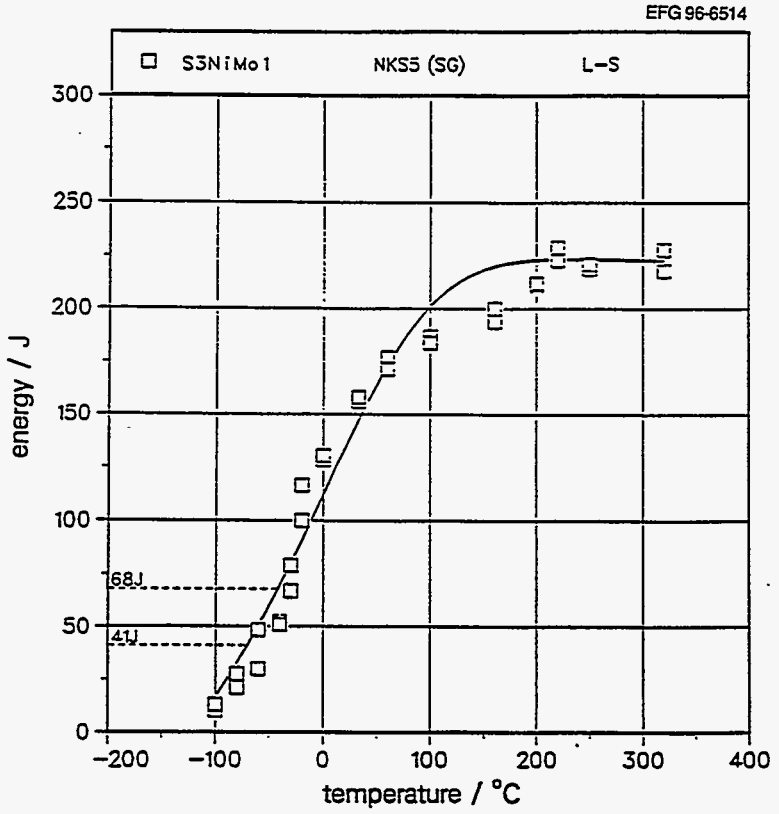

Figure 2.28 Charpy impact energy vs temperature for weld material of NKS-5 test specimen

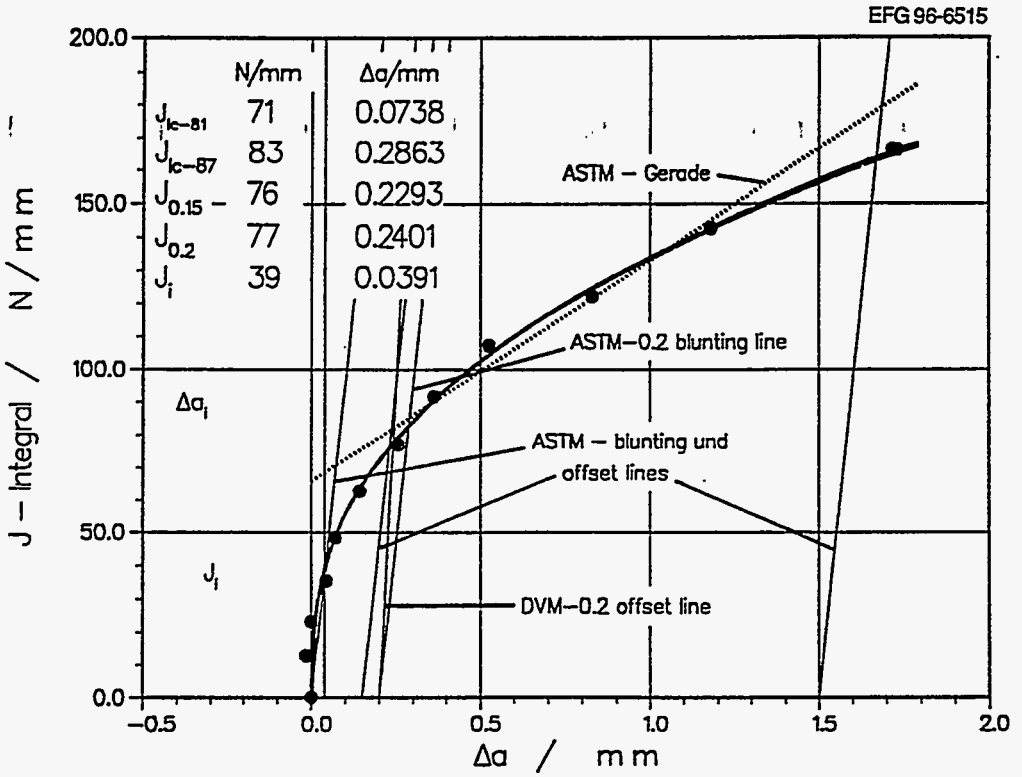

Figure 2.29 J-R curve data for NKS-5 base material determined from CT25 specimens at T = 160°C

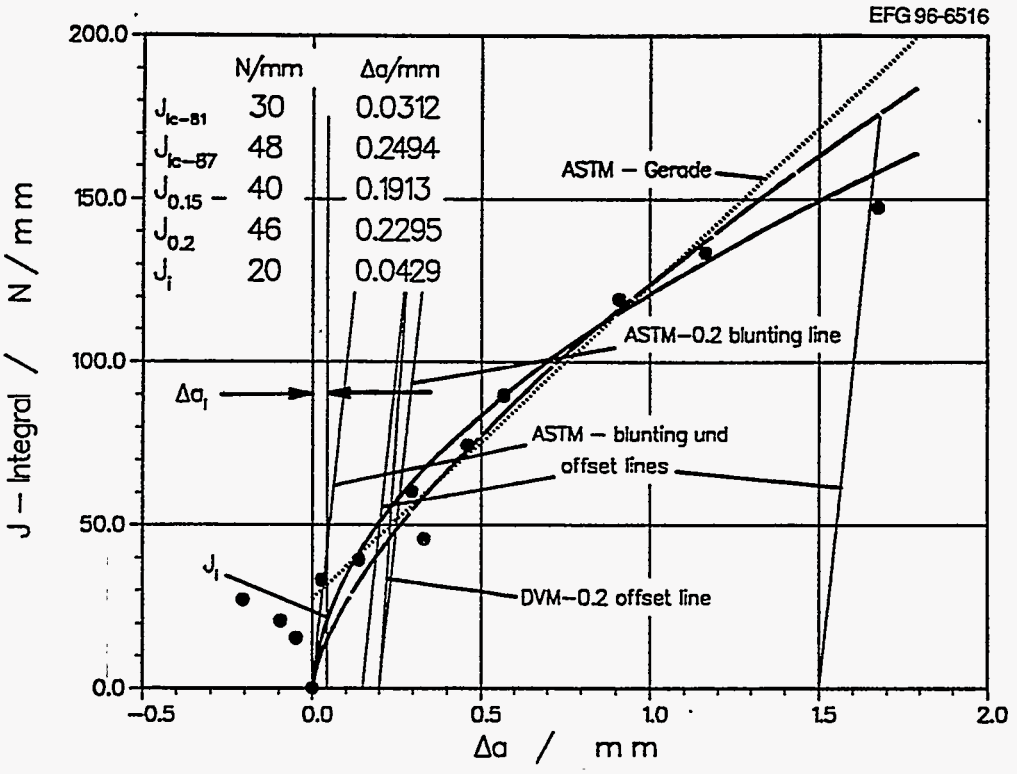

Figure 2.30 J-R curve data for NKS-5 base material determined from CT25 specimens at T = 200°C

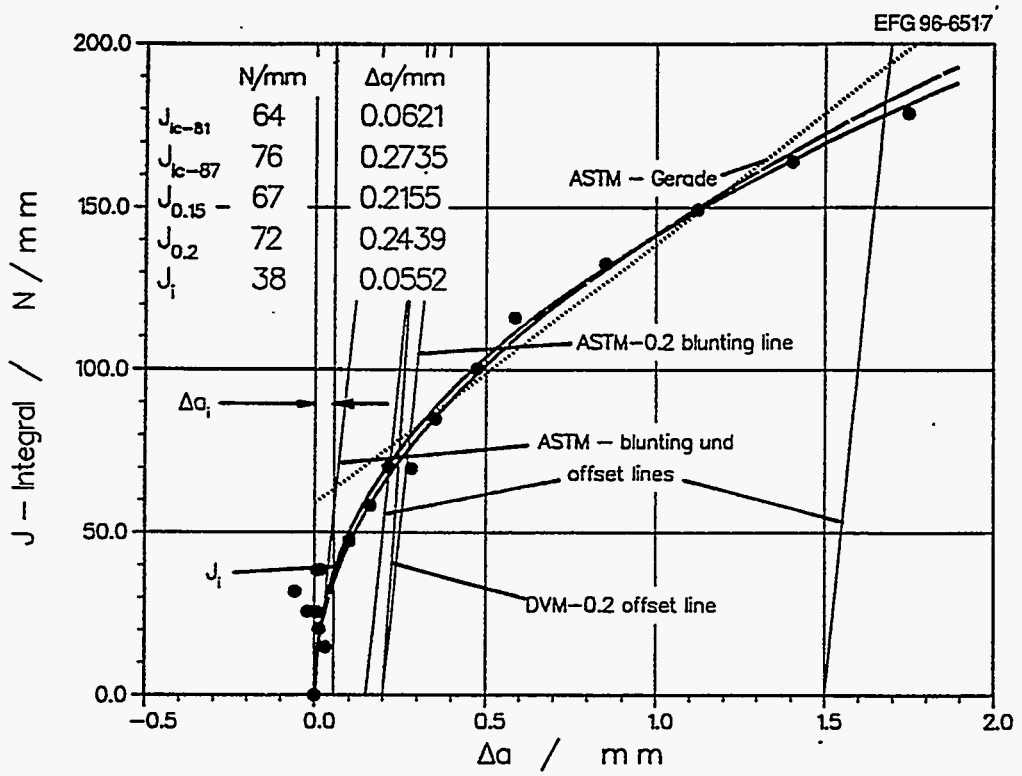

Figure 2.31 J-R curve data for NKS-5 base material determined from CT25 specimens at T = 240°C

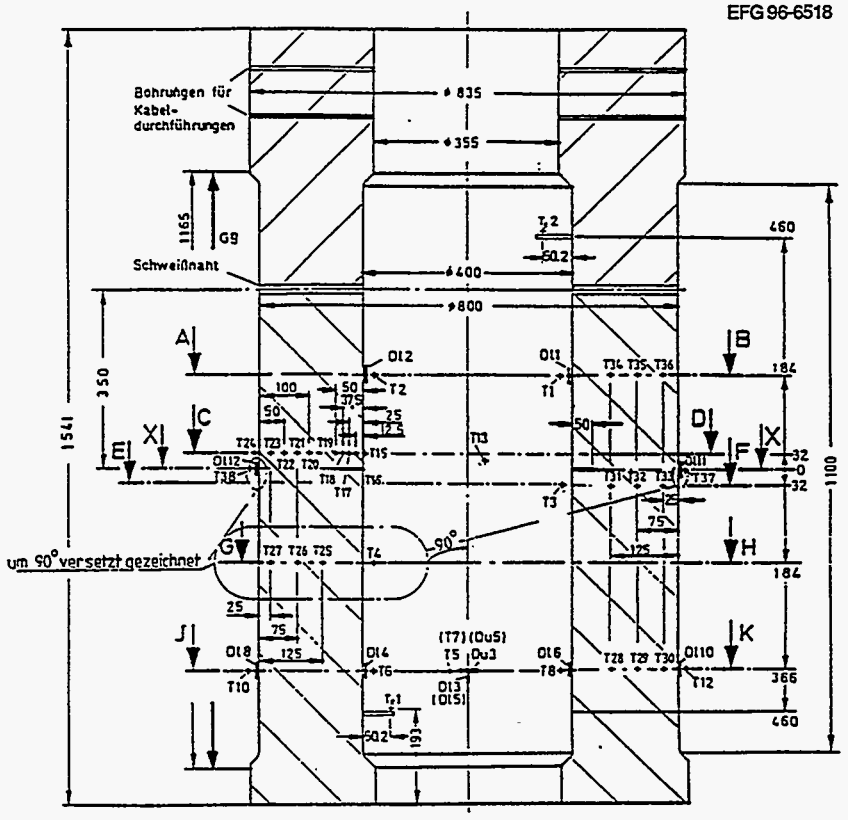

Figure 2.32 Measurement positions in specimen NKS-5 (Dl = longitudinal strain, Du = circumferential strain, T = temperature, and G = CMOD)

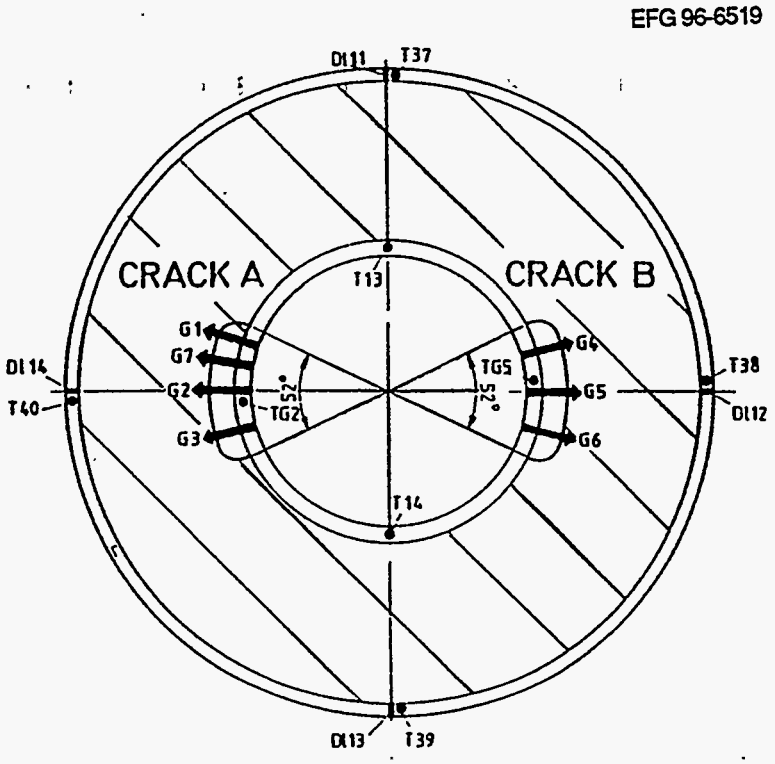

Figure 2.33 Measurement positions in fracture plane of specimen NKS-5 (Dl = longitudinal strain, Du = circumferential strain, T = temperature, and G = CMOD)

2.3.1.4 Experimental Results

Prior to the beginning of the thermal shock, the temperature was stabilized at 230°C on the inner wall of the specimen. The axial load was raised to the maximum of 100 MN at a rate of 3 MN/min just 11 min after cooling had started and was kept at that level until the end of the test. The axial load and internal pressure vs time, as well as the temperature profiles across the wall thickness of the specimen as a function of time, are shown in Fig. 2.26 for the NKS-5 experiment. Temperature vs time data recorded at thermocouple positions along Notch A and Notch B are given in Figs. 2.34 and 2.35, respectively. The axial expansion vs time for the specimen is given in Fig. 2.36.

During the test, the cracks initiated in the brittle regime and expanded in radial and circumferential "jumps" up to the tough weld material. These events are reflected in the measured CMOD vs time data shown in Figs. 2.37 and 2.38 for the A and B cracks, respectively. The fracture surface of specimen NKS-5 showed that the cracks propagated in cleavage both in the circumferential direction over an azimuthal angle of 220°, as well as in wall thickness direction, where they were arrested at a crack depth of 40 mm by the tough welded material. From the experimental data, it was not possible to determine whether the crack first extended in the radial or in the circumferential direction. The arrested configuration of the crack front is depicted in Fig. 2.39, along with the cutting plan for posttest sectioning of the test specimen. Inspection of the fracture surface indicated that the crack advanced essentially by cleavage. However, an exception was a seam of ductile fracture at the end of the fatigue crack, which can be interpreted as a stretched zone. Further assessments of the NKS-5 experiment are given in Ref. 4.

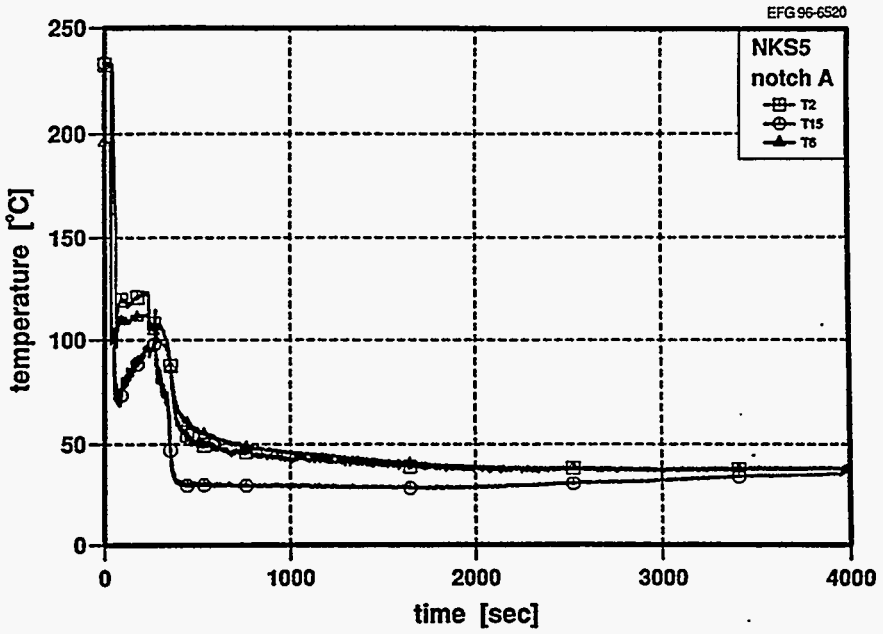

Figure 2.34 Temperature vs time data obtained at three thermocouple locations along Notch A in NKS-5 experiment

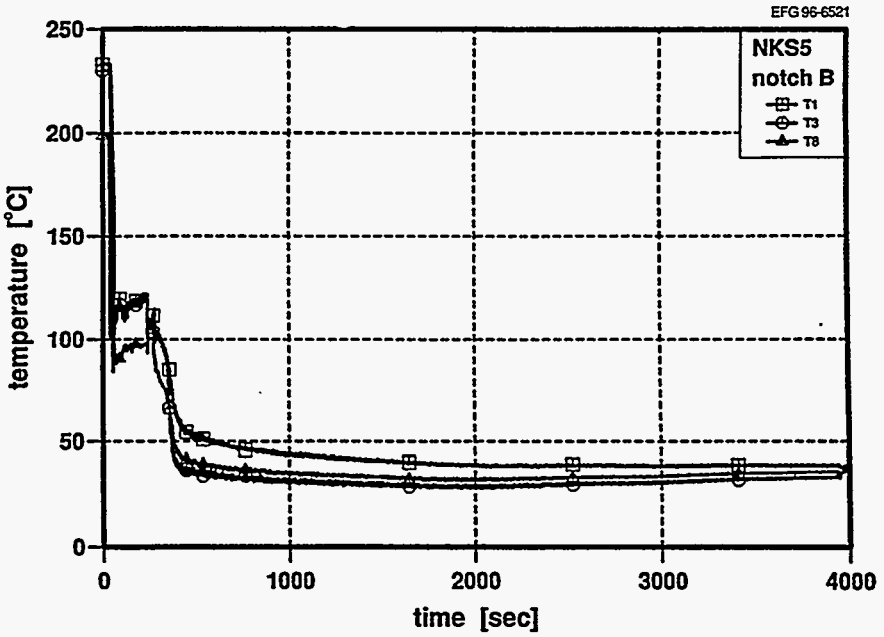

Figure 2.35 Temperature vs time data obtained at three thermocouple locations along Notch B in NKS-5 experiment

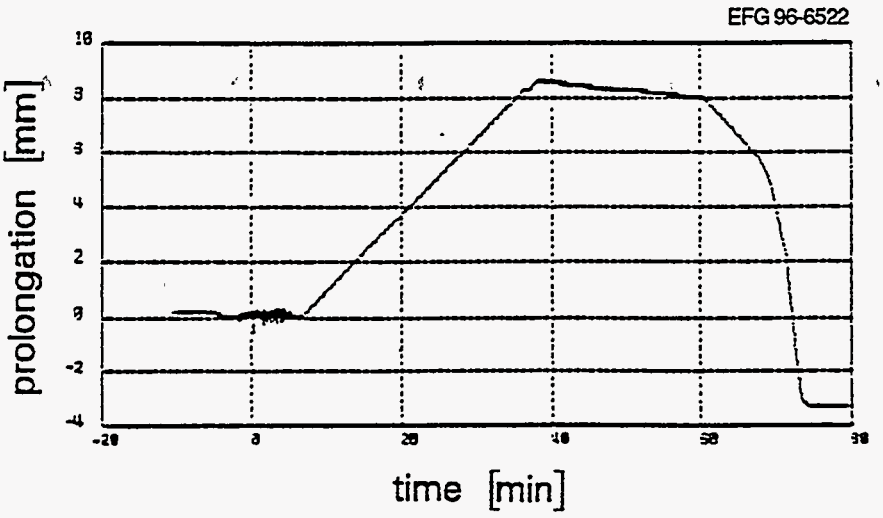

Figure 2.36 Measured axial elongation vs time in NKS-5 experiment

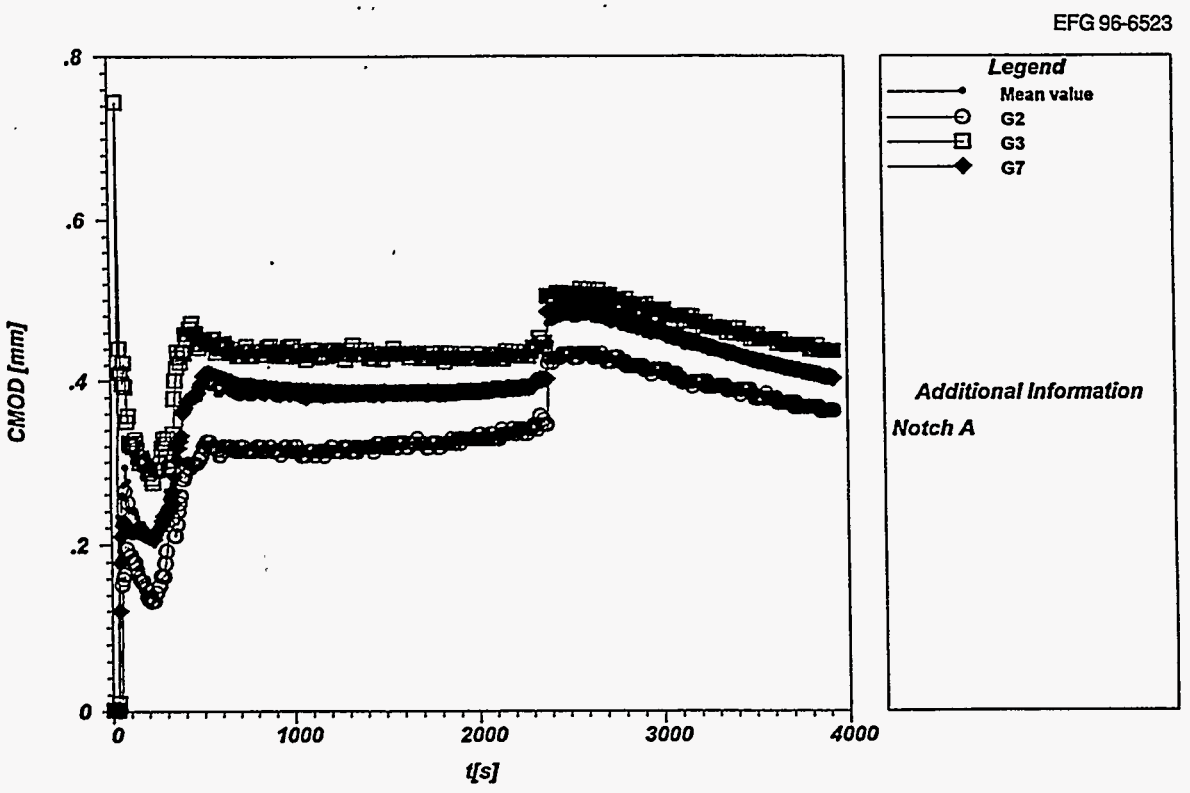

Figure 2.37 Measured CMOD vs time recorded at three gage locations (given in Fig. 2.33) along Notch A in NKS-5 experiment

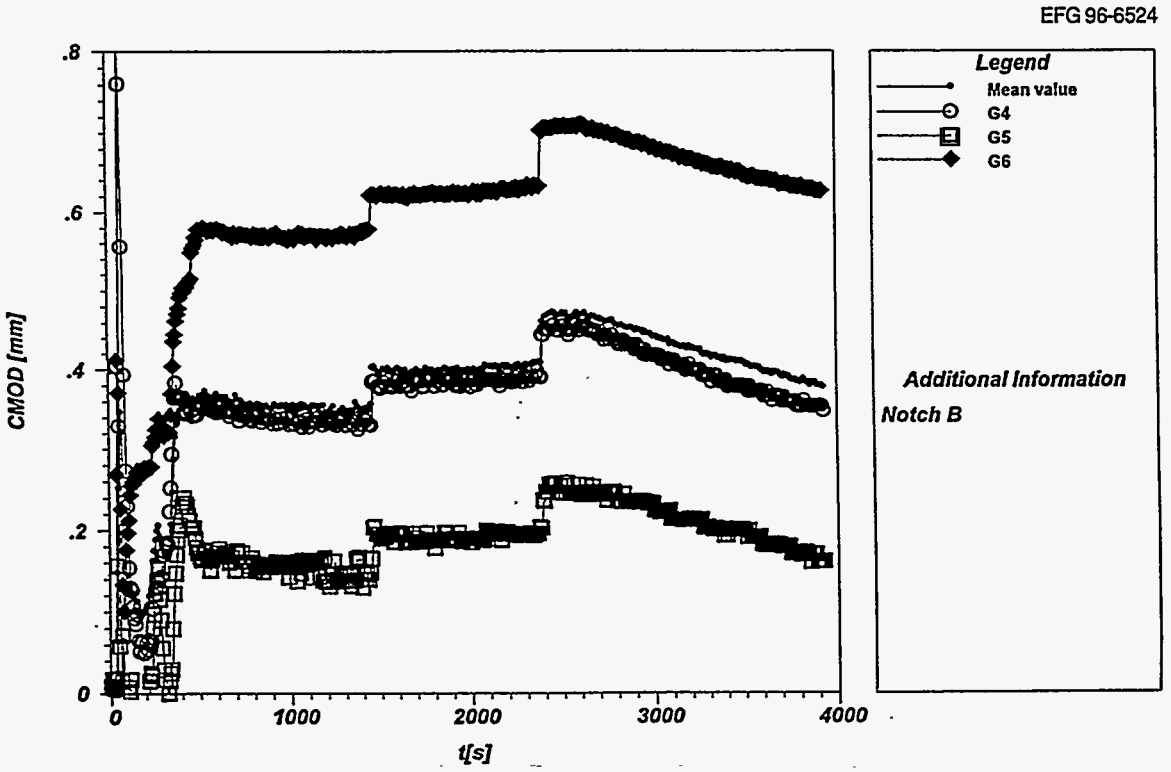

Figure 2.38 Measured CMOD vs time recorded at three gage locations (given in Fig. 2.33) along Notch B in NKS-5 experiment

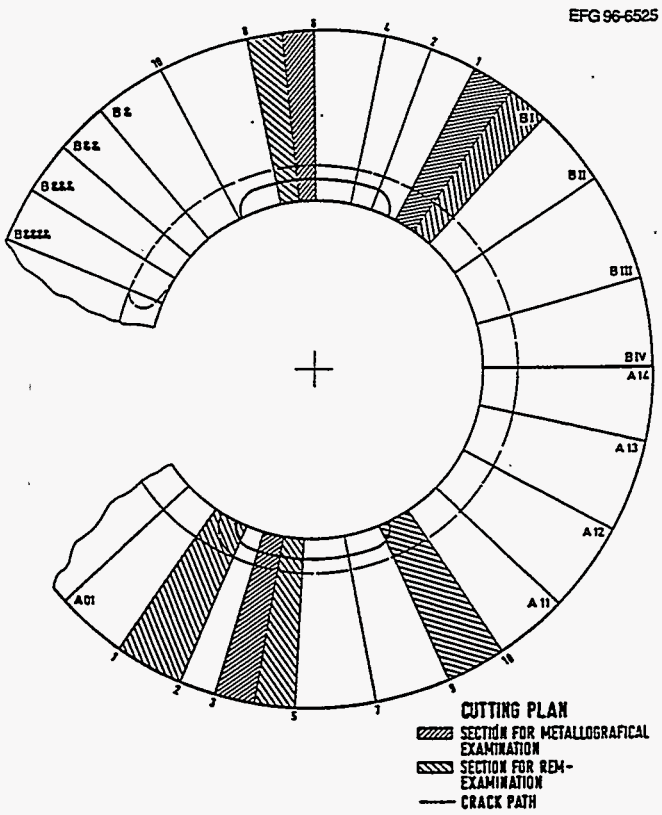

Figure 2.39 Arrested configuration of crack front in NKS-5 experiment, along with the cutting plan for posttest sectioning of test specimen

2.3.2 NKS-6

The purpose of the NKS-6 test was to conduct an experimental and numerical investigation of unstable crack propagation and arrest in a very low toughness vessel material under combined mechanical and thermal loading.

2.3.2.1 Specimen Geometry

The geometry of the composite NKS-6 specimen is depicted in Fig. 2.40. The test specimen contained a 360° circumferential flaw on the inner surface having an average depth of 37 mm; the flaw was fatigue precracked. As indicated in Fig. 2.41, the crack was located in an inner

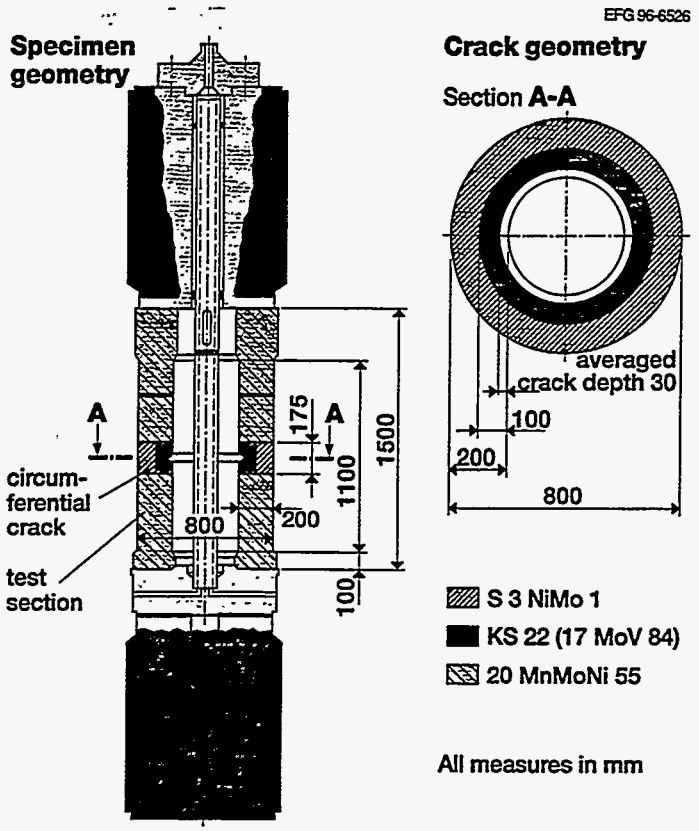

Figure 2.40 Geometry of composite NKS-6 specimen with circumferential crack on inner surface (MPA-Stuttgart, Germany)

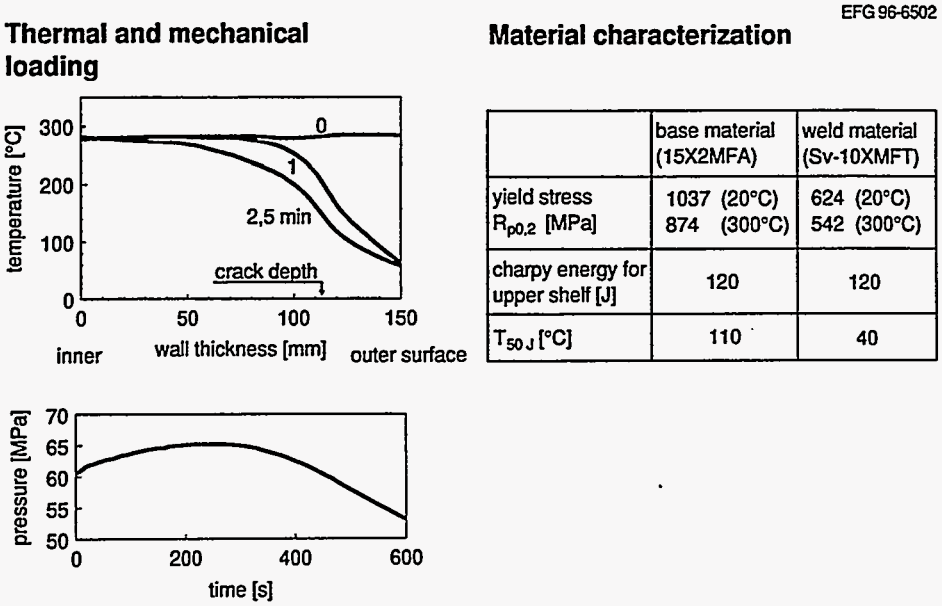

	base material (15X2MFA)	weld material (Sv-10XMFT)
yield stress $R_{p0.2}$ [MPa]	1037 (20°C) 874 (300°C)	624 (20°C) 542 (300°C)
charpy energy for upper shelf [J]	120	120
T_{50J} [°C]	110	40

Figure 2.41 Loading and test material data for NKS-6 specimen

ring of heat-treated material based on 17 MoV 84 (thickness = 100 mm). The latter material was specially developed by MPA–Stuttgart to have a Charpy upper-shelf energy of about 30 J and is referred to as KS 22. The specimen also included a shape-welded, high-toughness, 100-mm-thick, external ring of S3 NiMo 1 similar to that used in NKS-5. The remainder of the cylinder was manufactured from 20 MnMoNi 55 steel, which is similar to A 508 Class 3.

2.3.2.2 Material and Fracture Properties

The chemical composition and heat treatment of the KS 22 material used in the NKS-6 specimen are given in Table 2.18. Temperature-dependent tensile data for the three different materials constituting the specimen are given in Table 2.19. True stress–true strain curves for discrete temperatures are tabulated in Table 2.20. Physical properties of thermal conductivity, heat capacity, density, and heat transfer coefficient on the inner surface are summarized in Table 2.21. Temperature dependence of the thermal conductivity and heat capacity of the KS 22 material is depicted in Fig. 2.42. Data describing Charpy impact energy vs temperature for the KS 22 material in the S-T and S-L orientations are given in Fig. 2.43(*a*) and (*b*), respectively. Fracture toughness data describing K_{Ic}, K_{Ia}, K_{Id}, and K_J as a function of temperature for the KS 22 are given in Fig. 2.44. The FATT 50 temperature for the KS 22 material was given as 250°C. A J_R curve generated for the KS 22 material at a temperature of 350°C is given in Fig. 2.45.

2.3.2.3 Instrumentation

Thermocouples and strain gages were applied on the internal and external surfaces of the specimen at the positions given in Fig. 2.46. Also, temperatures through the wall thickness were measured with thermocouples inserted into boreholes. The CMODs were recorded with clip gages positioned at selected points along the crack on the inner surface. Locations of the transducers in selected axial planes (including the fracture plane) of the specimen are shown in Fig. 2.47.

2.3.2.4 Experimental Results

Conditions prior to the test included an initial temperature of ~300°C, internal pressure of 13 MPa, and an axial load of 25 MN. Axial force and internal pressure vs time, as well as temperature profiles across the wall thickness of the specimen as a function of time, are shown in Fig. 2.41. The combination of internal pressure and axial load resulted in K_I values just below the scatter band of the K_{Ic} values of the KS 22 material in which the crack resided. Subsequent to application of the thermal shock, crack propagation was achieved in the specimen in two steps with final crack arrest occurring at the interface of the tougher welded external ring. The measured CMOD vs time data for the crack at five gage locations (G3, G5, G6, G7, and G8 in Fig. 2.46) are shown in Fig. 2.48.

Two regions with different fracture modes were visible from fractographic examinations. The fracture surface immediately adjacent to the fatigue crack indicated predominantly cleavage fracture, which turned into a completely ductile fracture mode. In accordance with measurements on the fracture surface and acoustic emission results, the first phase included a cleavage crack jump and arrest corresponding to $\Delta a = 17$ mm. Following a quiet phase of a few seconds, crack extension continued with ductile crack growth up to the tough welded material ($\Delta a = 41$ mm). On reaching the weld material, no additional crack extension occurred. A time history of the crack extension constructed by MPA-Stuttgart is given in Table 2.22. Additional assessments of the NKS-6 experiment are described in Ref. 4.

Table 2.18 Chemical composition and thermal heat treatment of KS 22 material used in the NKS-6 specimen

Chemical composition (%)									
C	Si	Mn	P	S	Cr	Mo	Ni	Cu	V
0.16	0.3	0.69	0.004	0.026	0.32	1.01	0.25	0.08	0.31

Thermal treatment	
Austenize	3 h at 1050°C ± 10°C
Quench	Water
Temper	7 h at 610°C, air

Table 2.19 Temperature-dependent tensile data for the three different materials constituting the NKS-6 specimen

17 MoV 8 4

temperature °C	R p0,2 (MPa)	R m (MPa)	Young's modulus (MPa)	A 5 (%)	Z (%)
20	1092	1165	206900	4.8	6
100	1044	1120	197400	6.2	9.5
160	1017	1096	196500	8.6	11.5
250	1004	1086	187400	9.3	19
280	997	1080	177900	7.3	19
350	948	1027	171200	8.2	21

S3 NiMo 1

temperature °C	R p0,2 (MPa)	R m (MPa)	Young's modulus (MPa)	A 5 (%)	Z (%)
20	469	617	202400	29.2	70.5
120	492	569	204000	27	72.5
160	446	530	202400	25.7	71
220	428	534	199900	24.0	71.5
280	434	573	189500	23.4	69.5
320	427	583	192000	31.2	70.5

20 MnMoNi 5 5

temperature °C	R p0,2 (MPa)	R m (MPa)	Young's modulus (MPa)	A 5 (%)	Z (%)
20	488	651	212000	20	64
160	419	581	200000	20	63
280	414	612	188400	20	62
320	410	620	184400	25	60

Table 2.20 True stress–true strain curves at discrete temperatures for the three different materials constituting the NKS-6 specimen

Material MoV 8 4

True Stress-Strain Curve T = 20 °C

0.48333E-02	0.10000E+04
0.59991E-02	0.10550E+04
0.72779E-02	0.10920E+04
0.79891E-02	0.11150E+04
0.87519E-02	0.11280E+04
0.99906E-02	0.11360E+04
0.14411E-01	0.11610E+04
0.19431E-01	0.11650E+04
0.23627E-01	0.11850E+04
0.31485E-01	0.11970E+04
0.40753E-01	0.12110E+04
0.10652E+00	0.13500E+04

True Stress-Strain Curve T = 100 °C

0.40729E-02	0.80400E+03
0.49606E-02	0.92000E+03
0.72888E-02	0.10440E+04
0.11262E-01	0.10980E+04
0.11533E-01	0.11120E+04
0.17399E-01	0.11250E+04
0.26280E-01	0.11410E+04
0.40797E-01	0.11640E+04
0.10659E+00	0.13000E+04

True Stress-Strain Curve T = 160 °C

0.40916E-02	0.80400E+03
0.49819E-02	0.92000E+03
0.71756E-02	0.10170E+04
0.81486E-02	0.10510E+04
0.11266E-01	0.10740E+04
0.15437E-01	0.10880E+04
0.16778E-01	0.10960E+04
0.33035E-01	0.11270E+04
0.48442E-01	0.11480E+04
0.10656E+00	0.12900E+04

True Stress-Strain Curve T = 250 °C

0.44184E-02	0.82800E+03
0.57213E-02	0.94100E+03
0.73575E-02	0.10040E+04
0.89297E-02	0.10550E+04
0.10456E-01	0.10600E+04
0.12099E-01	0.10680E+04
0.15590E-01	0.10850E+04
0.17016E-01	0.10900E+04
0.24475E-01	0.11010E+04
0.29555E-01	0.11160E+04
0.10694E+00	0.13000E+04

Material S3 NiMo 1

True Stress-Strain Curve T = 20 °C

0.22530E-02	0.45600E+03
0.43172E-02	0.46900E+03
0.24279E-01	0.52200E+03
0.32837E-01	0.55400E+03
0.43730E-01	0.59300E+03
0.67372E-01	0.64200E+03
0.15154E+00	0.71600E+03

True Stress-Strain Curve T = 120 °C

0.22941E-02	0.46800E+03
0.44118E-02	0.49200E+03
0.35972E-01	0.54500E+03
0.51828E-01	0.57700E+03
0.68051E-01	0.60200E+03
0.84820E-01	0.61600E+03
0.94174E-01	0.62700E+03

True Stress-Strain Curve T = 160 °C

0.19763E-02	0.40000E+03
0.42036E-02	0.44600E+03
0.35341E-01	0.49400E+03
0.50974E-01	0.52100E+03
0.69122E-01	0.55100E+03
0.91736E-01	0.57400E+03
0.12276E+00	0.60000E+03

True Stress-Strain Curve T = 220 °C

0.20510E-02	0.41000E+03
0.41411E-02	0.42800E+03
0.22076E-01	0.47500E+03
0.36566E-01	0.51300E+03
0.51281E-01	0.53600E+03
0.70011E-01	0.56200E+03
0.88601E-01	0.58000E+03
0.11991E+00	0.60200E+03

True Stress-Strain Curve T = 280 °C

0.20739E-02	0.39300E+03
0.42902E-02	0.43400E+03
0.17612E-01	0.47600E+03
0.33618E-01	0.51500E+03
0.50939E-01	0.55700E+03
0.82193E-01	0.60500E+03
0.10824E+00	0.63300E+03
0.13858E+00	0.66000E+03

Material 20 MnMoNi 5 5

True Stress-Strain Curve T = 20 °C

0.18868E-02	0.40000E+03
0.43019E-02	0.48800E+03
0.21314E-01	0.53300E+03
0.31308E-01	0.57400E+03
0.51395E-01	0.63500E+03
0.60671E-01	0.65100E+03
0.79693E-01	0.67700E+03
0.88731E-01	0.68500E+03
0.10700E+00	0.70000E+03

True Stress-Strain Curve T = 160 °C

0.20000E-02	0.40000E+03
0.40950E-02	0.41900E+03
0.12035E-01	0.44700E+03
0.26950E-01	0.51000E+03
0.39565E-01	0.55300E+03
0.51805E-01	0.58100E+03
0.63405E-01	0.60100E+03
0.74785E-01	0.61700E+03
0.86555E-01	0.63100E+03
0.10330E+00	0.66000E+03

True Stress-Strain Curve T = 280 °C

0.20170E-02	0.38000E+03
0.41975E-02	0.41400E+03
0.72461E-02	0.44200E+03
0.12337E-01	0.47800E+03
0.28166E-01	0.54000E+03
0.39989E-01	0.58200E+03
0.52043E-01	0.61100E+03
0.64076E-01	0.63600E+03
0.75550E-01	0.65000E+03
0.87024E-01	0.66400E+03
0.98277E-01	0.67400E+03

Table 2.21 Physical properties of thermal conductivity, heat capacity, density, and heat transfer coefficient on the inner surface of NKS-6 specimen

Thermal expansion coefficient α, 1/K	**14.0×10^{-6}**
Density ρ, kg/m³	**7800**
Conductivity λ, W/m K	**45**
Heat capacity c, kJ/kg K	**0.550**

Heat transfer coefficient, h

Time (s)	h (W/m² K)
0	0
12	1,000
30	6,000
90	10,000
120	18,000
600	18,000

Cooling temperature, T_a

Time (s)	T_a (°C)
0	260
12	255
20	125
24	75
30	60
40	40
60	25
600	25

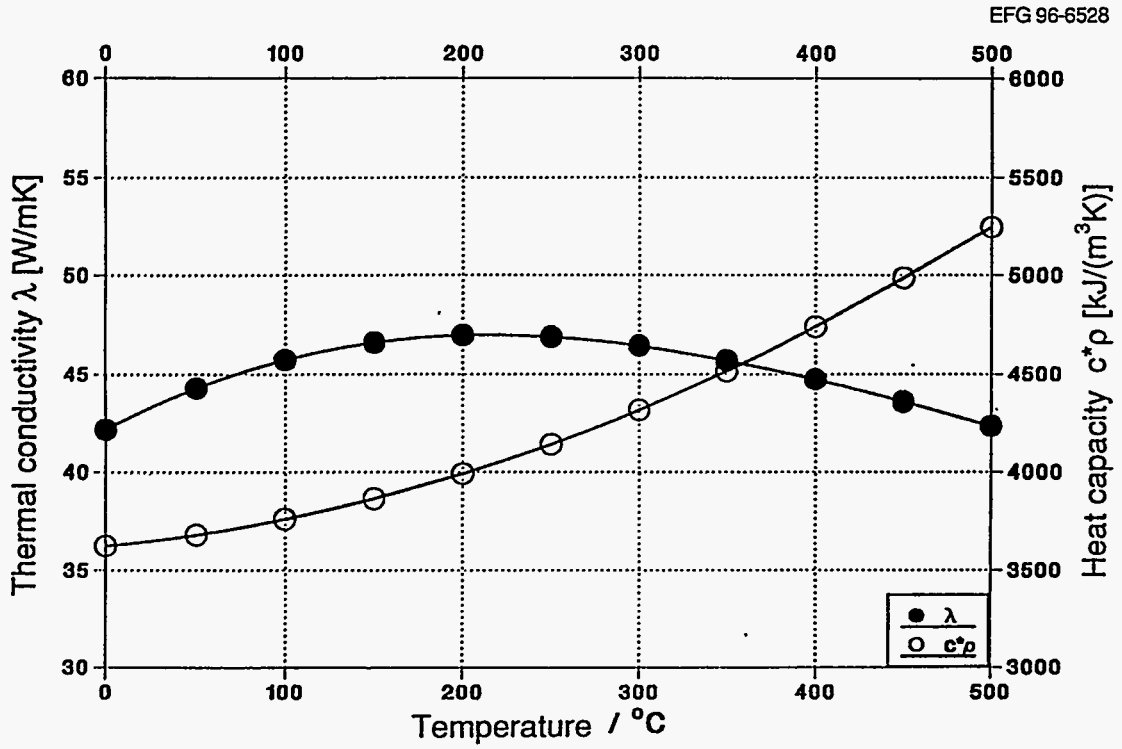

Figure 2.42 Temperature dependence of thermal conductivity and heat capacity of NKS-6 base material

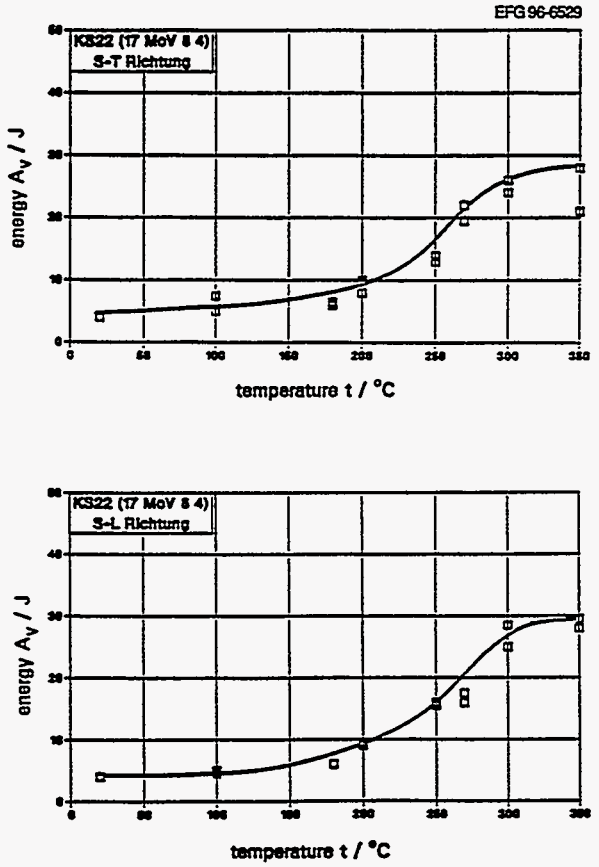

Figure 2.43 Charpy impact energy vs temperature for NKS-6 base material in S-T and S-L orientations

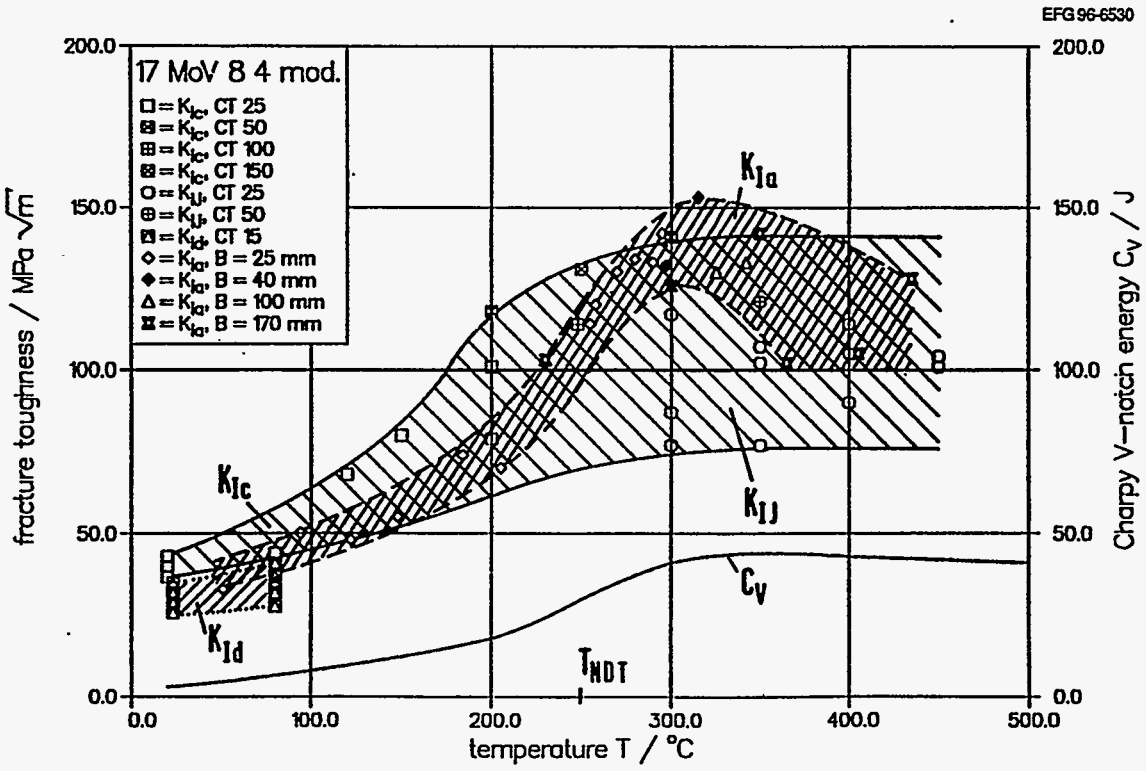

Figure 2.44 Fracture toughness data describing K_{Ic}, K_{Ia}, K_{Id}, and K_J as function of temperature for NKS-6 base material

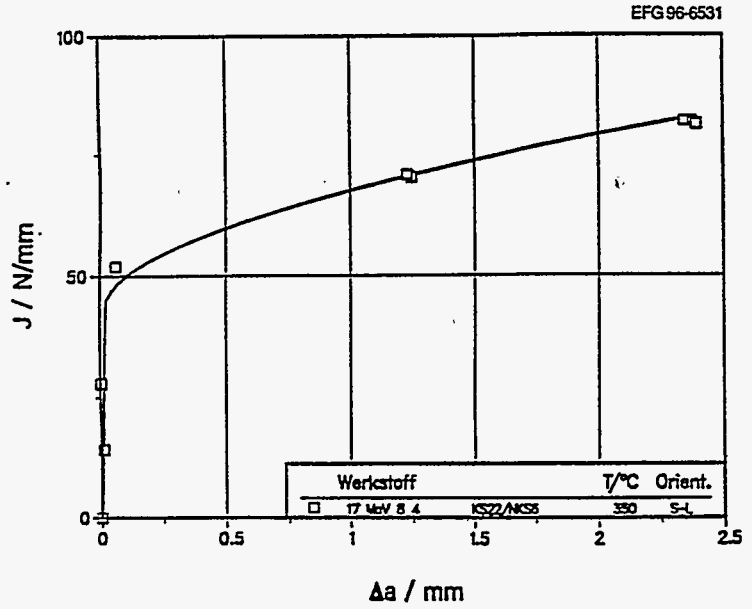

Figure 2.45 J_R curve for NKS-6 material generated at temperature of 350°C

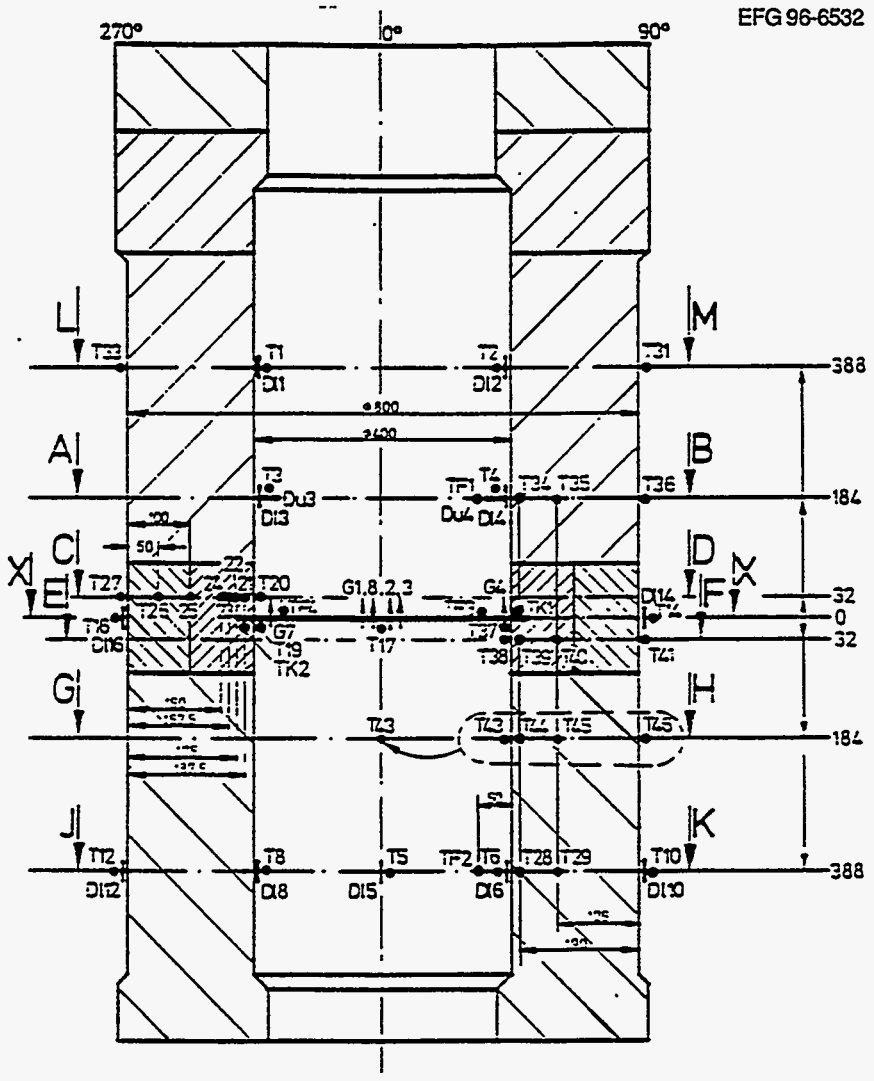

Figure 2.46 Measurement positions in specimen NKS-6 (Dl = longitudinal strain, Du = circumferential strain, T = temperature, and G = CMOD)

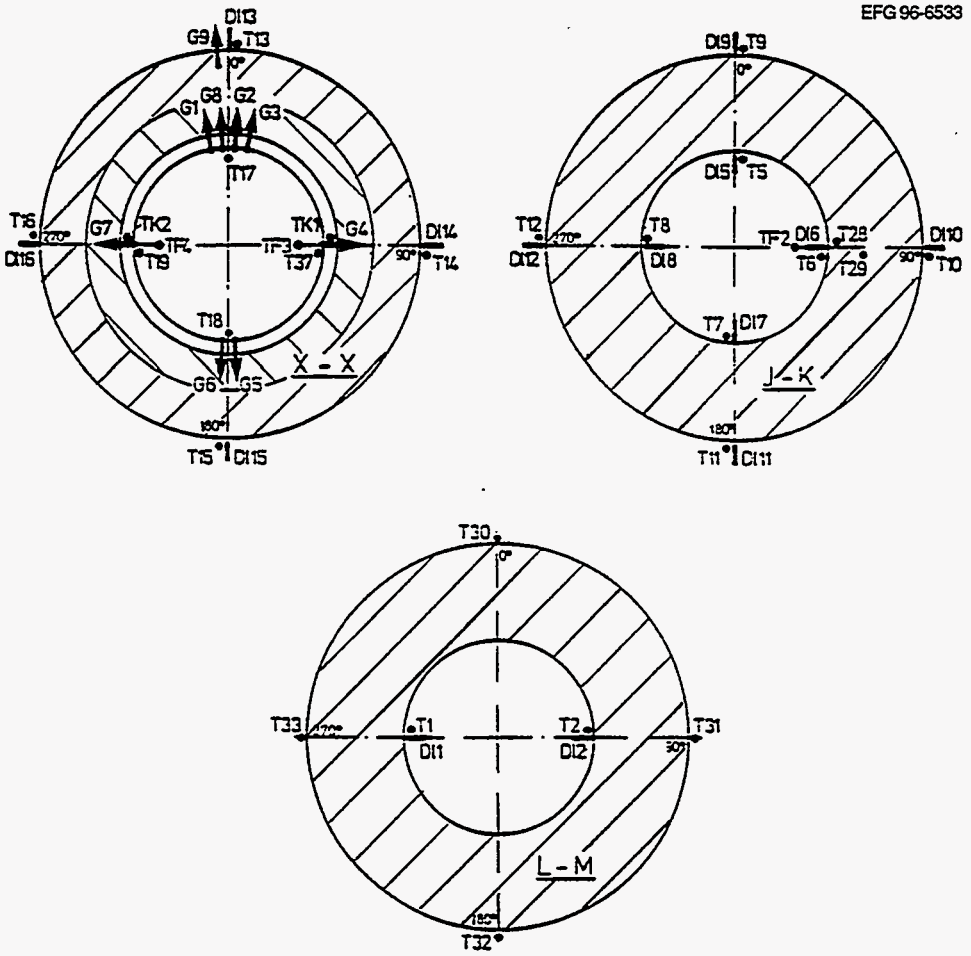

Figure 2.47 Measurement positions in selected axial planes of specimen NKS-6 (Dl = longitudinal strain, Du = circumferential strain, T = temperature, and G = CMOD)

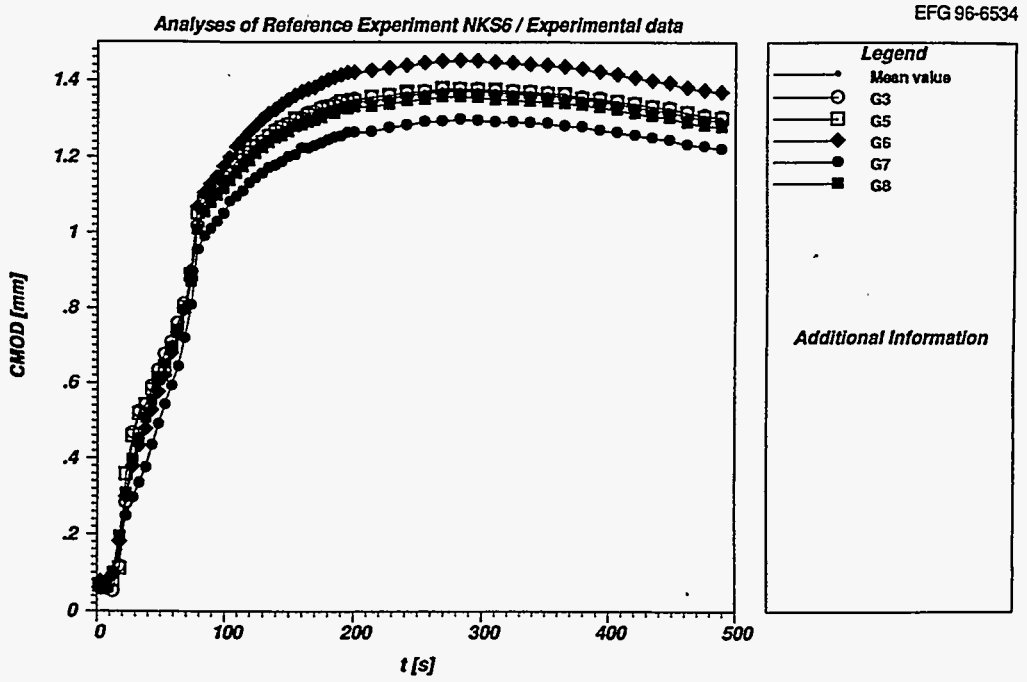

Figure 2.48 Measured CMOD vs time data at five gage locations (G3, G5, G6, G7, and G8 in Fig. 2.59) in NKS-6 experiment

Table 2.22 Time history of crack extension in NKS-6 experiment

Initial crack depth: a = 37 mm
At time t = 35 s: crack jump to 54 mm,
17-s standstill
At time t = 52 s: continuous crack growth
52 s → a = 54 mm
54 s → a = 58 mm
56 s → a = 62 mm
58 s → a = 66 mm
60 s → a = 70 mm
62 s → a = 74 mm
64 s → a = 78 mm
66 s → a = 82 mm
68 s → a = 86 mm
70 s → a = 89 mm
72 s → a = 91 mm
74 s → a = 93 mm
76 s → a = 95 mm

2.4 Clad Beam Experiments (DD2 and DSR3)

An experimental program is under way at EdF to provide data for evaluating different methods of fracture analysis used in RPV integrity assessments.[5] Experimental results are being compared with analysis predictions to validate different methods of fracture analysis and to evaluate their conservatism. Also, the effects of stainless steel cladding are being examined. The focus of these studies is a series of clad beams containing underclad cracks tested in four-point bending. The tests were performed at low temperatures (–170°C) to simulate severe radiation embrittlement and to investigate the effects of cladding on cleavage fracture in the base material. Test conditions were representative of near EOL for the base metal.

2.4.1 Specimen Geometry

The geometry of the four-point bend-bar specimen containing an underclad crack is shown schematically in Fig. 2.49.

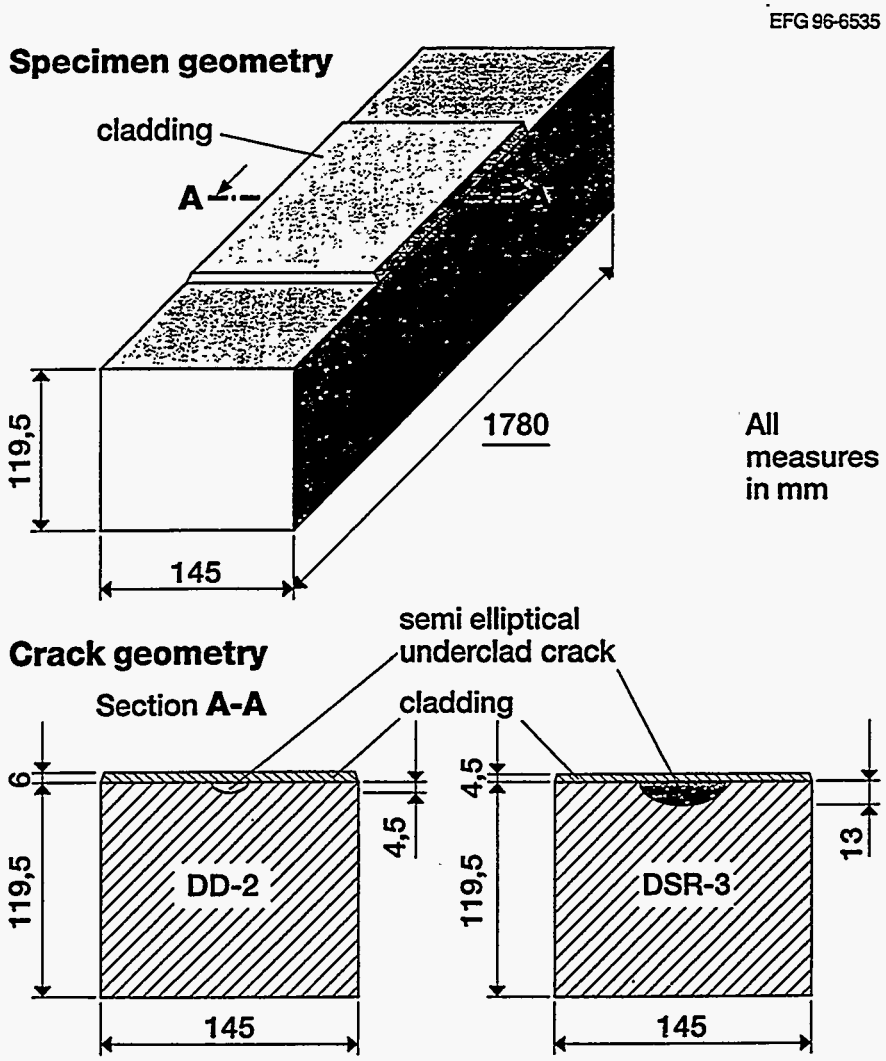

Figure 2.49 Clad bend-bar specimens, DD2 and DSR3, containing shallow semielliptical underclad cracks (EdF, France)

Description

A schematic diagram of the test frame used to apply a four-point bending load to the specimen is given in Fig. 2.50. The central part of each beam is A 508 class 3 steel (forging produced from a hollow ingot). The fabricated specimens have dimensions of ~120 × 145 × 1780 mm, with cladding on the top surface produced by an automatic submerged-arc welding process. Specimen DD2 has a 6.0-mm layer of cladding, while the cladding thickness in specimen DSR3 is 4.5 mm. The cladding is applied in two layers, the first of which is 309L stainless steel followed by a second layer of 308L. After the cladding process, a stress relief heat treatment was applied at 600°C for 8 h. The beams contain a small underclad crack (approximately semielliptical) with depth of 13 mm and length of 40 mm for DSR3 and a depth of 4.5 mm and length of 48 mm for DD2. Cracks on both specimens were generated by fatigue precracking.

2.4.2 Material Properties

Material characterization of the stainless steel cladding and the base metal included chemical analyses, Charpy impact tests, tensile tests, crack growth resistance, and fracture toughness. The chemical composition of the base metal is given in Table 2.23. Tensile properties for the cladding and base metal at the test temperature of –170°C are provided in Table 2.24. Also, the stress-plastic strain data for the base metal and the cladding at –170°C are given in Fig. 2.51 and in Table 2.25. The RT_{NDT} of the base metal was determined to be –40°C. The fracture toughness K_{Ic} of the base metal determined as a function of temperature from tests of CT25 specimens (a/W = 0.55, thickness of 25 mm) is depicted in Fig. 2.52.

2.4.3 Instrumentation

Data collected during the tests are load, load-line displacement (LLD), strains, and temperatures. Strains are measured with strain gages placed on the clad surface and on the opposite surface of the beam. Locations of strain gages on the DSR3 specimen are shown in Fig. 2.53. Temperatures are measured with thermocouples placed on the surface and inside the specimen.

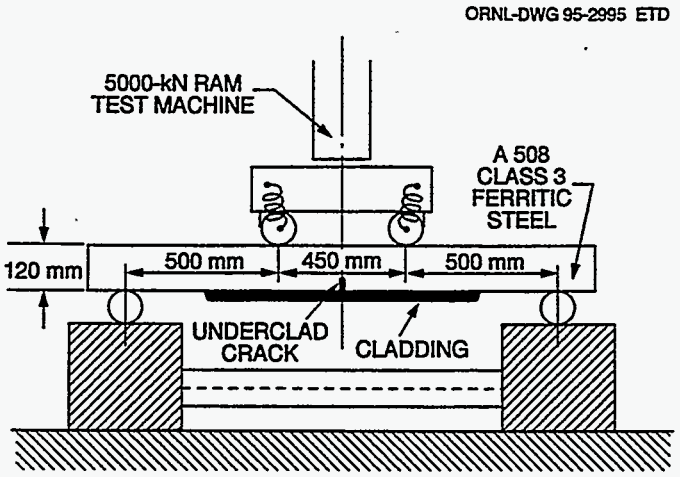

Figure 2.50 Schematic of test frame used by EdF in four-point bending fracture experiments

Table 2.23 Chemical composition of base metal in DD2/DSR3 clad beam specimens

	Chemical composition (%)											
	C	S	P	Mn	Si	Ni	Cr	Mo	V	Cu	Co	Al
RCCM specification	≤0.22	≤0.008	≤0.008	0.15 1.60	0.10 0.30	0.50 0.80	≤0.25	0.43 0.57	≤0.01	≤0.08	≤0.03	≤0.04
Inner surface	0.14	0.004	0.006	1.31	0.19	0.72	0.17	0.51	<0.01	0.07	<0.01	0.015
1/4 thickness	0.18	0.004	0.006	1.32	0.19	0.73	0.17	0.51	<0.01	0.07	≤0.01	0.016

Table 2.24 Tensile properties of cladding and base material

Engineering and true stress–strain tensile data at T = –170°C	
E-Modulus, MPa	
Base metal	210,000
Cladding	160,000
$R_{p0.2}$, MPa	
Base metal	768
Cladding	347
Poisson's ratio	ν = 0.3

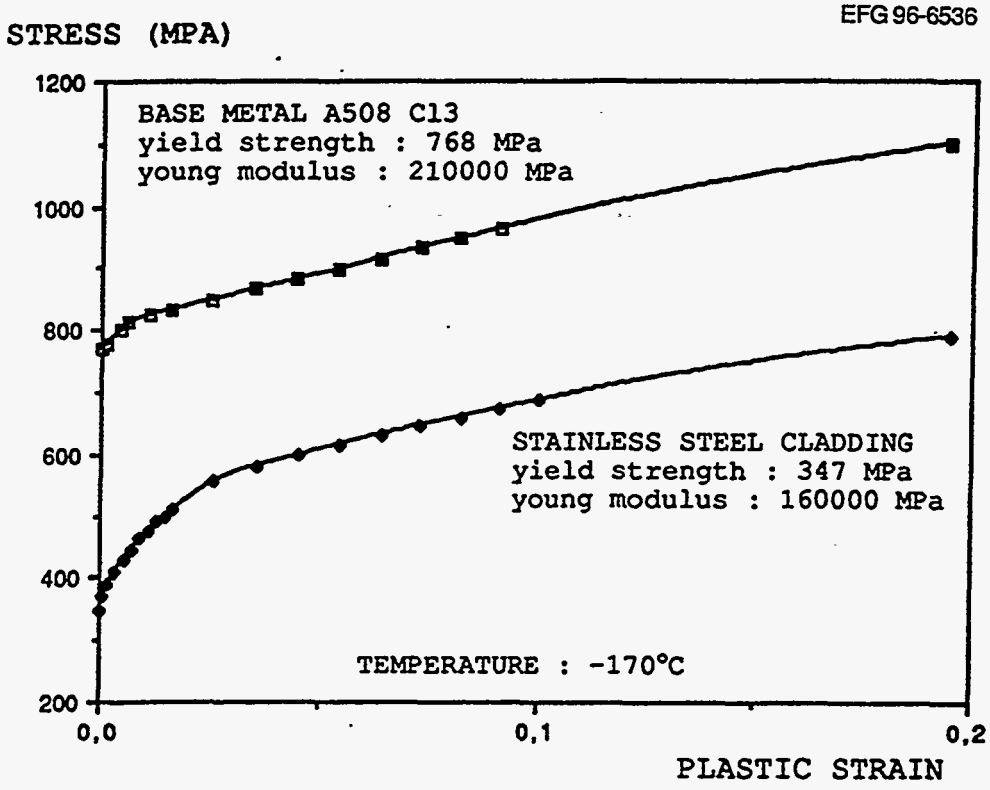

Figure 2.51 Stress-plastic strain curves (base metal and stainless-steel cladding) used in analyses of clad beam experiments

Table 2.25 Stress and plastic strain data for base metal and cladding in DD2/DSR3 material at –170°C

Base metal		Cladding	
Stress (MPa)	Plastic strain	Stress (MPa)	Plastic strain
768	0	347	0
779	0.0019	370	0.00069
787	0.0038	390	0.00156
811	0.0057	410	0.00344
823	0.0106	430	0.00531
832	0.0154	443	0.00723
847	0.0251	462	0.00901
865	0.0347	477	0.01090
881	0.0442	490	0.01280
896	0.0536	500	0.01470
915	0.0628	510	0.0166
932	0.0721	557	0.0261
947	0.0812	581	0.0356
963	0.0902	598	0.0451
		615	0.0545
		632	0.0637
		646	0.0730
		659	0.0821
		673	0.0911
		687	0.1000

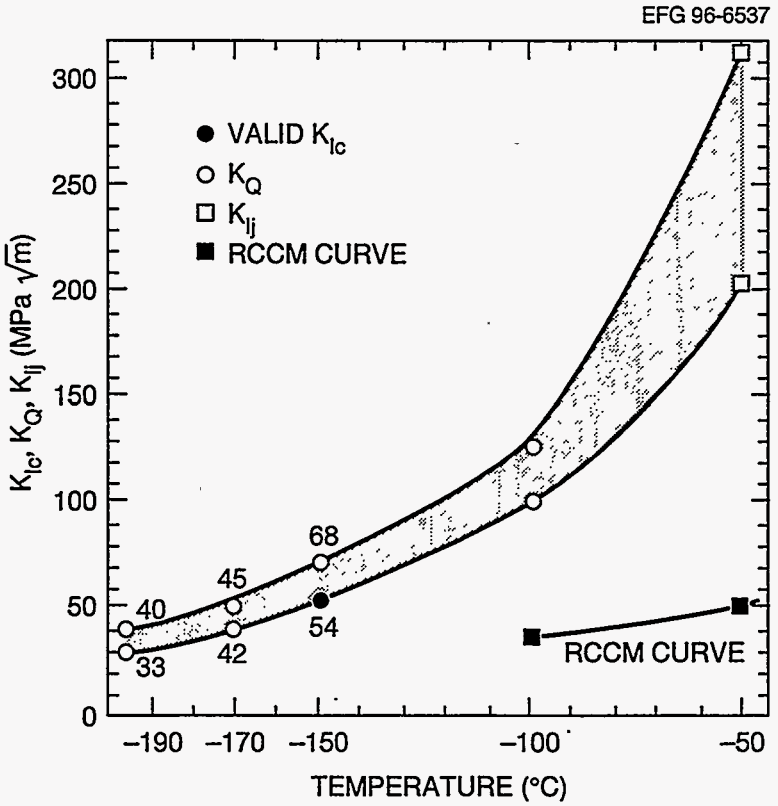

Figure 2.52 Fracture toughness vs temperature curves determined from CT25 specimens of base metal in clad beam experiments(RT_{NDT} = –40°C)

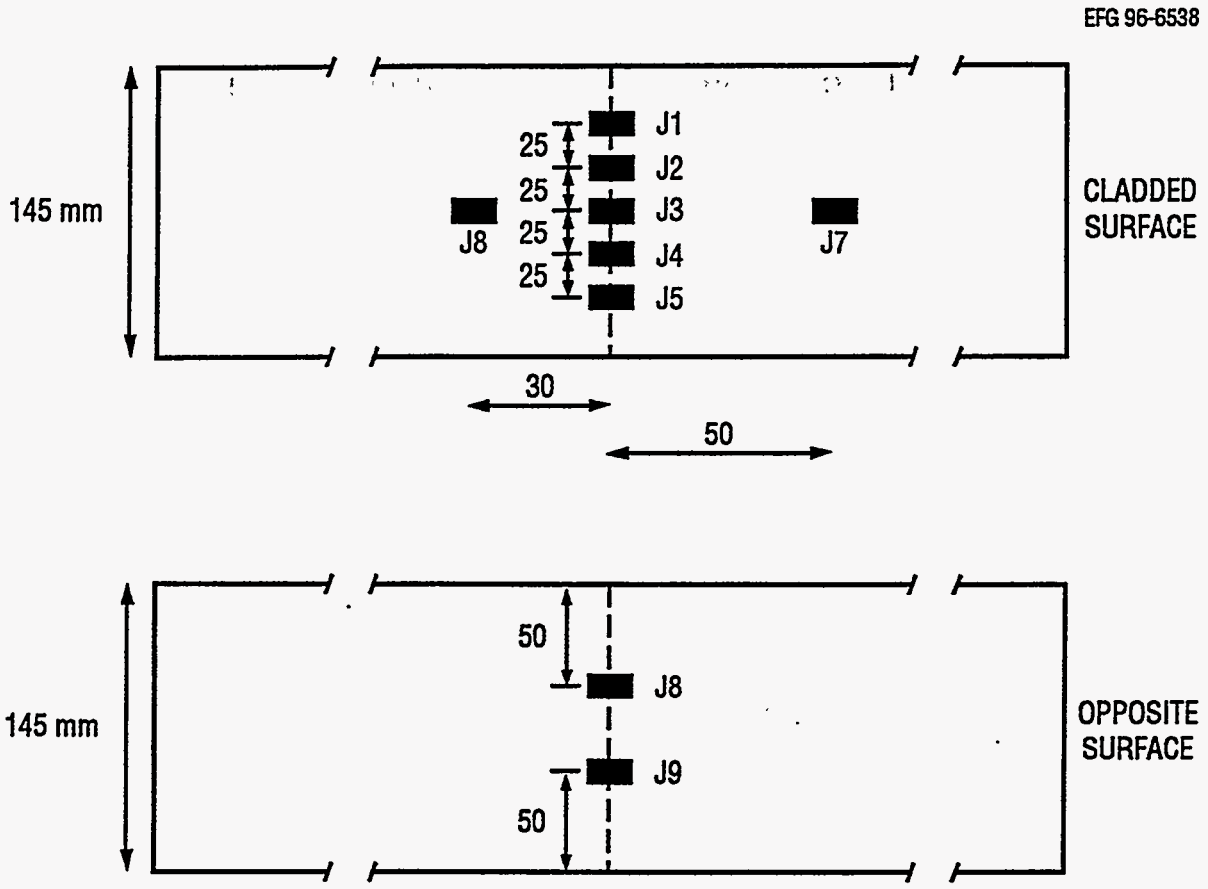

Figure 2.53 Locations of strain gages on clad beam specimen DSR3

2.4.4 Experimental Results

The objective of the tests is to obtain crack instability in the base metal by cleavage fracture under conditions that are potentially influenced by the presence of cladding. With this aim, the tests are performed at very low temperature, about –170°C. Before the mechanical test, the beam is cooled with liquid nitrogen such that the temperature is uniform inside the specimen after the cooling. The beam is insulated to avoid significant reheating during the fracture test. The specimens are then loaded in four-point bending with a 1450-mm major span and 450-mm minor span (see Fig. 2.50).

In the DSR3 test, the load on the beam at fracture was reported to be 695 kN. The cleavage fracture initiated in the ferritic base material with no crack arrest. The temperature at the crack tip at the time of fracture was between –165 and –170°C. In the DD2 test, the beam fractured at a load of 890 kN with no crack arrest. Measured loads vs LLD for the two tests are given in Fig. 2.54. Measured loads vs axial strain at three strain-gage locations for beams DSR3 and DD2 are depicted in Figs. 2.55 and 2.56, respectively.

Schematics of the fracture surfaces for DSR3 and DD2 are shown in Figs. 2.57 and 2.58, respectively. Measured coordinates of discrete points on the initial fatigue crack front are given in these figures for each beam specimen. Photographs of the corresponding fracture surfaces are given in Figs. 2.59 and 2.60. The point of cleavage initiation was located about 1.5 to 2 mm from the clad/base interface in DD2; the corresponding location in DSR3 was about 2.5 mm from the interface.

EFG 96-6539

Loading

4-point-bending
temperature: -170°C

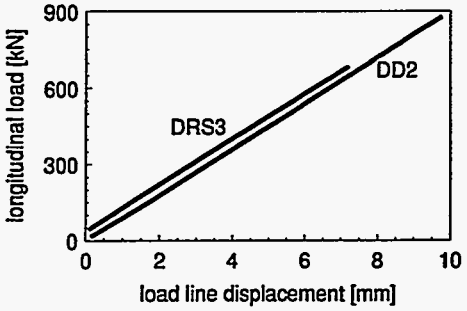

Material characterization

	base material (A508 C13)	cladding
yield stress $R_{p0,2}$ [MPa]	768	347
RT_{NDT}[°C]	-40	?

Figure 2.54 Loading and test material data for clad beam experiments DD2 and DSR3

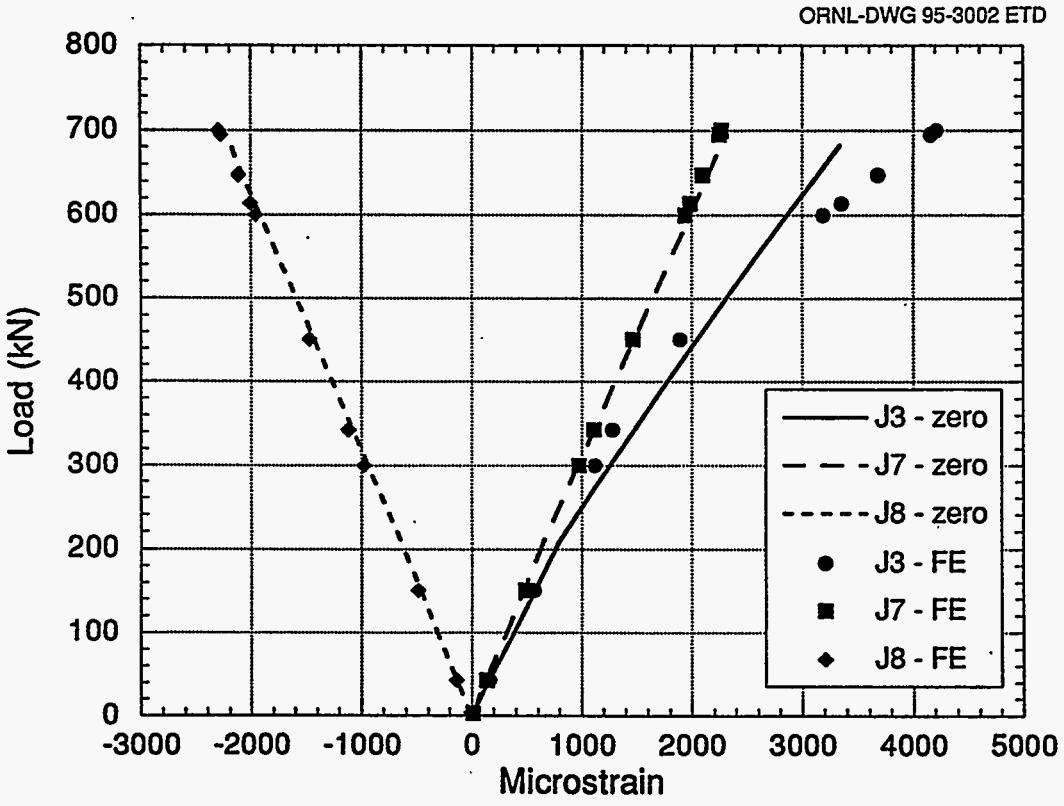

Figure 2.55 Measured load vs strain data (normalized to zero load) for clad beam experiment DSR3

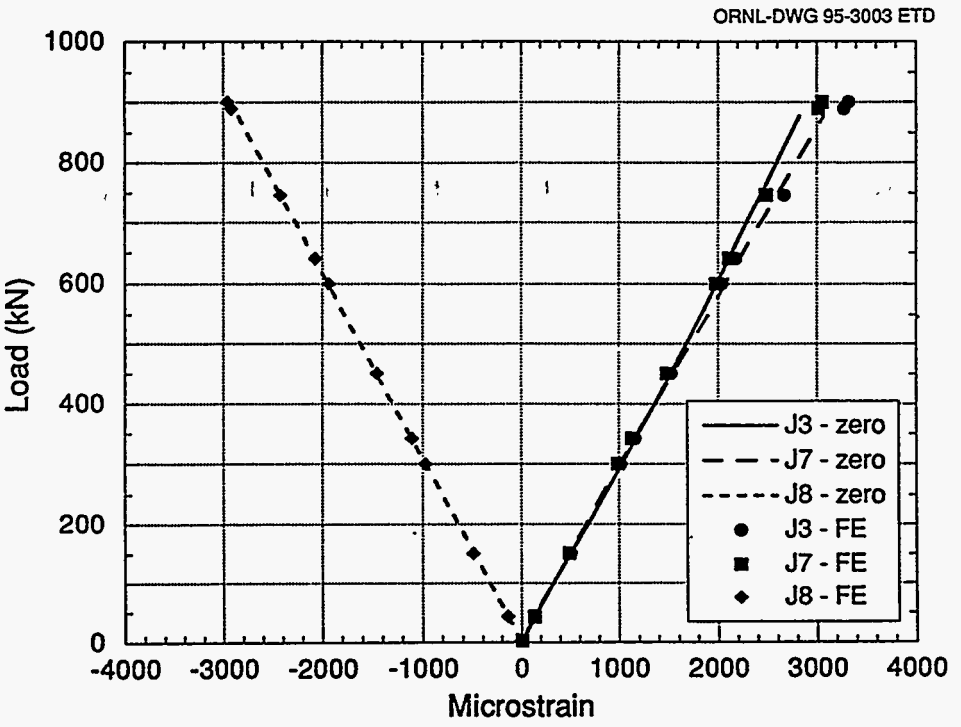

Figure 2.56 Measured load vs strain data (normalized to zero load) for clad beam experiment DD2

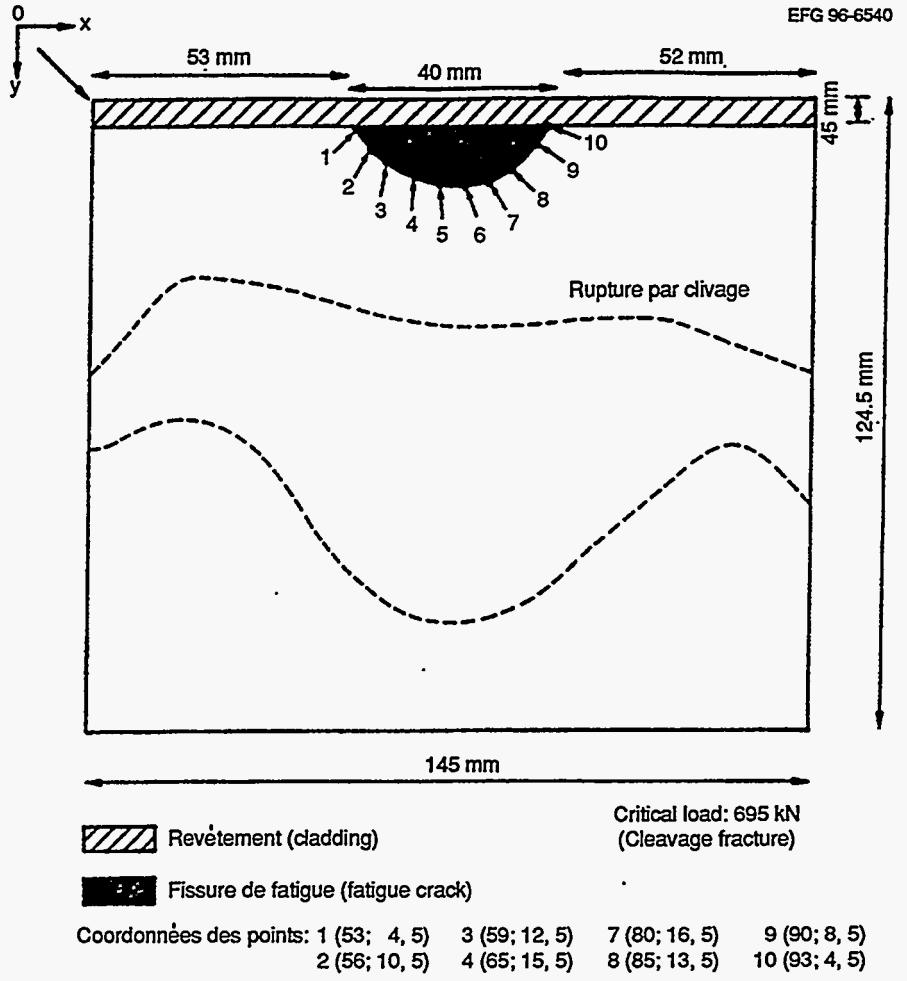

Figure 2.57 Schematic of posttest fracture surface from DSR3 clad beam specimen

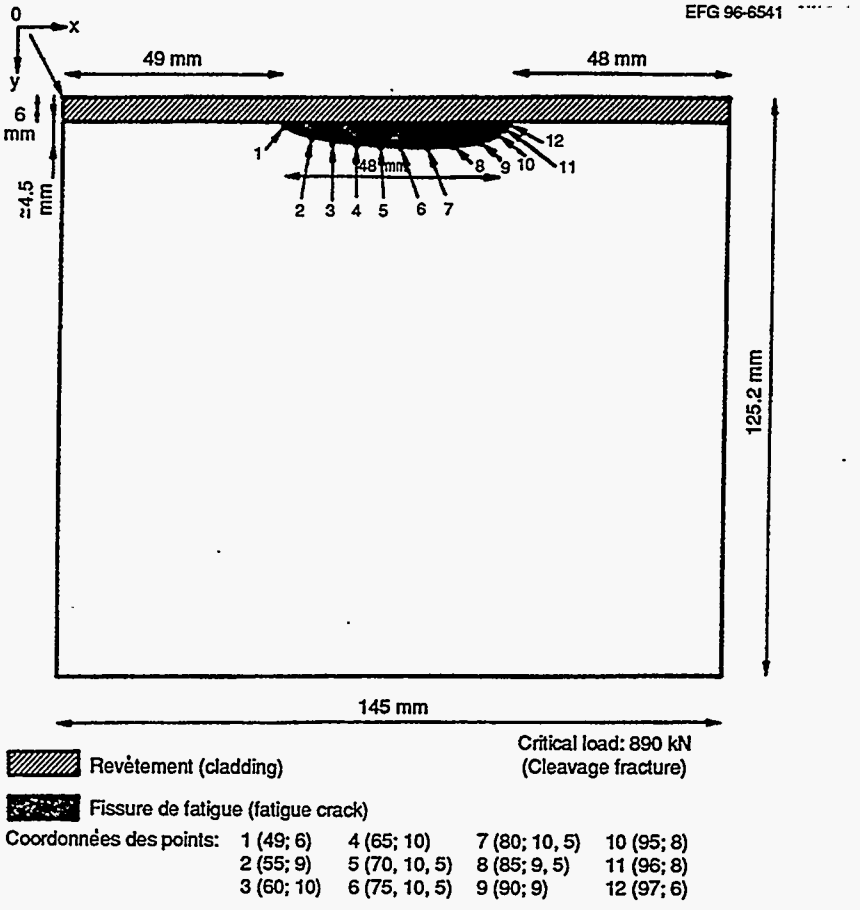

Figure 2.58 Schematic of posttest fracture surface from DD2 clad beam specimen

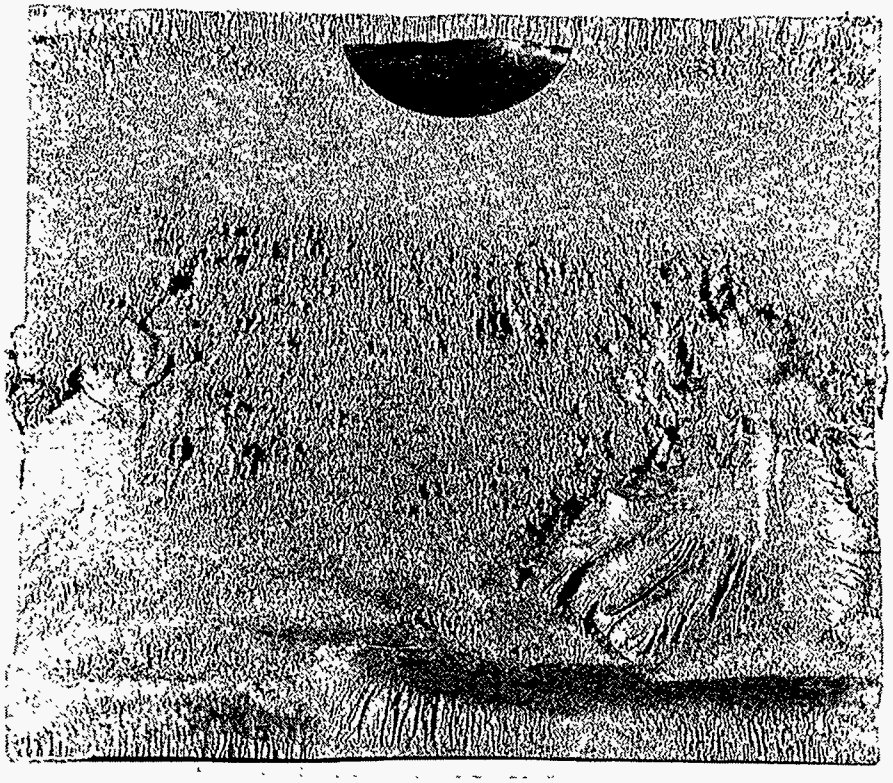

Figure 2.59 Photograph of posttest fracture surface from DSR3 clad beam specimen

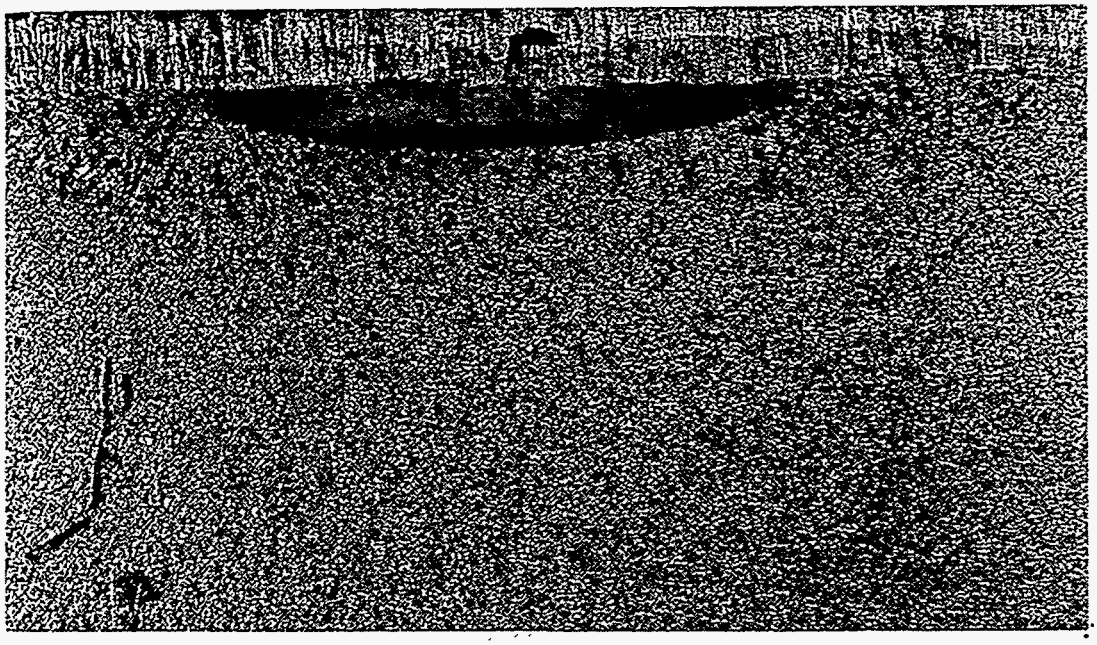

Figure 2.60 Photograph of posttest fracture surface from DD2 clad beam specimen

2.5 Cruciform Beam Experiment (BB-4)

A testing program[6] to examine the influence of biaxial loads on the fracture toughness of shallow-flaw specimens under conditions prototypic of an RPV was begun within the Heavy-Section Steel Technology (HSST) Program at ORNL. A typical biaxial stress field produced by PTS transient loading is shown in Fig. 2.61, together with a constant-depth shallow surface flaw. One of the principal stresses is seen to be aligned parallel to the crack front. There is no counterpart of this far-field out-of-plane stress in conventional uniaxial shallow-flaw fracture toughness test specimens. The far-field out-of-plane stress has the potential to increase stress triaxiality (constraint) at the crack tip and thereby reduce some of the fracture toughness elevation associated with shallow flaws.

A cruciform test specimen was developed at ORNL to investigate the effects of biaxial loading on the shallow-flaw fracture toughness of pressure vessel steels. Conceptual features of the specimen are shown in Fig. 2.62. The specimen design is capable of reproducing a linear approximation of the nonlinear biaxial stress distribution shown in Fig. 2.61. The cruciform test specimen design, coupled with a statically determinate load reaction system, permits the specimen to be loaded in either uniaxial or biaxial configurations. Tests of nominally identical specimens can thus be performed with the level of stress biaxiality as the only test variable.

Five cruciform bend specimens (i.e., BB-1 through -5) were tested in the initial development phase of the HSST biaxial testing program. The BB-4 specimen test was selected as a reference experiment for FALSIRE II.

2.5.1 Cruciform Bend Specimen

The specimen depicted in Fig. 2.62 has a cruciform-shaped geometry with a cross section of dimensions 9.1 by 10.2 cm (3.6 by 4.0 in.) and a straight through-crack of uniform depth 1.02 cm (0.4 in.) in the test section. The total length of this specimen in the longitudinal or transverse direction, including the test section and the loading arms, is 61 cm (26 in.). Three slots are machined into each arm to minimize diffusion of the load around the test section containing the through-crack. The crack is cut between two opposite central load-diffusion control slots to produce a two-dimensional (2-D) shallow crack with no singularity on the surface. Figure 2.62 shows the profile of the crack and the intersection of the crack with the central slots.

The test section of the specimen is fabricated from A 533 grade B class 1 steel plate previously employed in the HSST wide-plate and shallow-crack testing programs. The specimen is notched and precracked after the two longitudinal arms are electron-beam (EB) welded to the test section. EB welding is employed to ensure minimal distortion in the specimen and a relatively small heat-affected

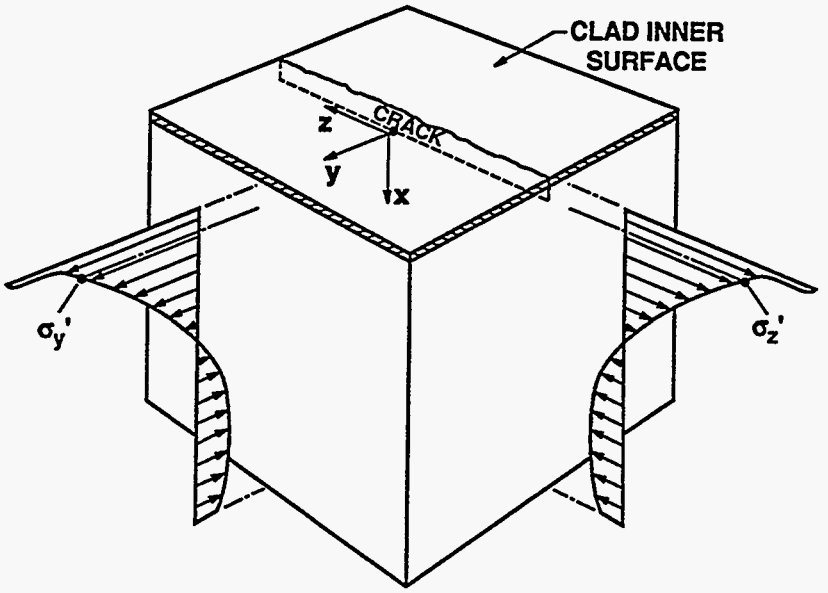

Figure 2.61 Schematic representation of biaxial far-field stresses in RPV wall during PTS transient with one component aligned parallel to front of longitudinal crack

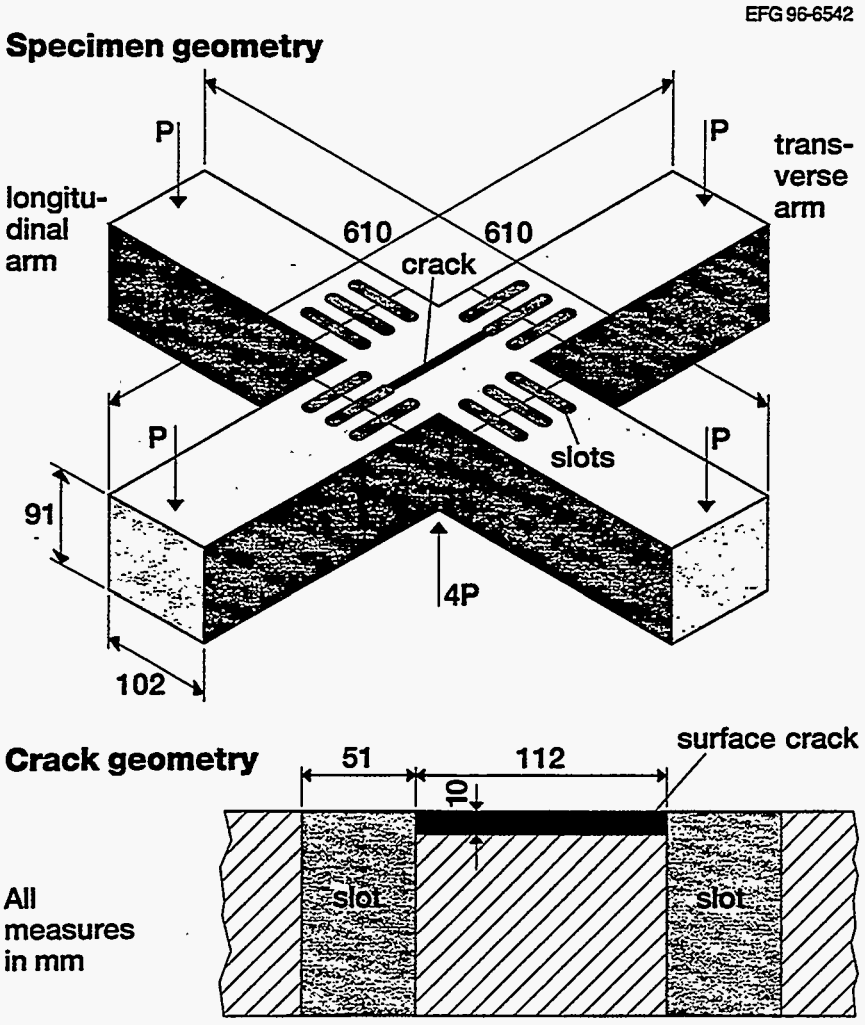

Figure 2.62 Cruciform bend specimen used in BB-4 biaxial loading experiment (ORNL, U.S.A.)

zone. Following precracking, a machining operation is performed to remove an embrittled layer of material [thickness ~0.38 mm (15 mils)] at the root of each central load-diffusion control slot where it intersects the crack. The embrittled layers are introduced into the specimen by an electrodischarge machining process used to cut the slots; then the transverse arms are EB welded to the specimen.

A special reaction system has been constructed for applying bending loads to the arms of the specimen in a statically determinant manner. Figure 2.63 schematically depicts the loading configurations for two biaxial loading ratios (0.5:1 and 1:1, herein abbreviated as transverse/ longitudinal load) and for the uniaxial case. Loading is applied at midspan to the specimen using a square, flat seat having rounded edges and the same planar dimensions as the test section. The load applied to the base of the specimen is reacted by means of one fixed support and three matched hydraulic cylinders (see Fig. 2.64). The test section bends into two orthogonal surfaces that contact the seat along the outer edges, resulting in eight-point bending (or four-point bending for the uniaxial case).

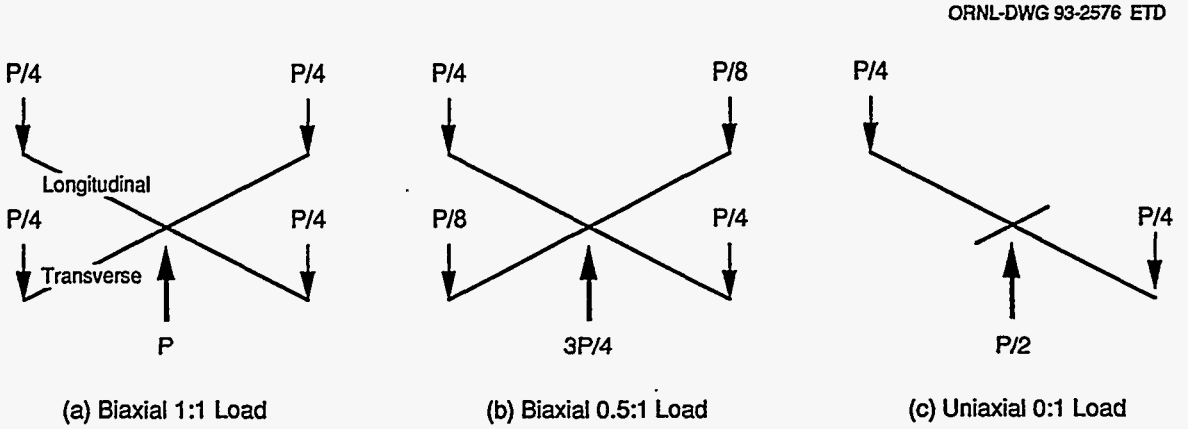

Figure 2.63 Schematic of biaxial and uniaxial bending loads applied to cruciform bend specimen

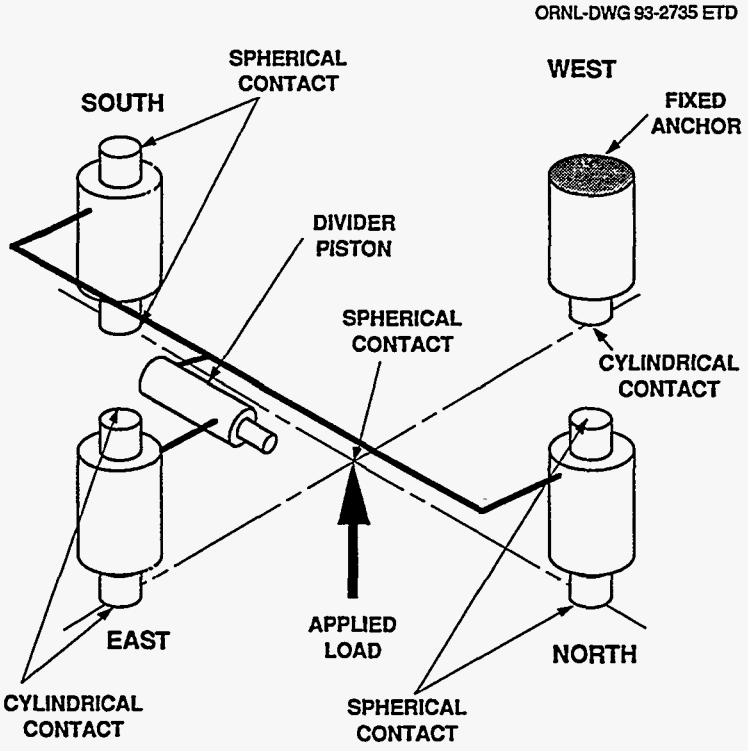

Figure 2.64 Schematic of biaxial loading fixture showing interface of load points with cruciform bend specimen

2.5.2 Material Characterization

The test section material for the initial series of five cruciform specimens was taken from the HSST WP-CE plate of A 533 grade B steel.[6] Initially, the material properties used for the finite-element analysis were based on pretest estimates for Young's modulus, Poisson's ratio, and yield stress. The hardening portion of the initial stress-strain curve was based on material characterization data[6] of HSST Plate 13A. For posttest analyses of the cruciform beams, the yield stress of the material was reduced by ~10% from its initial value based on previous shallow-crack experience and the pretest analysis results. The hardening portion of the stress-strain curve was kept consistent with previous estimates of the hardening of the material. The initial and adjusted stress-strain curves are shown in Fig. 2.65. Additional modifications included reduction of Poisson's ratio to 0.25 from the previously assumed value of 0.3, which is the typical value used for steel. However, for body centered steels such as A 533 B steel, a value of 0.25 for Poisson's ratio may be more appropriate. The value of Young's modulus was not altered for the posttest analysis. For completeness, the tensile properties for the WP-CE material are included in Table 2.26.

Drop-weight and CVN characterization tests were performed on material machined from a section that was flame-cut from the broken halves of a WP-CE wide-plate specimen.[6] The test specimen layout for these characterization studies is shown in Fig. 2.66. Because some of the wide-plate test section material originated from the near surface of the plate stock, tests were performed for each of four layers through the plate thickness to investigate potential variations in properties. The results of CVN impact testing in the L-T orientation are given as regression-fit hyperbolic tangent curves in Fig. 2.67. The hyperbolic tangent curve fits for the four layers are compared in Fig. 2.67(*a*). An average curve derived by fitting the hyperbolic tangent curve to all the CVN test data in the L-T orientation is shown in Fig. 2.67(*b*). The corresponding results of the CVN impact tests in the T-L orientation are given in Fig. 2.68. The RT_{NDT} for the material was determined from drop-weight and CVN impact test data to be –35°C and was governed by the drop-weight NDT temperature.

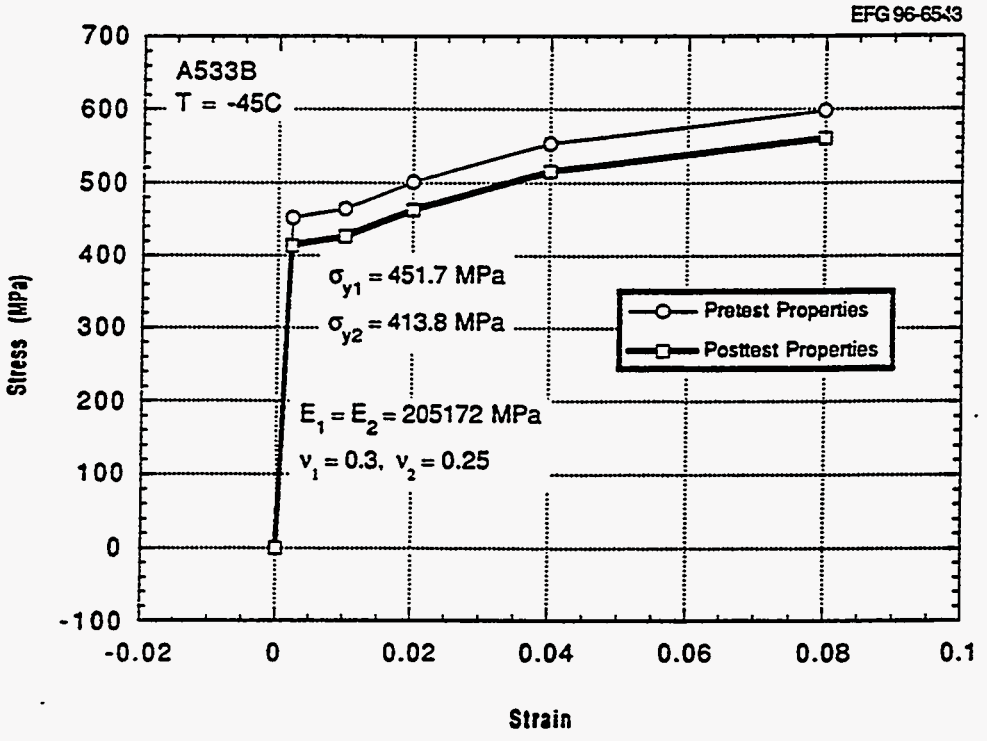

Figure 2.65 Pretest and posttest stress-strain curves used in analysis of BB-4 experiment

Table 2.26 Room- and elevated-temperature tensile properties of SA 533 grade B class 1 material used in BB-4 specimen

Block No.	Location (t)	Specimen code	Test temperature (°C)	Strength		Elongation (%)	Reduction (%)
				Yield (MPa)	Ultimate (MPa)		
6	1/4	253	RT	399	561	29	69
6	3/4	256	RT	390	553	32	74
6	3/4	251	66	423	552	29	71
6	3/4	252	66	401	530	29	72
6	1/4	254	93	404	538	29	70
6	3/4	255	93	421	546	31	70
6	1/4	257	121	395	521	29	73
6	1/4	25A	121	390	517	29	65
10	3/4	2K6	RT	400	554	27	67
10	1/4	2KD	RT	394	555	30	71
10	1/4	2K7	49	382	533	28	73
10	3/4	2KC	49	395	542	29	72
10	1/4	2KE	66	410	558	28	70
10	3/4	2KB	66	422	555	26	68

Source: From EPRI NP-5121SP (No. 130), *Test and Analyses of Crack Arrest in Reactor Vessel Materials*, Appendix G, "Material Characterization."

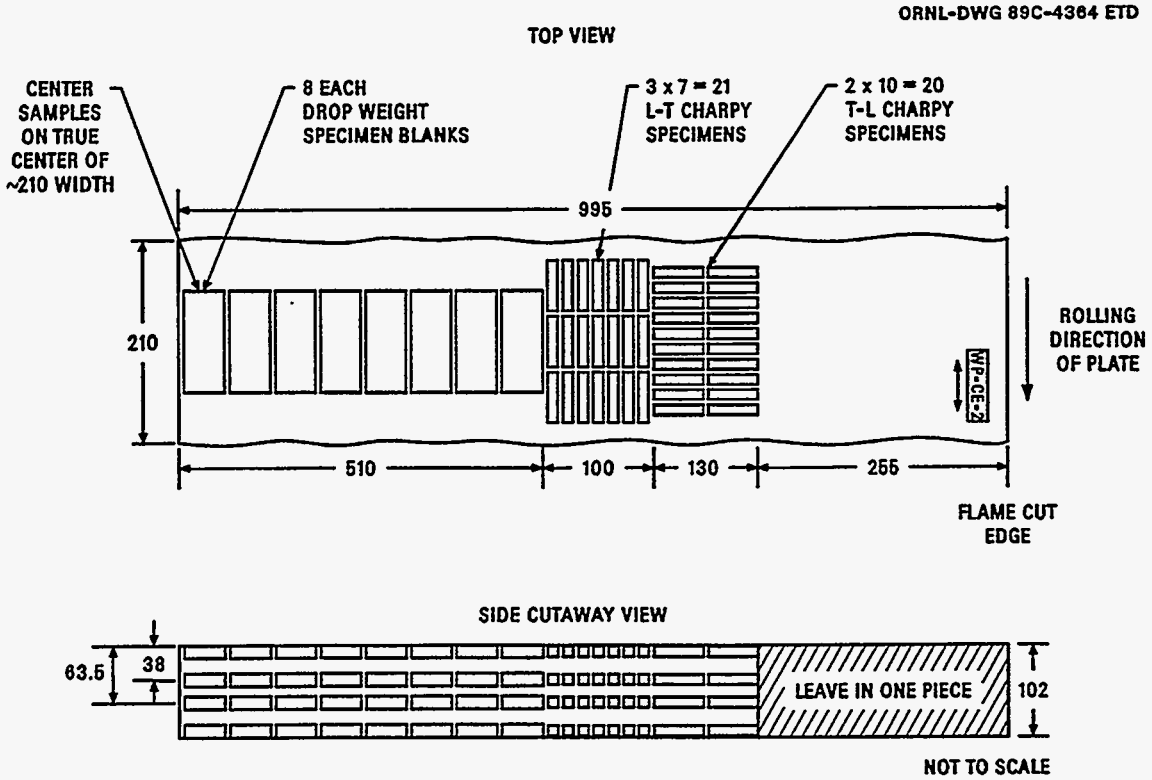

Figure 2.66 Drop-weight and CVN test specimen layout for characterization studies of BB-4 test material

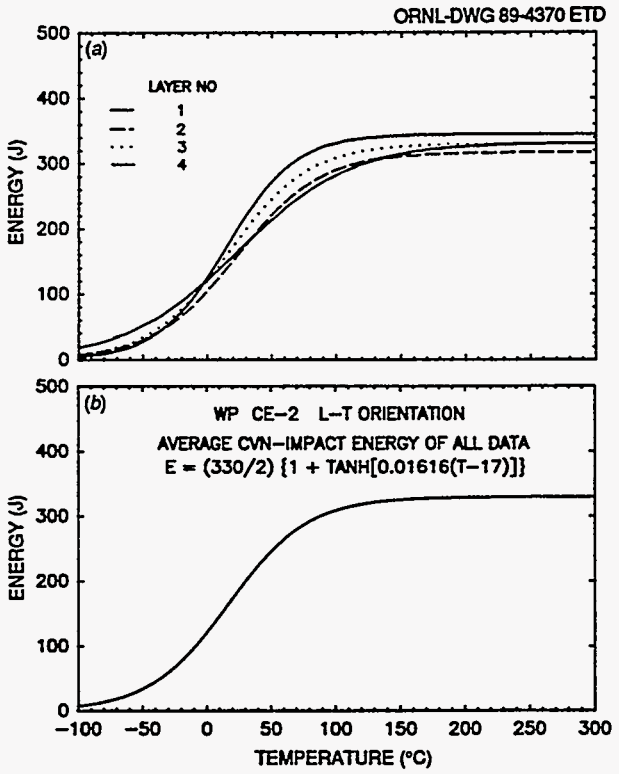

Figure 2.67 CVN impact energy (L-T orientation) vs temperature for (*a*) four layers of cruciform specimen characterization material and (*b*) average regression curve fit for all data

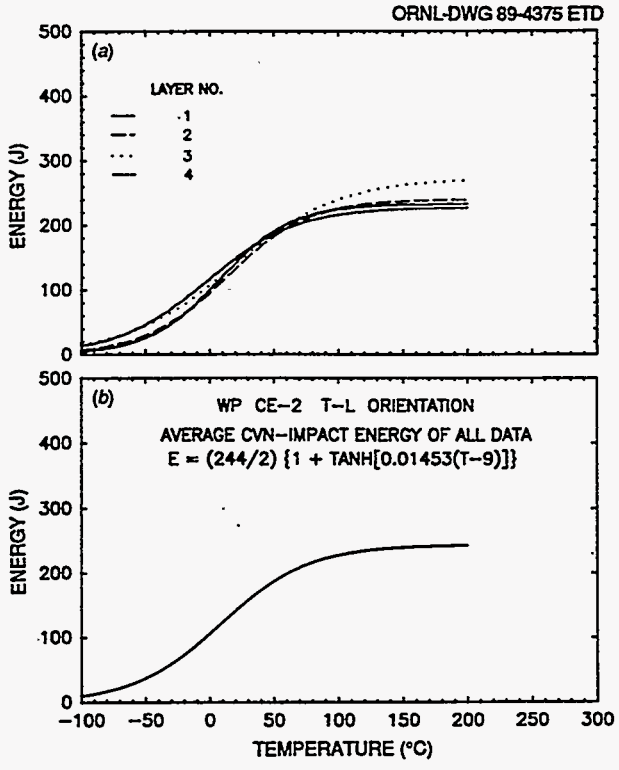

Figure 2.68 CVN impact energy (T-L orientation) vs temperature for (*a*) four layers of cruciform specimen characterization material and (*b*) average regression curve fit for all data

2.5.3 Instrumentation

Each specimen was instrumented with a collection of strain gages, potentiometers, clip gages, and thermocouples to provide assurance of correct loading, to measure the test temperature, and to collect data from which toughness could be determined. Strain gages were installed at various locations on the arms and test section of the specimens. The purpose of these gages was to monitor the biaxial load ratio applied to the cruciform specimen and to investigate the uniformity of the strains in the test section of the specimen. Six strain gage rosettes were installed in the test section, either along the specimen centerline or symmetrically about the centerline. The strains in the test section of each test indicate symmetric pure bending along the centerline of the specimen. In addition, the gages located on either side of the centerline indicate that the test section maintains a relatively uniform strain field. Strain gages applied at the same relative location in the specimen arms were also used to confirm the biaxial load ratio for each biaxial test.

The basic temperature control system consists of four pools of LN_2 to cool the beam and a collection of eight thermocouples to monitor the test section temperature. The pools of LN_2 are located on each beam arm about 89 mm from the center of the crack plane. LN_2 is fed into the pools either by direct pouring or through tubes. The pools of LN_2 extend across most of the beam arm widths and are roughly square-shaped. This ensures consistent and symmetric conductive cooling. The location of the thermocouples was selected to monitor the temperature of the center of the crack plane as accurately as possible without drilling into the test section itself. The distances from the thermocouples to the LN_2 pools are such that a consistent temperature profile from the eight thermocouples would provide reasonable assurance of an isothermal condition at the crack plane at the temperature indicated by the thermocouples.

Four clip gages were mounted directly on the mouth of the crack for each test specimen to provide CMOD data. The clip gages were located at the specimen centerline, 19 mm north and south of the centerline, and 38 mm south of the centerline. For each test, general agreement between the "north, south, and middle" clip gages was found, indicating symmetric loading of the specimen and a relatively constant CMOD profile across the central 40 mm of the crack. The "far south" CMOD is ~25% less than the middle CMOD as expected, based on pretest analysis. Future references to CMOD refer to the middle CMOD.

Potentiometers were used to measure the displacement of the arms relative to the test section for each test. The LLD is taken as the average of the displacements of the two longitudinal arms (i.e., the east and west arms). The north and south potentiometers record the deflection of the arms parallel to the crack plane; it is not expected to be the same as the LLD. In all cases, close agreement was indicated between the east vs west arms and the north vs south arms, revealing symmetric loading.

2.5.4 Test Matrix

The HSST Program assigned a total of five cruciform specimens to the development phase of the biaxial testing program. These "development" specimens were used to evaluate the performance of the test specimen, test fixture, and procedures and to develop a test specimen geometry suitable for the generation of biaxial fracture toughness data. All biaxially loaded cruciform specimens tested in this phase of the program were tested with a transverse-to-longitudinal load ratio of 0.6:1, as indicated in the summary of the test matrix shown in Table 2.27. The uniaxially loaded cruciform specimen allows comparison with previous uniaxial shallow-crack specimens under identical test conditions (crack depth, temperature, etc.). Testing cruciform specimens in both uniaxial and biaxial loading configurations allows toughness values to be measured with only one test condition changed, namely, the out-of-plane loading.

Table 2.27 Test matrix for development phase of biaxial testing program

Specimen No.	Test section configuration (see Fig. 2.69)	Load ratio
BB-1	*b*	0.6:1
BB-2	*c*	0:1
BB-3	*c*	0.6:1
BB-4	*d*	0.6:1
BB-5	*d*	0.6:1

2.5.5 Experimental Results

One of the criteria for a satisfactory specimen design is that the crack-driving forces be relatively constant with no significant edge effects. The primary concern is the stress concentration at the intersection of the crack and the two central load-diffusion control slots. To satisfy this requirement, the specimen must generate data in which the

initiation is not predisposed to occur at the intersection of the crack and the load-diffusion control slots. Four slot configurations were examined in the testing program (see Fig. 2.69). The slot configuration (*c*) produced an acceptable result under uniaxial loading (BB-2) but not under biaxial loading (BB-3). Only specimen BB-3 initiated directly in the corner of the crack and slot. This test result may include stress concentration effects due to the slot-crack interaction and, therefore, was not included in the interpretation of the results. Biaxial loading may or may not be responsible for shifting the initiation location to the corner. Specimen configuration (*d*) was developed and used to ensure that the crack initiation would take place away from the corner of the crack and slot. Both specimens BB-4 and -5, which used configuration (*d*), were tested under biaxial loading, and the cracks initiated well away from the corner. These specimens confirm specimen configuration (*d*) as being satisfactory for the generation of uniaxial and biaxial fracture toughness data.

The P vs LLD curve from the BB-4 biaxially loaded test specimen is given in Fig. 2.70. The P vs LLD and P vs CMOD curves for all five beam tests are compared in

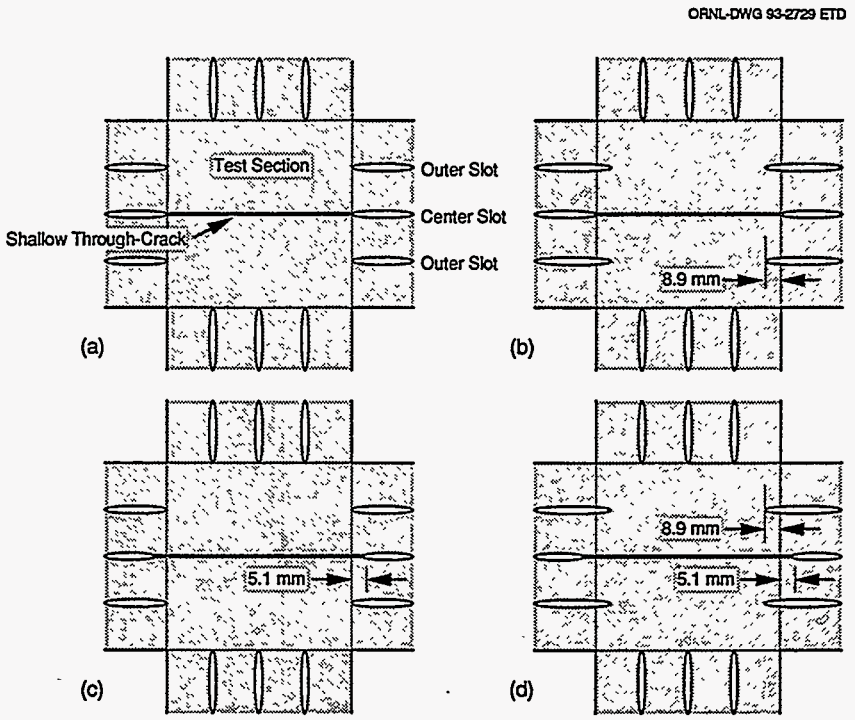

Figure 2.69 Slot configurations used in cruciform bend specimens: (*a*) BB-2 (tested under uniaxial loading) and (*b*) BB-4 and -5 (tested under 0.6 biaxial loading ratio)

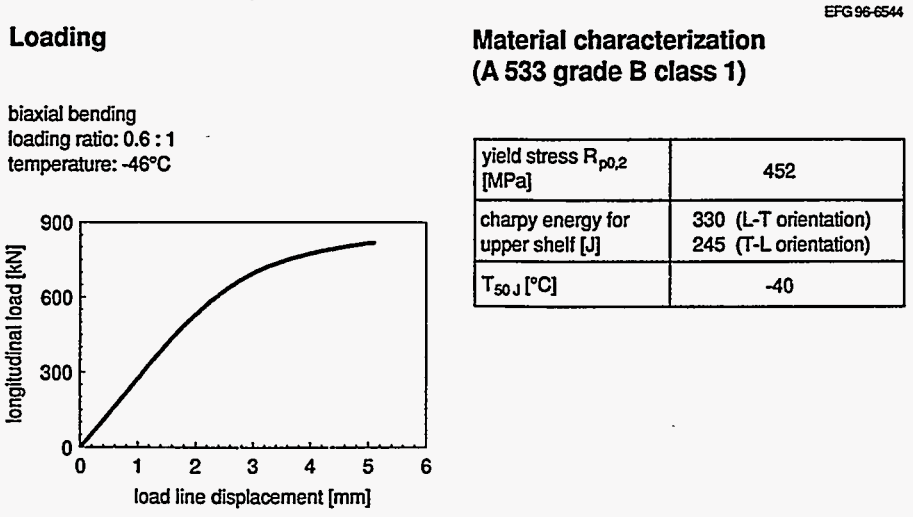

Figure 2.70 Loading and test material data for BB-4 specimen

Figs. 2.71 and 2.72, respectively. The conditions of each specimen at failure, test temperature, and specimen geometry are tabulated in Table 2.28. Also included in Table 2.28 are the plastic components of area under each P vs LLD curve (defined as U_{pl}) and P vs CMOD curve (defined as A_{pl}). Table 2.28 also lists the estimated toughness values for the tests, along with the parameters used to estimate the toughness. Load indicated in Figs. 2.70–2.72

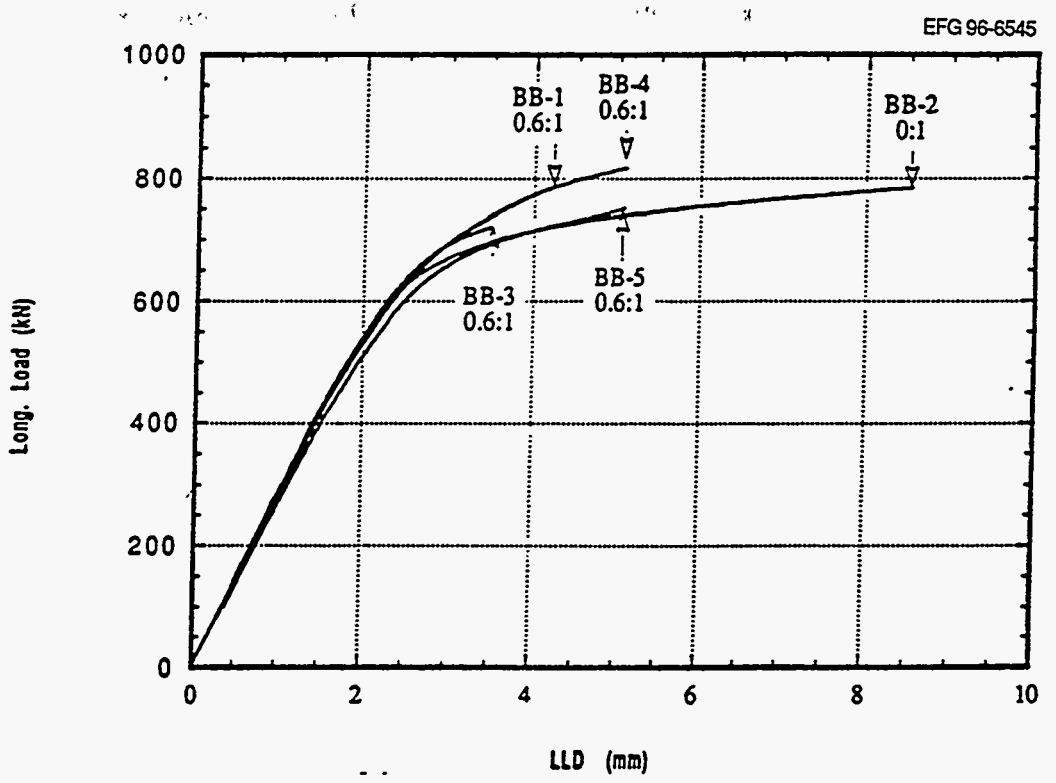

Figure 2.71 Load vs LLD response for cruciform bend specimen tests BB-1 through BB-5

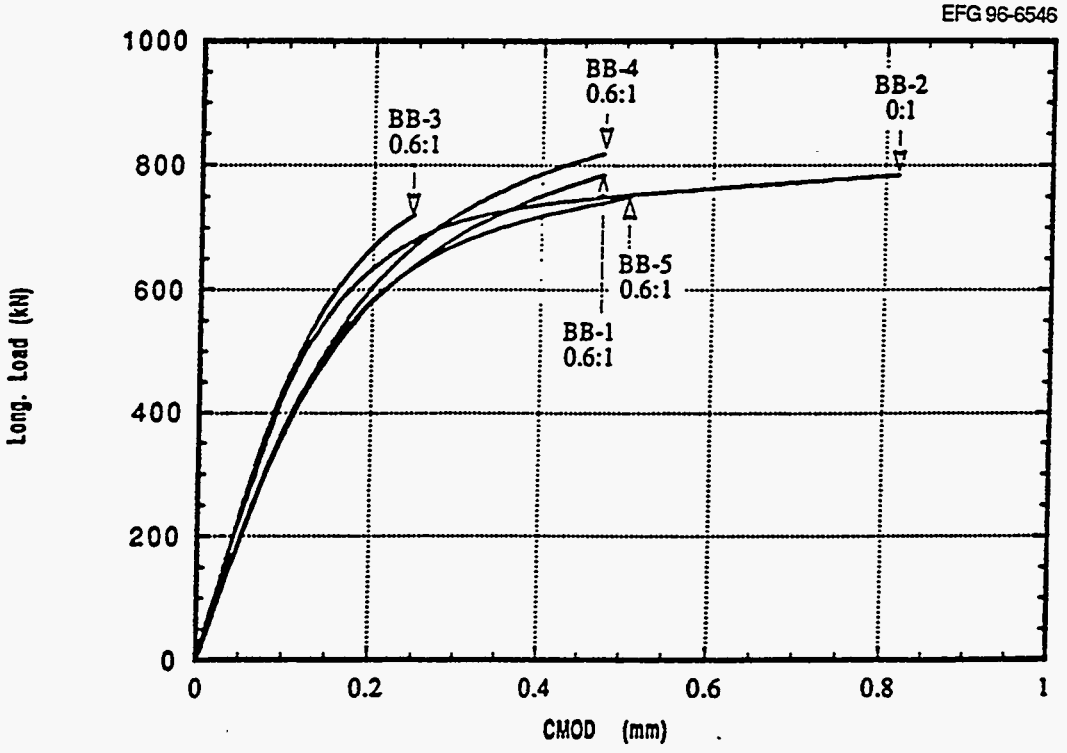

Figure 2.72 Load vs CMOD response for cruciform bend specimen tests BB-1 through BB-5

Table 2.28 Summary of results of the development phase of the biaxial testing program

	BB-1	BB-2	BB-3	BB-4	BB-5	Average SENB data (for comparison)
Load ratio	0.6:1	0:1	0.6:1	0.6:1	0.6:1	
Geometry						
B, mm	102	111	112	111	111	101
W, mm	91	91	91	91	91	102
a, mm	11.1	10.6	8.8	10.1	10.0	10.7
Temperature, °C	–45	–41	–47	–46	–44	–23[a]
Failure conditions			[b]			
P, kN	784	784		818	751	763
LLD, mm	4.20	8.51		5.10	5.08	4.06
CMOD, mm	0.47	0.82		0.47	0.51	0.65
U_{pl}, kN-mm	958	4110		1523	1501	1163
A_{pl}, kN-mm	168	455		181	206	329
η-factors			[b]			
η_{pl}^{ℓ}	0.195	0.117		0.189	0.190	1.15
η_{pl}^{c}	3.53	2.76		3.55	3.61	3.48
Fracture toughness			[b]			
Elastic component						
J_{el}, kN/m	66.7	67.4		72.6	61.2	67
K_I, MPa$\sqrt{m}$	120	120		125	115	122
P vs CMOD						
J_{pl}, kN/m	73.3	141		71.8	82.8	125
Total J, kN/m	140	209		144	144	192
K_{Jc}, MPa$\sqrt{m}$	175	214		178	178	206
P vs LLD						
J_{pl}	23.1	54.1		32.1	31.7	145
Total J	89.7	122		105	92.9	212
K_{Jc}	140	163		151	143	216

[a] RT_{NDT} for this material is –15°C, so T – RT_{NDT} for these tests is the same.
[b] Not reported due to initiation in the corner.

or Table 2.28 refers to the longitudinal load that is the total load (as measured by the load cell) divided by 1.6 for the biaxial tests. The results indicated in Figs. 2.71 and 2.72 and Table 2.28 reveal consistent, repeatable mechanical responses for the five tests. The data depicted for BB-4 and -5 indicate the scatter band in results for two tests that were designed to have essentially the same test conditions.

The test results indicate that the critical load for each specimen was similar but that in the uniaxial test (BB-2) the specimen was able to withstand substantially more (~60%) deflection (LLD or CMOD) than in the biaxial tests (BB-1, -4, and -5). In addition, the "work" at the crack tip as defined by either U_{pl} or A_{pl} in the three biaxial tests was about one-third of the corresponding uniaxial value of U_{pl} or A_{pl}. Furthermore, the critical displacements (LLD or CMOD) and work performed (U_{pl} or A_{pl}) were consistent for the three interpretable biaxial test results. These results indicate a pronounced reduction in the ductility of the material (as measured by critical displacement or work) due to biaxial loading.

The P vs CMOD response is more sensitive than the P vs LLD response to changes in the loading or specimen configurations because the clip gages are so close to the crack tip in shallow-crack specimens. The initial compliance (P vs CMOD) data for the five tests shown in Fig. 2.72 indicate that specimens BB-2 and -3 are stiffer than the other three specimens. This trend is expected because specimens BB-2 and -3 did not have the outboard load-diffusion control slots cut into the test section by 8.9 mm (0.35 in.) as did the remaining specimens. Figure 2.72 also

indicates that specimen BB-3 is somewhat stiffer than BB-2 once yielding begins at the crack tip. Note that no influence of biaxial loading was evident in the linear-elastic portion of either the P vs LLD response or P vs CMOD response.

For the cruciform specimen design to be successful in this biaxial testing program, the specimen must yield uniaxial results that are similar to previous shallow-crack beam testing. Comparison of measured responses in BB-2 (uniaxial) and shallow-crack beams indicates consistent load vs CMOD behavior. As expected, the cruciform specimen is stiffer than the beams due to the addition of the transverse arms.

2.5.6 Fractographic Examinations

A fractographic examination was conducted on the specimens to examine the fracture modes, cleavage origins, and other characteristic surface features. The examination included optical and scanning electron microscope (SEM) observations as well as measurements of key parameters. A traveling microscope was used to estimate the extent of precleavage ductile tearing across the crack front. Samples were cut, and areas around the suspected cleavage origins were examined in detail in a SEM. Figure 2.73 depicts the fracture surface for the cruciform specimen BB-4 with the fracture initiation site indicated by the river patterns. Post-test examination of the BB-4 fracture surface revealed the fracture initiation site to be 18 mm from the north edge of the specimen, well within the flaw region to yield valid toughness results.

ORNL-PHOTO 8258-94

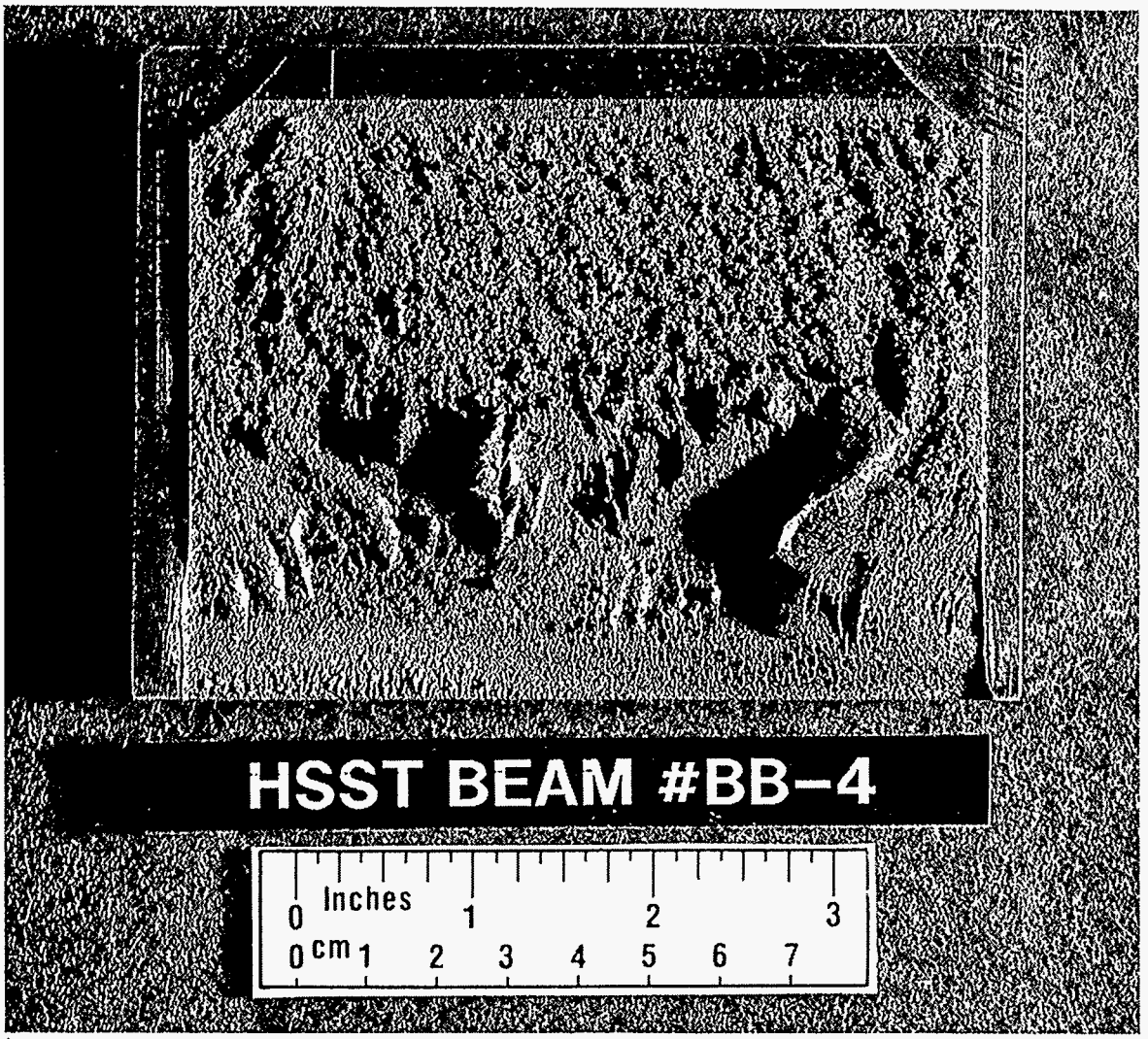

Figure 2.73 Fracture surface of shallow-flaw cruciform specimen BB-4 with fracture initiation site indicated

References

1. D. J. Lacey et al., "Spinning Cylinder Test 4: An Investigation of Transition Fracture Behavior for Surface Breaking Defects in Thick-Section Steel Specimens," AEA Technology Report AEA TRS 4098, June 1991.

2. H. Keinänen et al., "Pressurized Thermal Shock Tests with Model Pressure Vessels Made of VVER-440 Reactor Steel," pp. 275–88 in *IAEA Specialists' Meeting on Fracture Mechanics Verification by Large-Scale Testing, Oak Ridge, Tennessee, October 26–29, 1992*. USNRC Conference Proceeding NUREG/CP-0131 (ORNL/TM-12413), October 1993.*

3. K. Wallin, R. Rintamaa, M. Valo, and K. Törrönen, "Validity of Surveillance-Size Specimen Fracture Toughness Estimates for Predicting Reactor Pressure Vessel Behaviour," *The Third International Conference on Material Science Problems in NPP Equipment Production and Operation, June 14–20, 1994, Moscow–St. Petersburg, Russia*, Vol. 1, pp. 83–100, 1994.

4. L. Stumpfrock et al., "Fracture mechanic investigations on cylindrical large-scale specimens under thermal-shock loading," *Nucl. Eng. Des.*, 144, 31–44 (1993).*

5. D. Moinereau et al., "Cleavage Fracture of Specimens Containing an Underclad Crack," *PVP* Vol. 233, *Pressure Vessel Fracture, Fatigue and Life Management* (American Society for Mechanical Engineers, 1992).†

6. T. J. Theiss et al., Martin Marietta Energy Systems, Inc., Oak Ridge Natl. Lab., "Initial Results of the Influence of Biaxial Loading on Fracture Toughness," USNRC Report NUREG/CR-6036 (ORNL/TM-12349), June 1993.*

*Available for purchase from the National Technical Information Service, Springfield, VA 22161.
†Available from public technical libraries.

3 Comparative Assessments and Discussion of the Analysis Results

In this chapter, the results of finite-element and estimation scheme analyses provided by the participants in the FALSIRE II project are discussed. The distribution of the analyses of the reference experiments performed by the participating organizations and discussed at the workshop in Atlanta during November 1994 is given in Table 3.1. Pertinent information concerning each of the analyses that were submitted to the OC is summarized in Tables 3.2 through 3.12. Where appropriate, summary tables are included for both thermal and structural analyses of the experiments. Information provided in the tables includes the identity of the computer program employed in the analysis, features of the finite-element models (i.e., spatial dimensions, number of nodes and elements, etc.), as well as essential characteristics of the solution schemes, the material models, the stress-strain approximations, and the fracture methodologies used to predict crack behavior. Analyses provided by organizations participating in FALSIRE II are identified in the summary tables and comparative plots by an alphanumeric code to preserve the public anonymity of the contributors.

For each reference experiment, the OC prepared a list of SRs that were distributed to participating analysts. The SRs, which are comprised of a set of quantities that characterize the structural behavior of the test specimens and the fracture behavior of the cracks, are given in the appendix of this report. Prior to the Atlanta workshop, participants provided the OC with analytical results for the parameters included in the SRs, which the OC then used to develop comparative assessments of the analyses. A computerized data base of the results of these comparisons has been established, and a selection of the available plots is given in this chapter. The discussion below focuses on the comparative plots generated from this data base and on reasons for discrepancies among the various analyses of the reference experiments.

Note that most of the FALSIRE II analyses were performed by participating analysts who worked under imposed constraints of limited time and financial resources. Consequently, parametric studies were carried out only to a very limited extent, and in certain cases, discrepancies arising from comparisons of measured data and calculated results were not completely resolved.

3.1 Fourth Spinning Cylinder Test (SC-4)

Features of the FALSIRE II thermal analyses of the SC-4 experiment are given in Table 3.2. Measured and computed

Table 3.1 Distribution of analyses of FALSIRE II reference experiments among participating organizations

NKS-5 (8)	MPA	CEA	VTT	BARC	Kurchatov	Framatome	IPS	Siemens	
NKS-6 (6)	MPA	BARC	NE	PSI	Kurchatov	GRS			
PTS I/6 (4)	VTT	Uni. Tokyo	Kurchatov	BARC					
SC IV (9)	AEA	ECS	GRS	EDF	IWM	ANPA/ Univ. Pisa	IPS	PSI	Univ. Maryland
BB-4 (6)	ORNL	Onsala Inq.	GRS	AEA	Kurchatov	NE			
DD2 DSR3 (12)	EDF "	ORNL "	CEA -	FMC "	Kurchatov "	IWM "	Prometey -		

Σ 45 (current status , May 15, 1995)

Table 3.2 FALSIRE II: test SC-4, temperature analysis

Plot-Code	Analysis	FE-Code	Model-dimension	Elements	Number of nodes	Degrees of freedom	Integration scheme	Equilibrium iteration method	Material properties	Additional information
A_3	FE	ADINA-T	2D	-	-	-	3*3	Cholesky conjungate gradient method	prob.state.	-
A_11	FE	ABAQUS	2D axisym.	480 8-noded	1595	1595	2*2	Newton	prob.state.	-
A_12	FE	ADINA-T	2D axisym.	600 8-noded	1901	1901	3*3	Full Newton	prob.state.	discrepancy in assumption for HTC
A_13	FE	ASTER	3D	-	7329	7329	-	-	temperature independent	at inner surface measured data used, no results sent
A_15	FE	MF	2D axisym.	13 8-noded quads	68	136	2*2 reduced	Full Newton	prob.state.	-
A_19	FE	SAFE-2D	2D axisym.	895 Triangle	-	-	-	-	prob.state.	discrepancy in assumption for HTC (lower values)

Table 3.3 FALSIRE II: test SC-4, structure analysis

Plot-Code	FE-Code	Model-dimension	Number of nodes	material model	Stress - Strain approximation	fracture mechanics	additional information
A_3	ADINA	3D	18736	thermo-elastic-plastic	multilinear	J-integral (VCE), constraint parameters evaluated	-
A_11	ABAQUS	3D	11037	thermo-elastic-plastic	true, multilinear	J-integral (domain integral method); T-stress, Q-stress evaluated	-
A_12	ADINA	3D	6692	elastic-plastic	multilinear	J-integral (VCE)	larger alpha-values due to transformation to reference temperature 305°C
A_13	ASTER	3D	7329	elastic-plastic	multilinear	G energy release rate with theta-method	-
A_14	ABAQUS	3D	5780	elastic-plastic	multilinear	J-integral (domain integral method)	thermal shock based on measured temperatures
A_15	TAKT	3D	4390/4492	thermo-elastic-plastic	multilinear	J-integral (equivalent domain integral method)	rotation not accounted
A_7	- *)	-	-	elastic-plastic	-	SIF based on weight functions	-
A_8	- *)	-	-	-	-	SIF based on weight functions	stresses/strains/temperature: results of A_11 used
A_19	- *)	2D axisym.	-	elastic-plastic	-	KI-SIF based on weight functions with stresses for body without crack	-

*) Estimation scheme (ES)

Table 3.4 FALSIRE II: test PTS-I/6, temperature analysis

Plot-Code	Analysis	FE-Code	Model-dimension	Elements	Number of nodes	Degrees of freedom	Integration scheme	Equilibrium iteration method	Material properties	Additional information
A_1	FE	ADINA-T	2D-axisym.	1692 8-noded	5387	5387	Euler backward integration	-	prob.state.	-
A_9	FE	WELTEM	2D-axisym.	1020 4-noded	1125	1125	Full 2*2	Crank Nicolson	prob.state. (lin. interpol.)	-
A_16	FE	CORPUS_D	2D-axisym.	-	-	-	2*2*2	Method of initial stresses	prob.state.	-
A_18	FE	MARC	2D-axisym.	2768 8-noded biquad.	8767	8767	-	-	prob.state.	-

Table 3.5 FALSIRE II: test PTS-I/6, structure analysis

Plot-Code	FE-Code	Model-dimension	Number of nodes	material model	Stress - Strain approximation	fracture mechanics	additional information
A_1	ADINA	3D	5737	thermo-elastic-plastic	multilinear	J-integral	crack arrest analysis available
A_9	ABAQUS	3D	5973	thermo-elastic	-	stress intensity factor	crack arrest analysis available
A_16	CORPUS-D	3D	4986	thermo-elastic-plastic	bilinear	J-integral, equivalent domain integral method	-
A_18	MARC	3D	21806	elastic-plastic	-	-	-

Table 3.6 FALSIRE II: test NKS-5, temperature analysis

Plot-Code	Analysis	FE-Code	Model-dimension	Elements	Number of nodes	Degrees of freedom	Integration scheme	Equilibrium iteration method	Material properties	Additional information
A_1	FE	ADINA-T	2D axisym.	50 8-noded	253	253	Euler backward integration	Modified Newton	prob.state.	-
A_5	FE	CASTEM2000	2D axisym.	52 4-noded	106	106	-	-	prob.state.	HTC slightly different
A_6	FE	SYSTUS	2D axisym.	31 linear-4-noded	62	62	-	-	prob.state.	-
A_9	FE	ABAQUS	3D	1196 20-noded	5939	5939	2*2*2	-	prob.state.	-
A_16	FE	CORPUS-D	3D	338 8-noded	558	-	2*2*2	Method of initial stresses	prob.state.	-
A_19	FE	SAFE-2D	2D axisym.	895 triangle	-	-	-	-	prob.state.	-
A_21	FE	ADINA-T	2D	630	1410	-	3*3	-	prob.state.	-

Table 3.7 FALSIRE II: test NKS-5, structure analysis

Plot-Code	FE-Code	Model-dimension	Number of nodes	material model	Stress - Strain approximation	fracture mechanics	additional information
A_1	ADINA	3D	5395	thermo-elastic-plastic	base:multilinear; weld:bilinear	J-integral, stress intensity factor	component from pressure added to axial force
A_4	ABAQUS	3D	7605	thermo-linear-elastic	-	J-integral (VCE-method)	nodal temperatures based on measurement
A_5	CASTEM2000	3D	16234	thermo-linear-elastic	-	energy release rate with thermal strains and pressure forces, stress intensity factor	pressure 30 MPa, axial force 100MN
A_6	SYSTUS	3D	8054	thermo-linear-elastic	-	energy release rate with thermal strains and pressure forces	pressure 30 MPa, axial force 100MN
A_9	ABAQUS	3D	5939	thermo-linear-elastic	-	J-integral (VCE-method) with thermal strains	Crack jump of 13 mm in depth considered in analysis A_9-2
A_16	CORPUS-D	3D	5956	thermo-elastic-plastic	bilinear	J-integral, equivalent domain integral method	initial crack length: 25 mm
A_1-2	- *)	-	-	linear-elastic	-	SIF and J-integral by VTTSIF-program	Computation by MASI; temperatures and stresses by DIFF-program (axisym. assumption)
A_19	- *)	2D axisym.	-	elastic-plastic	-	stress intensity factor based on weight functions with stresses for body without crack	-
A_21	- *)	2D	1410	linear-elastic	-	KI weight function method	-

*) Estimation scheme (ES)

Table 3.8 FALSIRE II: test NKS-6, temperature analysis

Plot-Code	Analysis	FE-Code	Model-dimension	Elements	Number of nodes	Degrees of freedom	Integration scheme	Equilibrium iteration method	Material properties	Additional information
A_3	FE	ADINA-T	2D axisym.	2396 8-noded	6993	-	3*3	Full Newton with line search	prob.state.	20 MnMoNi 55: temperature dependent values used
A_9	FE	THESIS, WELTEM	2D axisym.	2627 4-noded	2734	-	2*2	Stand. modified Newton Raphson	prob.state.	-
A_10-1	FE	BERSAFE	2D axisym.	- 8/6 node quads	2553	2553	2*2	initial/tangent stiffness	prob.state.	-
A_10-2	FE	BERSAFE	2D axisym.	- 8/6 node quads	2553	2553	2*2	initial/tangent stiffness	prob.state.	-
A_12	FE	ADINA-T	2D axisym.	621 8-noded	1992	1992	3*3	Full Newton	prob.state.	-
A_16	FE	CORPUS_D	2D axisym.	650 8-noded	2035	2035	2*2	Method of initial stresses	prob.state.	-
A_10-3	FD	-	1D axisym.	-	11	-	Runge-Kutta	-	prob.state.	temperature dependent values

Table 3.9 FALSIRE II: test NKS-6, structure analysis

Plot-Code	FE-Code	Model-dimension	Number of nodes	material model	Stress - Strain approximation	fracture mechanics	additional information
A_3	ADINA	2D-axisym.	6993	thermo-elastic-plastic	bilinear	J-integral (VCE),crack growth calculated by KIc-KIa criterium, propagation by node release technique	20 MnMoNi 55: slightly different alpha-values
A_4	ABAQUS	2D-axisym.	8094	thermo-elastic-plastic	-	J-integral (VCE-method), crack surface leaded	nodal temperatures based on measured values, crack growth data of Table 2.22 used
A_9	THESIS, WELTEM	2D-axisym.	2734	thermo-elastic-plastic	multilinear	SIF calculation, pressure on crack face;J-integral (VCE-method)	axial force 25 MN, crack growth data of Table 2.22 used
A_10-1	BERSAFE	2D-axisym.	2553	elastic-plastic	multilinear	J-integral (VCE-method)	J-R curve constructed
A_10-2	BERSAFE	2D-axisym.	2553	elastic-plastic	multilinear	KIc+KIa-criteria	KIc and KIa derived from ASME
A_12	ADINA	2D-axisym.	1992	thermo-elastic-plastic	multilinear	J-integral (VCE-method)	axial force 25 MN (J-R curve extrapolated)
A_16	CORPUS_D	2D-axisym.	2035	thermo-elastic-plastic	multilinear	J-integral (equivalent domain integral method), KIc+KIa-criteria	-
A_10-3	- *)	-	-	-	-	J-integral estimated using weight function methods in conjunction with R6	thermal transient and elastic stress analyses performed by an in-house program for 1D stress problems

*) Estimation scheme (ES)

Table 3.10 FALSIRE II: test DD2, structure analysis

Plot-Code	FE-Code	Model-dimension	Number of nodes	material model	Stress - Strain approximation	fracture mechanics	additional information
A_2	ABAQUS	3D	16178	elastic-plastic	multilinear,true (prob.state.)	J-integral	-
A_5	CASTEM2000	2D plane strain	5170	elastic with plastic corrections	multilinear	K from J-integral	crack length extended 0,2mm in the cladding
A_13	SYSWELD	2D plane strain	1939	elastic with plastic corrections	multilinear	K from J-integral, local approach of cleavage fracture	with/without extension of crack length by 0.2 mm in the cladding
A_16	CORPUS_D	3D	4352	elastic-plastic	bilinear	J-integral, equivalent domain integral method	-
A_20	ABAQUS	2D plane stress	10856	elastic-plastic	multilinear	J-integral	-
A_8	- *)	-	-	-	-	-	own estimation method, plastic deformation of cladding considered
A_22	-	-	-	elastic-plastic	-	-	results with regard of the cladding welding process and heat treatment available

*) Estimation scheme (ES)

Table 3.11 FALSIRE II: test DSR3, structure analysis

Plot-Code	FE-Code	Model-dimension	Number of nodes	material model	Stress - Strain approximation	fracture mechanics	additional information
A_2	ABAQUS	3D	16178	elastic-plastic	multilinear,true (prob.state.)	J-integral	-
A_13	SYSWELD	2D plane strain	2467	elastic with plastic corrections	multilinear	K from J-integral	crack length extended 0,2mm in the cladding, additional 3D elastic-plastic analysis has been completed recently
A_16	CORPUS_D	3D	5464	elastic-plastic	bilinear	J-integral, equivalent domain integral method	-
A_20	ABAQUS	2D plane stress	11654	elastic-plastic	multilinear	J-integral	-
A_8	- *)	-	-	-	-	-	own estimation method, plastic deformation of cladding considered

*) Estimation scheme (ES)

Table 3.12 FALSIRE II: test BB-4, structure analysis

Plot-Code	FE-Code	Model-dimension	Number of nodes	material model	Stress - Strain approximation	fracture mechanics	additional information
A_2	ABAQUS	3D	14360	elastic-plastic	multilinear	J-integral (domain integral approach), KJ based on plane-strain formulation	stress-strain curve (posttest), poisson ratio = 0,25
A_3	ADINA	3D	31995	elastic-plastic	multilinear	J-integral (VCE), constraint parameters evaluated	stress-strain curve (posttest), poisson ratio = 0,28
A_10	BERSAFE	3D	4297	elastic-plastic	multilinear	J-integral (VCE)	stress-strain curve (posttest), poisson ratio = 0,25
A_11	ABAQUS	3D	10018	elastic-plastic	multilinear	J-integral, T-stress, Q-stress	stress-strain curve (posttest), poisson ratio = 0,3
A_16	CORPUS_D	3D	6979	thermo-elastic-plastic	-	J-integral (equivalent domain integral method)	stress-strain curve (pretest), poisson ratio = 0,3
A_17	ADINA	3D	-	elastic-plastic	multilinear	J-integral (VCE), K from J through relationship in plane strain	stress-strain curve (posttest)

temperature distributions through the cylinder wall at time t = 1 and 5 min into the thermal-shock transient are compared in Figs. 3.1 and 3.2, respectively. Good agreement was achieved in the transient temperature analyses of the SC-4 experiment. Differences between analyses observed at early times can be traced to different approximations concerning the time dependence of the heat transfer coefficient at the inner surface of the cylinder.

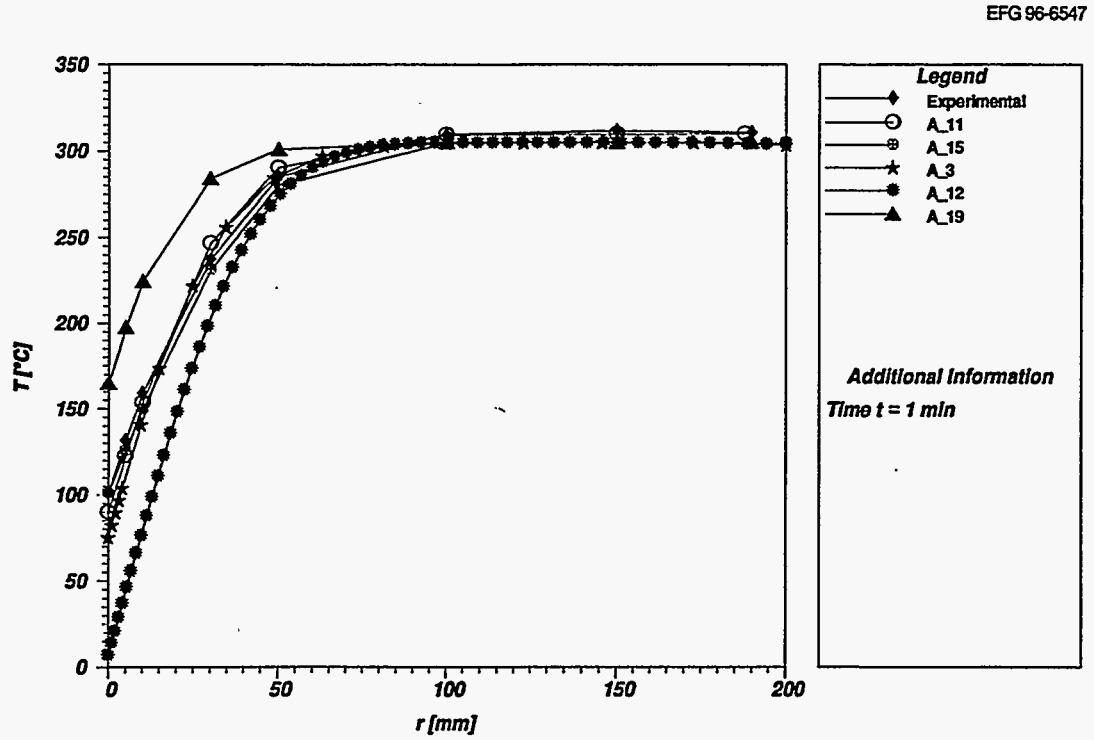

Figure 3.1 Temperatures vs wall thickness at t = 1 min (SC-4 experiment)

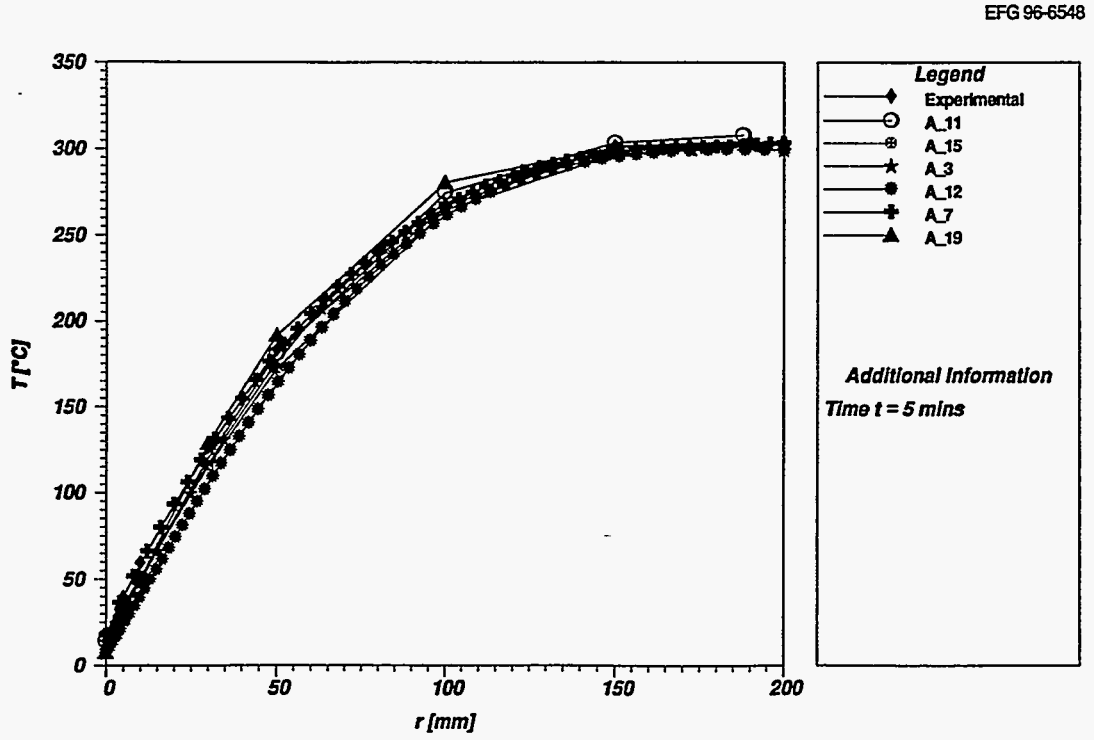

Figure 3.2 Temperatures vs wall thickness at t = 5 min (SC-4 experiment)

Essential elements of the SC-4 structural and fracture analyses are summarized in Table 3.3. Measured and computed outer surface strains at the center of the cylinder are compared in Figs. 3.3 (circumferential) and 3.4 (axial), respectively. The computed strains tend to overestimate the measured values in both cases. Differences in the calculated outer surface strains, with absolute values less than 0.15%, can be traced to differences in approximating the temperature dependence of the elastic modulus, E, and the stress-strain curve. In Fig. 3.5, computed values of the outside axial strains at the top of the cylinder generally underestimate the measured data.

EFG 96-6549

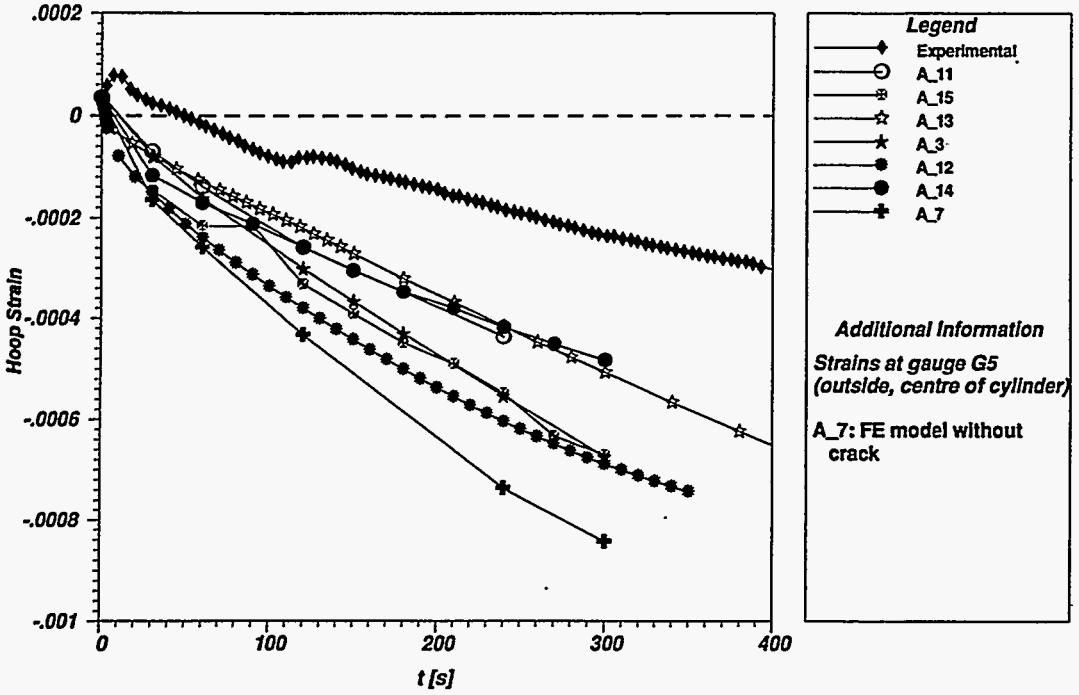

Figure 3.3 Circumferential strain vs time on outer surface of cylinder (gage G5) in SC-4 experiment

EFG 96-6550

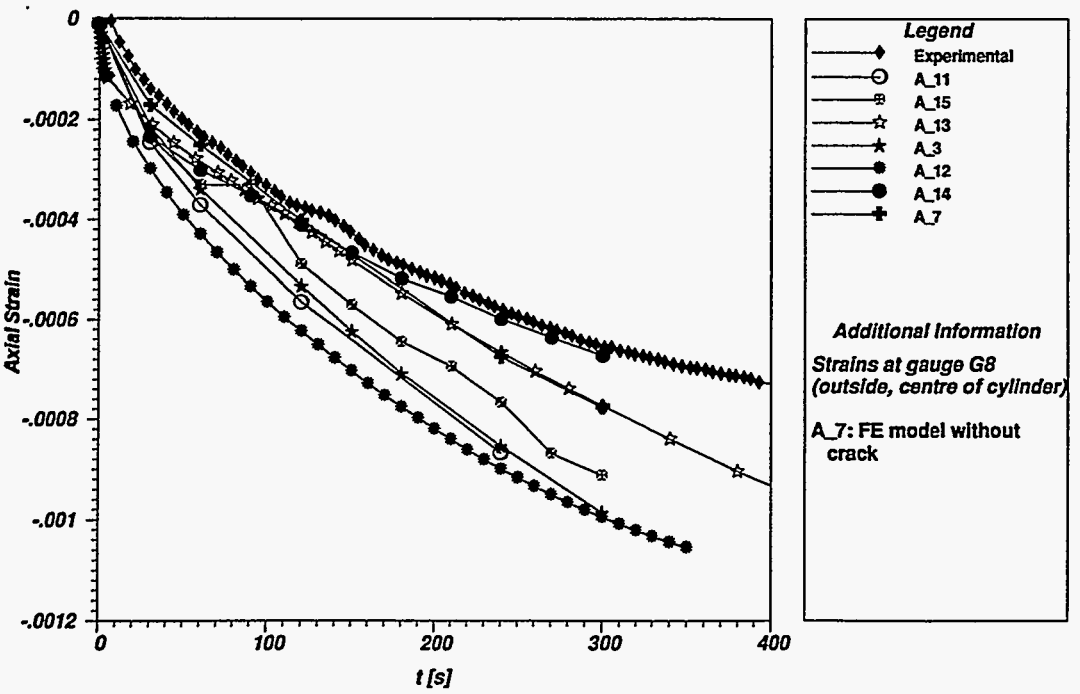

Figure 3.4 Axial strain vs time on outer surface of cylinder (gage G8) in SC-4 experiment

EFG 96-6551

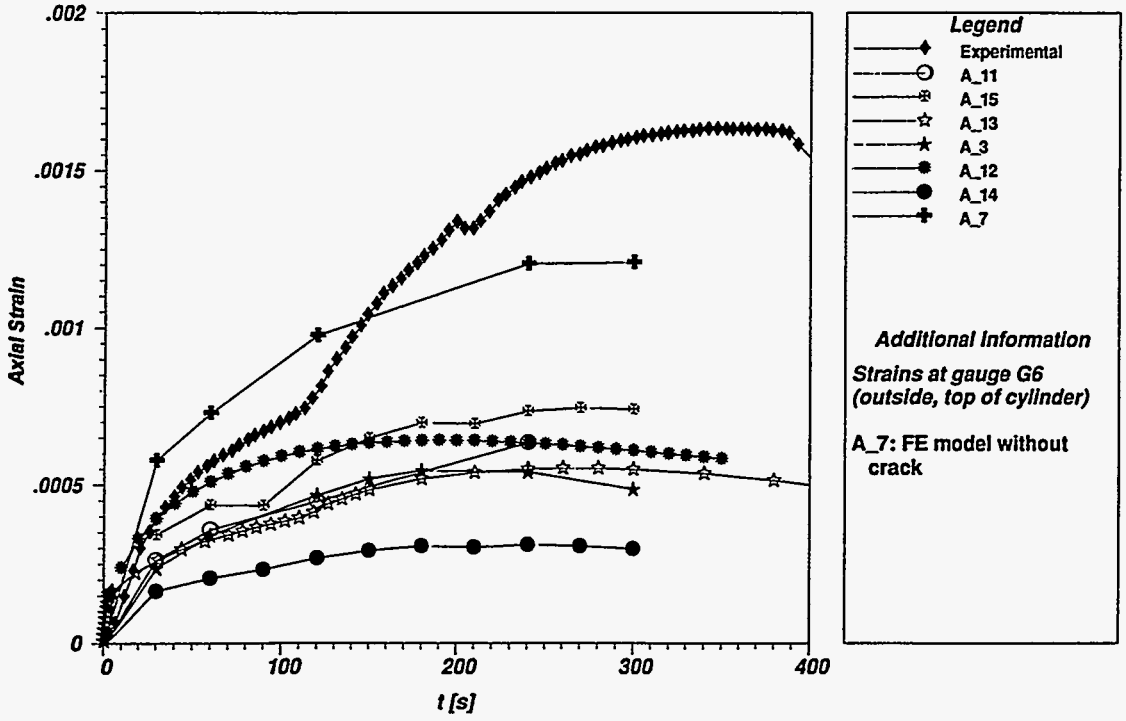

Figure 3.5 Axial strain vs time on outer surface of cylinder (gage G6) in SC-4 experiment

Computed time histories of CMOD at the deepest point of the 40- and 60-mm inner surface cracks are compared in Figs. 3.6 and 3.7, respectively. These comparisons reflect good agreement among the analysts in calculations of CMOD.

Computed distributions of circumferential and effective stresses through the wall of the cylinder at time t = 4 min into the thermal shock, without influence of the crack, are compared in Figs. 3.8 and 3.9, respectively. Effective stresses on the ligament of the 40-mm crack at time t = 4 min are compared at a near-surface point and at the deepest point of the crack in Figs. 3.10 and 3.11, respectively. Generally, good agreement was achieved among the analysts in these stress calculations. The comparisons between the effective stresses and the yield stresses show that significant plasticity developed only near the inner surface.

In Fig. 3.12, time histories of the J-integral are compared at a near-surface point of the 40-mm flaw (at a location about 4 mm from the inner surface of the cylinder). Computations of the J-integral vs crack front angle for the 40-mm flaw at time t = 4 min into the transient are compared in Fig. 3.13. The differences between the J-integral values of the different analyses are much larger in the near-surface region, where plasticity effects play a significant role.

In Fig. 3.14, K_I values at a near-surface point (about 4 mm below the surface) of the 40-mm flaw are shown vs crack-tip temperatures. Except for one analysis (A_19), these analytical results are generally consistent with the previous toughness estimates for the SC-4 specimen given in Ref. 1. Also in Fig. 3.14, fracture toughness is plotted against temperature for the upper and lower bounds of the compact tension (CT) specimen data. A range of crack initiation temperatures that reflects the uncertainty in crack-tip temperature at initiation[1] is shown in Fig. 3.14.

Based on the lower-bound fracture toughness curve measured by deeply notched standard CT specimens, initiation of the 40-mm/60-mm deep crack would be predicted at the near-surface point after about 140 s/120 s. However, initiation occurred after ~240 s at a stress-intensity factor (K_I) of ~160 MPa$\sqrt{m}$. This represents a substantial increase in fracture toughness compared with deeply notched standard fracture specimens. Results for K_I vs temperature depicted in Fig. 3.15 for the 40-mm flaw imply that no initiations are predicted at the deepest point of the flaw. The latter result is consistent with the observed behavior of the flaw during the SC-4 test that was described in Sect. 2.1 (see Fig. 2.13). Analogous results for K_I vs temperature for the 60-mm flaw at a near-surface point and the deepest point, given in Figs. 3.16 and 3.17, respectively, are also consistent with the observed initiation in the near-surface region.

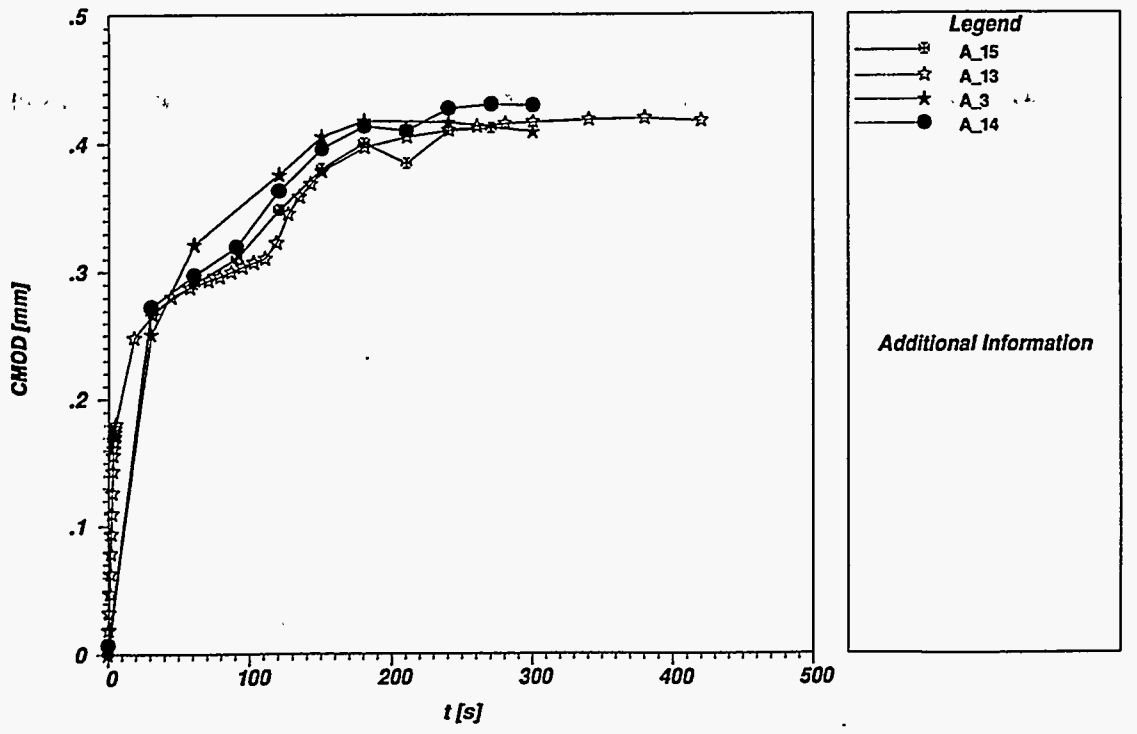

Figure 3.6 CMOD vs time for 40-mm crack in SC-4 experiment

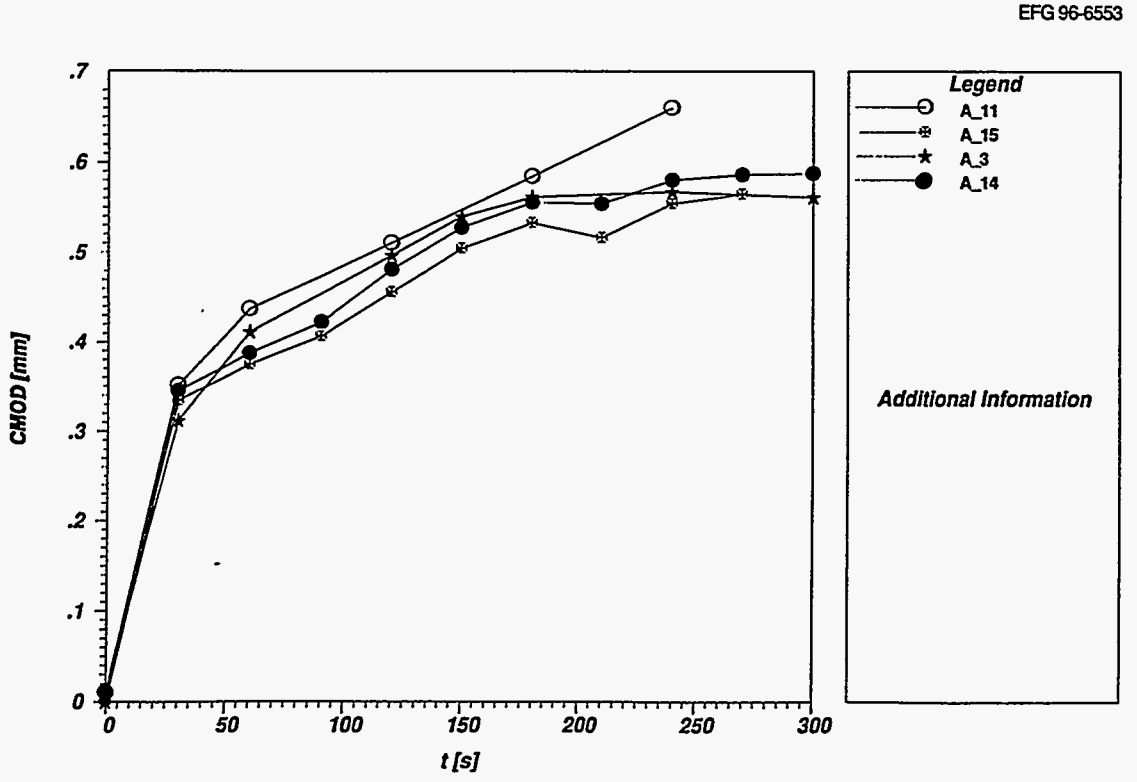

Figure 3.7 CMOD vs time for 60-mm crack in SC-4 experiment

EFG 96-6554

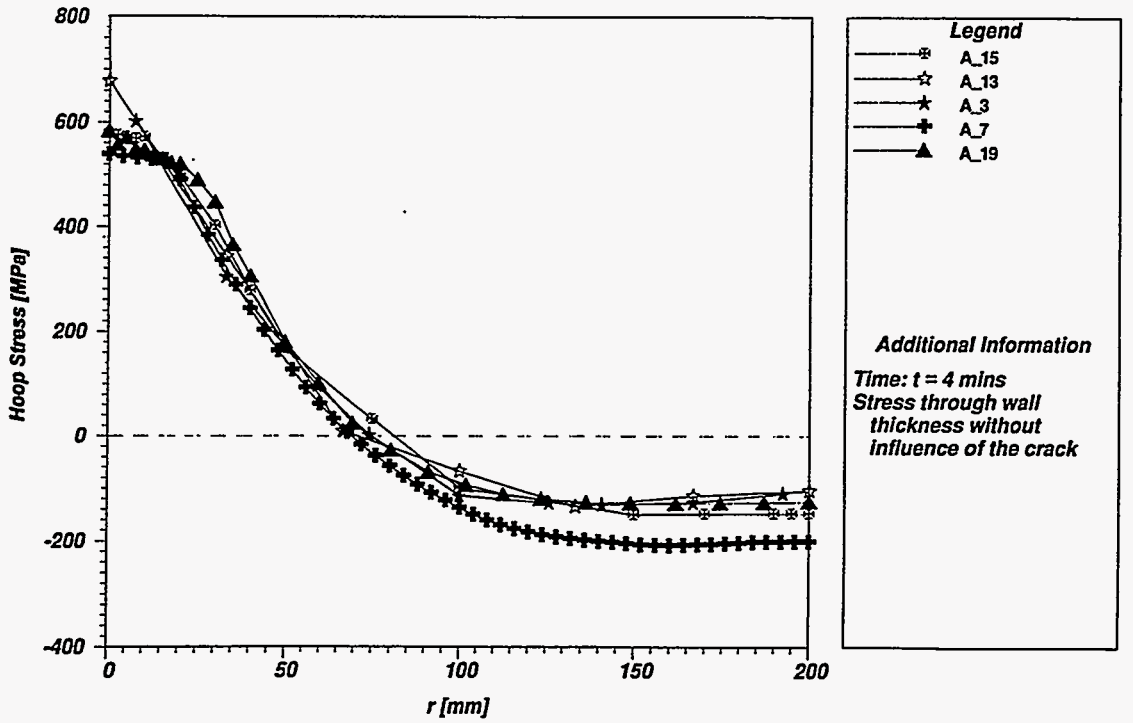

Figure 3.8 Circumferential stress vs wall thickness without influence of crack at t = 4 min (SC-4 experiment)

EFG 96-6555

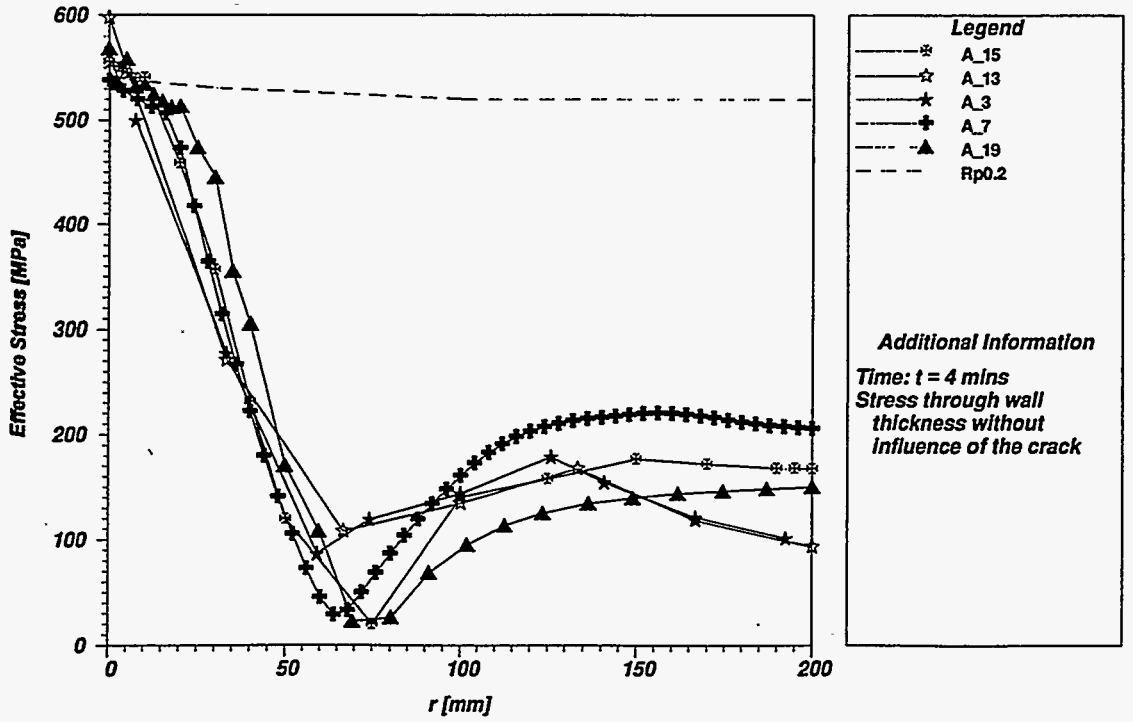

Figure 3.9 Effective stress vs wall thickness without influence of crack at t = 4 min (SC-4 experiment)

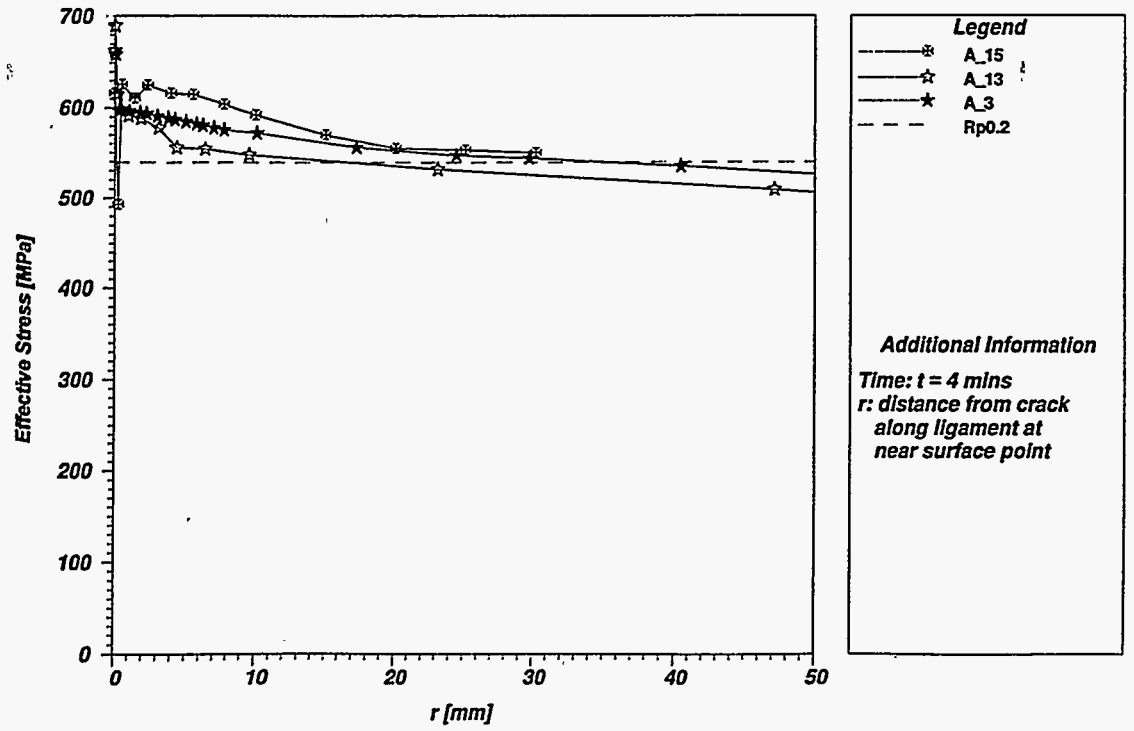

Figure 3.10 Effective stress vs distance from 40-mm crack along ligament at near-surface point at t = 4 min (SC-4 experiment)

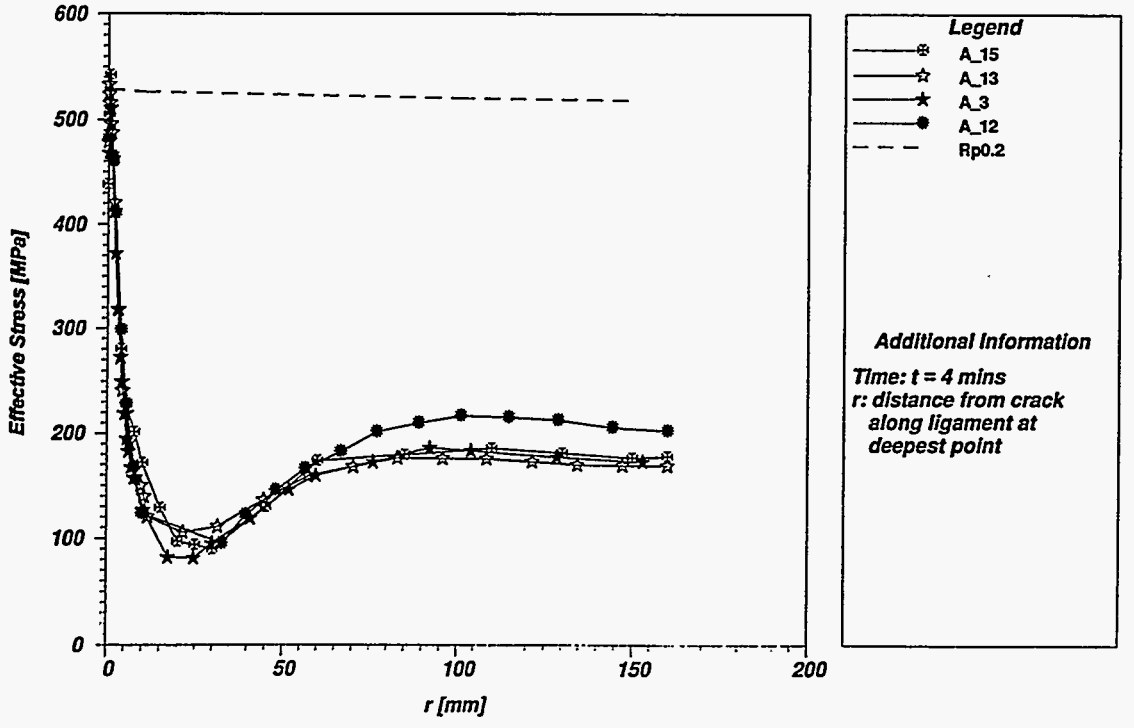

Figure 3.11 Effective stress vs distance from 40-mm crack along ligament at deepest point at t = 4 min (SC-4 experiment)

EFG 96-6558

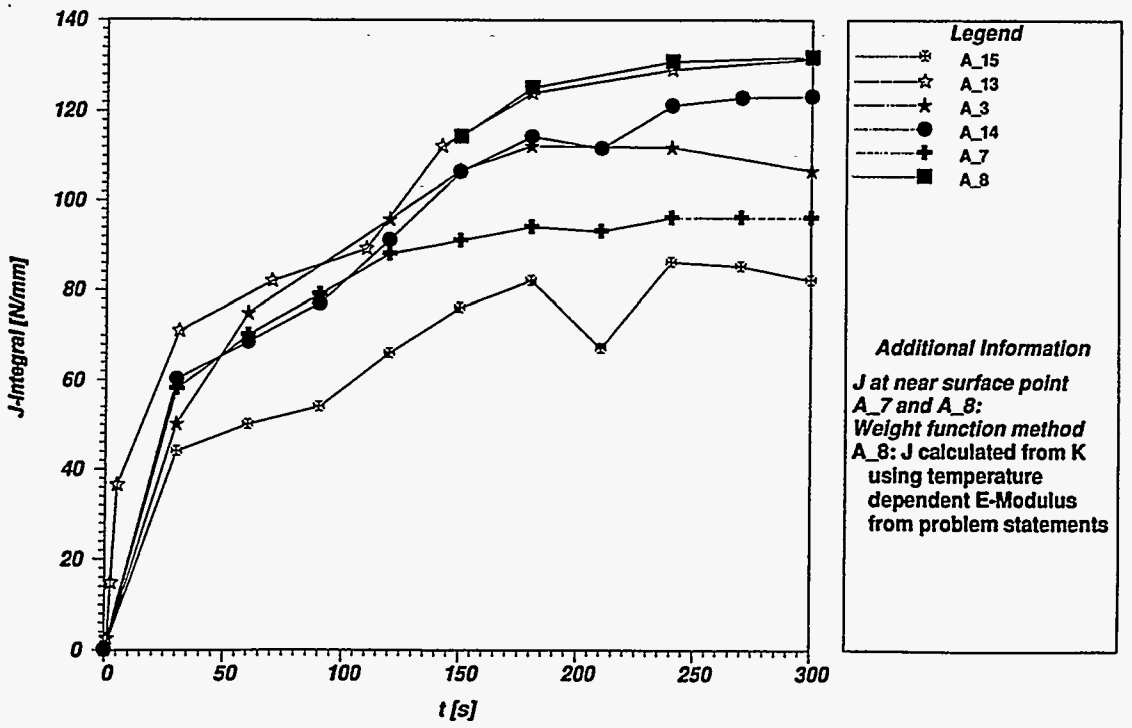

Figure 3.12 J-integral vs time at near-surface point of 40-mm crack(SC-4 experiment)

EFG 96-6559

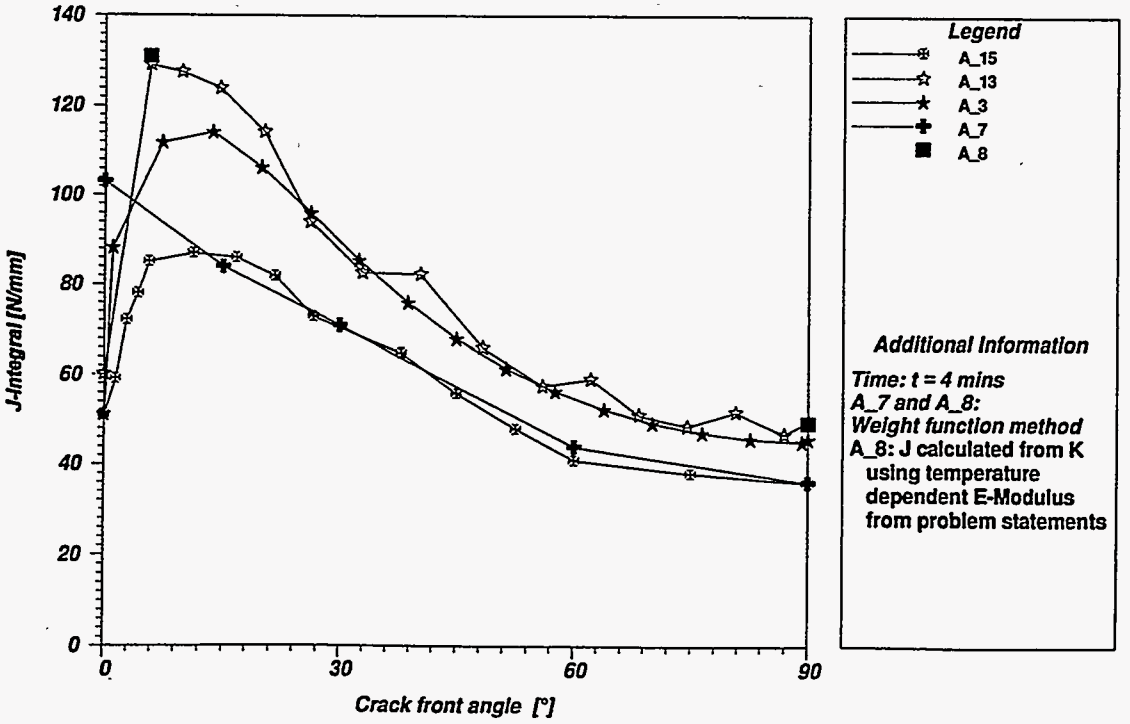

Figure 3.13 J-integral vs crack front angle for 40-mm crack at t = 4 min (SC-4 experiment)

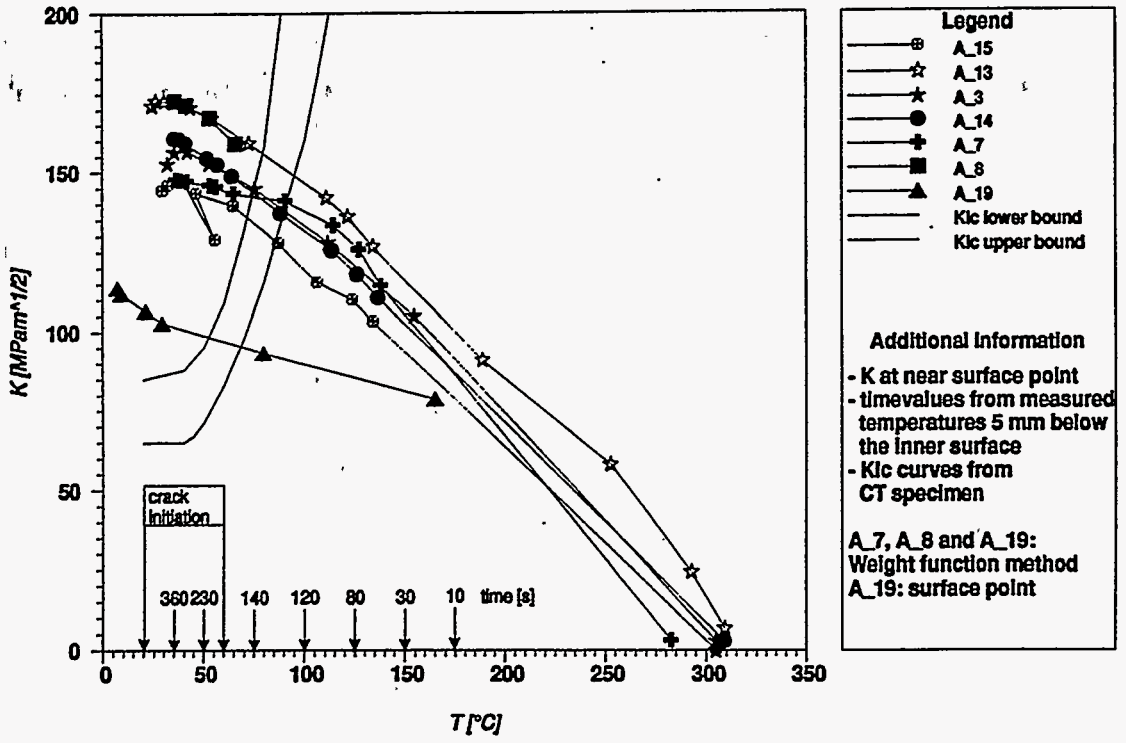

Figure 3.14 Comparison of applied K vs temperature at near-surface point of 40-mm crack with fracture toughness curves from CT specimens (SC-4 experiment)

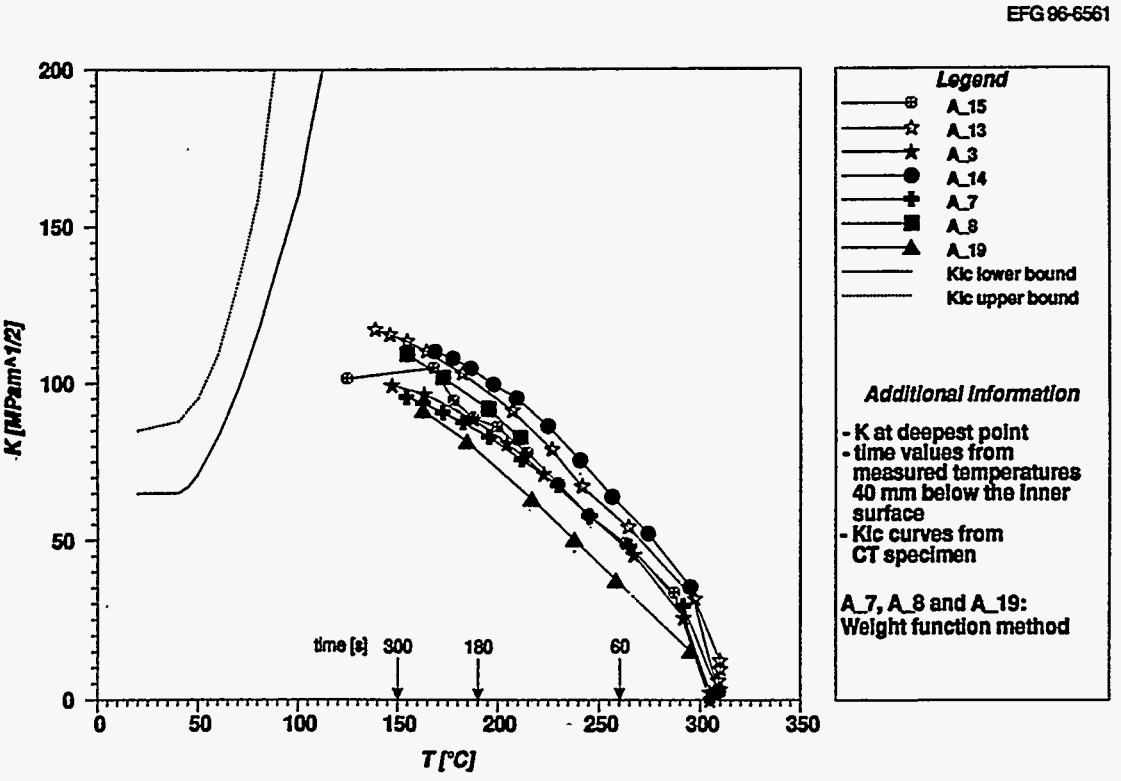

Figure 3.15 Comparison of applied K vs temperature at deepest point of 40-mm crack with fracture toughness curves from CT specimens (SC-4 experiment)

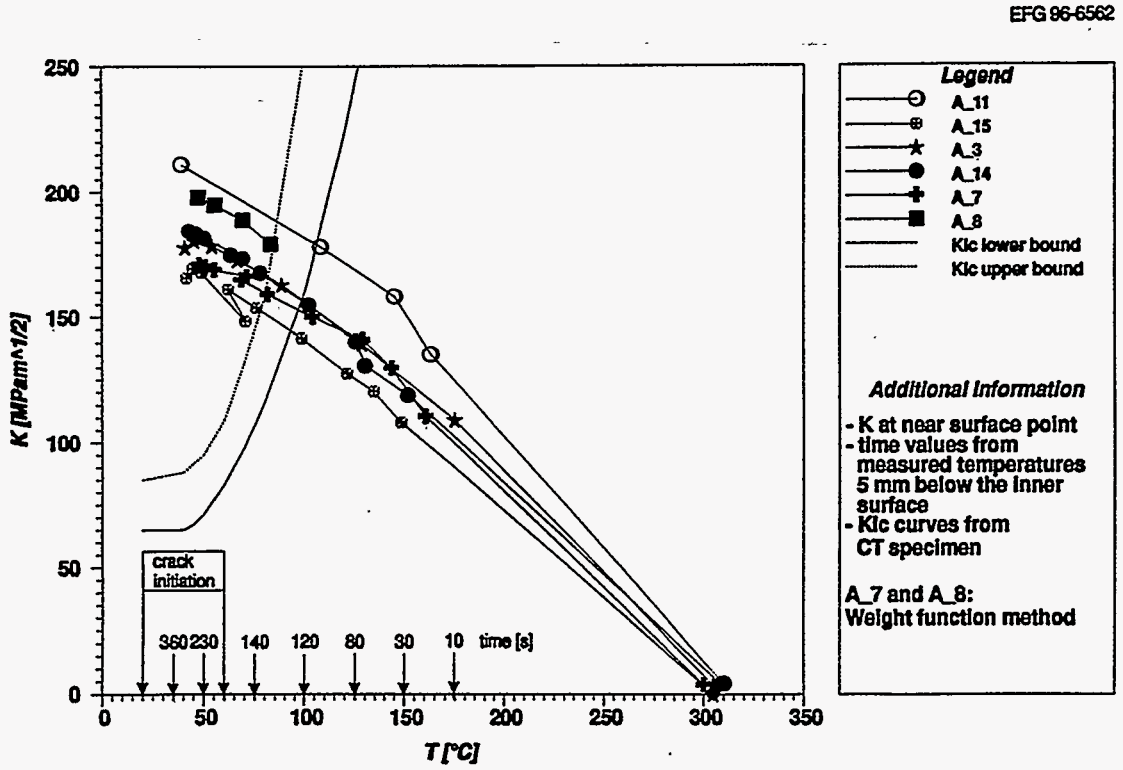

Figure 3.16 Comparison of applied K vs temperature at near-surface point of 60-mm crack with fracture toughness curves from CT specimens (SC-4 experiment)

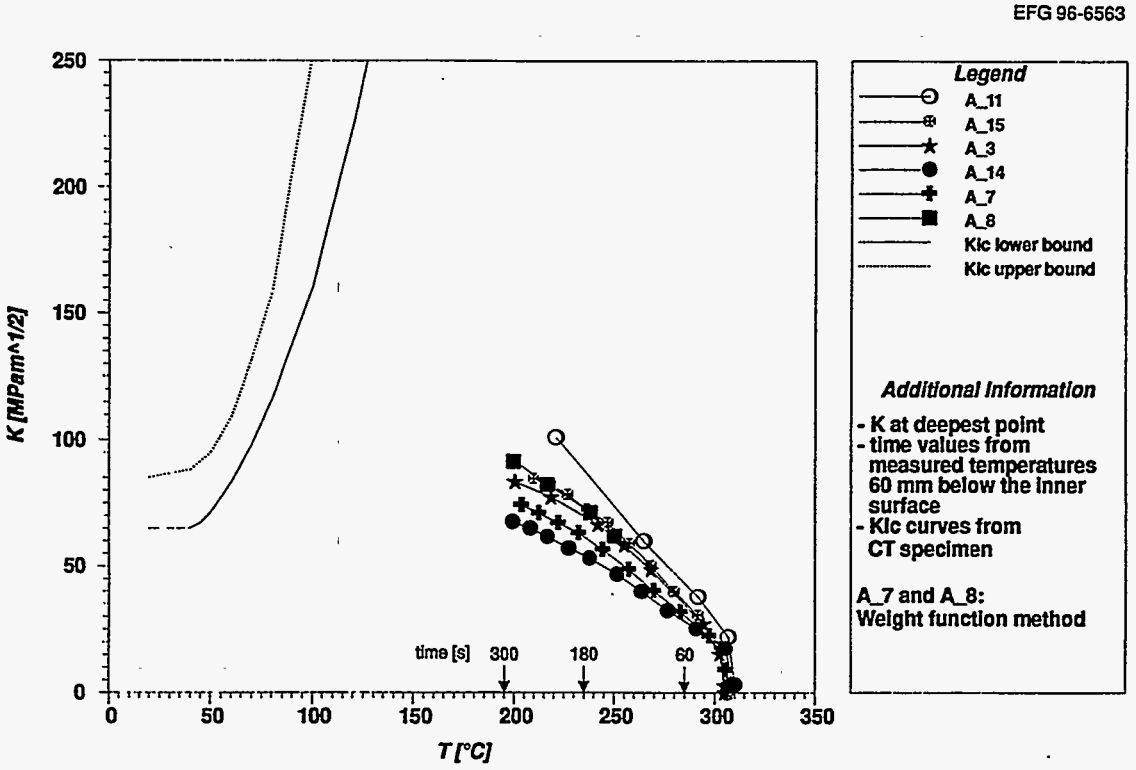

Figure 3.17 Comparison of applied K vs temperature at deepest point of 60-mm crack with fracture toughness curves from CT specimens (SC-4 experiment)

The elevation in toughness observed in the SC-4 experiment is attributed to a loss of constraint on the ligament of the near-surface points in the cylinder specimen relative to that of the highly constrained deep-flaw CT specimens. Evaluations of the constraint parameter Q (Ref. 2) on the ligaments of both cracks at near-surface points show a loss of constraint in the range of Q = –0.8 to –0.6 and almost no loss of constraint at the deepest points (Q = ~ –0.1 to –0.2). Figure 3.18 depicts the variation of constraint parameter Q vs normalized distance from the crack tip at a near-surface point of the 60-mm flaw, computed at time t = 4 min into the transient. Evaluations of the stress triaxiality factor h (Ref. 3) (i.e., hydrostatic stress/effective stress) on the ligament of the 60-mm flaw show a distribution between the plane-strain state for deeply notched specimens (h ≃ 2.2) and the plane-stress state (h ≃ 0.7). The differences between the distributions on the ligaments of the deepest points and the near-surface points are not significant (see Figs. 3.19 and 3.20).

3.2 Prometey—Sixth Pressurized-Thermal-Shock Test (PTS-I/6)

The PTS-I/6 analyses submitted by the participating organizations are summarized in Table 3.4 (thermal analyses) and in Table 3.5 (structural and fracture analyses). The computed temperature distributions through the cylinder wall at time t = 1 and 2.5 min into the thermal-shock transient are compared with measured values in Figs. 3.21 and 3.22, respectively. In both cases, the calculated temperatures proved to be in good agreement with the measured values. It appears that the data shown for thermocouple T1 (25 mm below the surface) underestimated the actual temperatures at that position.

In Fig. 3.23, computed circumferential strains are compared with measured values recorded on the outer surface

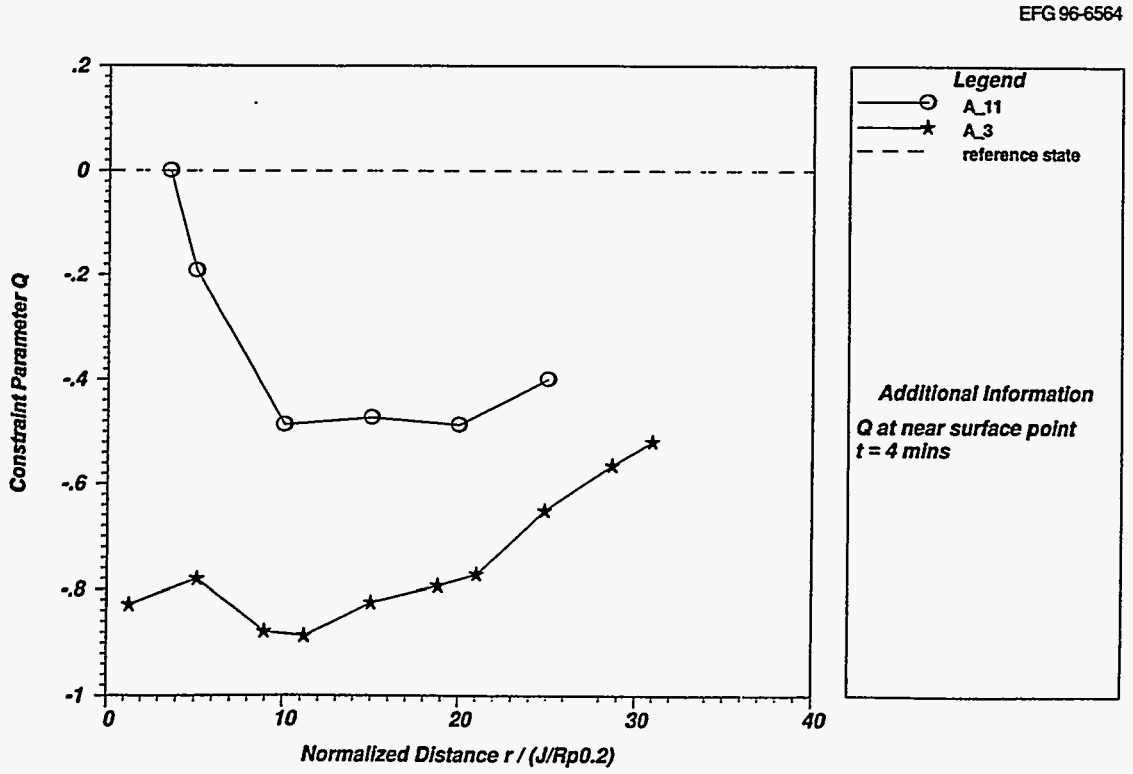

Figure 3.18 Constraint parameter Q vs normalized distance from 60-mm crack along ligament at near-surface point at t = 4 min (SC-4 experiment)

EFG 96-6565

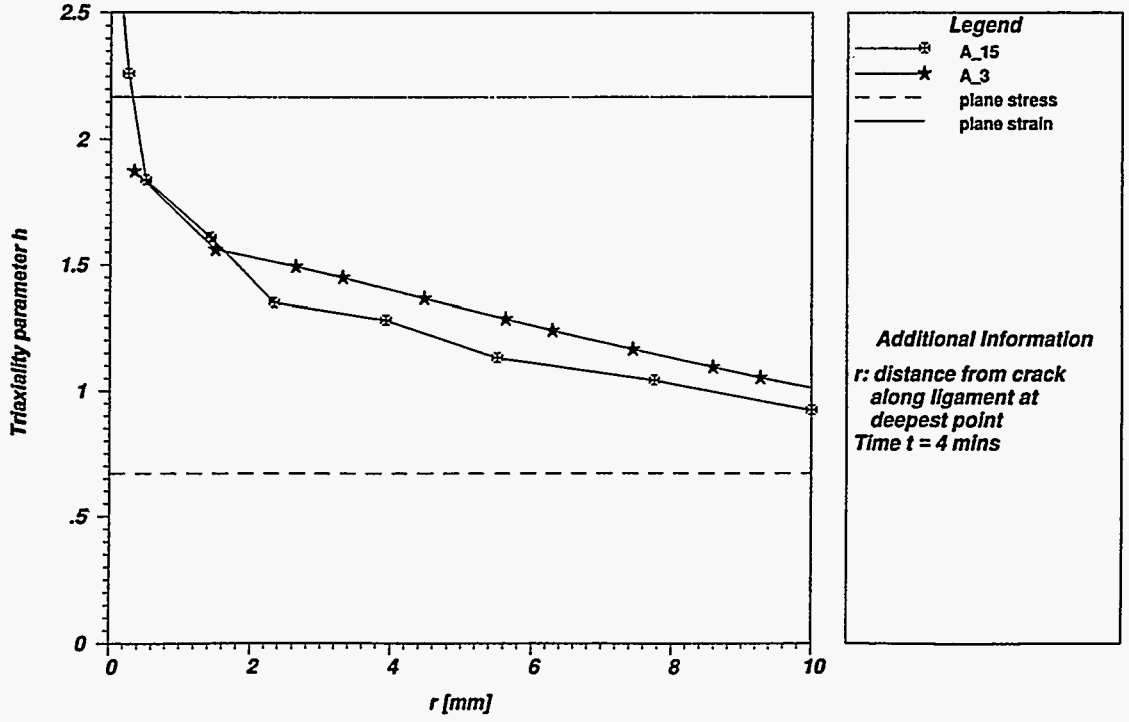

Figure 3.19 Triaxiality parameter h vs distance from 60-mm crack along ligament at deepest point at t = 4 min (SC-4 experiment)

EFG 96-6566

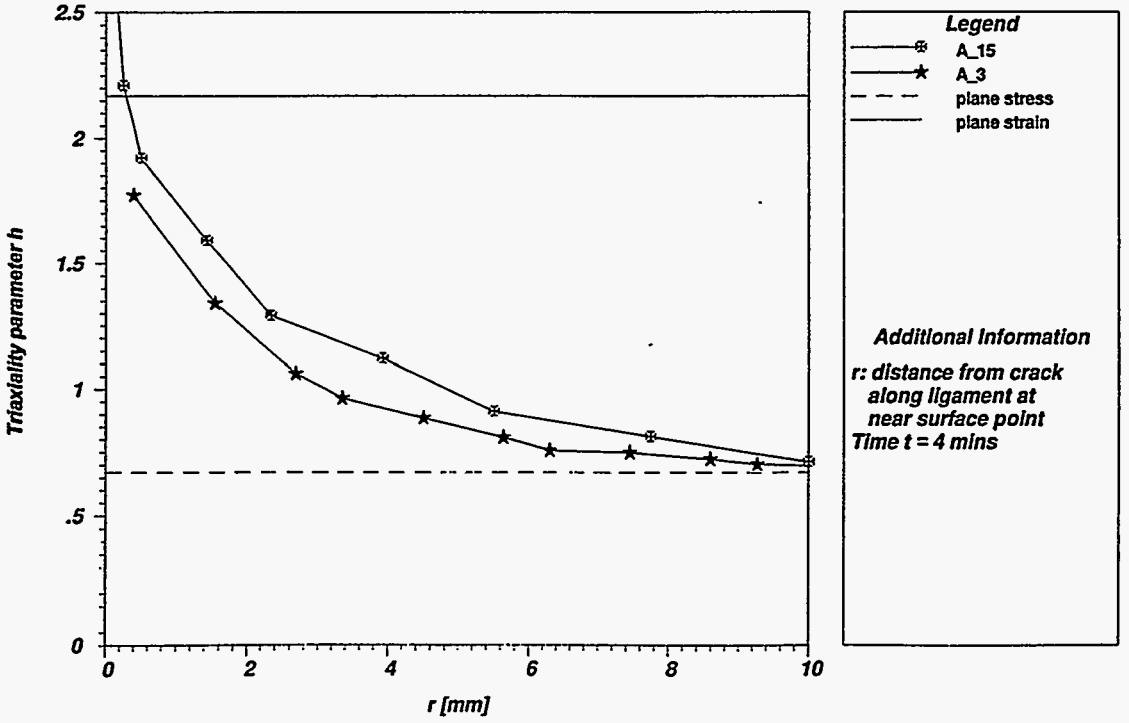

Figure 3.20 Triaxiality parameter h vs distance from 60-mm crack along ligament at near-surface point at t = 4 min (SC-4 experiment)

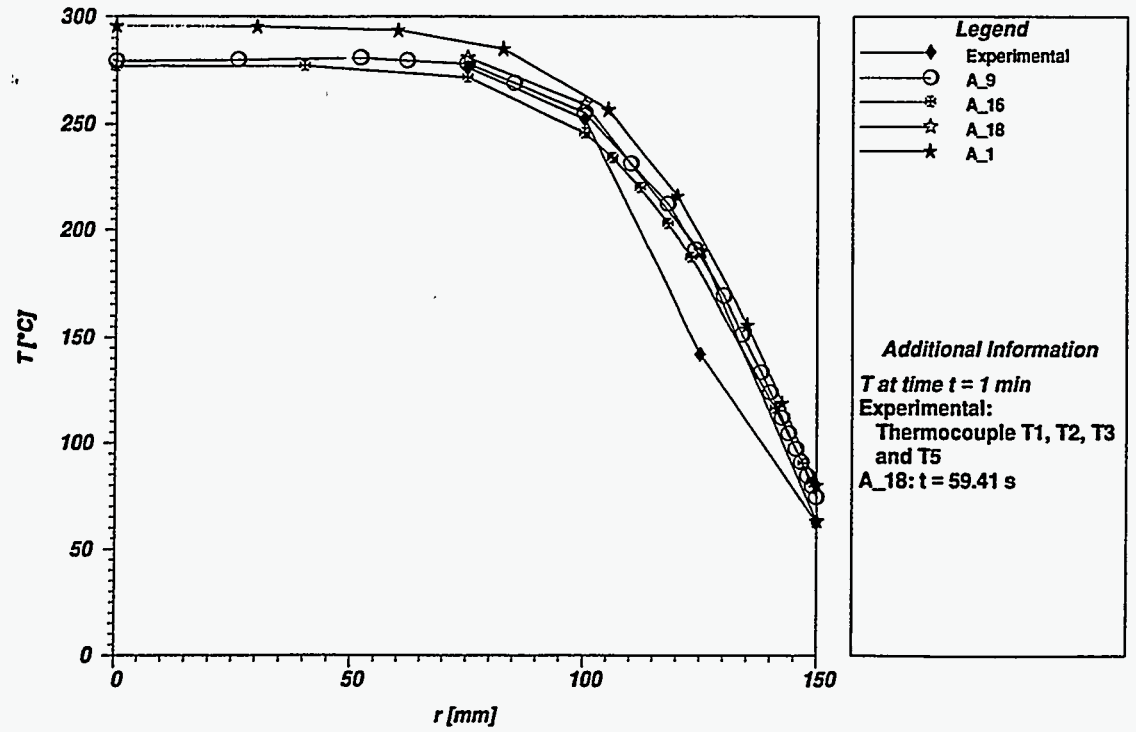

Figure 3.21 Temperatures vs wall thickness at t = 1 min (PTS-I/6 experiment)

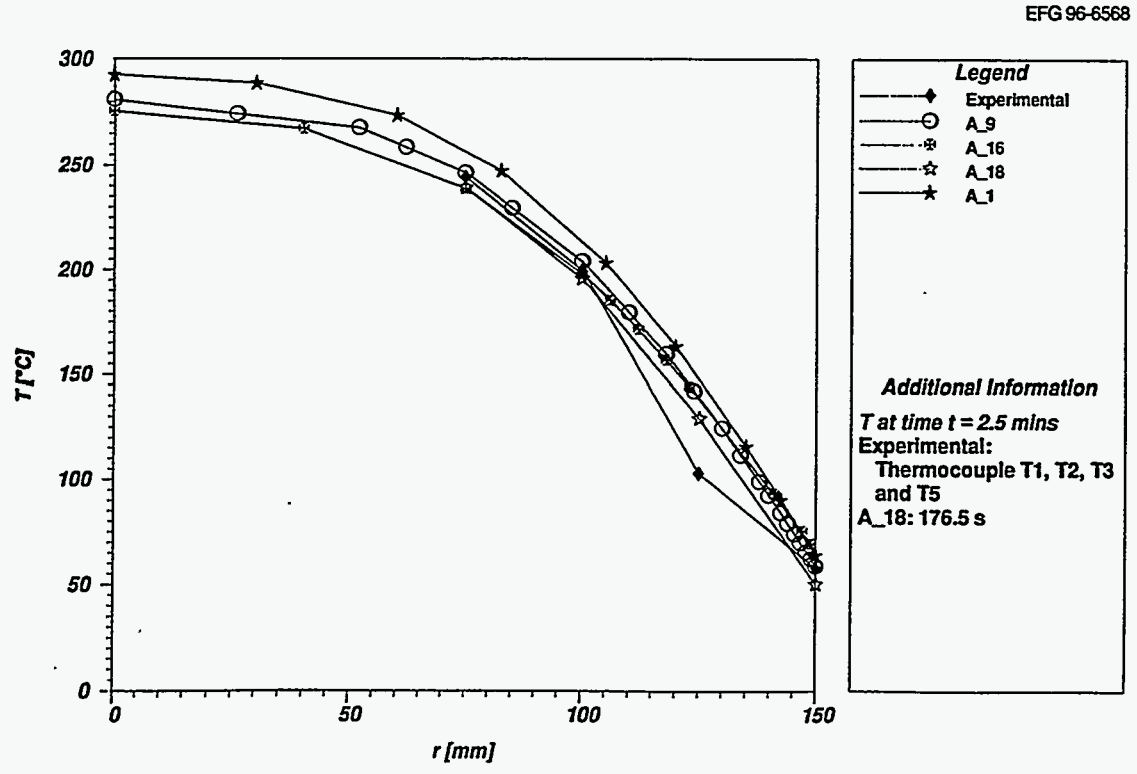

Figure 3.22 Temperatures vs wall thickness at t = 2.5 min (PTS-I/6 experiment)

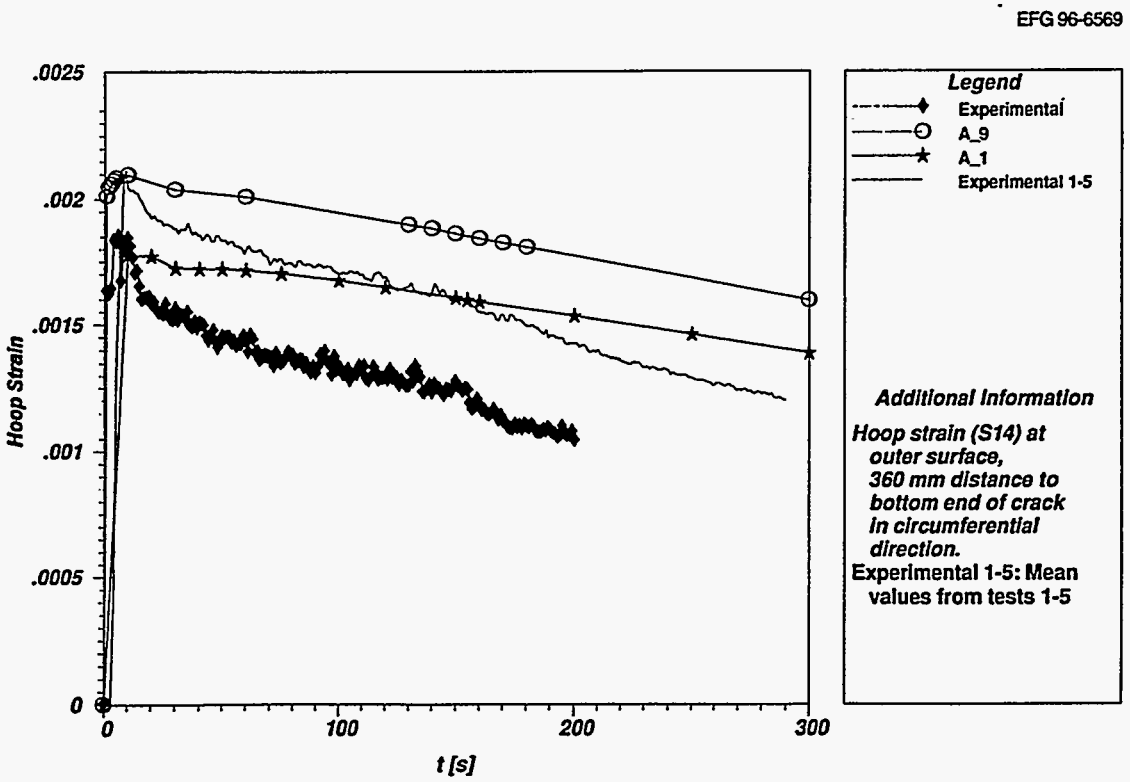

Figure 3.23 Circumferential strain vs time on outer surface of cylinder (gage S14) in the PTS-I/6 experiment

at a point located 36 cm from the crack line and 74 cm from the bottom of the vessel (S14 in Fig. 2.21). The computed strains overestimate the measured values for both analyses given in Fig. 3.23. These discrepancies may be traced to possible errors in the measured data due to effects of temperature on the strain gage calibration. The computed circumferential strains tend to be in better agreement with the mean strain values determined from data recorded in the previous PTS tests 1–5 (Ref. 4), also shown in Fig. 3.23.

Circumferential and effective stresses, corresponding to conditions time t = 2.5 min into the transient and computed along the ligament of the crack at location 21 in Fig. 2.24, are compared in Figs. 3.24 and 3.25, respectively. Analysis A_9 utilized a thermoelastic material model in the calculation of effective stresses, whereas analysis A_1 was based on a thermoelastic-plastic formulation. Consequently, the two calculations of the effective stress differ at distances close to the crack tip where plasticity effects are present (see Fig. 3.25).

In Fig. 3.26, analysis results for CMOD vs time are compared with measured data at a point on the crack front located in the base metal near the interface with the weld. With one exception (analysis A_18), the analytical predictions are in reasonably good agreement with the data up to the time of cleavage initiation. The analytical models used to generate the results in Fig. 3.26 did not take into account the crack propagation event that occurred near t = 155 s. The deviation of analysis A_18 from the other analyses is possibly because of the application of a different stress-strain curve in the analytical model.

The time histories of the J-integral computed at location 21 in Fig. 2.24 during the time interval from t = 0 to 5 min are compared in Fig. 3.27. Again, there is reasonably good agreement among the analyses, with the exception of analysis A_18, possibly because of the reason mentioned in the previous paragraph. Also, note that the results from analysis A_18 are strongly dependent on the path used to evaluate the J-integral.

Comparisons of the stress-intensity factor vs crack front angle computed for times t = 0 and 2.5 min into the transient are compared in Figs. 3.28 and 3.29, respectively. The agreement is generally good for that part of the crack located in base metal but is less good in the weld metal at t = 2.5 min. Analysis A_9 overestimates the crack loading in the weld region because the results are based on a thermoelastic material model. However, plasticity effects are not negligible in the region due to a much lower yield stress in the weld material compared with the base metal (see Table 2.12).

EFG 96-6570

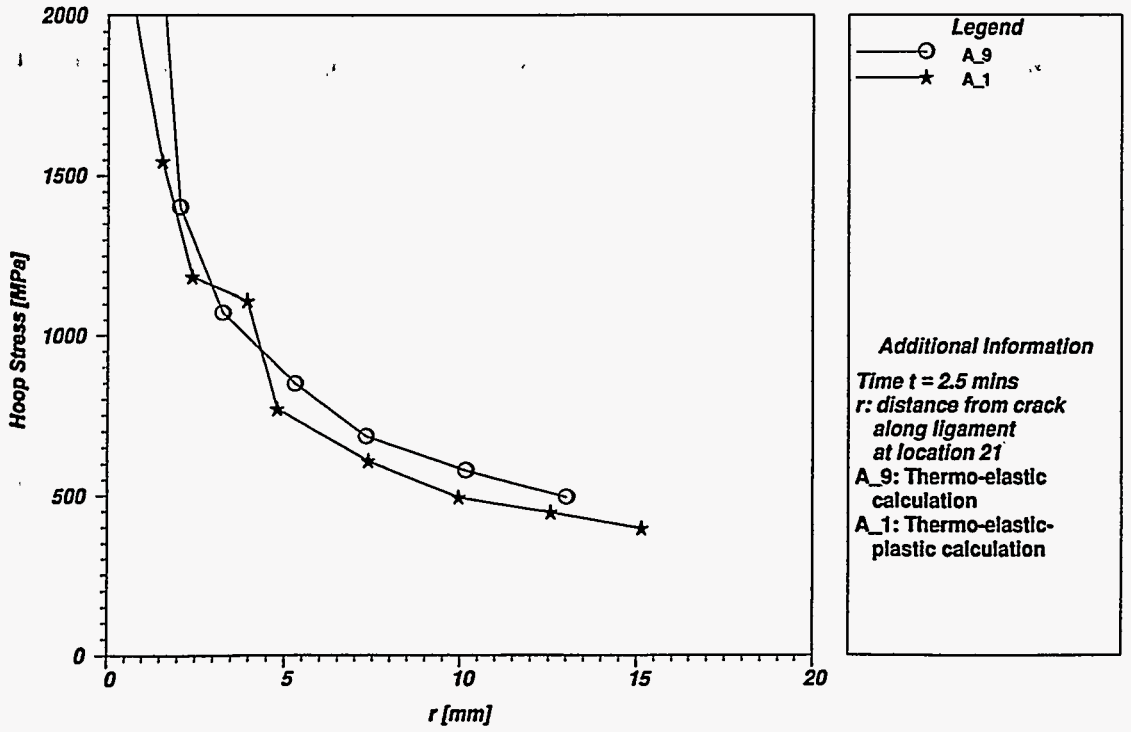

Figure 3.24 Circumferential stress vs distance from crack along ligament at location 21 at t = 2.5 min (PTS-I/6 experiment)

EFG 96-6571

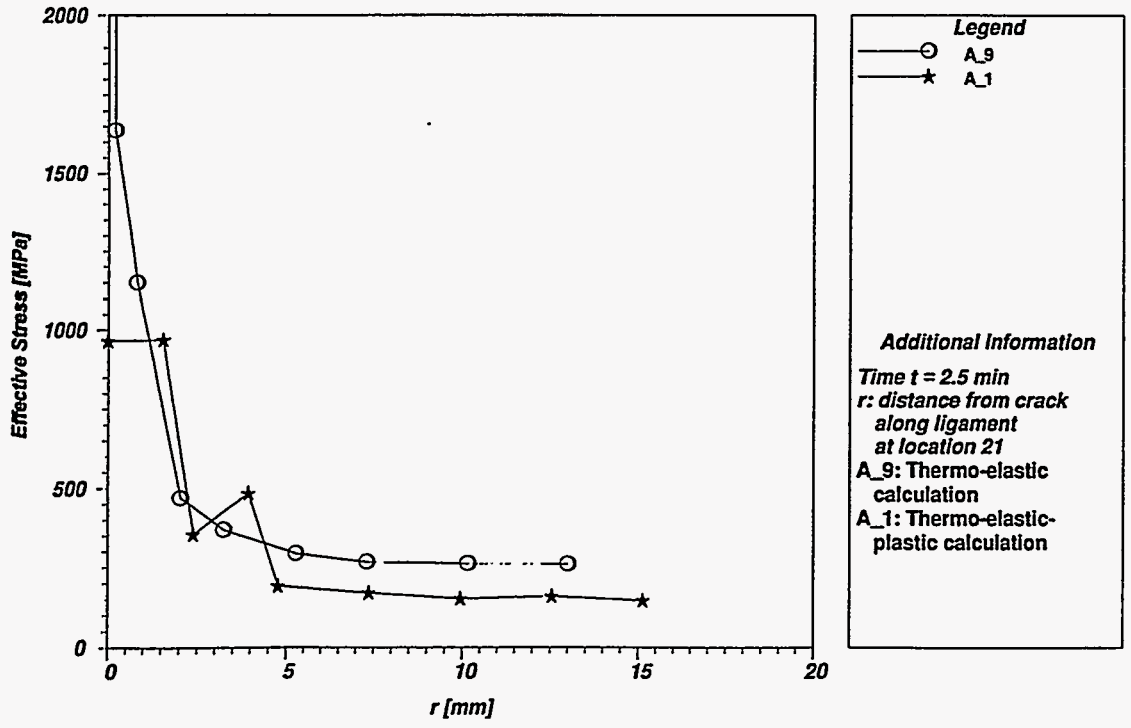

Figure 3.25 Effective stress vs distance from crack along ligament at location 21 at t = 2.5 min (PTS-I/6 experiment)

EFG 96-6572

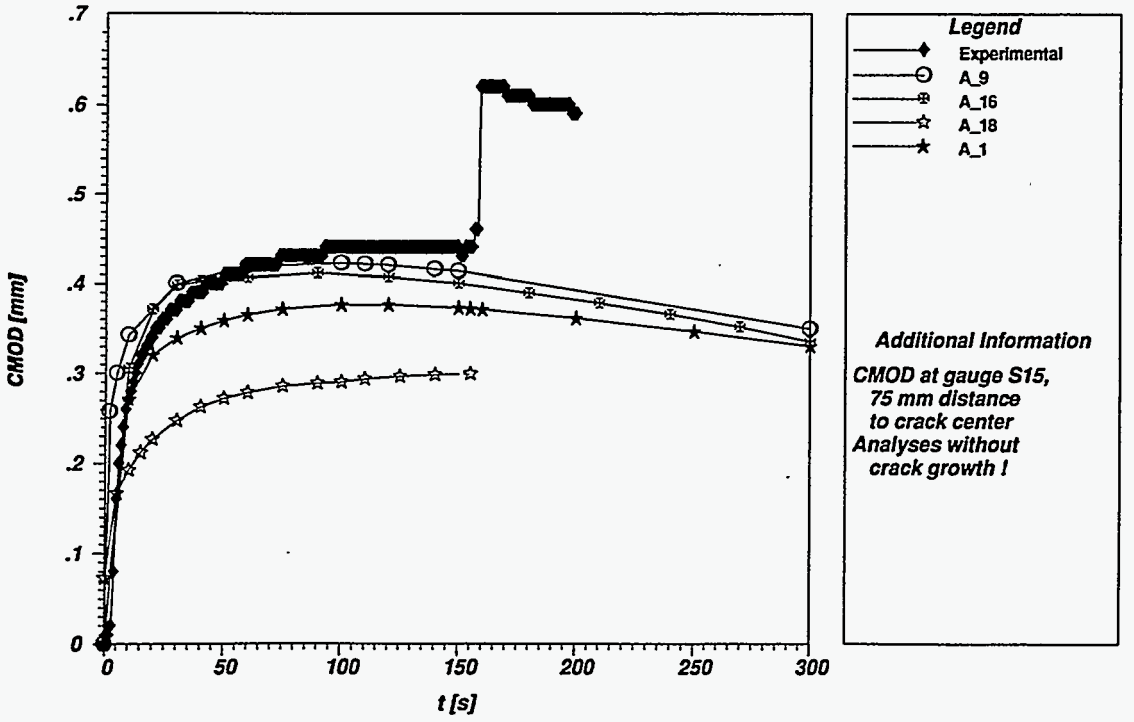

Figure 3.26 CMOD vs time at gage S15 (75-mm distance to crack center) in the PTS-I/6 experiment

EFG 96-6573

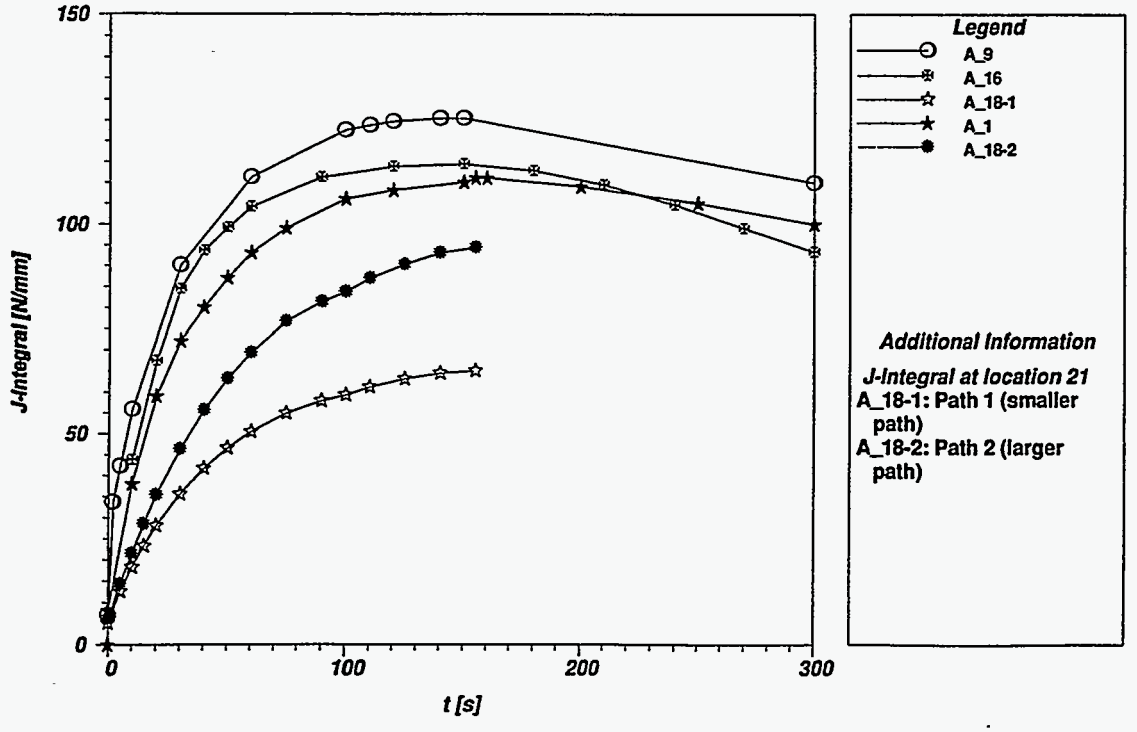

Figure 3.27 J-integral vs time at location 21 in PTS-I/6 experiment

EFG 96-6574

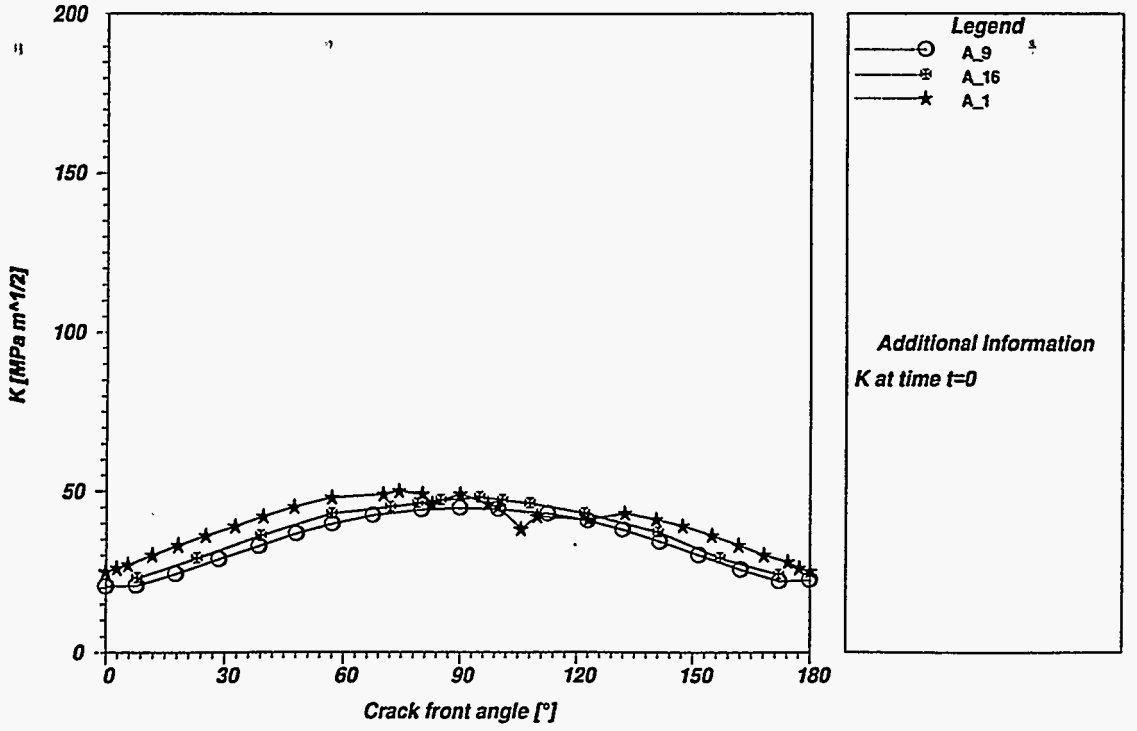

Figure 3.28 Applied K vs crack front angle at t = 0 min in PTS-I/6 experiment

EFG 96-6575

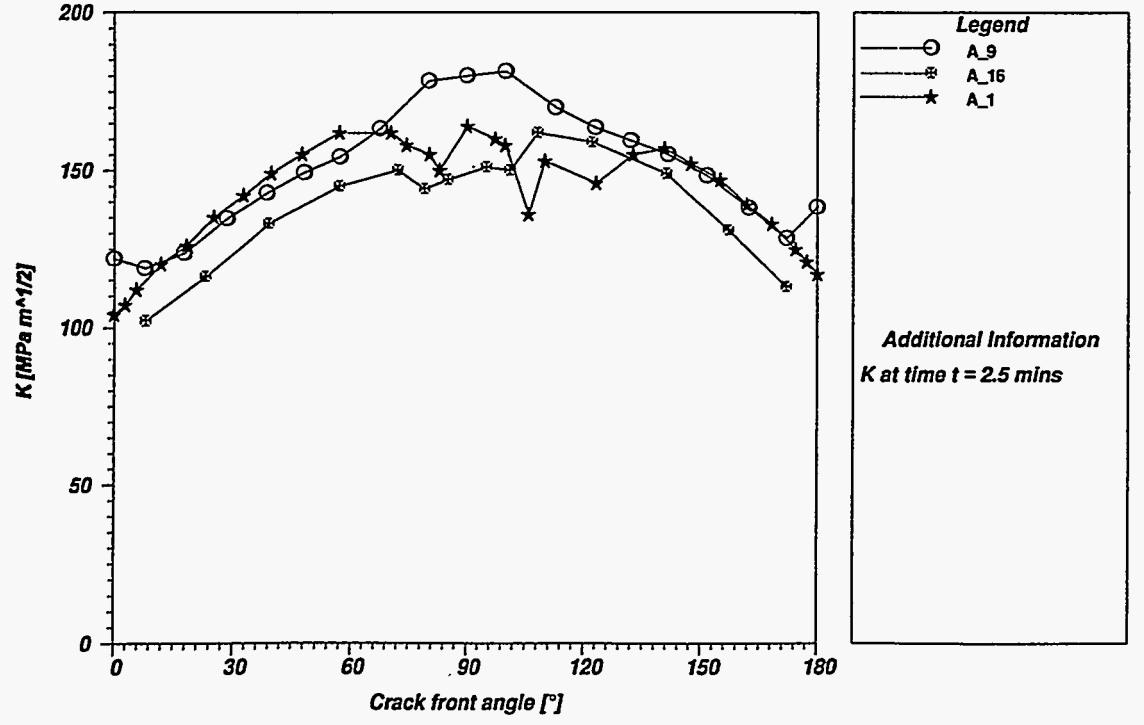

Figure 3.29 Applied K vs crack front angle at t = 2.5 min in PTS-I/6 experiment

Comparative

In Fig. 3.30, computed values of K_I vs crack-tip temperature are compared with K_{Ic} fracture toughness curves generated from small specimen data. The analytical results were determined at a point in the base metal near the maximum depth of the flaw. With the one exception of analysis A_18, the calculated results are closely grouped. Based on the measured lower-bound K_{Ic} curve, cleavage initiation is predicted about 80 s into the transient. This prediction substantially underestimates the measured time for crack initiation at 155 s, which suggests that constraint effects should be investigated as a possible explanation for the discrepancy.

Variations of the stress triaxiality parameter h in two analyses (A_1 and A_9) computed on the ligament near position 21 of Fig. 2.21 at time t = 2.5 min are compared in Fig. 3.31. As previously mentioned, analyses A_1 and A_9 were based on thermoelastic-plastic and thermoelastic material models, respectively. Thus, it is anticipated that the two analyses would produce differing results in the near-crack-tip region where plasticity effects are present. On the other hand, the distribution of h on the ligament near position 21 ranges about the plane strain value and shows no clear indication of a constraint effect. None of the participants provided calculations for the Q-stress parameter.

3.3 Pressurized-Thermal-Shock Test NKS-5

Analyses of the NKS-5 experiment[5] are summarized in Table 3.6 (thermal analyses) and in Table 3.7 (structural and fracture analyses). Comparisons of calculated and measured temperatures at time t = 1, 5, and 10 min into the thermal transient are given in Figs. 3.32–3.34, respectively. Calculated temperatures near the cooled inner surface showed strong scatter during t < 5 min of the transient due to differences in assumptions concerning the heat-transfer coefficient.

Time histories of the measured and computed circumferential and axial strains on the inner surface at a location 388 mm below the crack ligament (i.e., at gages DL5/DU5 in Fig. 2.32) are compared in Figs. 3.35 and 3.36, respectively. Only the mechanical components of strain are given in Figs. 3.35 and 3.36, that is, without the thermal part ($\alpha\,\Delta T$). Analyses A_1 and A_16 were performed as elastic-plastic calculations, while all other analyses were based on linear elastic models. Also, analysis A_9 incorporated a crack extension of 13 mm into the calculations. For both strain histories, there is reasonable agreement between the computed values and measured data.

EFG 96-6576

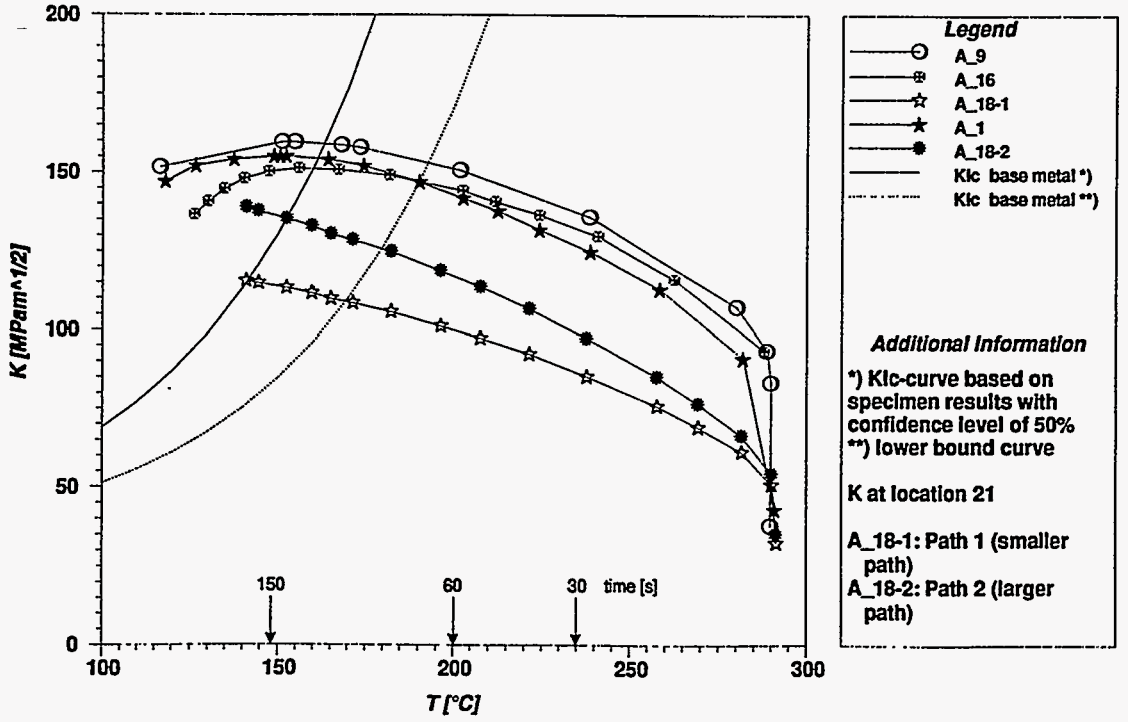

Figure 3.30 Comparison of applied K vs temperature at location 21 along crack front with fracture toughness curves from CT specimens (PTS-I/6 experiment)

EFG 96-6577

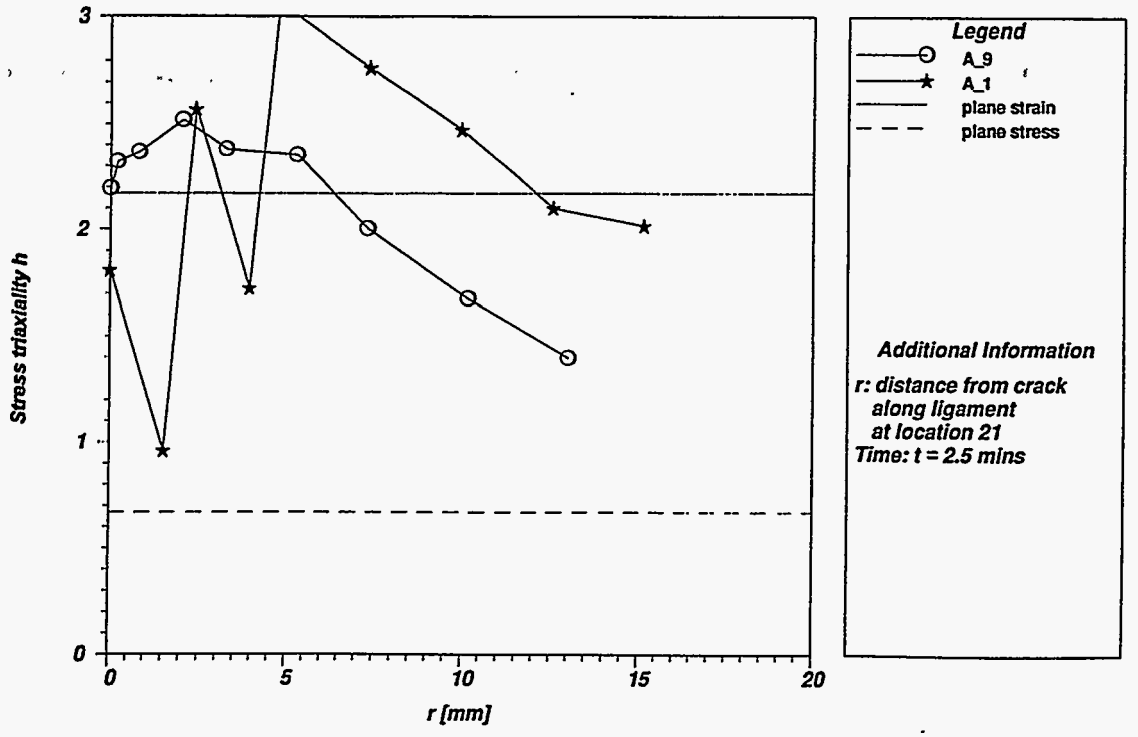

Figure 3.31 Triaxiality parameter h vs distance from crack along ligament at location at t = 2.5 min (PTS-I/6 experiment)

EFG 96-6578

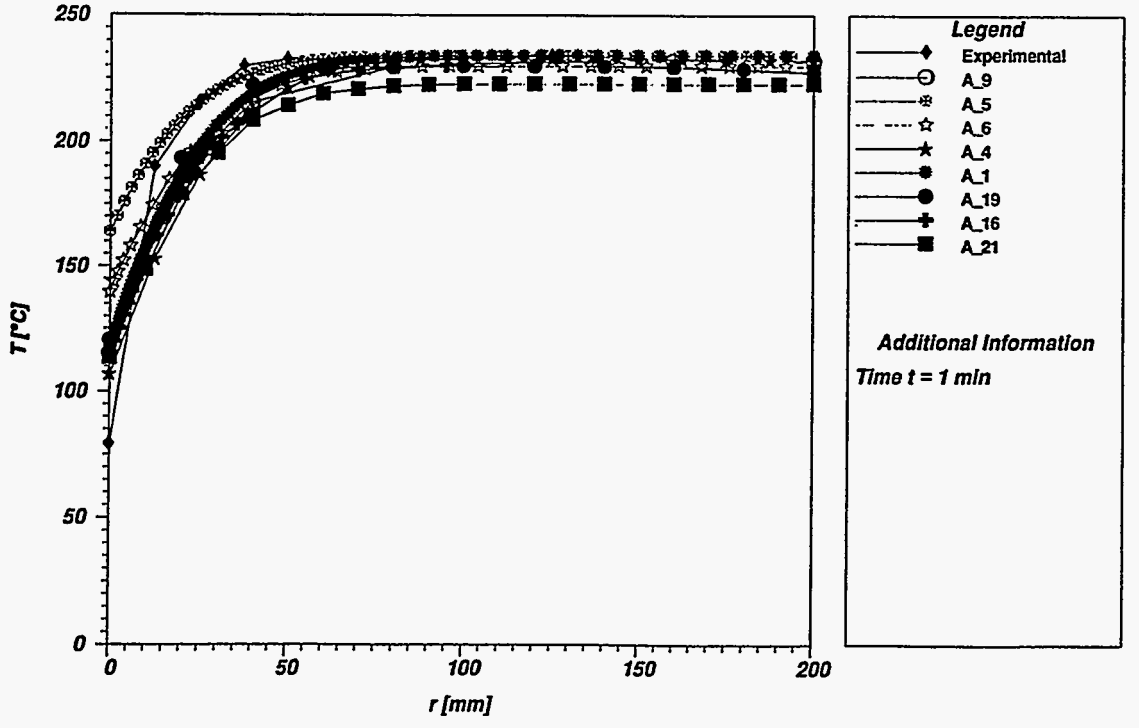

Figure 3.32 Temperatures vs wall thickness at t = 1 min (NKS-5 experiment)

EFG 96-6579

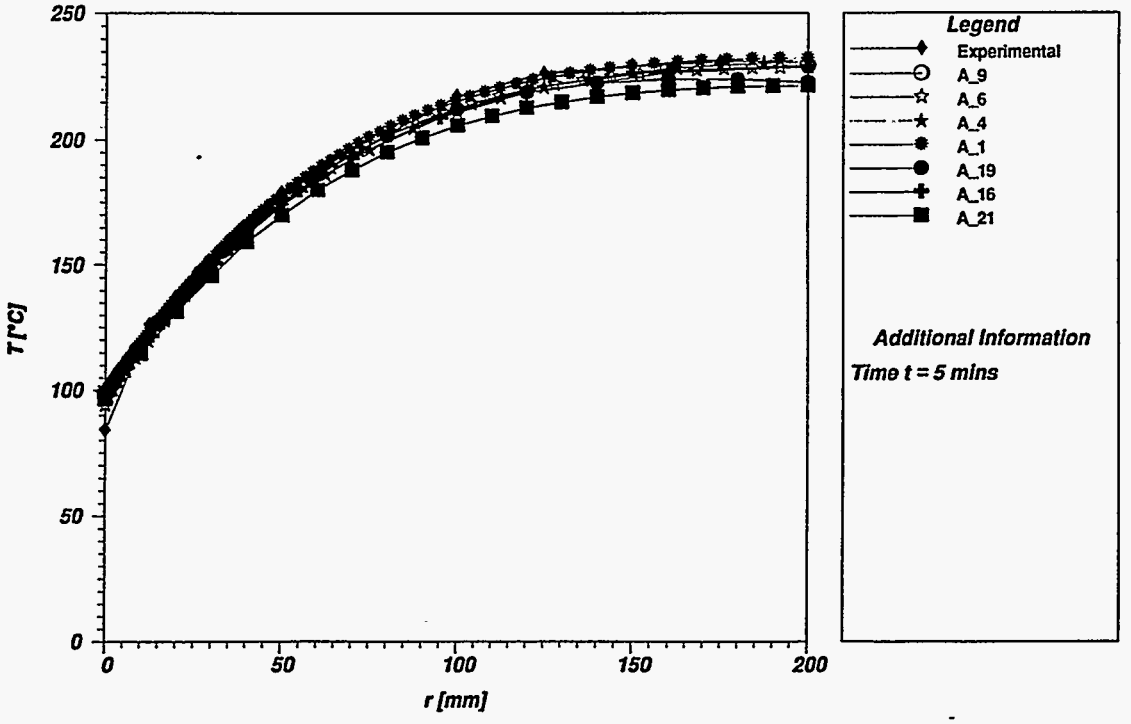

Figure 3.33 Temperatures vs wall thickness at t = 5 min (NKS-5 experiment)

EFG 96-6580

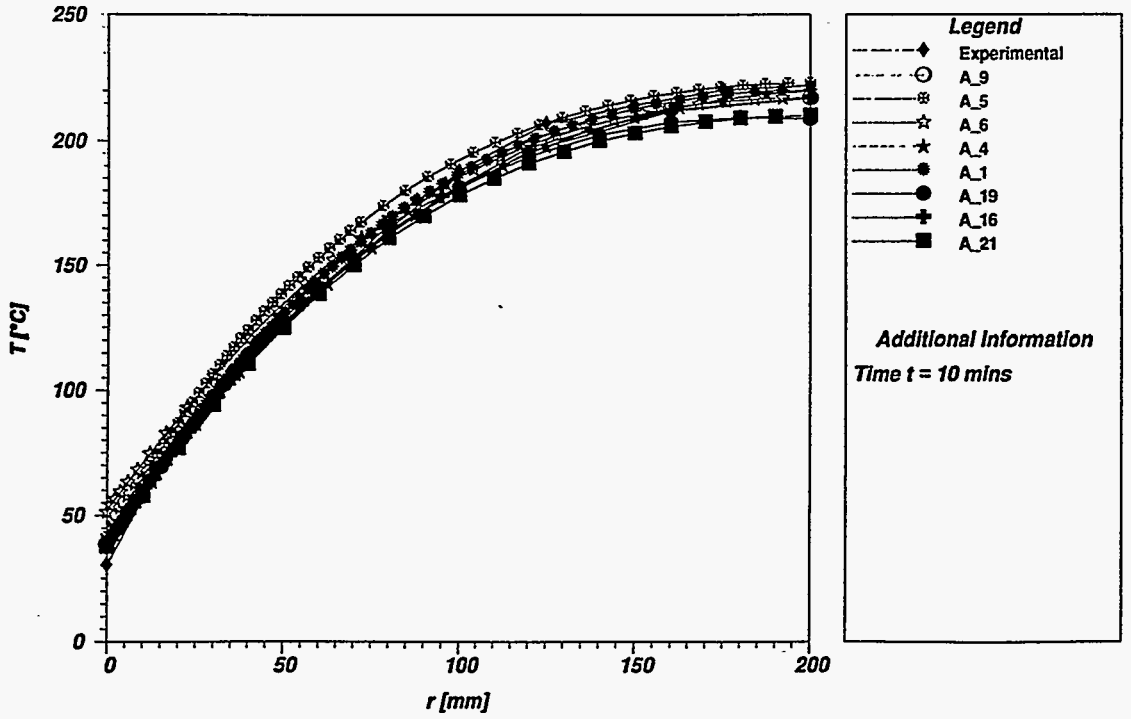

Figure 3.34 Temperatures vs wall thickness at t = 10 min (NKS-5 experiment)

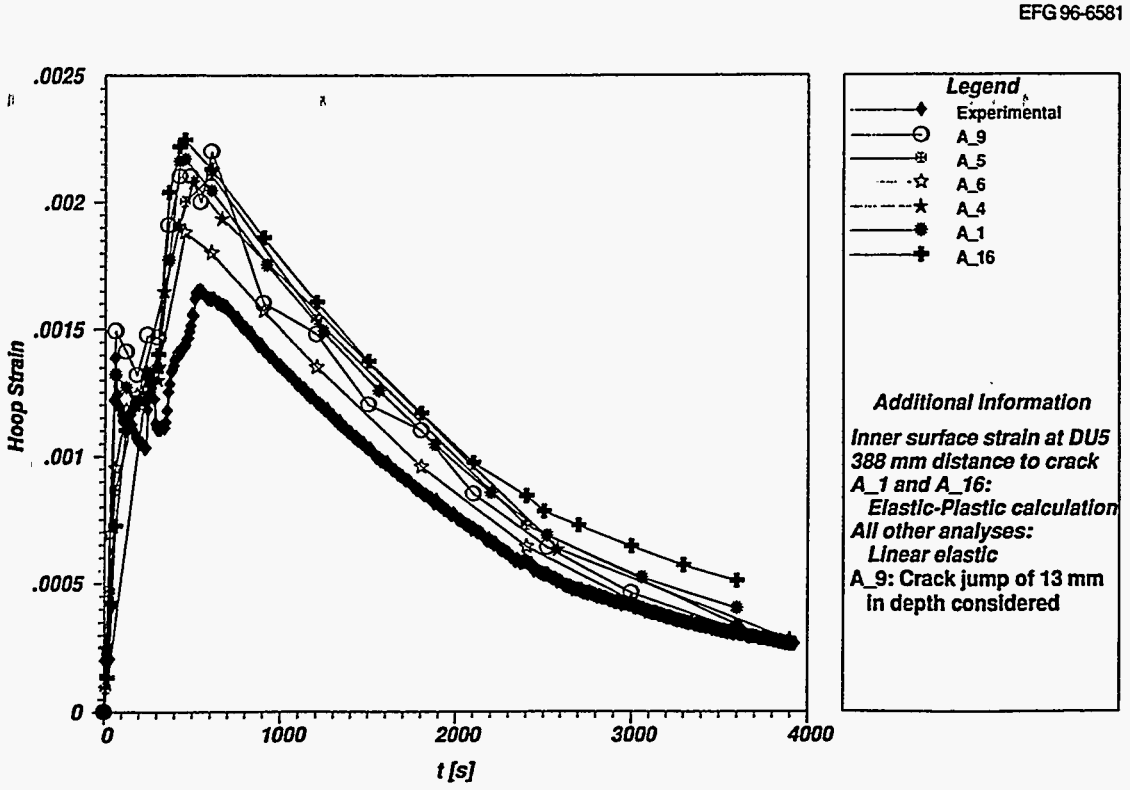

Figure 3.35 Circumferential strain vs time on inner surface of cylinder (gage DU5) in NKS-5 experiment

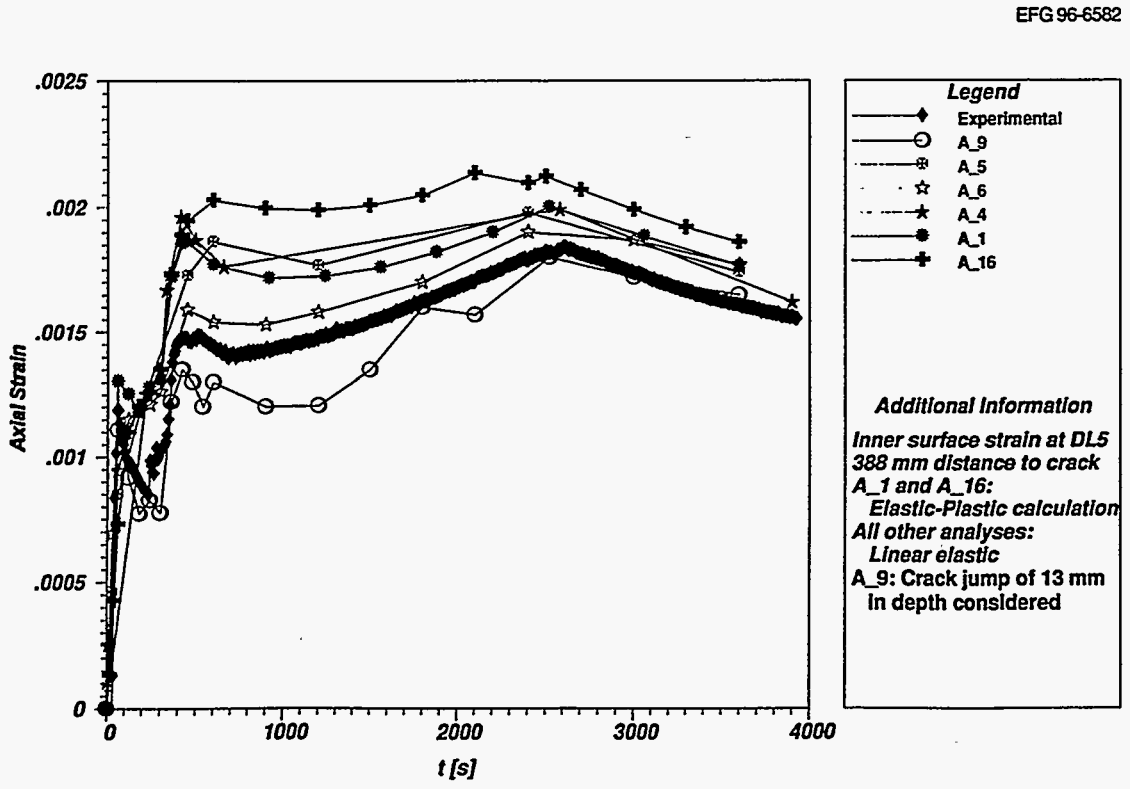

Figure 3.36 Axial strain vs time on inner surface of cylinder (gage DL5) in NKS-5 experiment

Comparative

In Fig. 3.37, measured data from CMOD gages (G5 and G6) located at midspan and outboard points of Notch B (see Fig. 2.33) depict CMOD vs time for the latter crack during the thermal-shock transient. Values of computed CMOD vs time at the midspan of Notch B are also included in Fig. 3.37. Portions of these data are plotted using an expanded time scale for t ≤ 10 min in Fig. 3.38. These data suggest that both radial and circumferential crack jump events could have occurred in the 5- to 10-min time interval following initiation of the thermal shock. However, late event crack jumps (at time t > 1000 s) are also noted on the CMOD record. Data are insufficient to

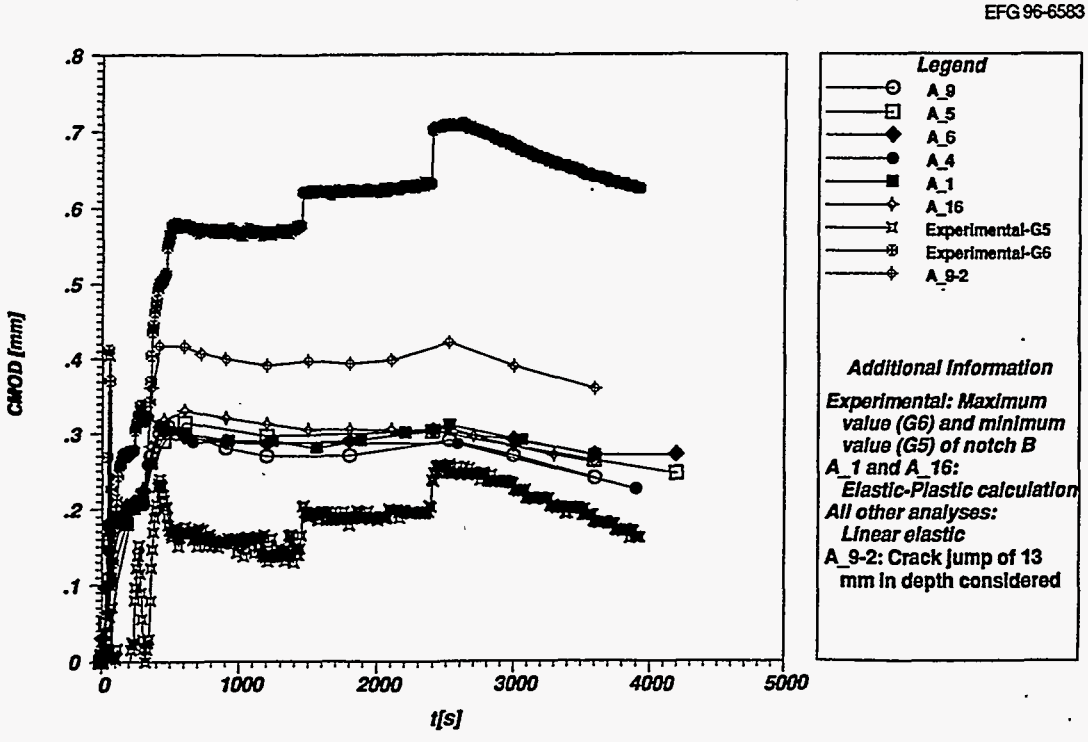

Figure 3.37 CMOD vs time for Notch B in the NKS-5 experiment

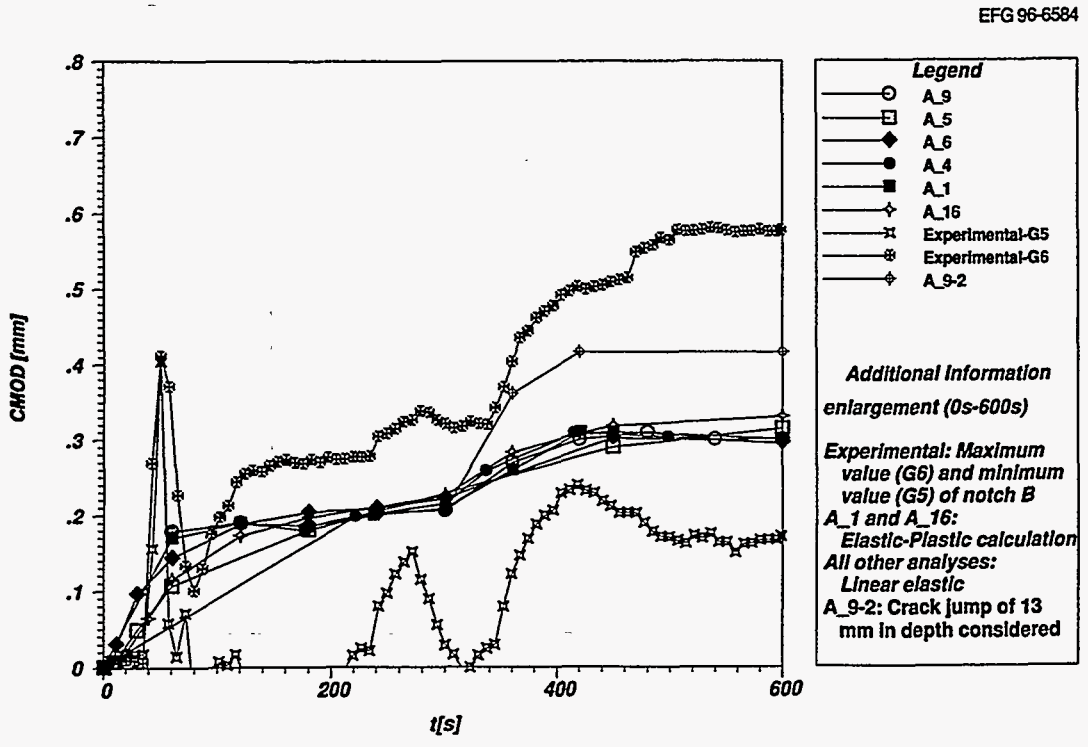

Figure 3.38 CMOD vs time (with expanded time scale) for Notch B in NKS-5 experiment

determine the sequence of the crack jumps, that is, whether the radial or the circumferential crack jump occurred first. The analytical predictions of CMOD vs time, which are tightly grouped in Figs. 3.37 and 3.38, did not account for propagation of the crack. The model used to generate the A_9-2 results incorporated a crack jump of 13 mm in the radial (or depth) direction at ~5 min into the transient.

The CMOD data measured at different positions along both crack fronts (Notches A and B) showed unusual behavior, which proved difficult to interpret. In particular, CMOD data from the midspan gage (G5) of Notch B indicated crack closure during the early part of the transient (see Fig. 3.38), which is inconsistent with positive values from the outboard gage (G6). Furthermore, data from the two gages show substantial differences in CMOD values even at the end of the transient, when Notches A and B had grown together over a circumferential region of about 220°. The differences between the CMOD gages remain essentially constant after the first 500 s. A check of additional temperature measurements at different positions along the inner surface showed no strong indications of asymmetric loading during this period.

In the early part of the transient (t < 5 min), there was more axial variation in temperature on the side of the vessel containing Notch A when compared with the side containing Notch B. During this period, the measured temperature and CMOD data imply that Notch A was subjected to a loading-partial unloading-reloading sequence that was not experienced by Notch B. Also, in this period, Notch A experienced lower temperatures than Notch B.

In Figs. 3.39–3.42, computed axial and effective stress variations through the vessel wall without influence of the crack are depicted for times t = 5 and 10 min into the transient. Differences in the computed results are present at t = 10 min near the inner surface of the vessel, where analyses A_1 and A_16 exhibit effects of plasticity that are not captured in the linear elastic models of the other analyses. Comparisons of axial and effective stresses computed along the ligament in front of the crack at the deepest point at t = 10 min show good agreement in Figs. 3.43 and 3.44, respectively.

EFG 96-6585

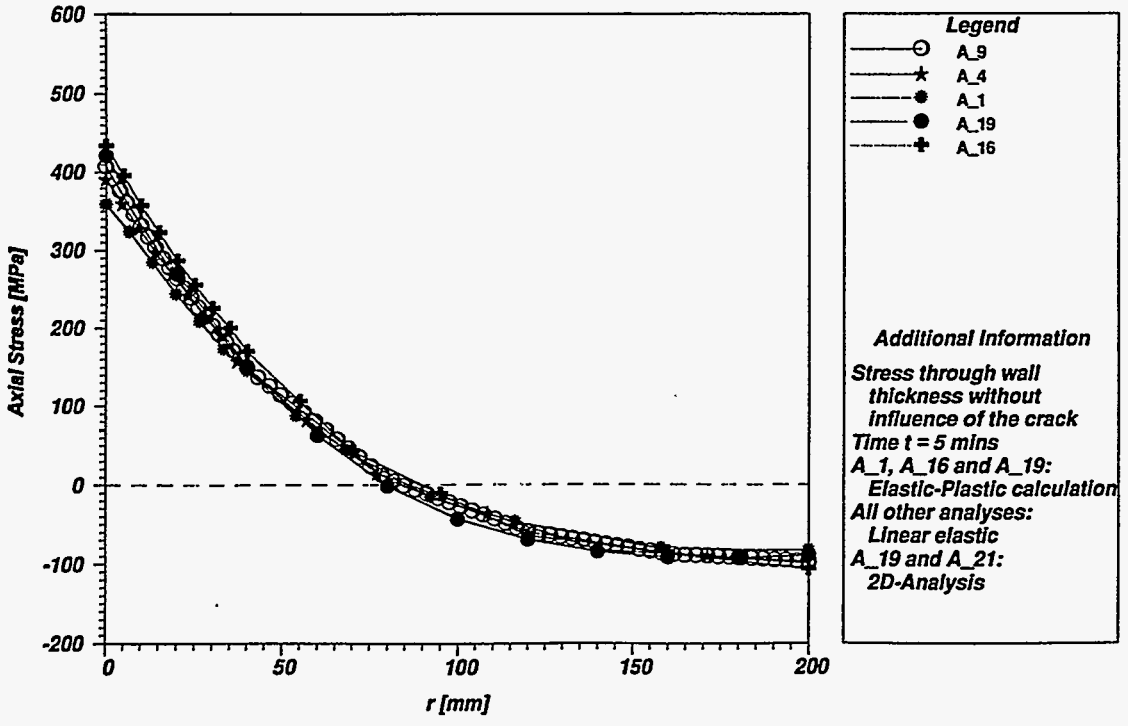

Figure 3.39 Axial stress vs wall thickness without influence of crack at t = 5 min (NKS-5 experiment)

EFG 96-6586

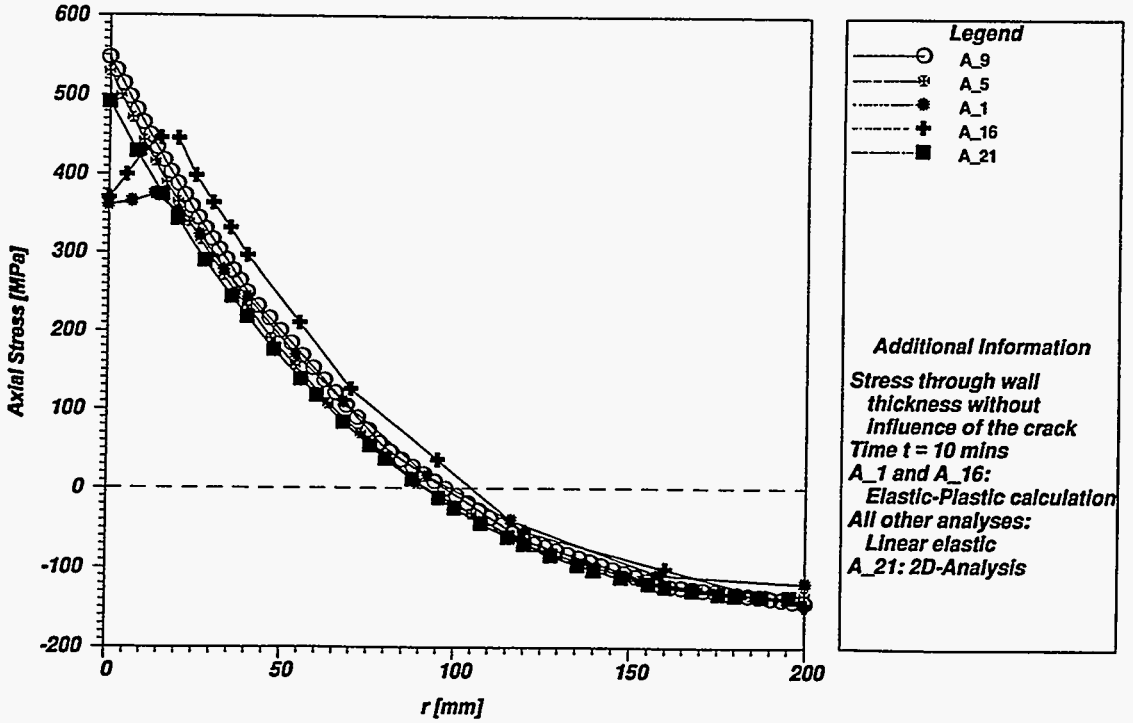

Figure 3.40 Axial stress vs wall thickness without influence of crack at t = 10 min (NKS-5 experiment)

EFG 96-6587

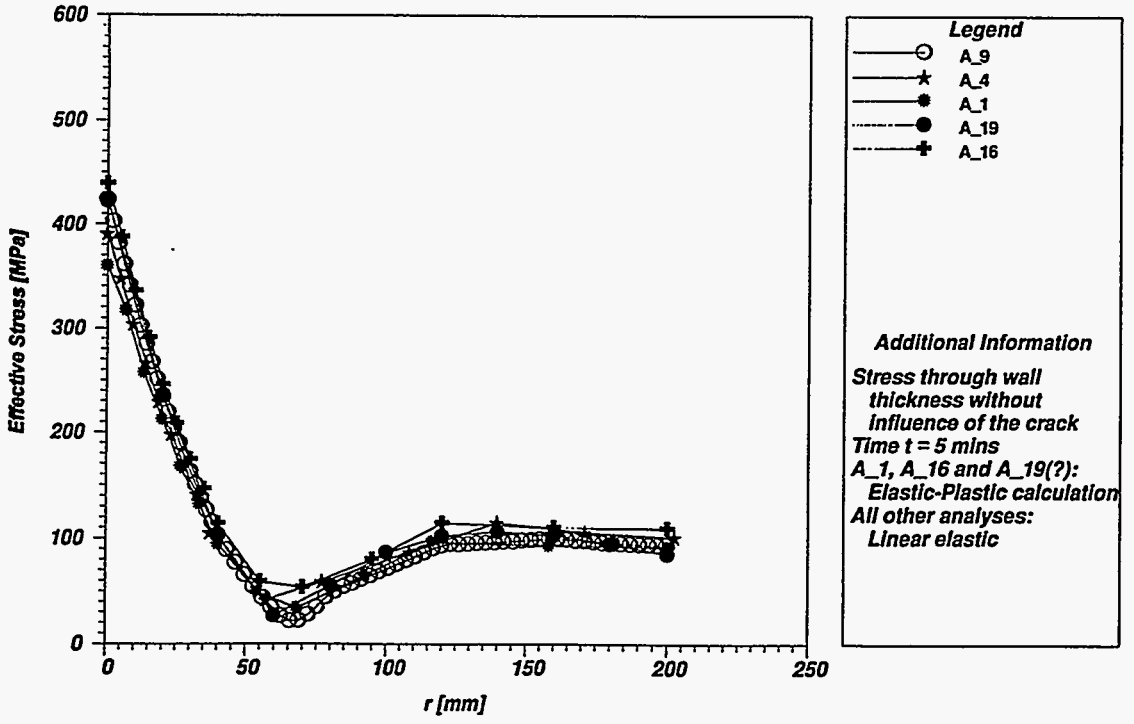

Figure 3.41 Effective stress vs wall thickness without influence of crack at t = 5 min (NKS-5 experiment)

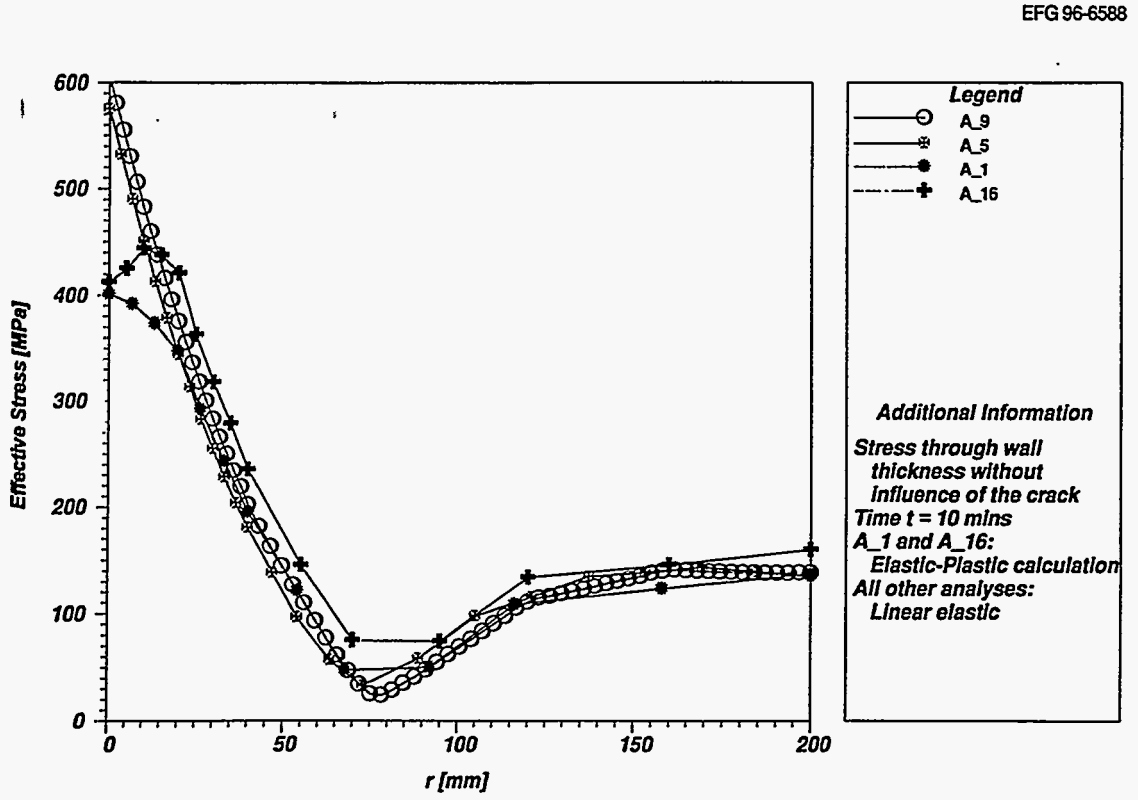

Figure 3.42 Effective stress vs wall thickness without influence of crack at t = 10 min (NKS-5 experiment)

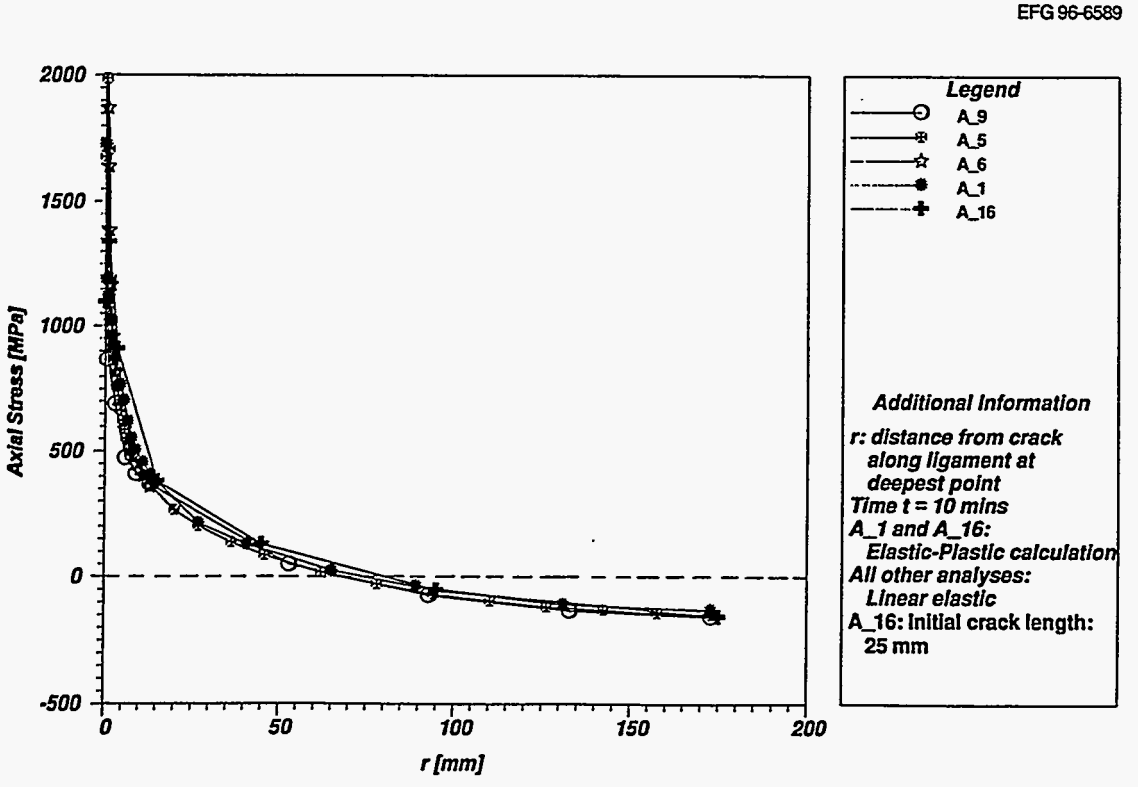

Figure 3.43 Axial stress vs distance from crack along ligament at deepest point at t = 10 min (NKS-5 experiment)

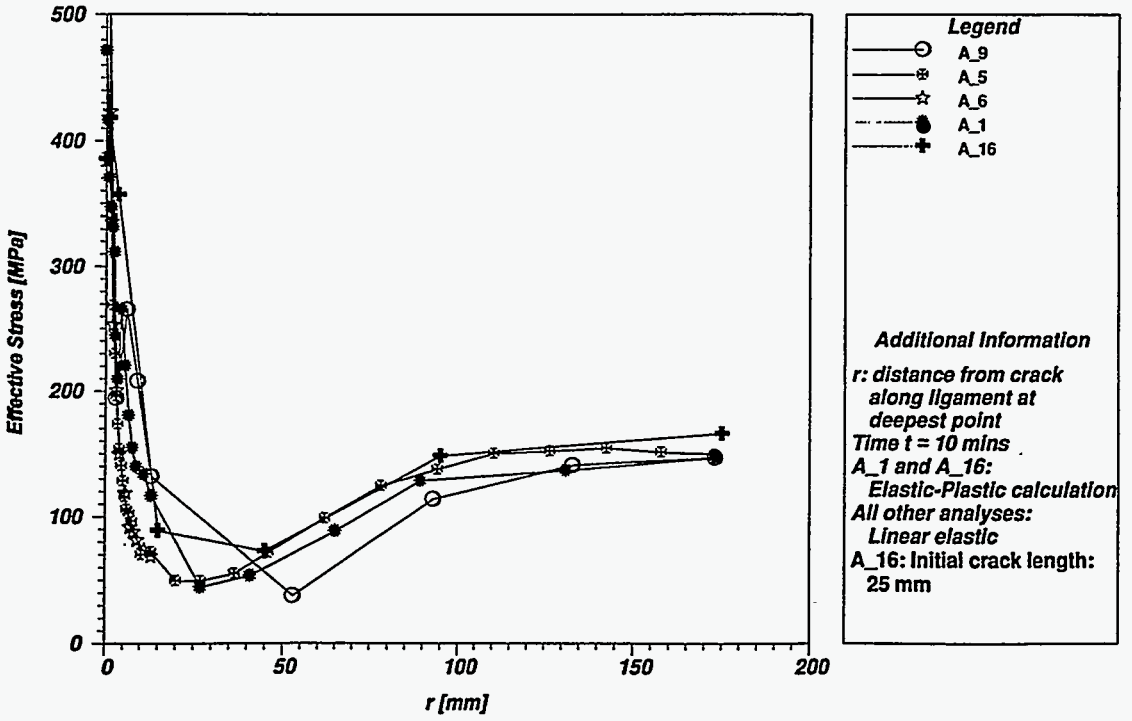

Figure 3.44 Effective stress vs distance from crack along ligament at deepest point at t = 10 min (NKS-5 experiment)

Time histories of the J-integral computed at the surface and at the deepest point of the crack are compared in Figs. 3.45 and 3.46, respectively. In Fig. 3.45, differences between elastic-plastic (A_1 and A_16) and linearly elastic (A_4, A_5, and A_6) analyses are pronounced because of significant plasticity effects that are present at the inner surface of the vessel. These differences are not present at the deepest point of the crack (Fig. 3.46), where plasticity effects are not significant. In Fig. 3.46, the results obtained from the estimation scheme analysis A_21-2 deviate substantially from the rest of the group partly because of an assumed crack depth of 40 mm. The variations of J-integral with crack front angle at t = 5 and 10 min are given in Figs. 3.47 and 3.48. Again, differences in the analysis results are most pronounced near the inner surface at t = 10 min (Fig. 3.48) due to effects of plasticity.

A lower-bound fracture toughness (K_{Jc}) curve generated from small specimen data is compared with K_I vs temperature results computed at the inner surface and at the deepest point of the crack in Figs. 3.49 and 3.50, respectively. Also included in these figures are the ASME K_{Ic} and K_{Ia} fracture toughness curves referenced to a temperature T = 122°C. A fracture assessment based on these plots predicts crack initiation at the deepest point of the crack ~6 min into the transient (see Fig. 3.50). Constraint effects appear to be responsible for delayed initiation near the inner surface up to 10 min into the transient (see Fig. 3.49). The stress triaxiality parameter h on the ligament of the crack at the inner surface (see Fig. 3.51) tends to a plane stress condition, reflecting the anticipated near-surface loss-of-constraint effect. In contrast, the stress triaxiality on the ligament at the deepest point (see Fig. 3.52) implies a more highly constrained condition on the ligament at that point. The constraint parameter Q was not evaluated by the participating analysts.

EFG 96-6591

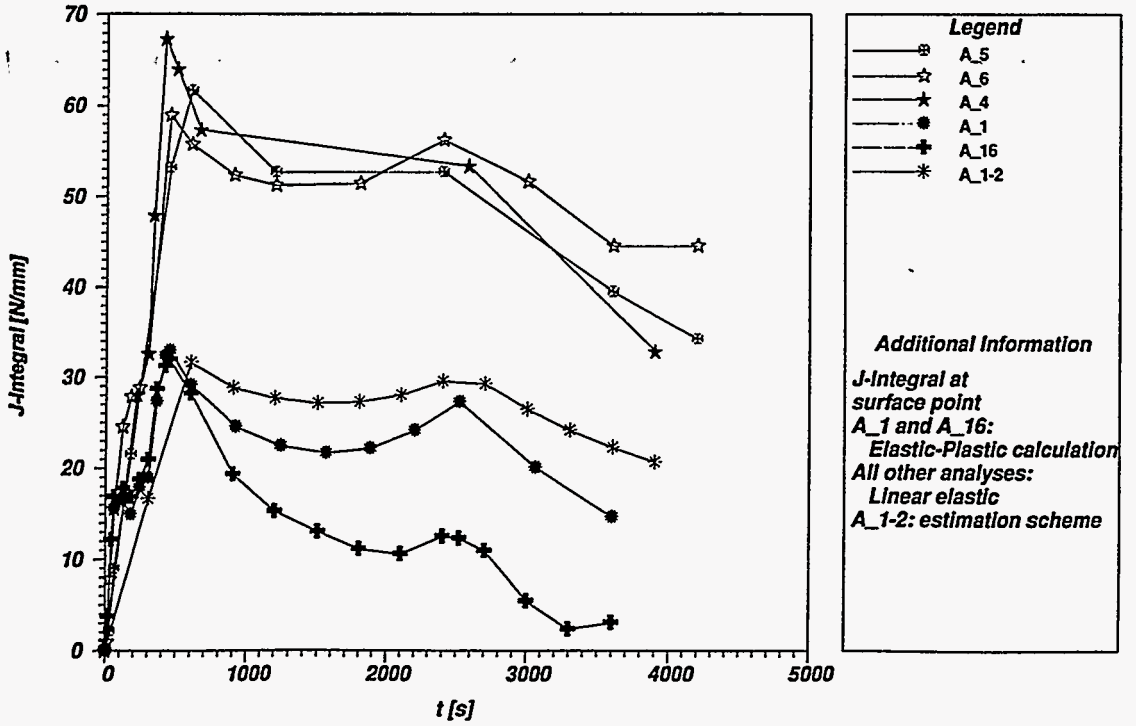

Figure 3.45 J-integral vs time at surface point of crack in NKS-5 experiment

EFG 96-6592

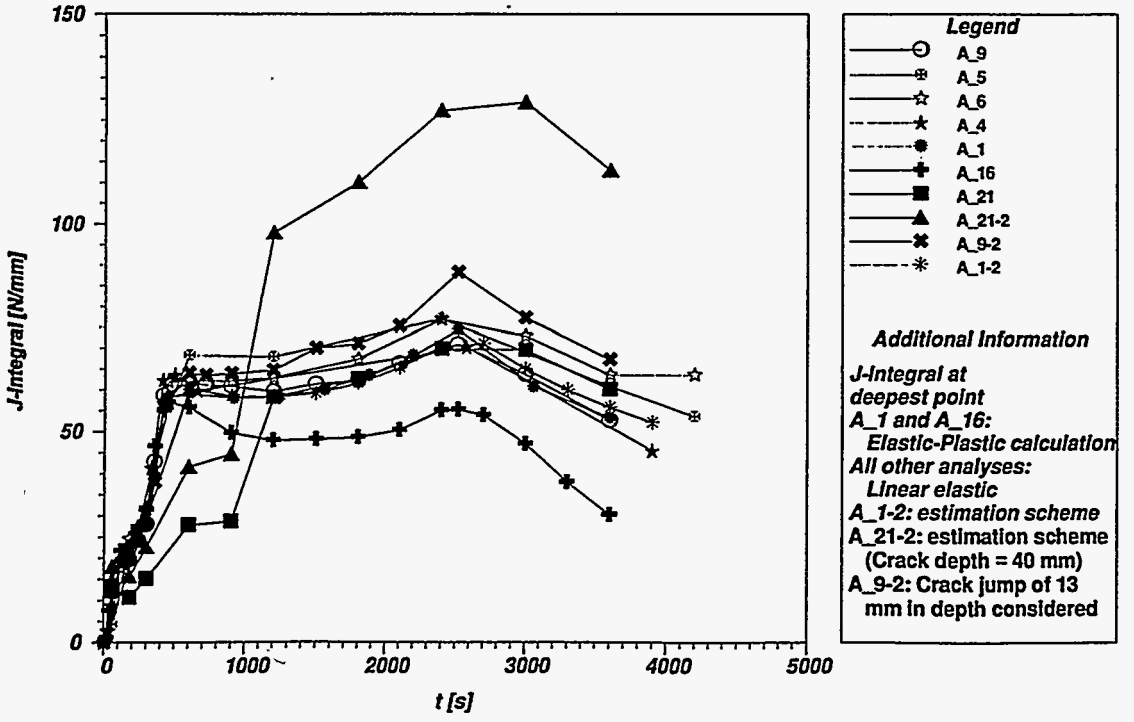

Figure 3.46 J-integral vs time at deepest point of crack in NKS-5 experiment

EFG 96-6593

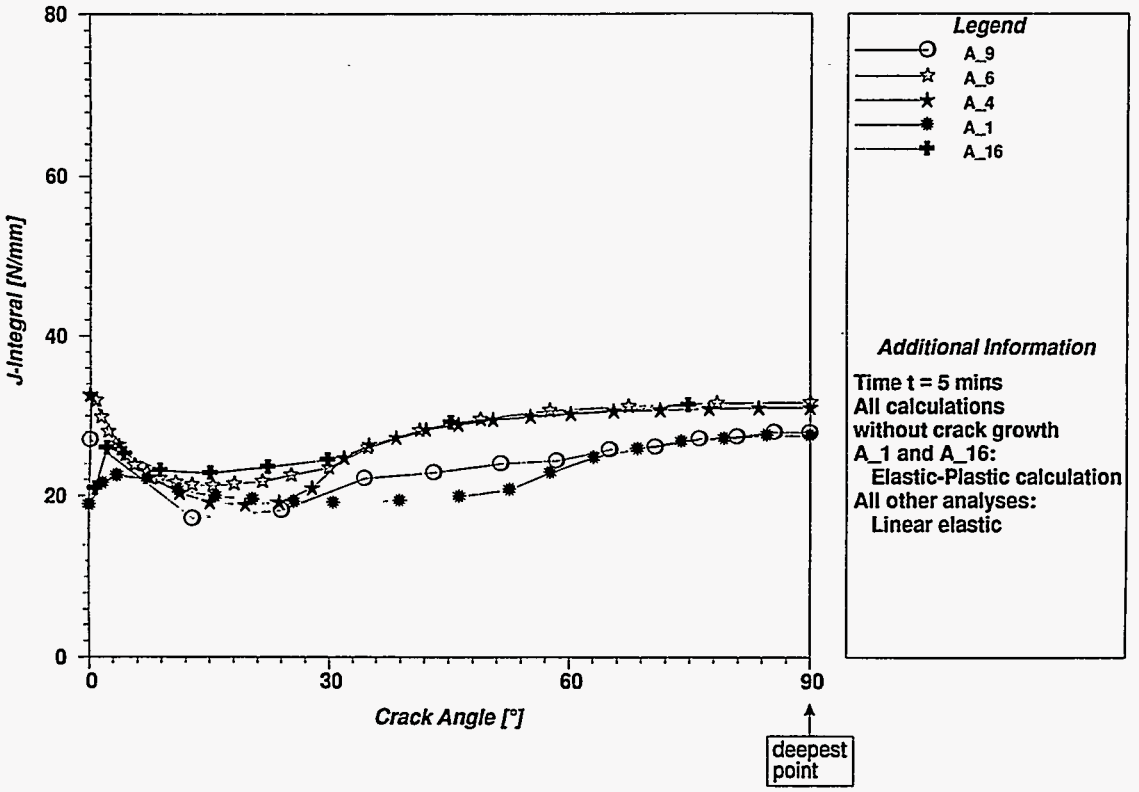

Figure 3.47 J-integral vs crack front angle for crack at t = 5 min (NKS-5 experiment)

EFG 96-6694

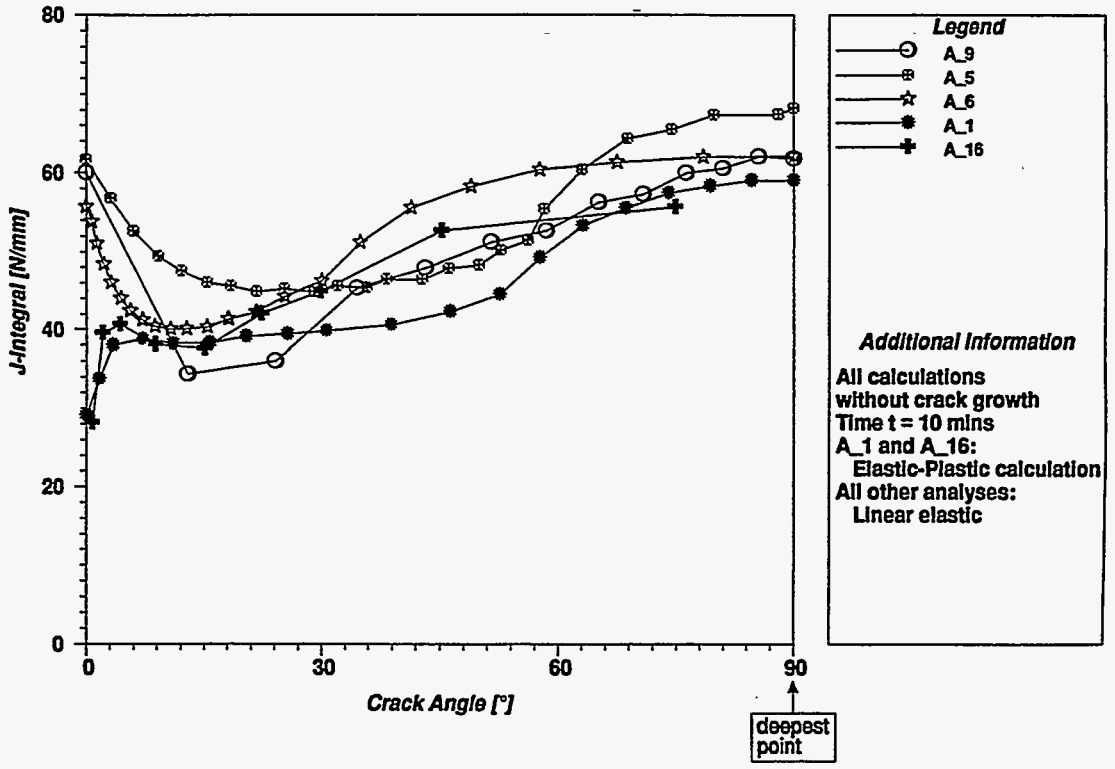

Figure 3.48 J-integral vs crack front angle for crack at t = 10 min (NKS-5 experiment)

EFG 96-6595

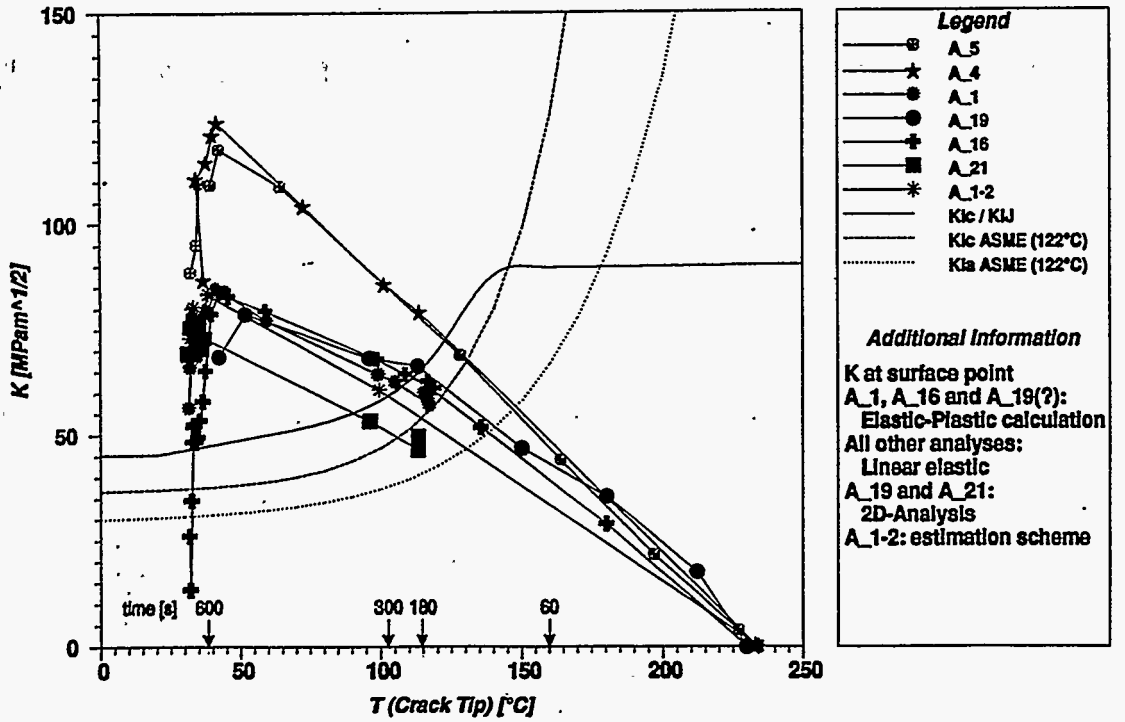

Figure 3.49 Comparison of applied K vs temperature at surface point of crack front with fracture toughness curves from CT specimens and from ASME Code (NKS-5 experiment)

EFG 96-6596

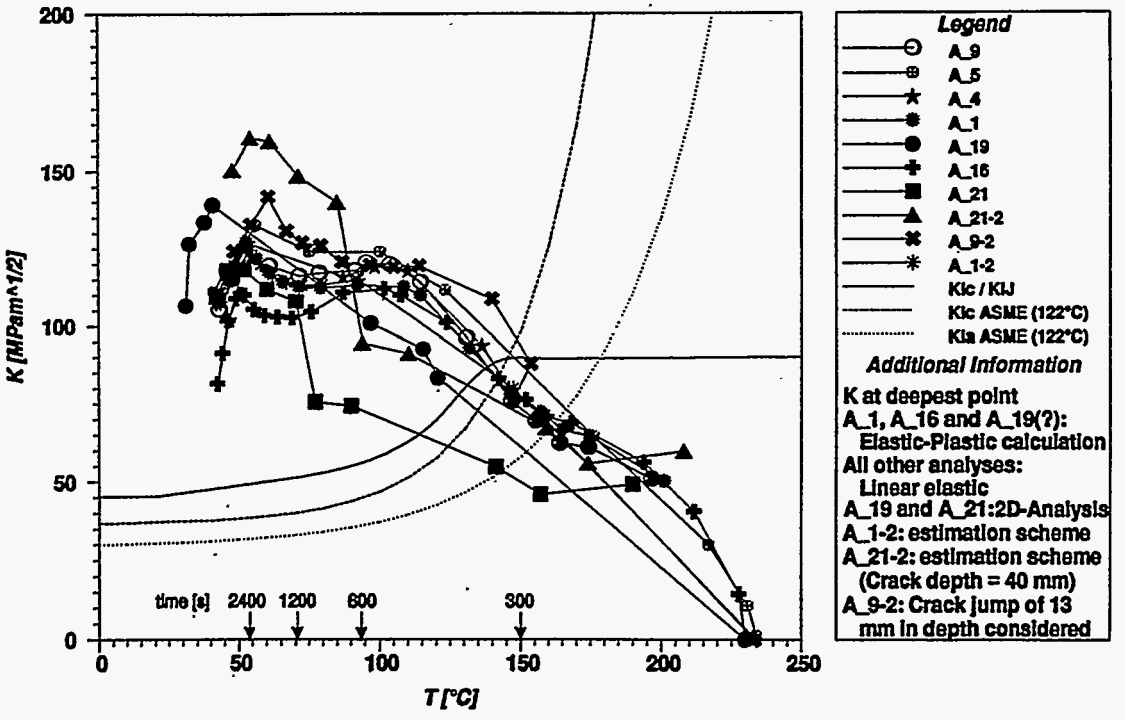

Figure 3.50 Comparison of applied K vs temperature at deepest point of crack front with fracture toughness curves from CT specimens and from ASME Code (NKS-5 experiment)

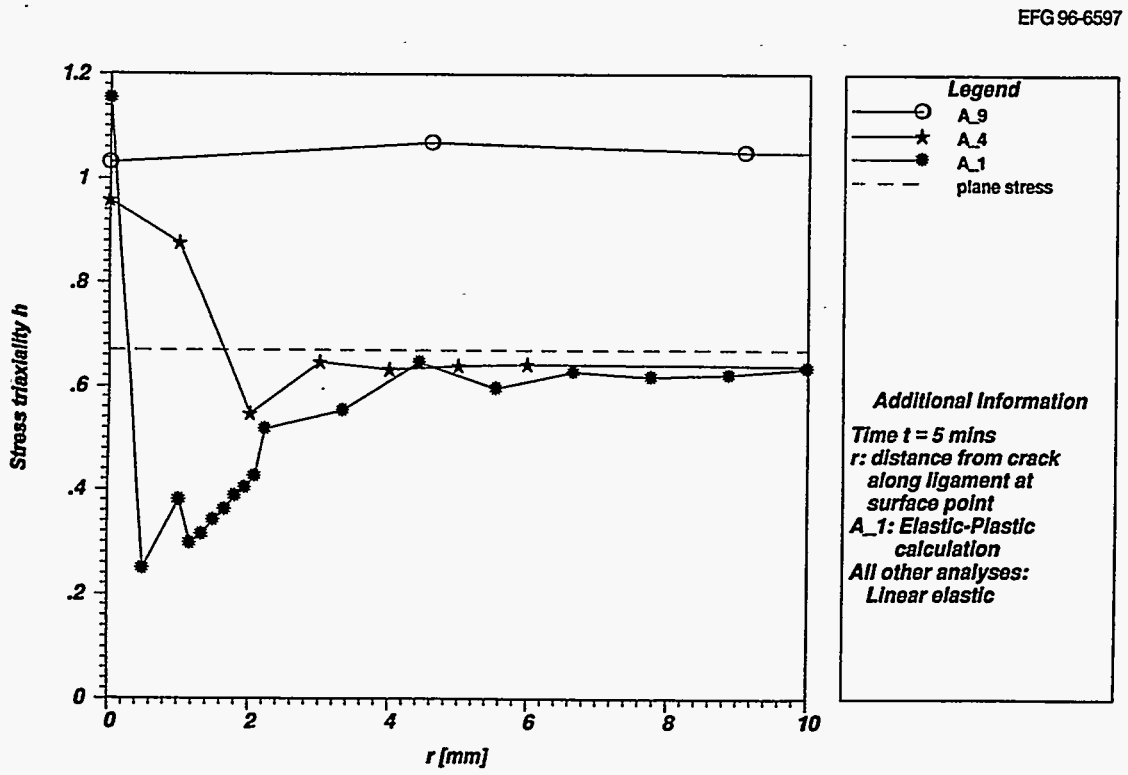

Figure 3.51 Triaxiality parameter h vs distance from crack along ligament at surface point at t = 5 min (NKS-5 experiment)

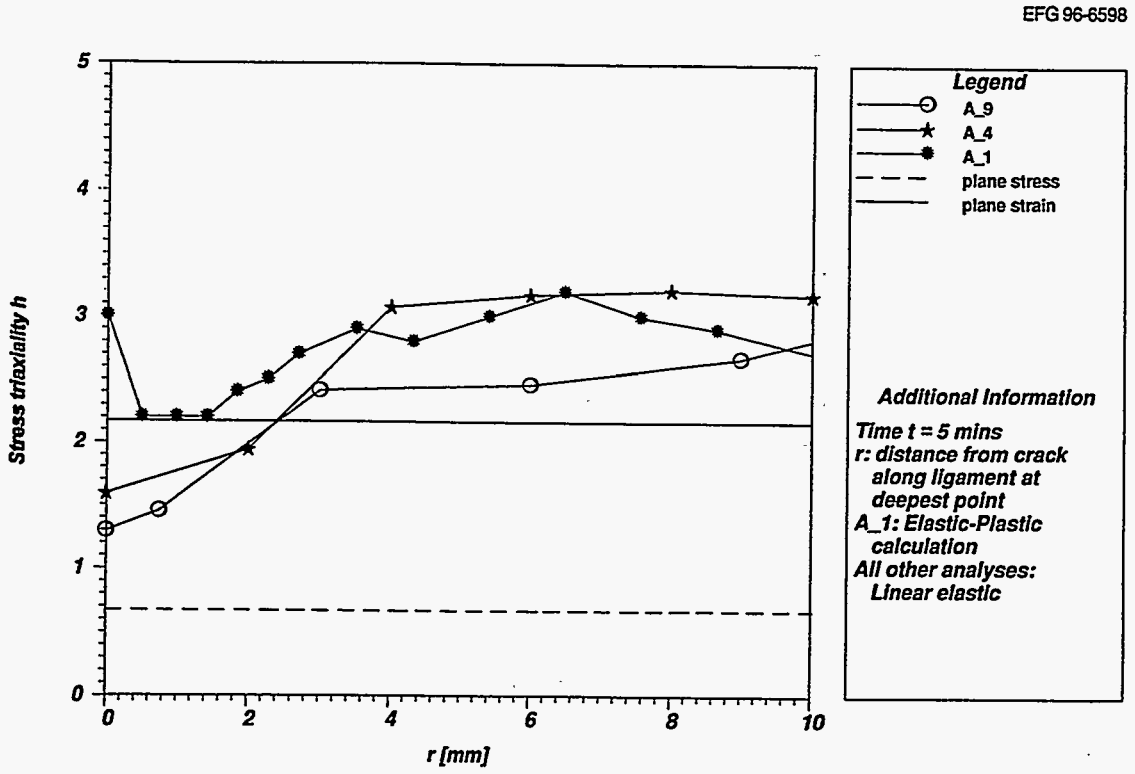

Figure 3.52 Triaxiality parameter h vs distance from crack along ligament at deepest point at t = 5 min (NKS-5 experiment)

3.4 Pressurized-Thermal-Shock Test NKS-6

Summaries of the NKS-6 analyses are given in Table 3.8 (thermal analyses) and in Table 3.9 (structural and fracture analyses). Calculated temperatures at time t = 0.5 and 2 min into the thermal transient, given in Figs. 3.53 and 3.54, respectively, show little variation. In Fig. 3.54, computed temperatures also agreed very well with measured data recorded in the test at t = 2 min.

Time histories of the measured and computed circumferential and axial strains (without the thermal part $\alpha \Delta T$) on the inner surface at a location 184 mm above the crack ligament (i.e., at gages DL3/DU3 in Fig. 2.46) are compared in Figs. 3.55 and 3.56, respectively. Analyses A_4 and A_9 made use of the crack extension data previously discussed in Table 2.25.

Measured data representing CMOD vs time during the thermal-shock transient at two gages positioned on the fully circumferential flaw are depicted in Fig. 3.57. The data imply a cleavage initiation event occurring ~30 s into the transient, when the crack jumped from 37 to 54 mm in wall depth. For NKS-6, the scatter in measured CMOD values at different gage locations is much smaller than that observed in the NKS-5 experiment. With one exception (analysis A_12), the calculated time histories of CMOD shown in Fig. 3.57 are generally in good agreement with the measured data.

Computed axial and effective stress variations through the vessel wall without influence of the crack are depicted for times t = 0.5 and 2 min in Figs. 3.58–3.61, respectively. Results for A_10-3 were obtained from a linearly elastic analysis of a one-dimensional structural model (Table 3.9). Thus, differences between A_10-3 and the other elasto-plastic analyses are present near the inner surface of the vessel, where effects of plasticity are active. The effective stresses computed from the elasto-plastic analyses are in reasonably good agreement for the two transient times represented by Figs. 3.60 and 3.61. Comparisons of axial and effective stresses computed along the ligament in front of the crack at t = 0.5 and 2 min are given in Figs. 3.62–3.65, respectively. Generally, the results show good agreement with the exception of analysis A_12, in which the crack growth was underestimated due to the use of an extrapolated J-R resistance curve.

Time histories of the J-integral computed for the transient are compared in Fig. 3.66. The K_I vs temperature results computed for the crack are given in Figs. 3.67 and 3.68,

EFG 96-6599

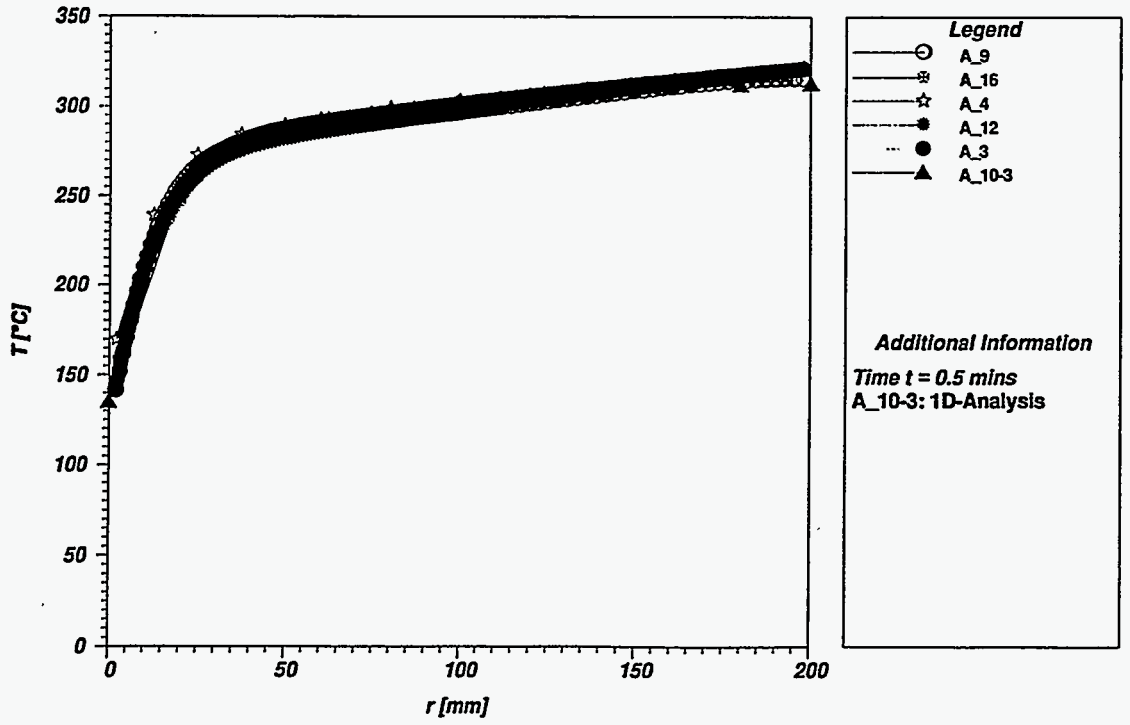

Figure 3.53 Temperatures vs wall thickness at t = 0.5 min (NKS-6 experiment)

EFG 96-6600

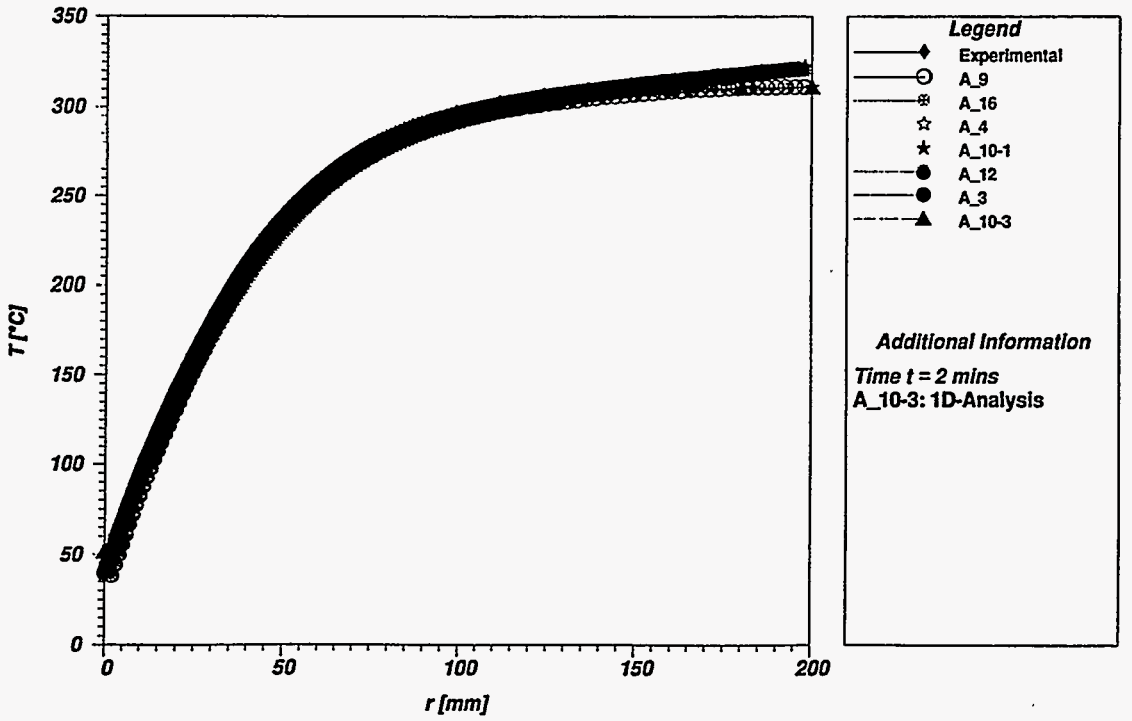

Figure 3.54 Temperatures vs wall thickness at t = 2 min (NKS-6 experiment)

EFG 96-6601

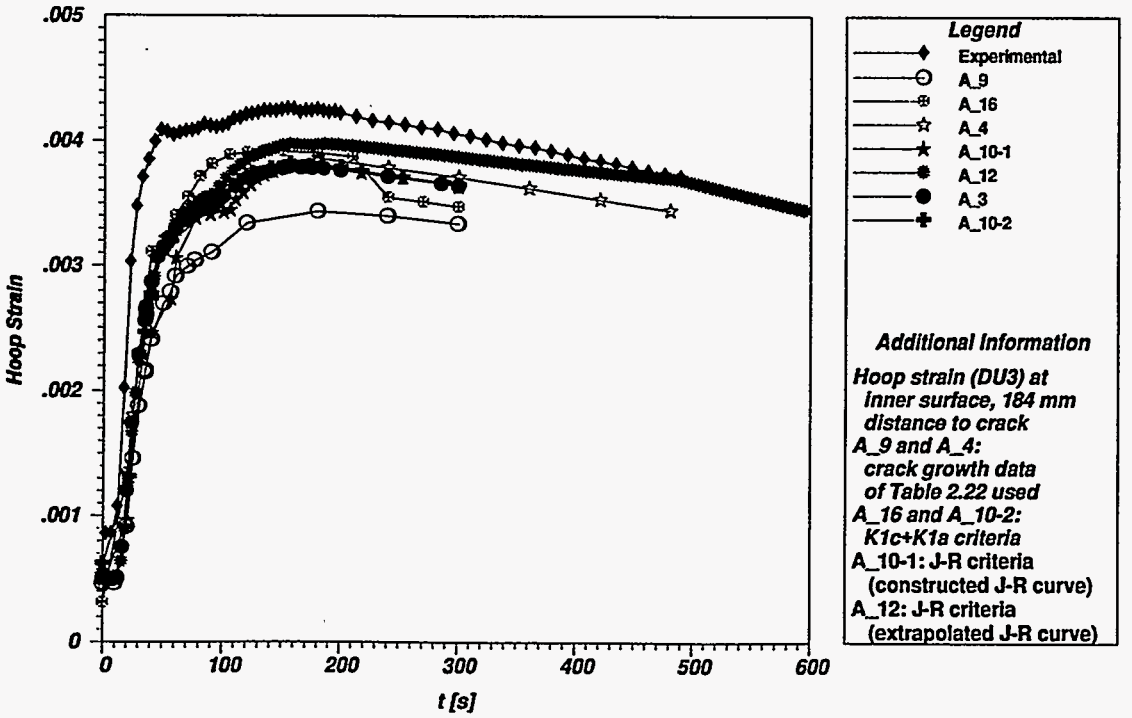

Figure 3.55 Circumferential strain vs time on inner surface of cylinder (gage DU3) in NKS-6 experiment

EFG 96-6602

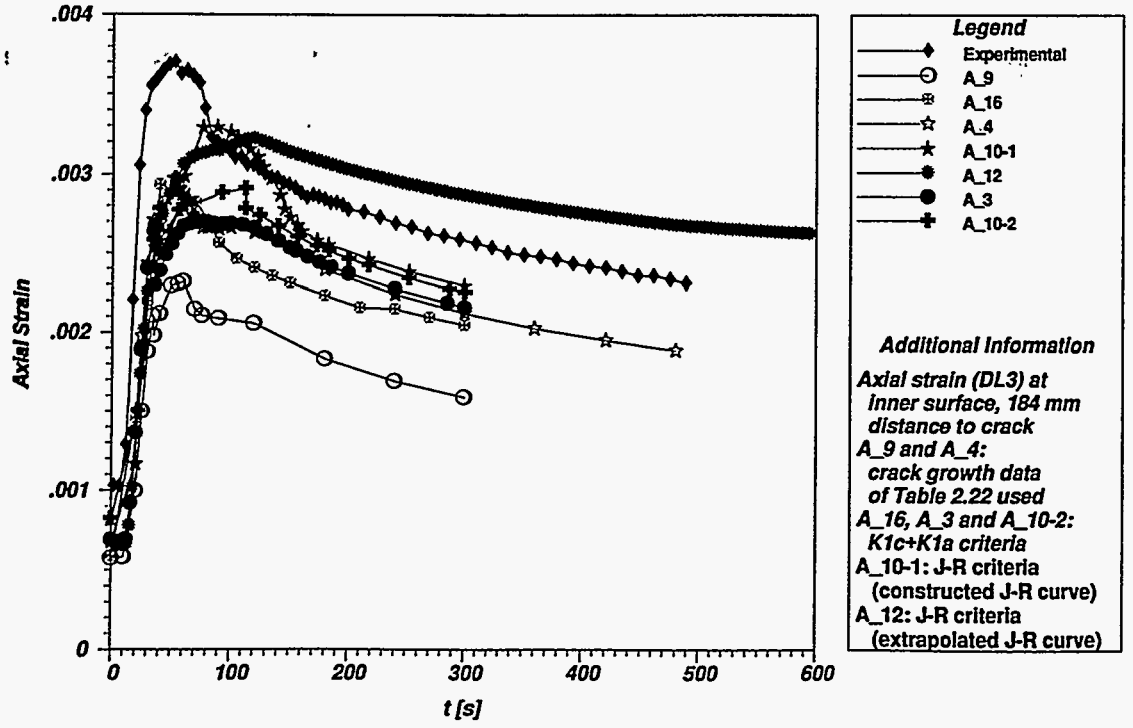

Figure 3.56 Axial strain vs time on inner surface of cylinder (gage DL3) in NKS-6 experiment

EFG 96-6603

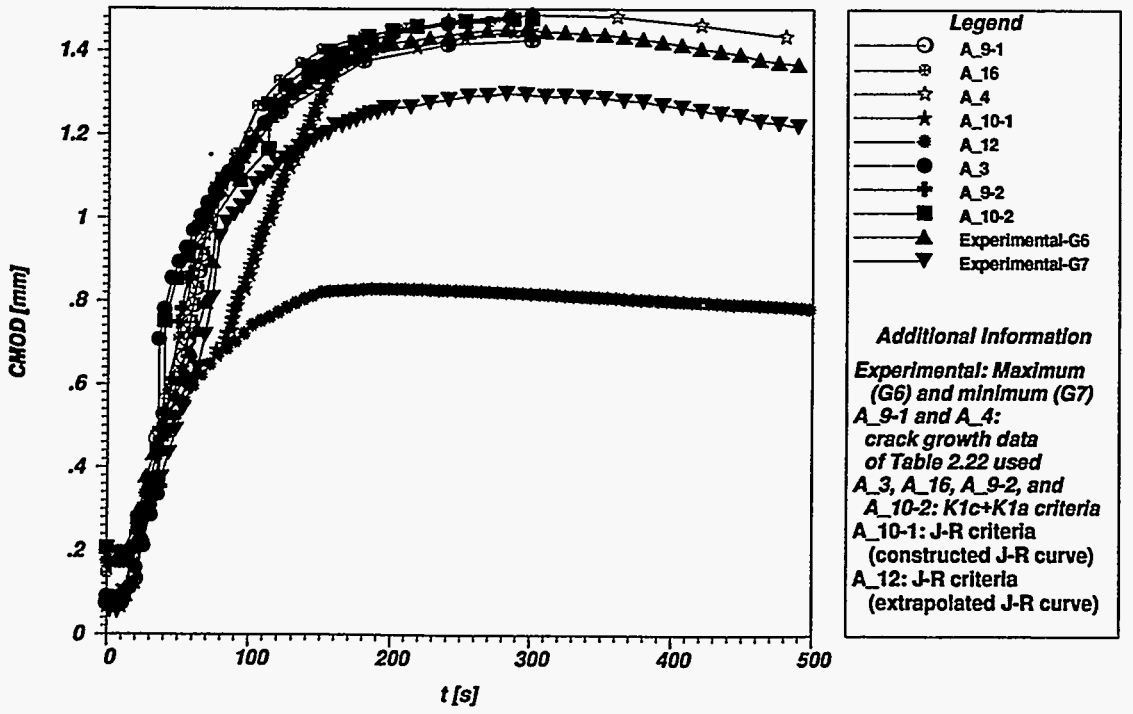

Figure 3.57 CMOD vs time for circumferential crack in NKS-6 experiment

EFG 96-6604

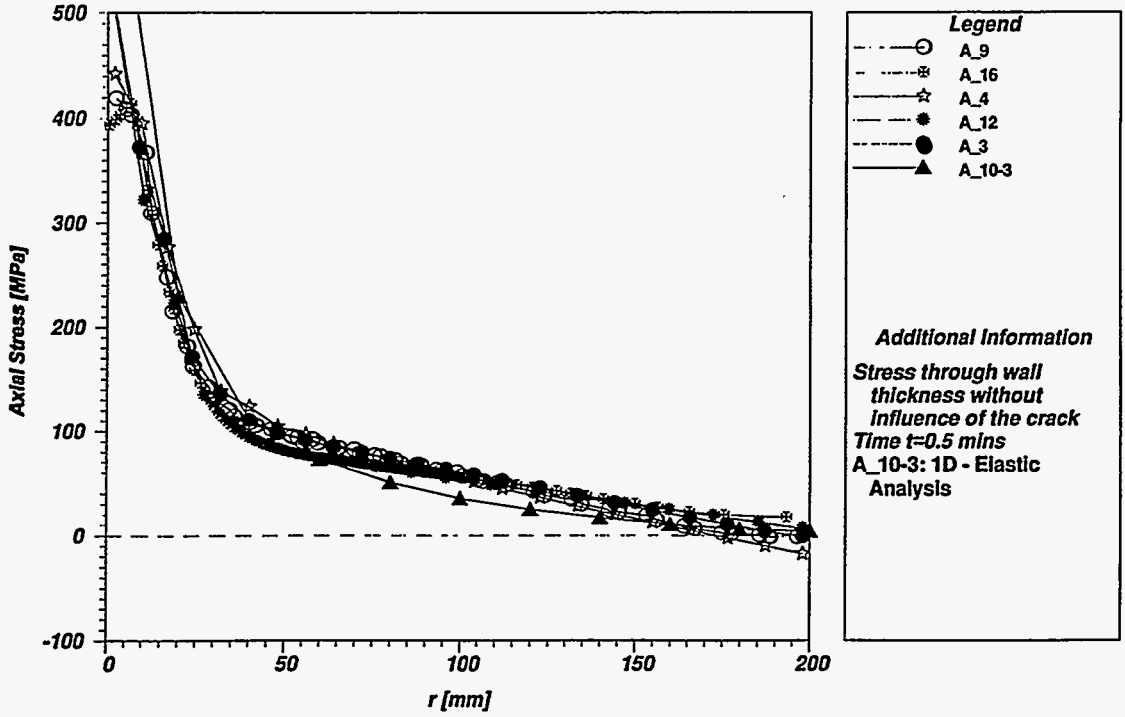

Figure 3.58 Axial stress vs wall thickness without influence of crack at t = 0.5 min (NKS-6 experiment)

EFG 96-6605

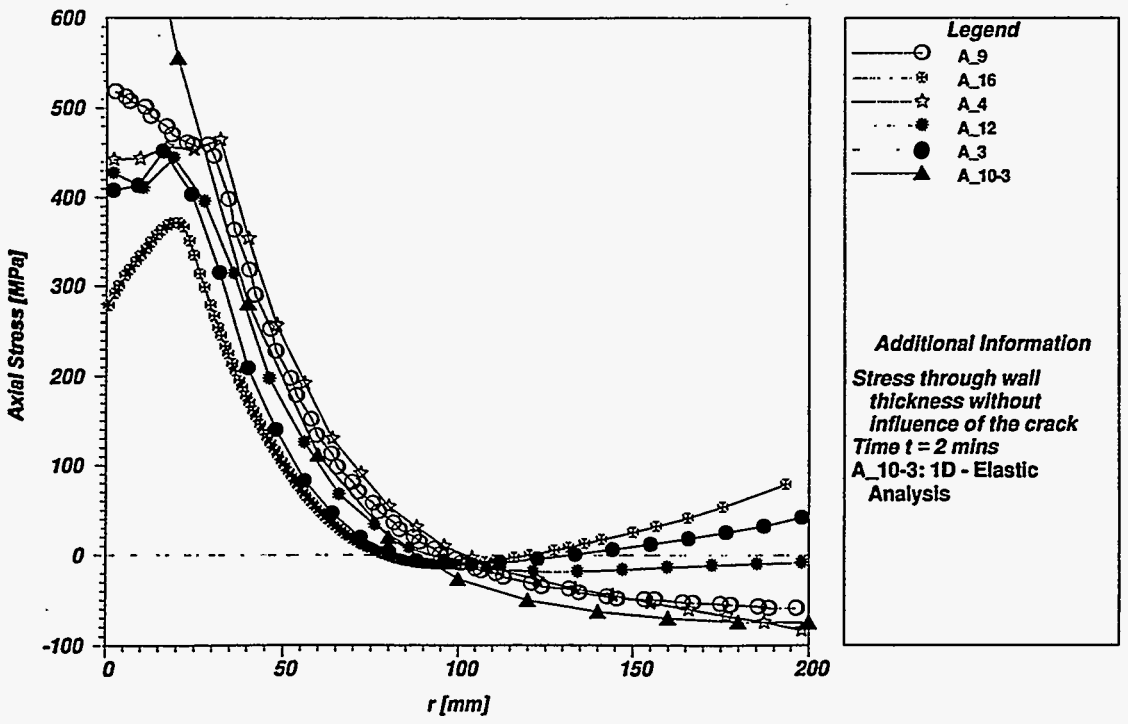

Figure 3.59 Axial stress vs wall thickness without influence of crack at t = 2 min (NKS-6 experiment)

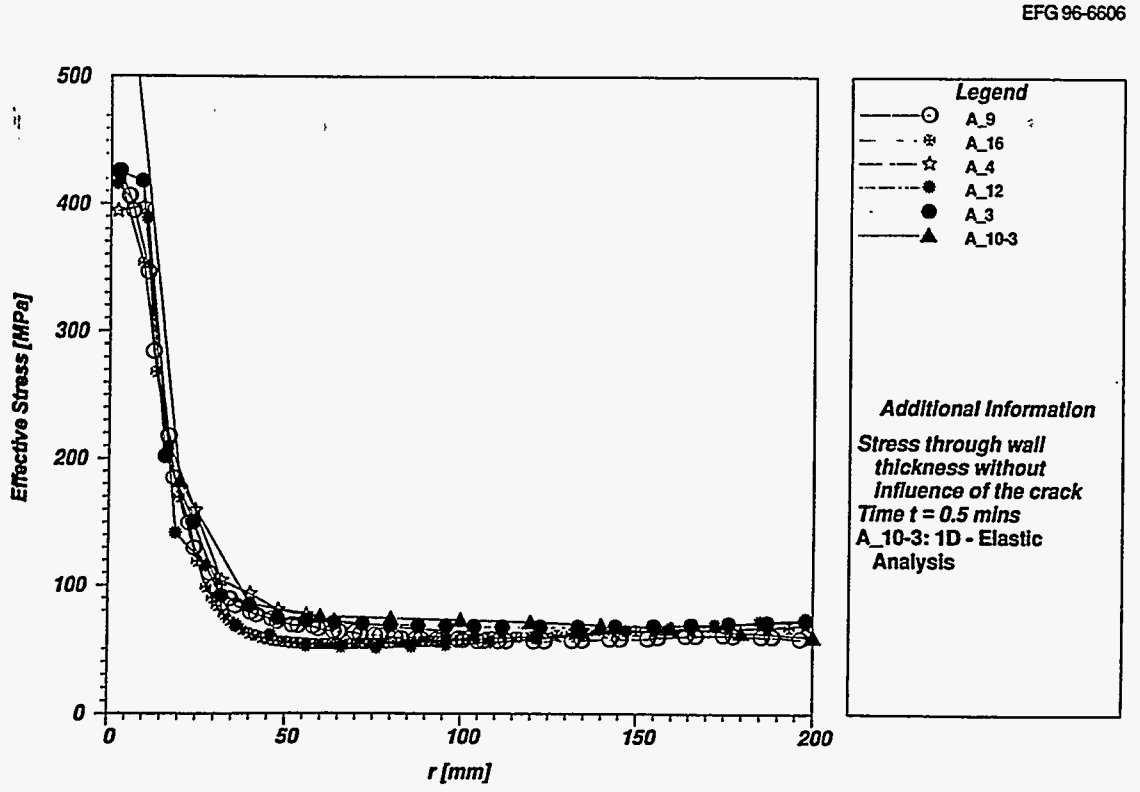

Figure 3.60 Effective stress vs wall thickness without influence of crack at t = 0.5 min (NKS-6 experiment)

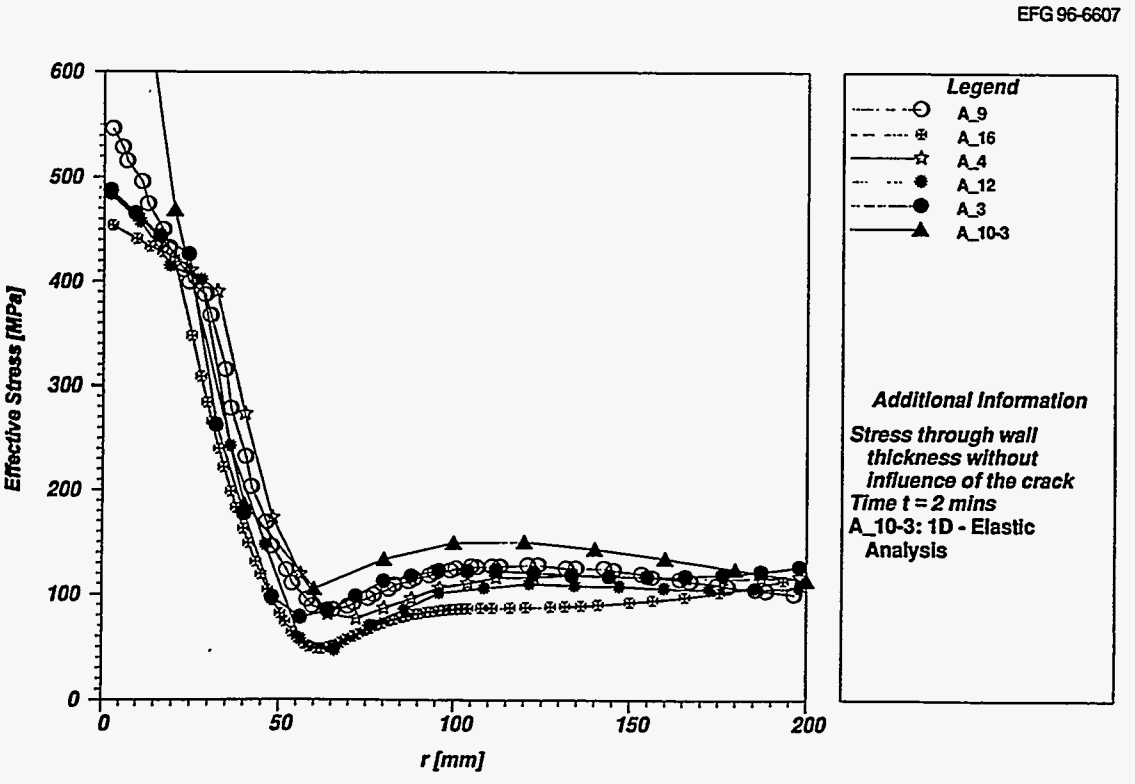

Figure 3.61 Effective stress vs wall thickness without influence of crack at t = 2 min (NKS-6 experiment)

EFG 96-6608

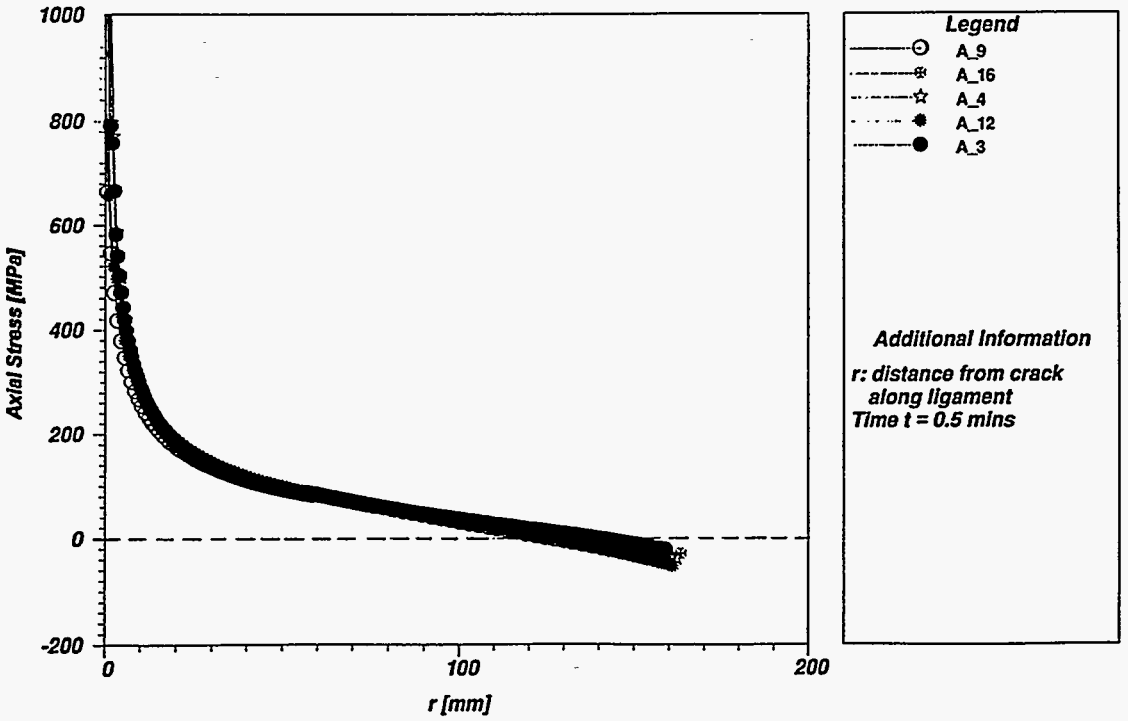

Figure 3.62 Axial stress vs distance from crack along ligament at t = 0.5 min (NKS-6 experiment)

EFG 96-6609

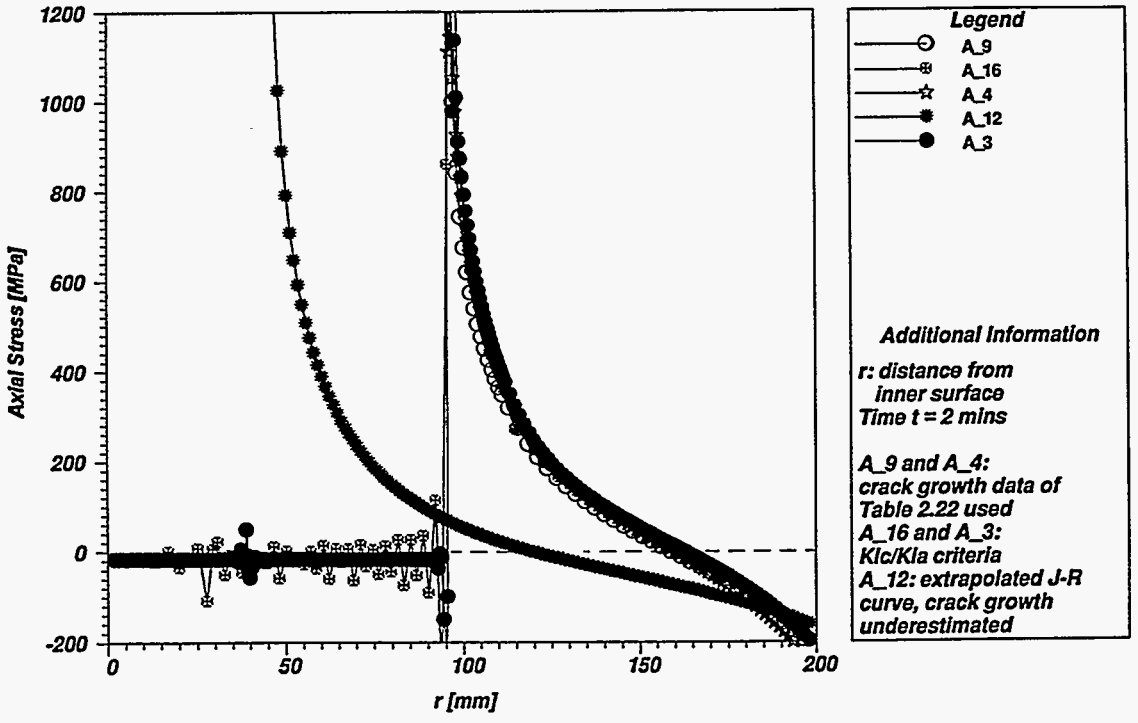

Figure 3.63 Axial stress vs distance from crack along ligament at t = 2 min (NKS-6 experiment)

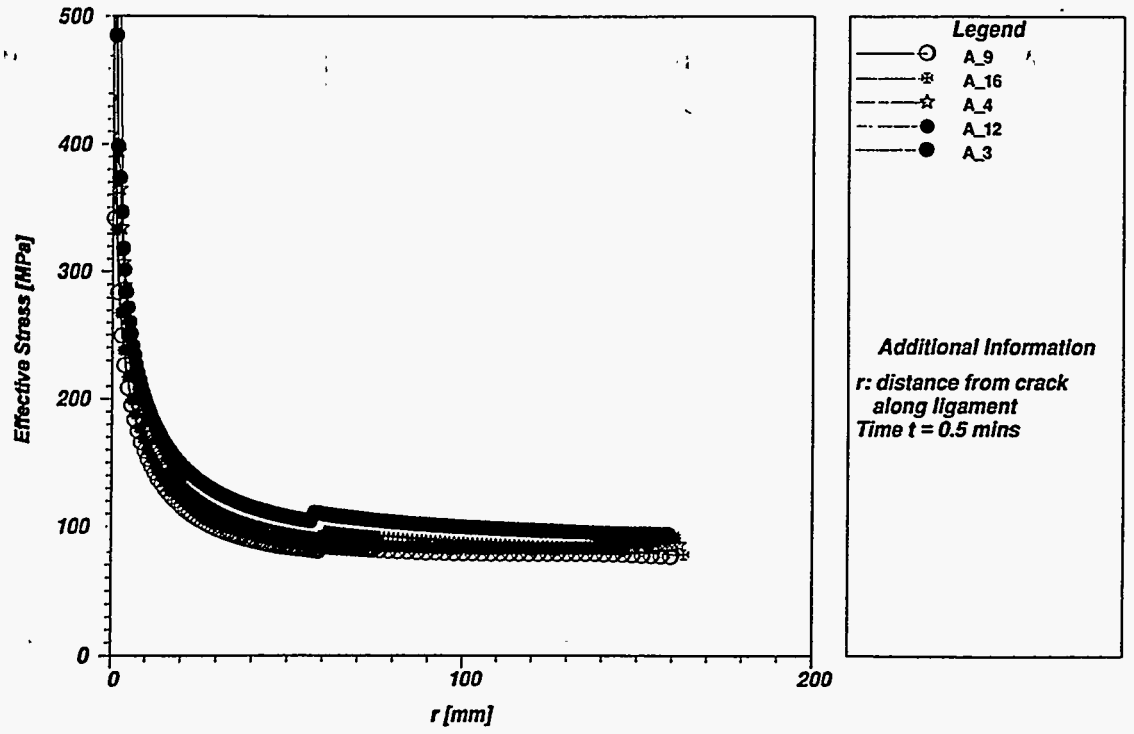

Figure 3.64 Effective stress vs distance from crack along ligament at t = 0.5 min (NKS-6 experiment)

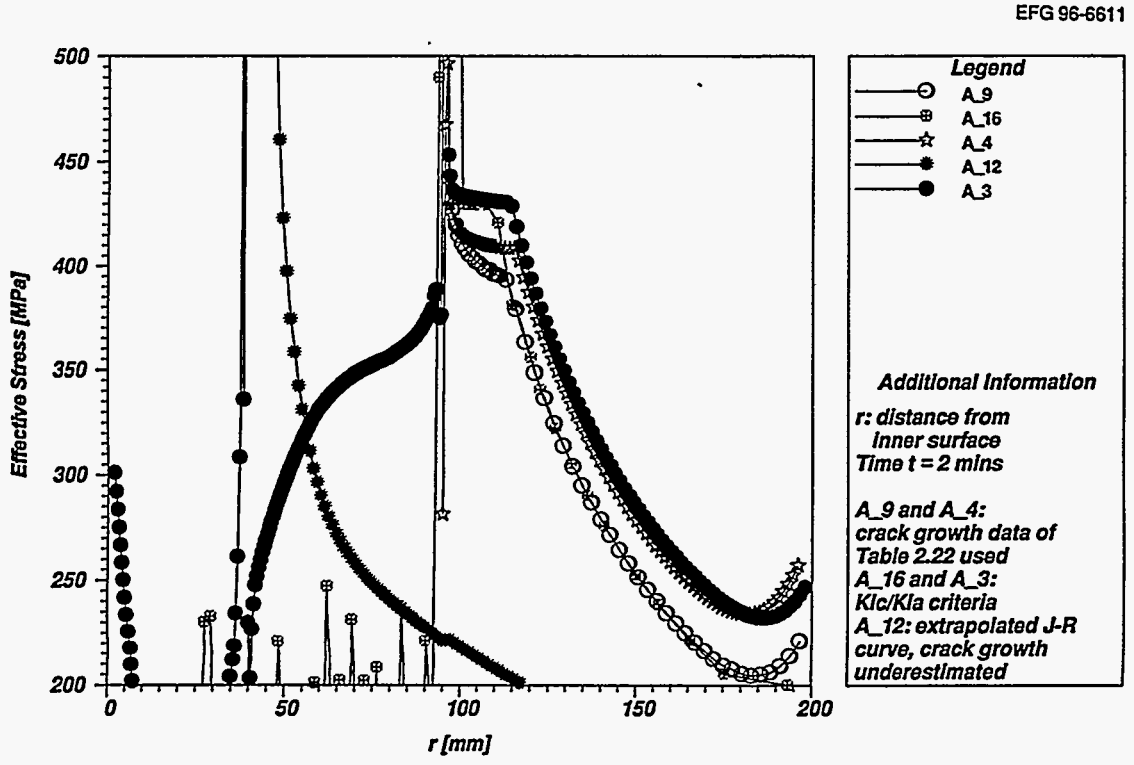

Figure 3.65 Effective stress vs distance from crack along ligament at t = 2 min (NKS-6 experiment)

EFG 96-6612

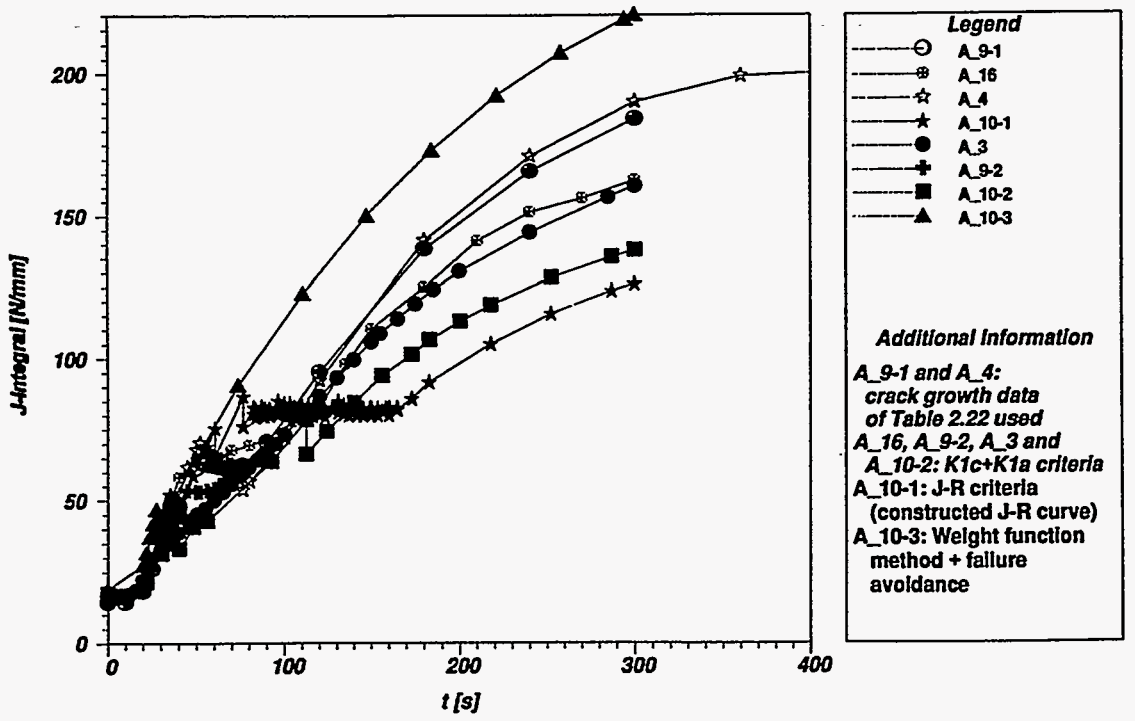

Figure 3.66 J-integral vs time for the circumferential crack in NKS-6 experiment

EFG 96-6613

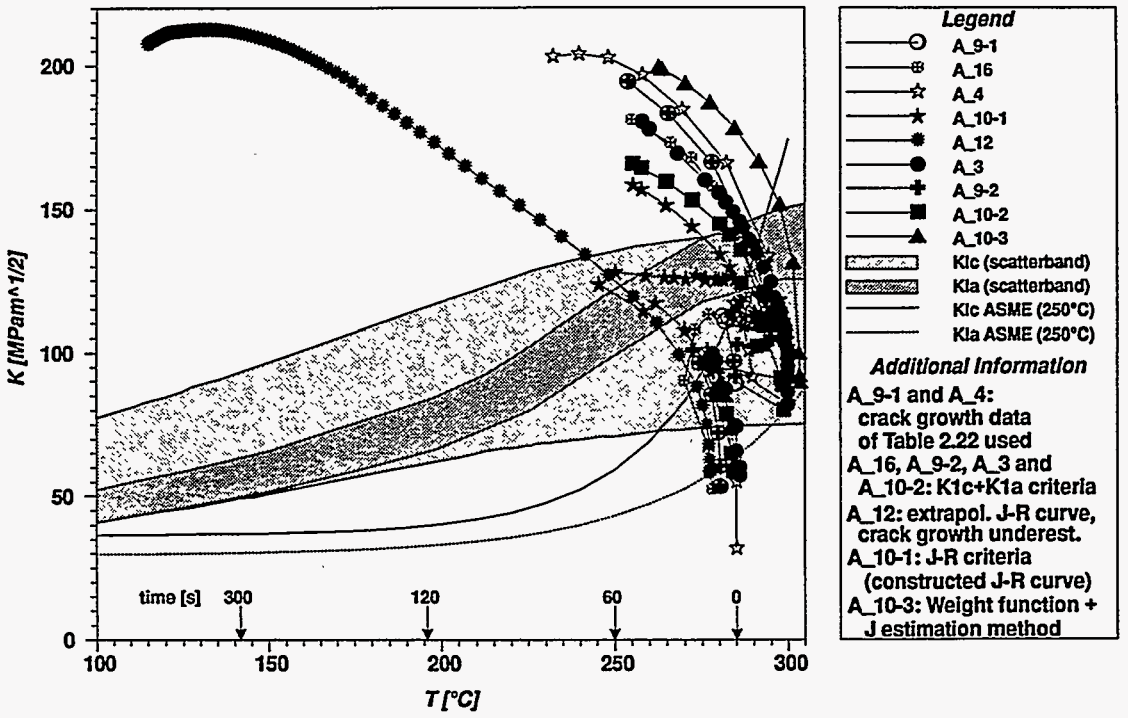

Figure 3.67 Comparison of applied K vs temperature for circumferential crack with fracture toughness curves from CT specimens and from ASME Code (NKS-6 experiment)

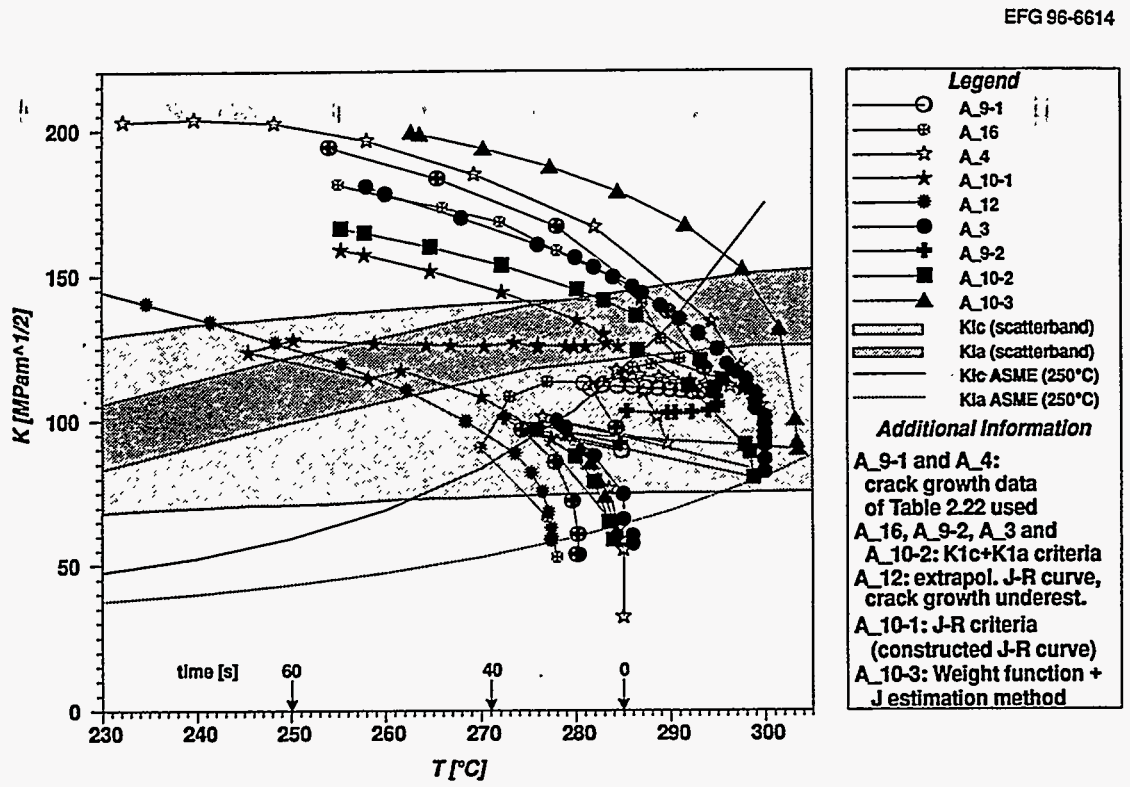

Figure 3.68 Comparison of applied K vs temperature (with expanded temperature scale) for circumferential crack with fracture toughness curves from CT specimens and from ASME Code (NKS-6 experiment)

along with relevant fracture toughness curves. Included are the scatter bands for K_{Ic} and K_{Ia} toughness data generated from small specimens, as well as the ASME K_{Ic} and K_{Ia} toughness curves for which FATT 50 = 250°C is taken as the reference temperature. Discrete times in the transient where the crack tip experienced selected temperatures are also identified in Fig. 3.67. These K_I vs temperature curves are plotted in Fig. 3.68 using an expanded temperature scale that extends from 230°C to 305°C. In Figs. 3.67 and 3.68, results obtained from the analysis A_12 (based on an extrapolated J-R curve) deviate from the rest of the group, which used cleavage criteria to simulate crack extension.

The calculated values of J-integral and K_I, as well as CMOD and axial strain, were strongly dependent on specific assumptions concerning crack growth approximation, particularly how the final crack depth was reached. To model crack growth, some analysts used the crack depth vs time sequence (i.e., Table 2.22) constructed by MPA from a best estimate approximation of measured CMOD data.

Others used fracture toughness curves obtained from the scatter band of measured data provided in the NKS-6 problem statement or from the ASME toughness curve with FATT 50 as transition temperature. The time of initiation (36 s) can be approximated well with the FATT 50–ASME curve and is somewhat underestimated by the measured lower bound curve. In Fig. 3.57, the A_12 analysis was based on a J-R criterion in which a J-R curve was extrapolated to model large amounts of crack growth. However, application of the extrapolated J-R curve did not reflect the cleavage event and, therefore, resulted in a substantial underprediction of the measured crack growth and, therefore, the CMOD time history. These results are also reflected in the leftward shift of the K_I vs temperature curve for analysis A_12 in Figs. 3.67 and 3.68.

In Fig. 3.69, evaluation of stress triaxiality factors showed almost plane strain conditions on the ligament of the 360° circumferential crack. This implies that constraint effects did not play a significant role in crack initiation.

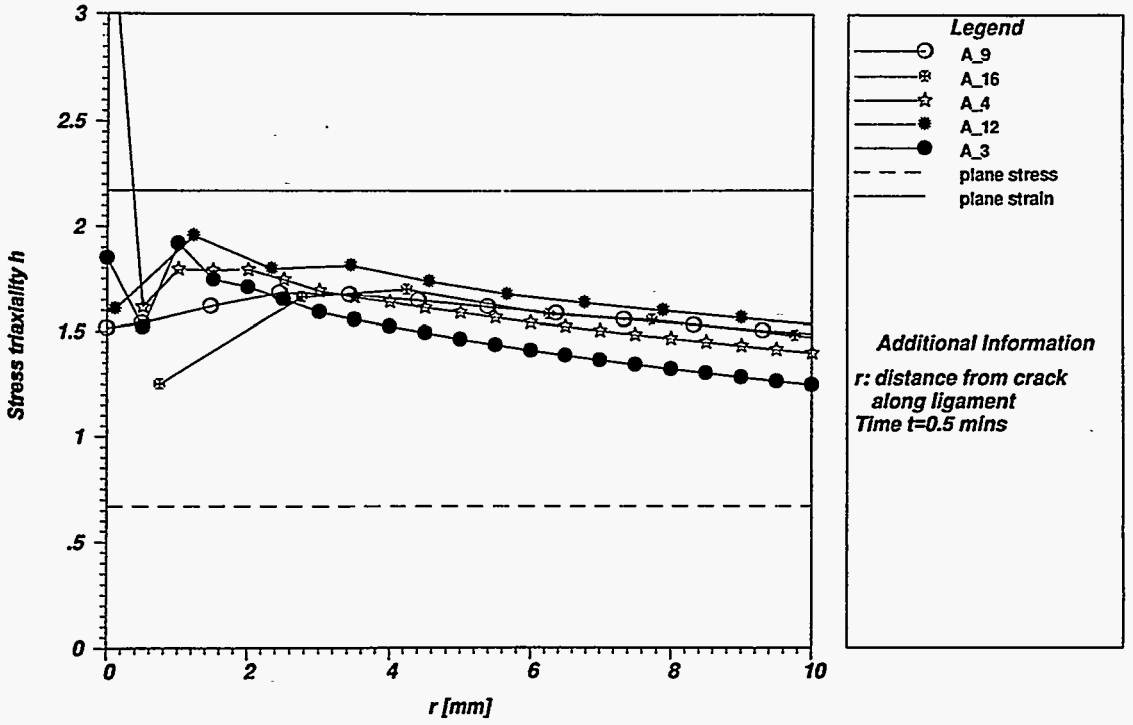

Figure 3.69 Triaxiality parameter h vs distance from crack along ligament at t = 0.5 min (NKS-6 experiment)

3.5 Clad Four-Point Bending Beam Experiment DD2

Summaries of the DD2 structural and fracture analyses are given in Table 3.10. In Fig. 3.70, computed results for load vs LLD are generally in good agreement with measured data for the experiment.[6] Computed crack-opening displacements vs distance from the cladding/base metal interface at the position of the crack symmetry plane are compared in Fig. 3.71 for an applied load of ~900 kN. Calculations of applied load vs maximum CMOD (which include a factor of 2 on CMOD due to symmetry conditions) are compared in Fig. 3.72. Both Figs. 3.71 and 3.72 show that the 2-D calculations overestimate the crack opening when compared with 3-D analyses. Analysis A_22-2 incorporated an approximation of the welding process in the clad beam model, which resulted in substantially greater computed CMOD values when compared with the other analyses.

The computed bending load vs longitudinal strains are compared with measured data at the locations of three surface strain gages (gages J3, J7, and J8 in Fig. 2.53) in Figs. 3.73–3.75, respectively. Except for one analysis (A_20), the comparisons show reasonably good agreement, which indicates that the overall structural response has been modeled appropriately. The 2-D analyses A_5 and A_13 are based on a plane strain approximation, while A_20 is based on plane stress. However, it has not been established that these modeling differences provide an explanation for the differences in the analysis results.

Crack-opening stress and effective stress vs distance along the ligament at the deepest point of the crack are compared in Figs. 3.76 and 3.77, respectively. These results were computed for an applied load of ~900 kN and, except for those from analysis A_22-2, are generally in good agreement. Plasticity in the ligament near the deepest point is negligible due to the high yield stress of the base metal (768 MPa).

The computed values of K_I vs applied load at the deepest point of the crack are shown in Fig. 3.78, along with the lower- and upper-bound small-specimen (CT25) fracture toughness curves at the test temperature (which range from ~40 to 50 MPa $\sqrt{m}$). Computed K_I values vs crack-front angle near the loading at fracture are compared in Fig. 3.79. At the fracture load, peak K_I values lie between the lower- and upper-bound small-specimen fracture toughness curves. However, test results for DD2 indicate that the crack initiated at a point in the heat-affected zone (HAZ) located 1.5 to 2 mm from the interface, which implies an initiation toughness of ~33 MPa $\sqrt{m}$. Thus, the computed toughness at the initiation site falls well below

EFG 96-6616

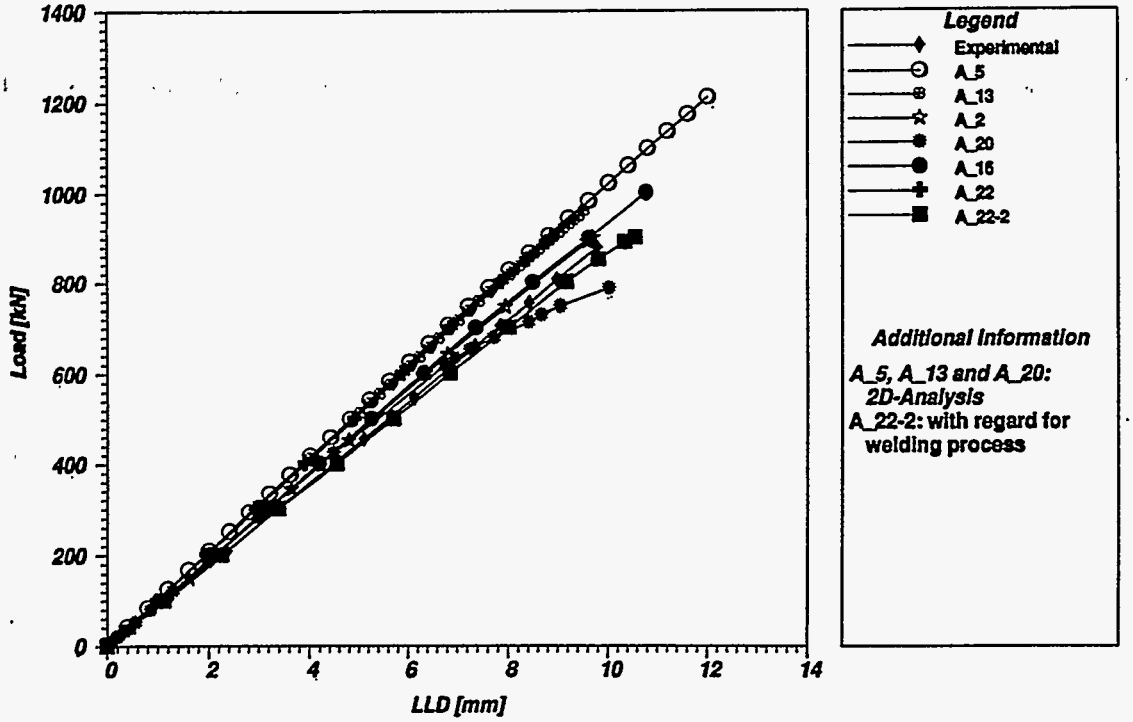

Figure 3.70 Load vs LLD for clad beam in DD2 experiment

EFG 96-6617

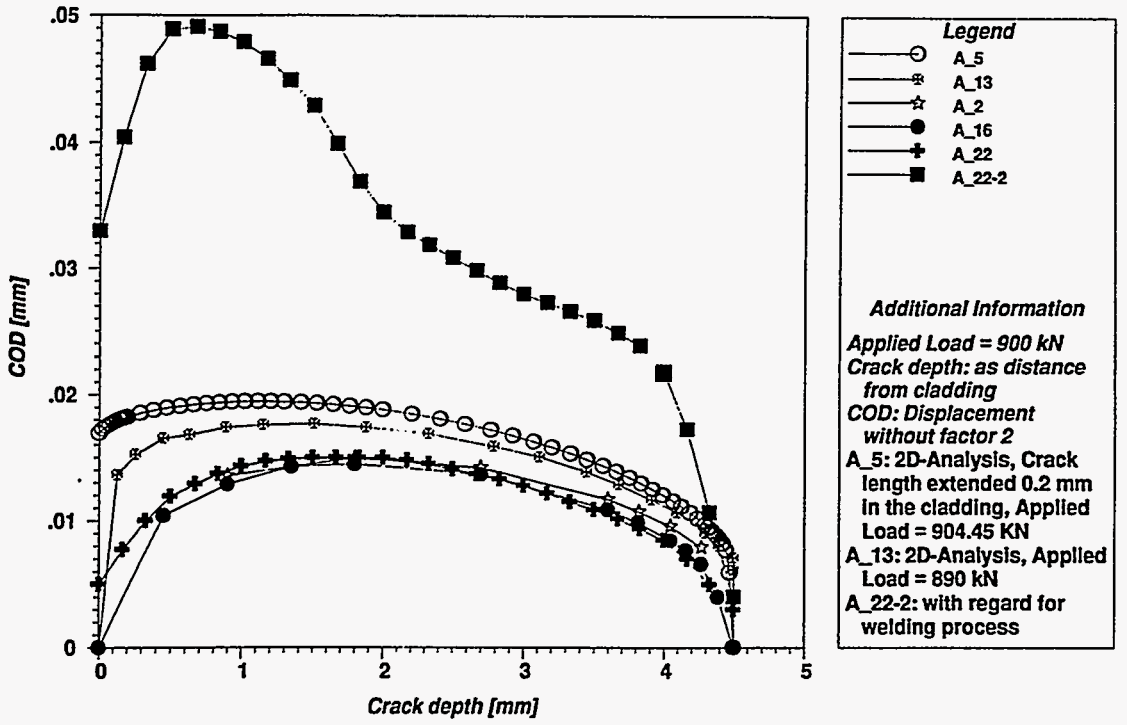

Figure 3.71 Computed COD vs distance from cladding interface at applied load of 900 kN in DD2 experiment

EFG 96-6618

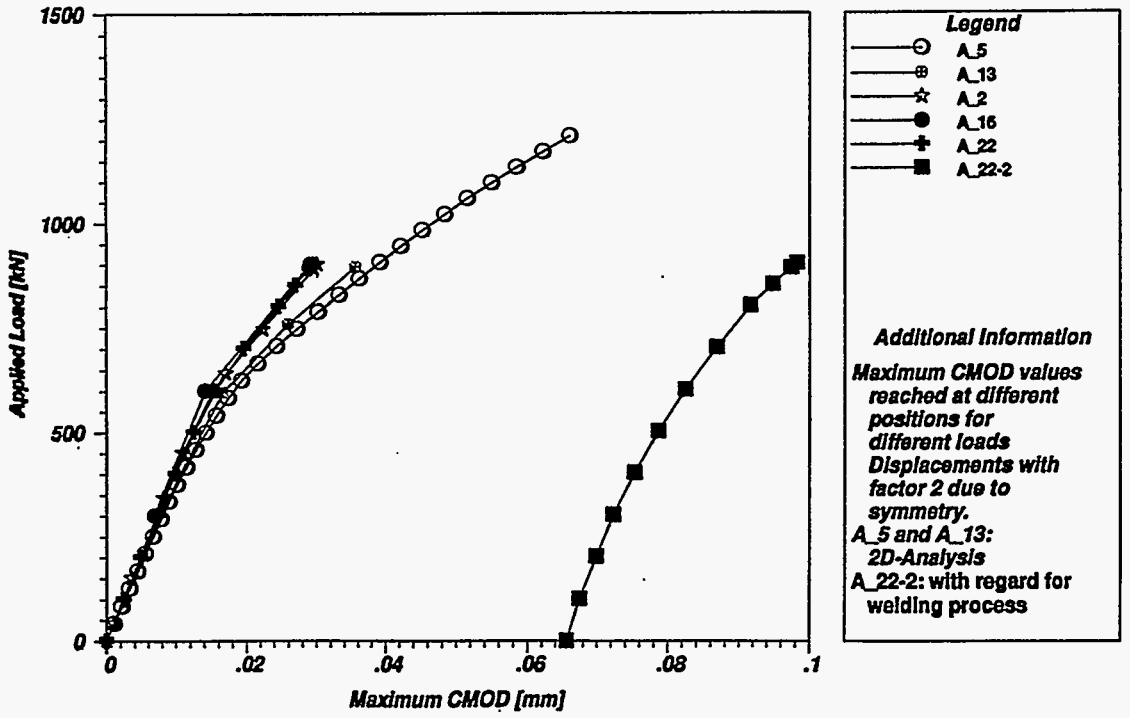

Figure 3.72 Applied load vs maximum CMOD in DD2 experiment

EFG 96-6619

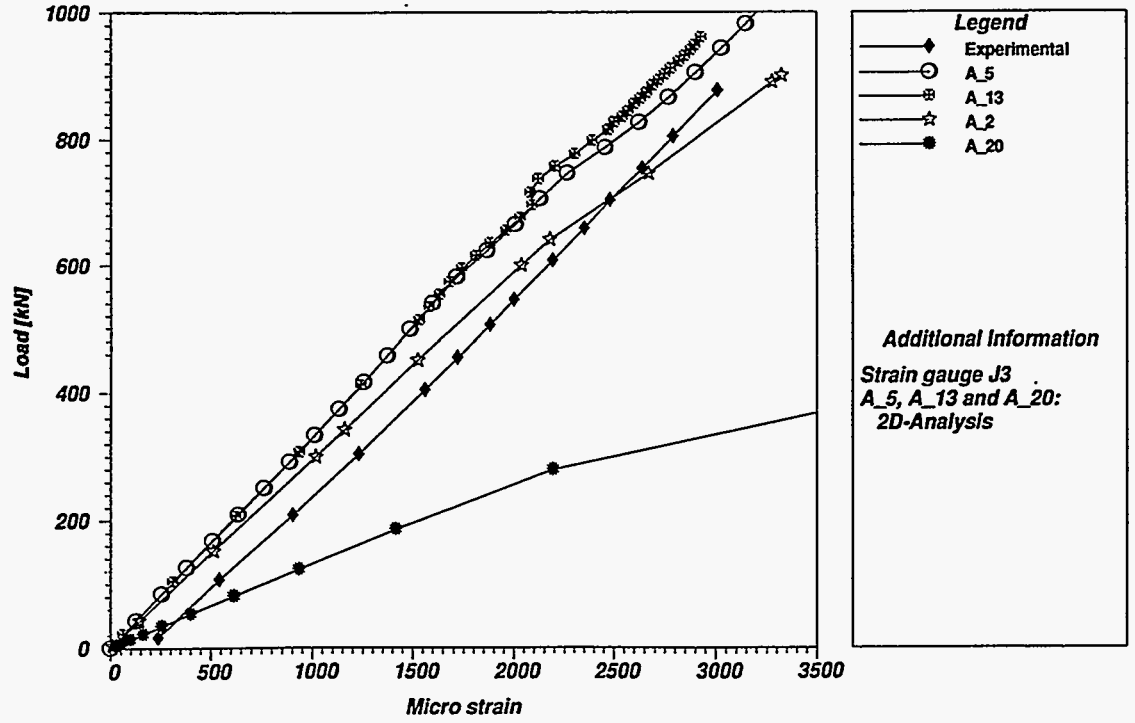

Figure 3.73 Load vs surface strain at gage J3 in DD2 experiment

EFG 96-6620

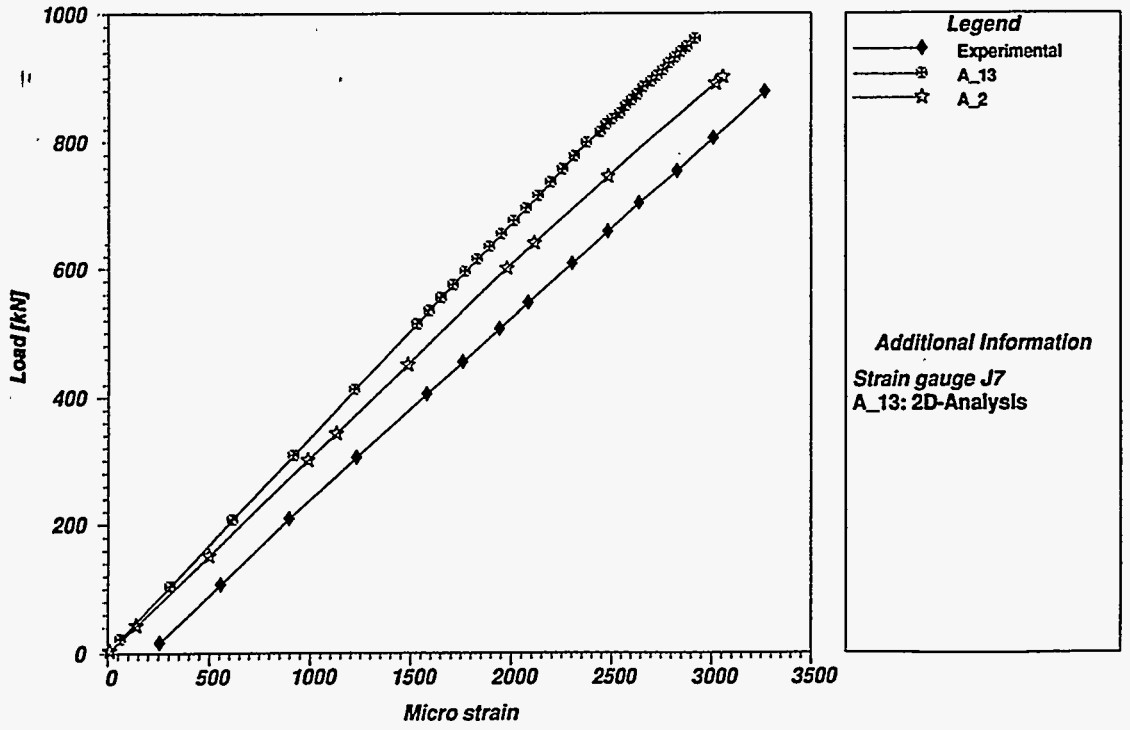

Figure 3.74 Load vs surface strain at gage J7 in DD2 experiment

EFG 96-6621

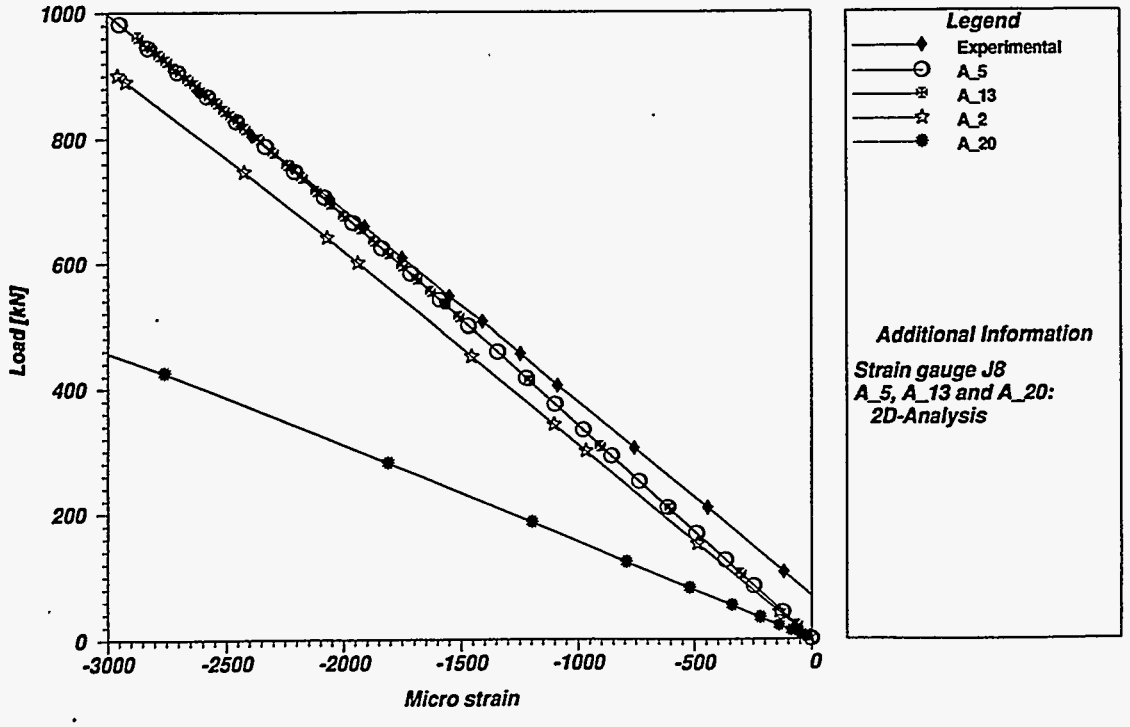

Figure 3.75 Load vs surface strain at gage J8 in DD2 experiment

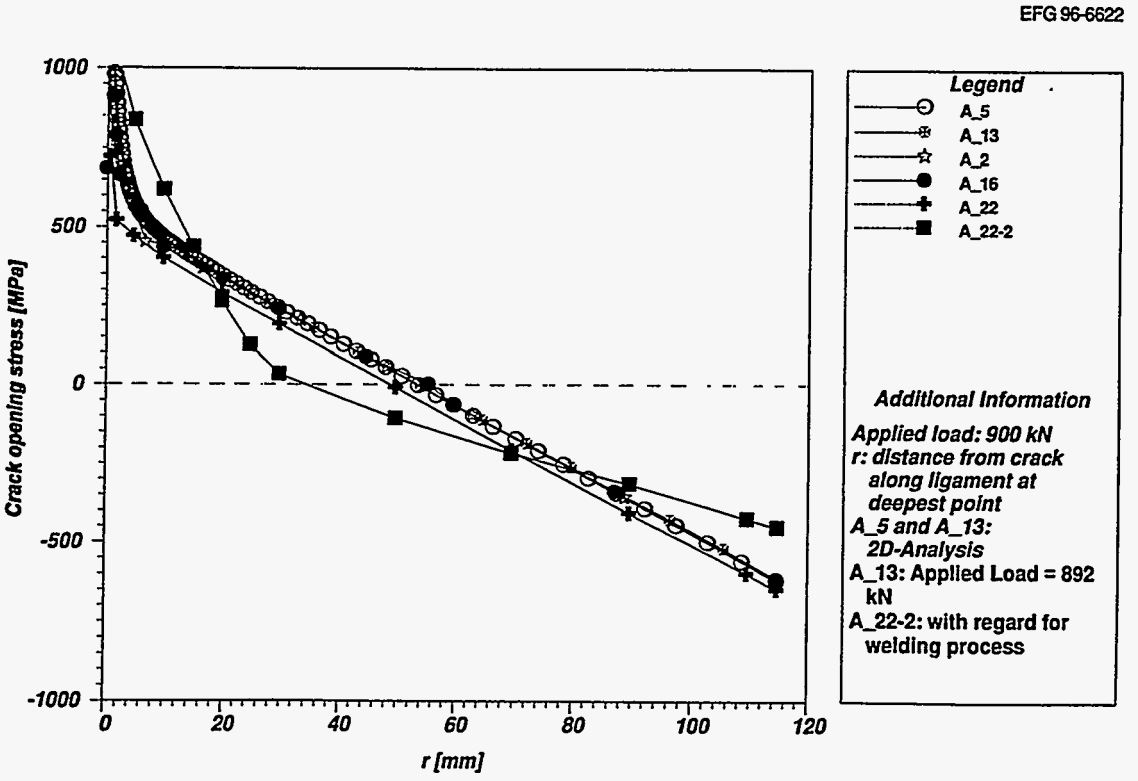

Figure 3.76 Crack-opening stress vs distance from crack along ligament at deepest point in DD2 experiment

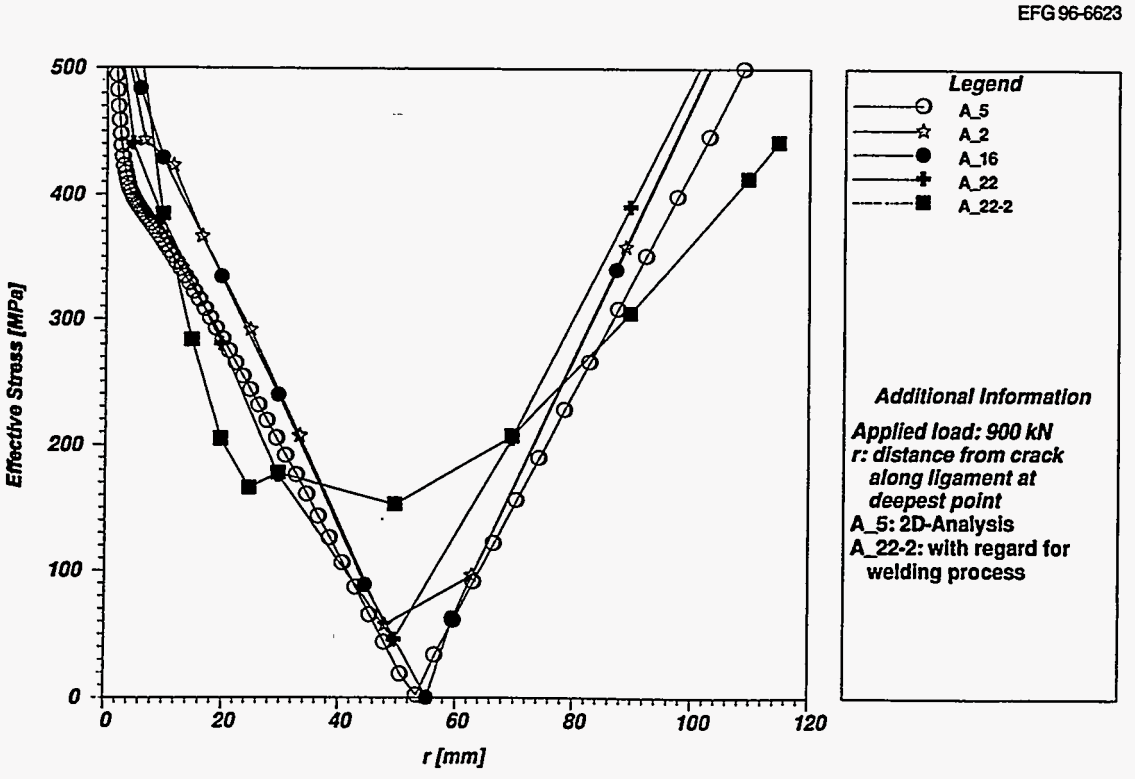

Figure 3.77 Effective stress vs distance from crack along ligament at deepest point in DD2 experiment

EFG 96-6624

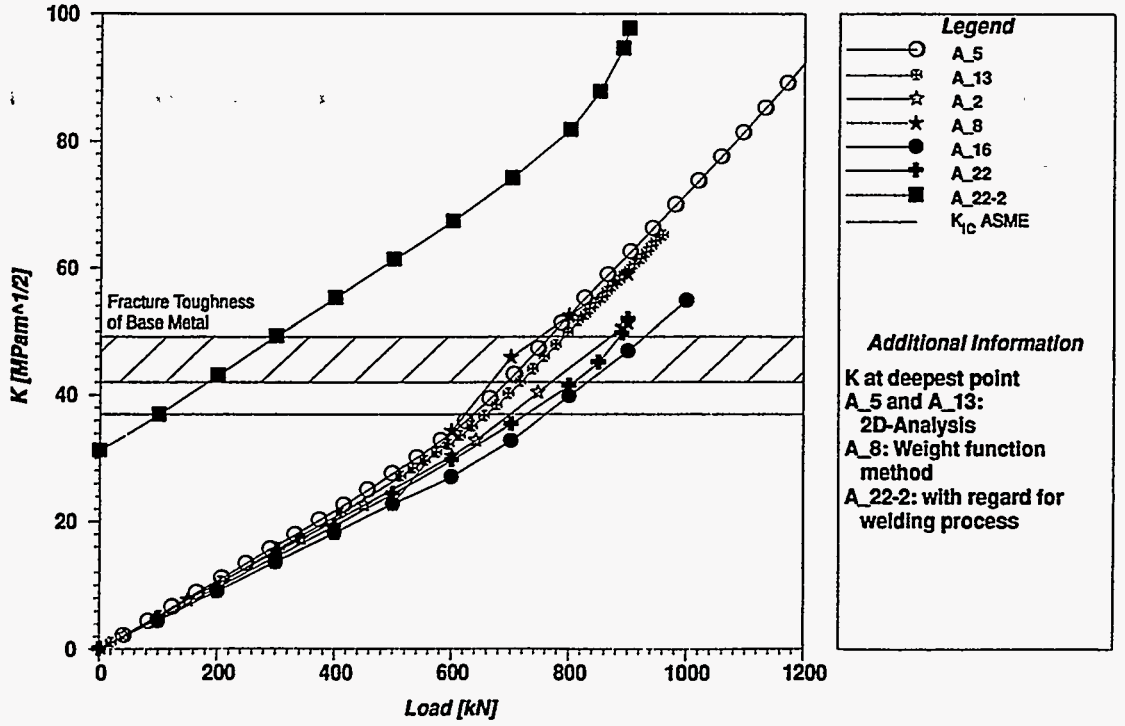

Figure 3.78 Comparison of applied K vs load for crack at deepest point with fracture toughness from CT specimens and from ASME Code (DD2 experiment)

EFG 96-6625

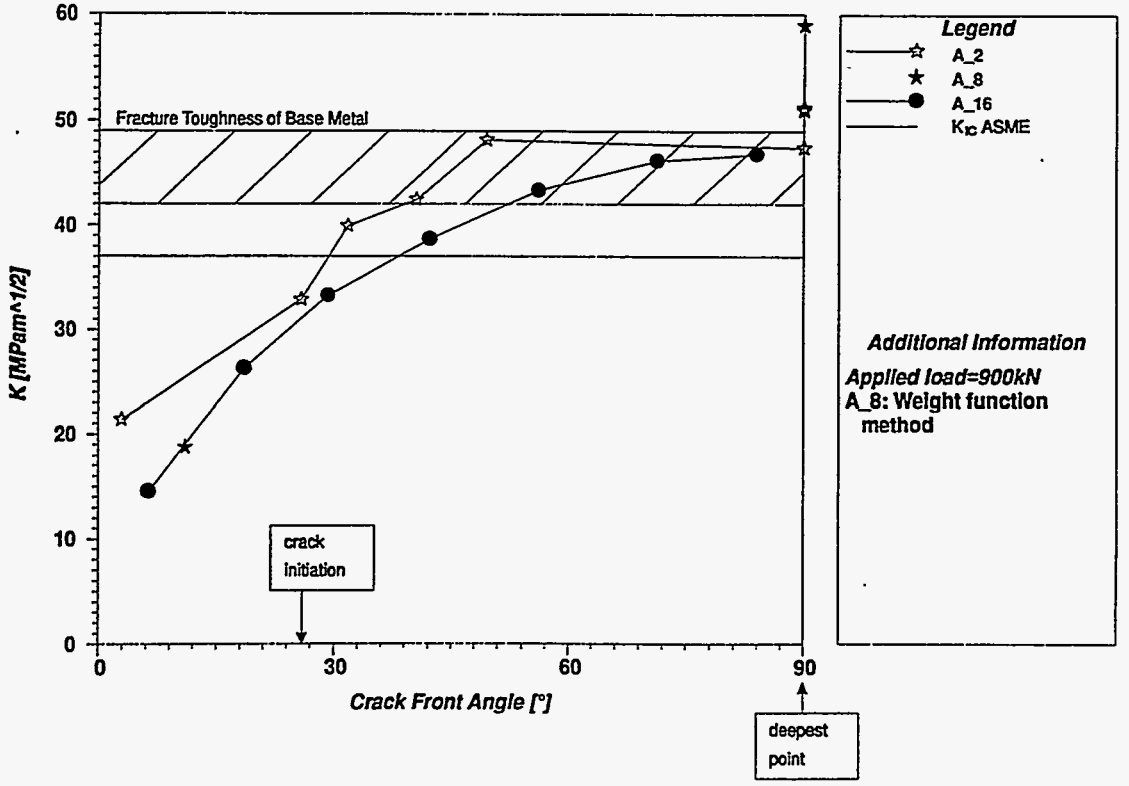

Figure 3.79 Comparison of applied K vs crack front angle with fracture toughness from CT specimens and from ASME Code (DD2 experiment)

the lower-bound fracture toughness of the base metal CT25 specimens at the test temperature. These results suggest a lower fracture toughness for the HAZ than the base metal at –170°C.

The stress triaxiality parameter h vs distance along the ligament at the deepest point of the crack is shown in Fig. 3.80. These results indicate a significant loss of constraint ahead of the crack tip, which would imply an increased fracture toughness in that region. The evaluation of Q on the ligament at the deepest point shows a value of about –0.6 at the failure load. Results for constraint parameters on the ligament at the initiation point near the interface between the cladding and base metal were not provided by the participants.

3.6 Clad Four-Point Bending Beam Experiment DSR3

Structural and fracture analyses of the DSR3 experiment are summarized in Table 3.11. Computed results for load vs LLD are generally in good agreement with measured data for the experiment (Fig. 3.81). Crack-opening displacements vs distance from the cladding/base metal interface at the position of the crack symmetry plane are compared in Fig. 3.82 for an applied load near fracture (~700 kN). Calculations of applied load vs maximum CMOD (which include a factor of 2 on CMOD due to symmetry conditions) are compared in Fig. 3.83. Increased differences between the 2-D approximations (A_13) and 3-D approximations (A_2 and A_16) of CMOD are associated with the deeper crack in DSR3 (compared with DD2).

The computed bending load vs longitudinal strains are compared with measured data at the locations of three surface strain gages (gages J3, J7, and J8 in Fig. 2.29) in Figs. 3.84–3.86, respectively. Results of these comparisons are similar to those observed for the DD2 experiment (see Figs. 3.73 and 3.75); except for analysis A_20, reasonably good agreement is obtained with the experimental data.

Crack-opening stress and effective stress vs distance along the ligament at the deepest point of the crack are compared in Figs. 3.87 and 3.88, respectively. These results are generally in good agreement at an applied load of ~700 kN (near fracture load).

The computed values of K_I vs applied load at the deepest point of the crack are shown in Fig. 3.89, along with the lower- and upper-bound small-specimen (CT25) fracture

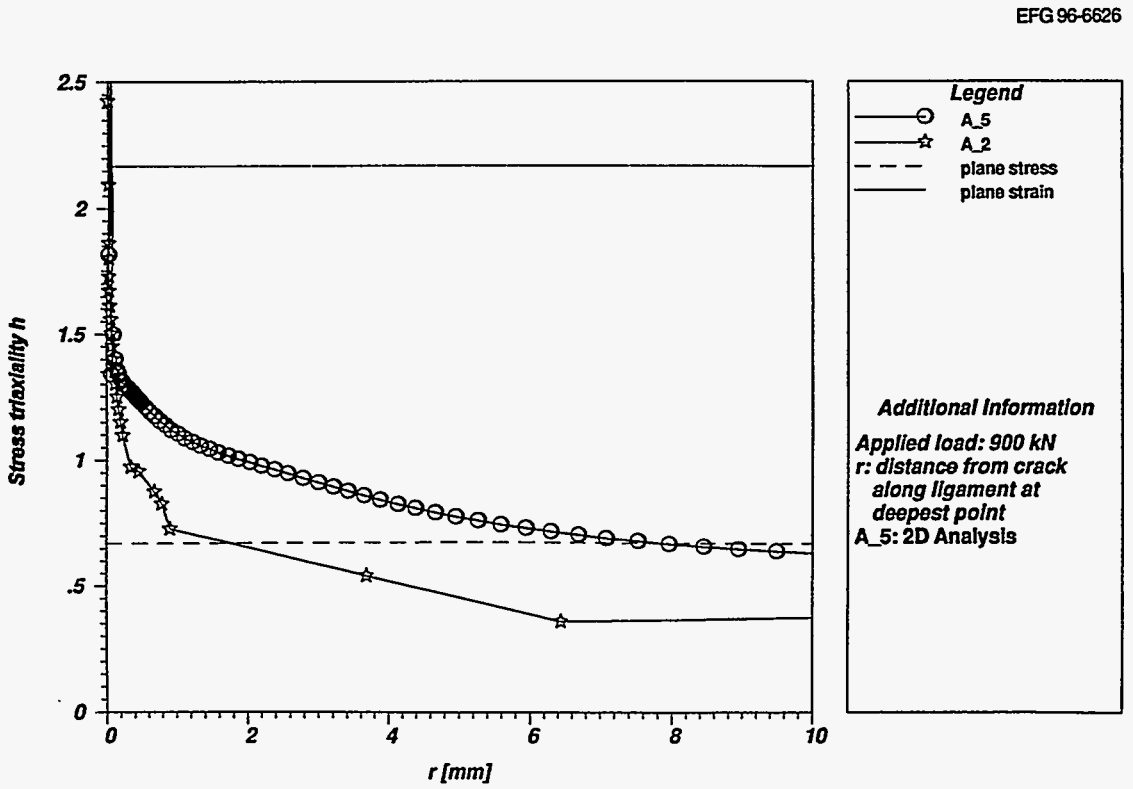

Figure 3.80 Triaxiality parameter h vs distance from crack along ligament at deepest point at applied load of 900 kN (DD2 experiment)

EFG 96-6627

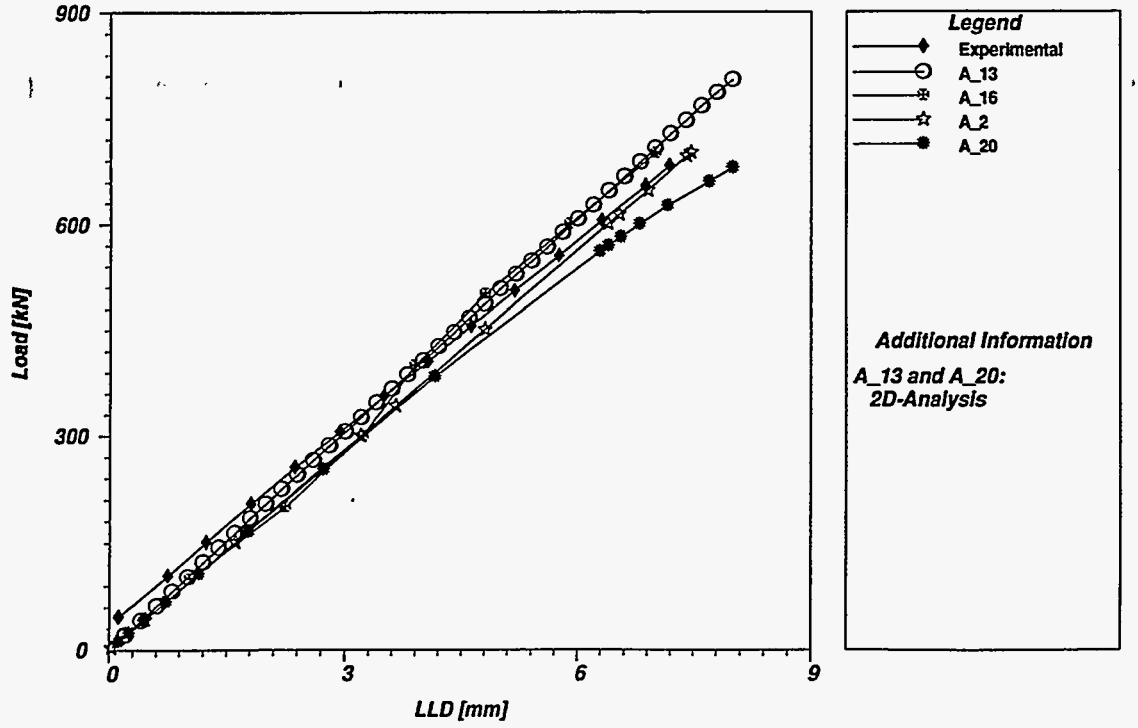

Figure 3.81 Load vs LLD for clad beam in DSR3 experiment

EFG 96-6628

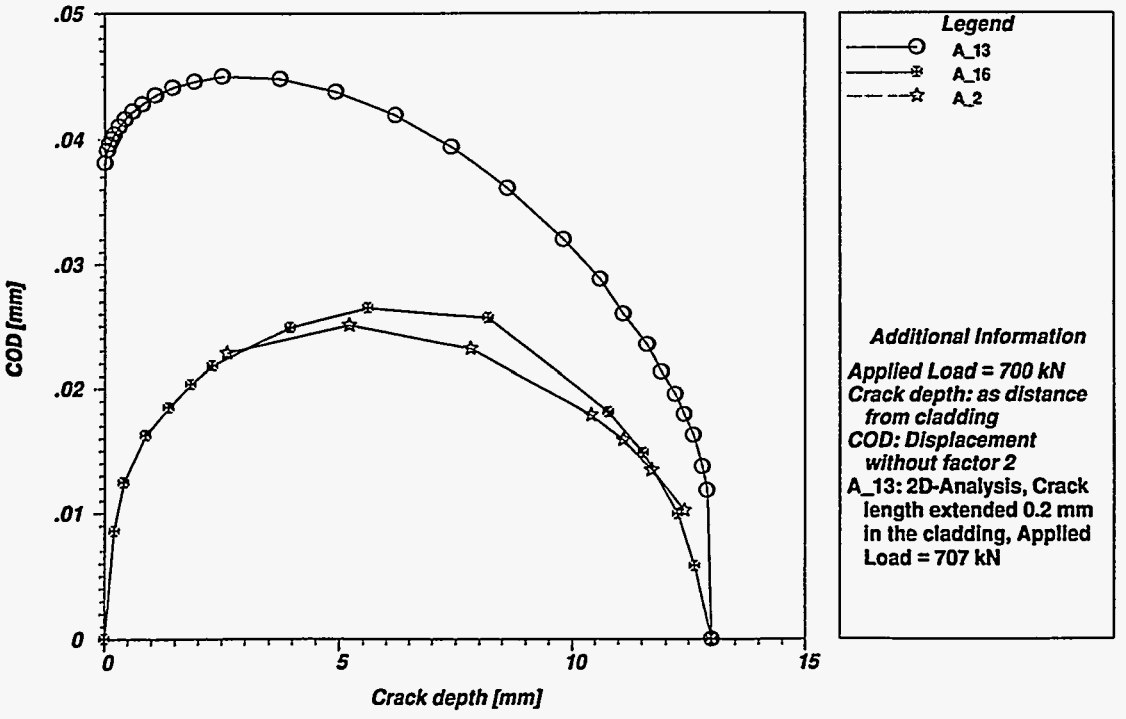

Figure 3.82 Computed COD vs distance from cladding interface at applied load of 700 kN in DSR3 experiment

EFG 96-6629

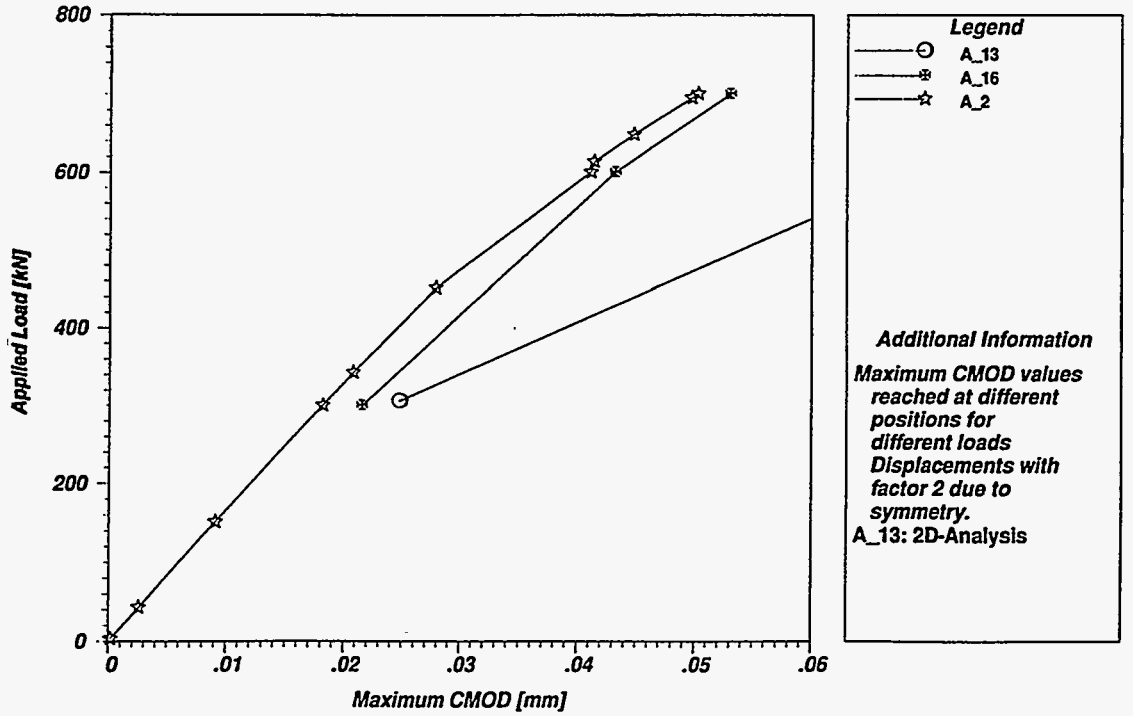

Figure 3.83 Applied load vs maximum CMOD in DSR3 experiment

EFG 96-6630

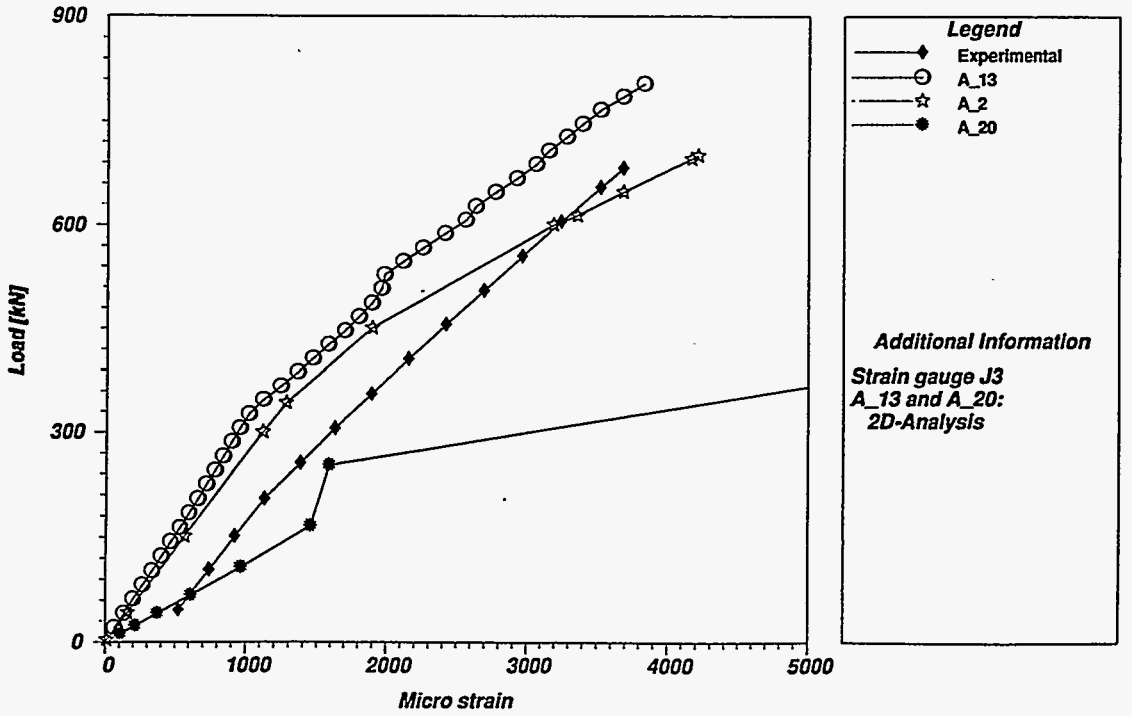

Figure 3.84 Load vs surface strain at gage J3 in DSR3 experiment

EFG 96-6631

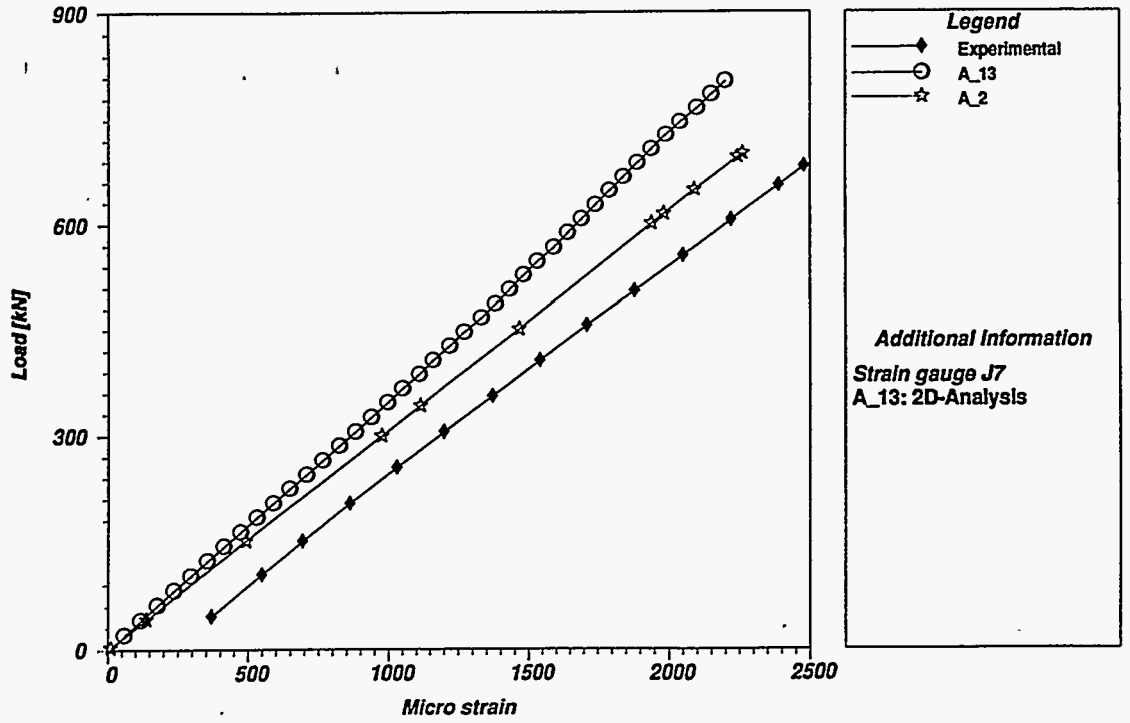

Figure 3.85 Load vs surface strain at gage J7 in DSR3 experiment

EFG 96-6632

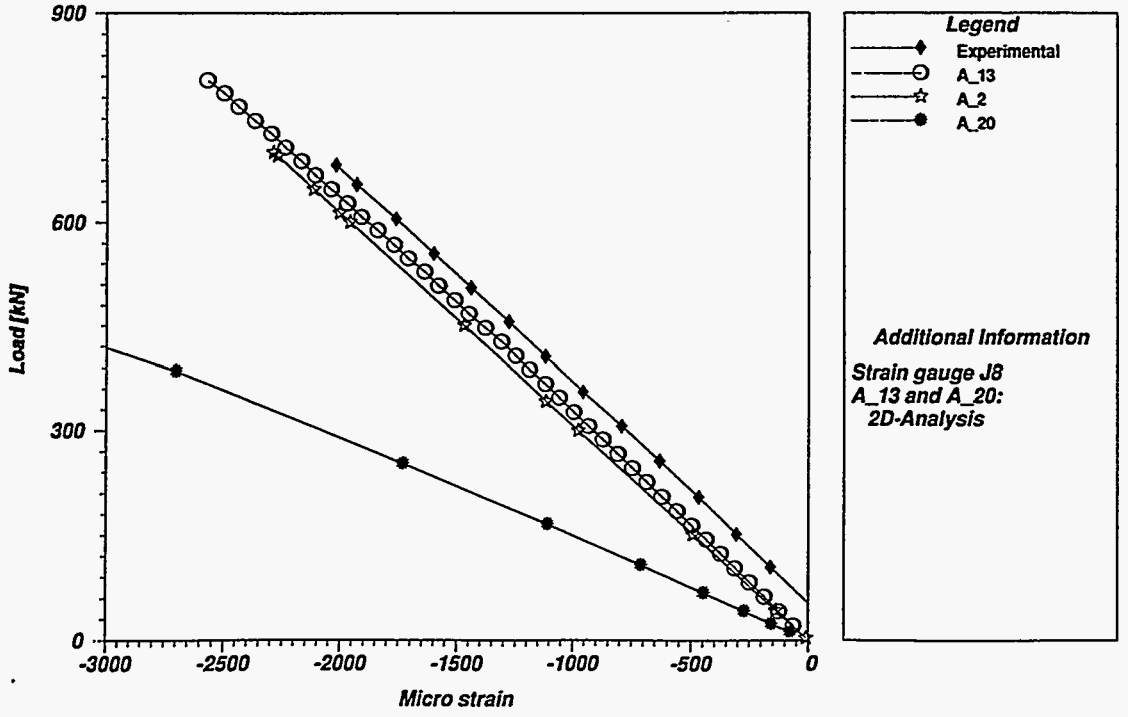

Figure 3.86 Load vs surface strain at gage J8 in DSR3 experiment

EFG 96-6633

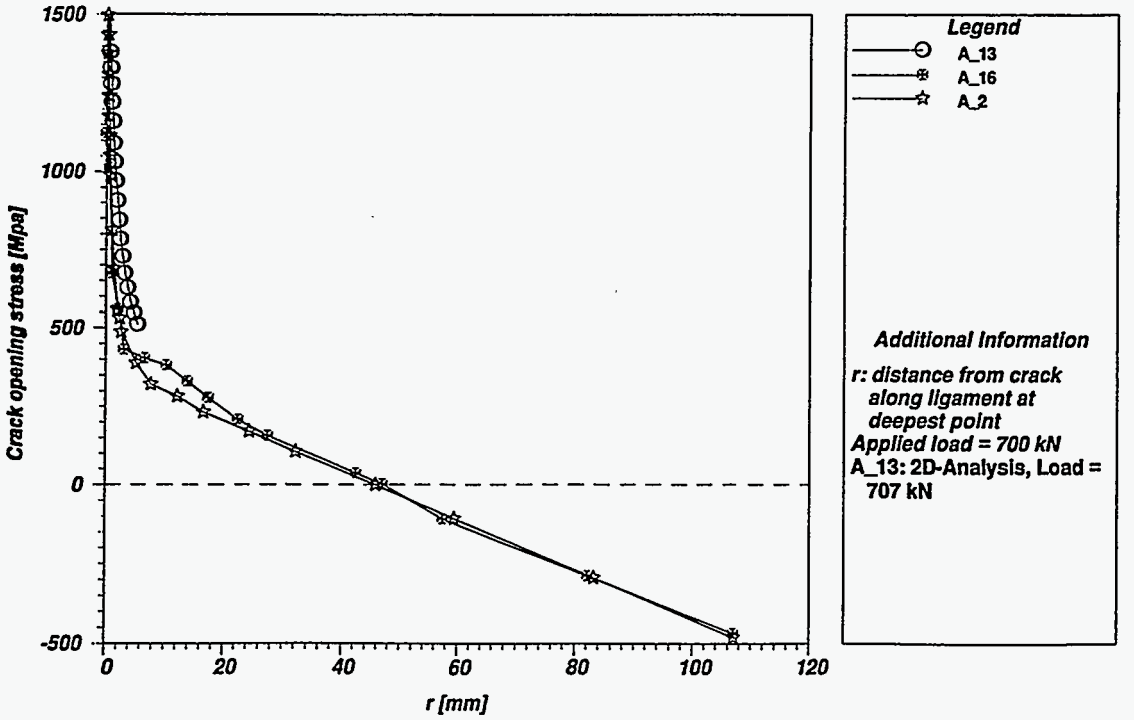

Figure 3.87 Crack-opening stress vs distance from crack along ligament at deepest point at applied load of 700 kN in DSR3 experiment

EFG 96-6634

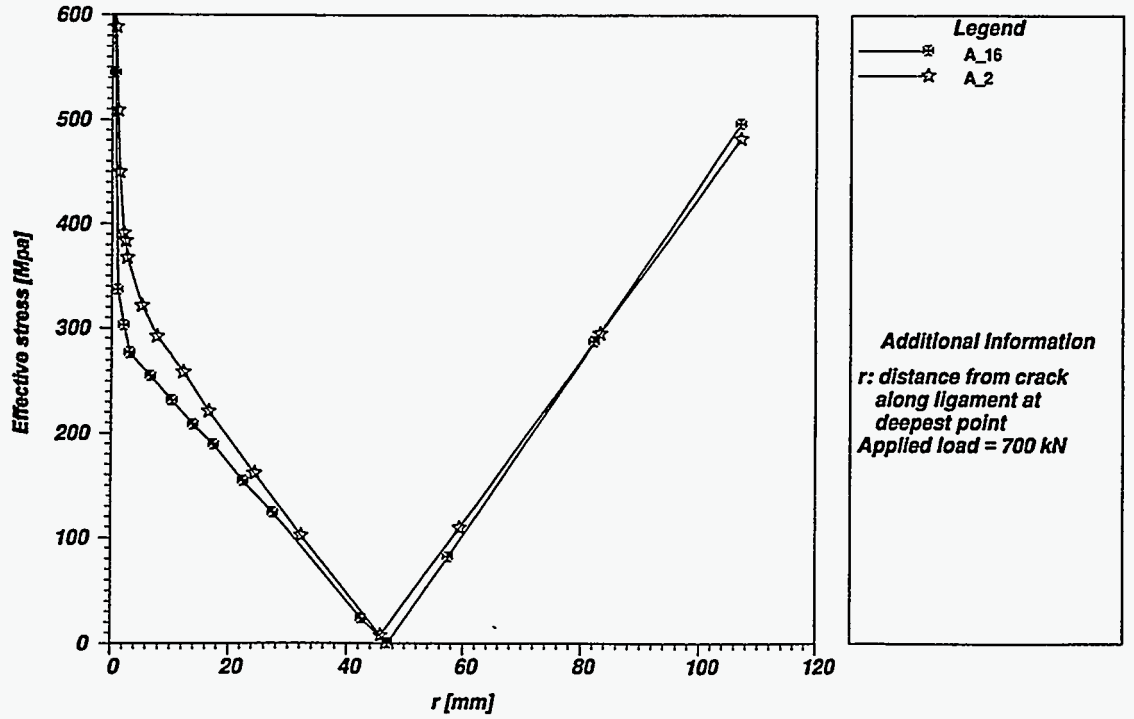

Figure 3.88 Effective stress vs distance from crack along ligament at deepest point at applied load of 700 kN in DSR3 experiment

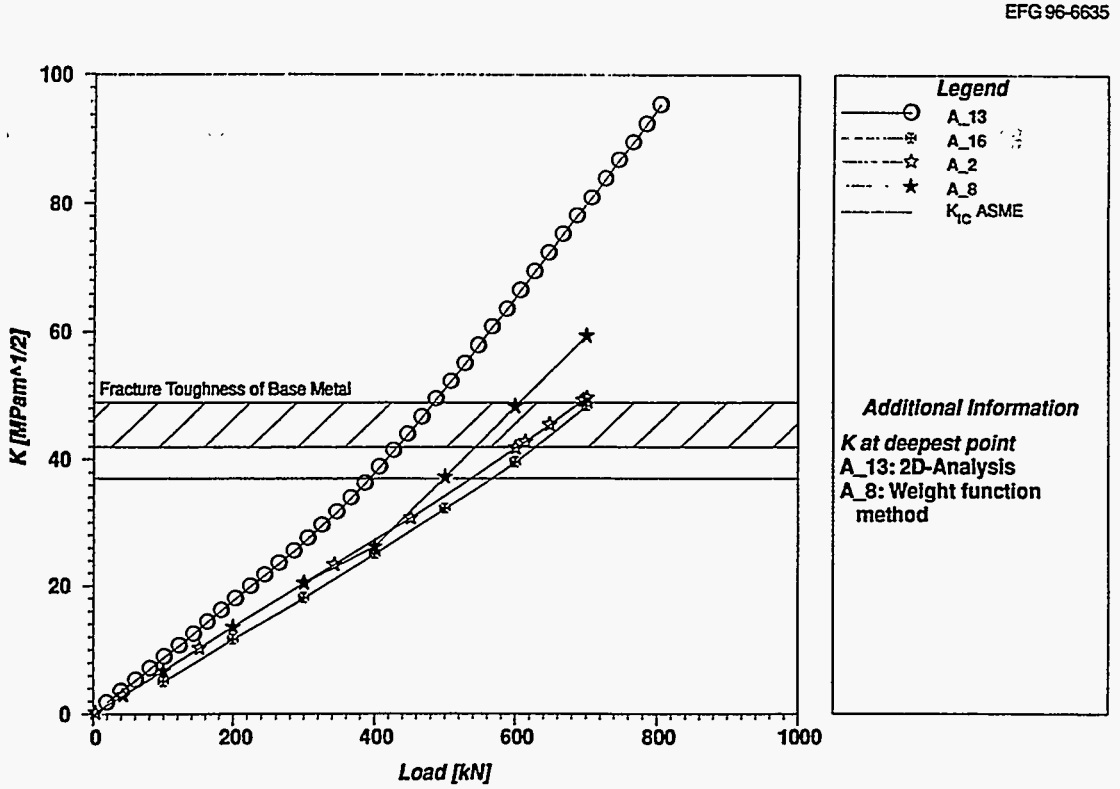

Figure 3.89 Comparison of applied K vs load for crack at deepest point with fracture toughness from CT specimens and from ASME Code (DSR3 experiment)

toughness curves at the test temperature (K values range from ~40 to 50 MPa$\sqrt{m}$). Computed K_I values vs crack-front angle near the loading at fracture are compared in Fig. 3.90. At the fracture load, peak K_I values lie near the upper-bound small-specimen fracture toughness curve. Test results for DSR3 indicate that the crack initiated at a point in the HAZ located about 2 mm from the interface, which gives an initiation toughness of ~40 MPa$\sqrt{m}$. Thus, the computed toughness at the initiation site falls below the lower-bound fracture toughness of the base metal CT25 specimens at the test temperature. These results for DSR3 are consistent with those observed in the DD2 experiment and discussed in the previous section.

Residual stress measurements performed in the clad beams after stress relief were reported to show tensile stresses (between 200 and 300 MPa) in the cladding and low compressive stresses (about 50 MPa) in the HAZ. The analysis results depicted in Figs. 3.89 and 3.90 for the DSR3 experiment (and in Figs. 3.78 and 3.79 for DD2) assume that the test temperature of –170°C is the stress-free temperature, which may not adequately reflect the effects of residual stresses in the HAZ. Adoption of a different stress-free temperature in the analyses may have a significant effect on calculated K_I values near the clad/base interface.

The stress triaxiality parameter h vs distance along the ligament at the deepest point of the crack obtained from analysis A_2 is shown in Fig. 3.91. These results tend toward a plane stress condition, indicating a significant loss of constraint ahead of the crack tip. The calculated Q-stress parameter in that region has a value of approximately –0.4 at the failure load.

Results of the clad beam fracture assessments depicted in Figs. 3.79 and 3.90 highlight the need for improved models of cleavage fracture toughness in the HAZ. EdF has reported the development of an extensive research program* on the latter topic that is being carried out in conjunction with CEA. Currently, this program is focussing on the effects of thermal aging and irradiation in the clad HAZ.

Bass et al.[7] have identified locally intensified strain-aging embrittlement (LISAE) as a factor that has potential for influencing crack initiation in the clad HAZ of the EdF beams. Dawes[8] has provided a review of situations where

*D. Moinereau, EdF, Direction des Etudes et Recherches, Les Renardières Moret-sur-Loing, France, Private Communication to J. Sievers, GRS, Köln, Germany, and B. R. Bass, ORNL, U.S.A., March 26, 1996.

EFG 96-6636

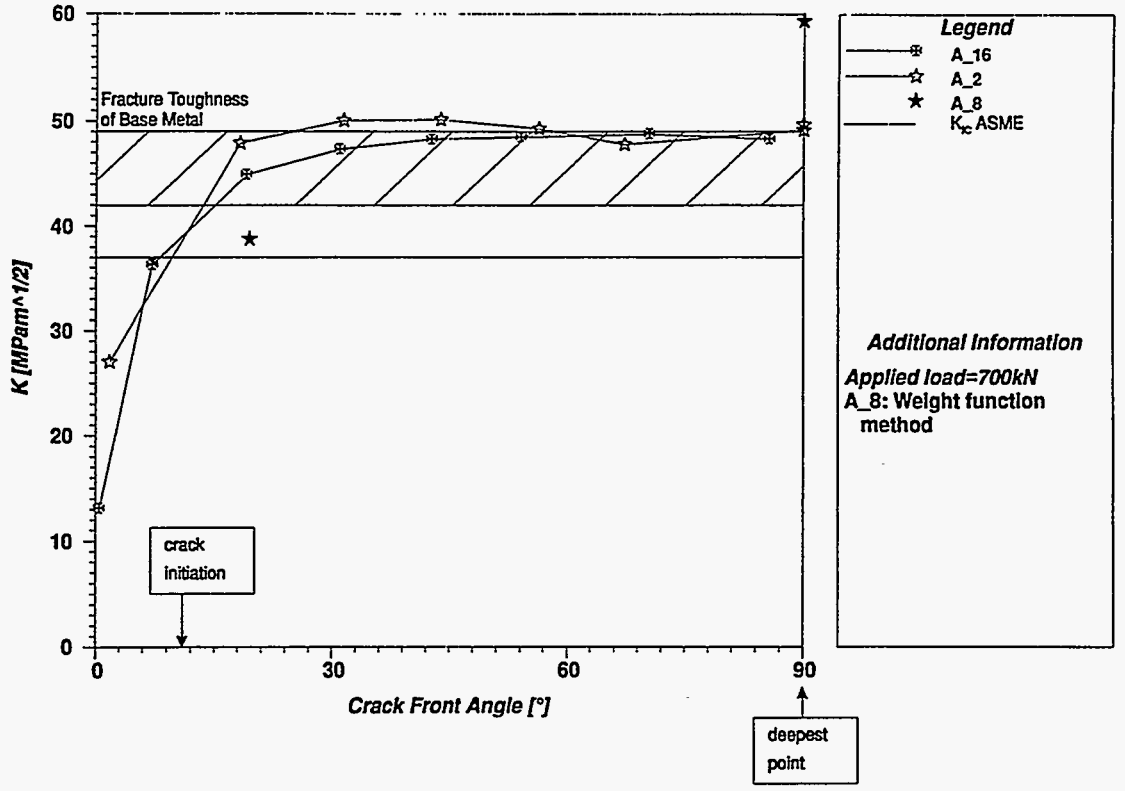

Figure 3.90 Comparison of applied K vs crack front angle with fracture toughness from CT specimens and from ASME Code (DSR3 experiment)

EFG 96-6637

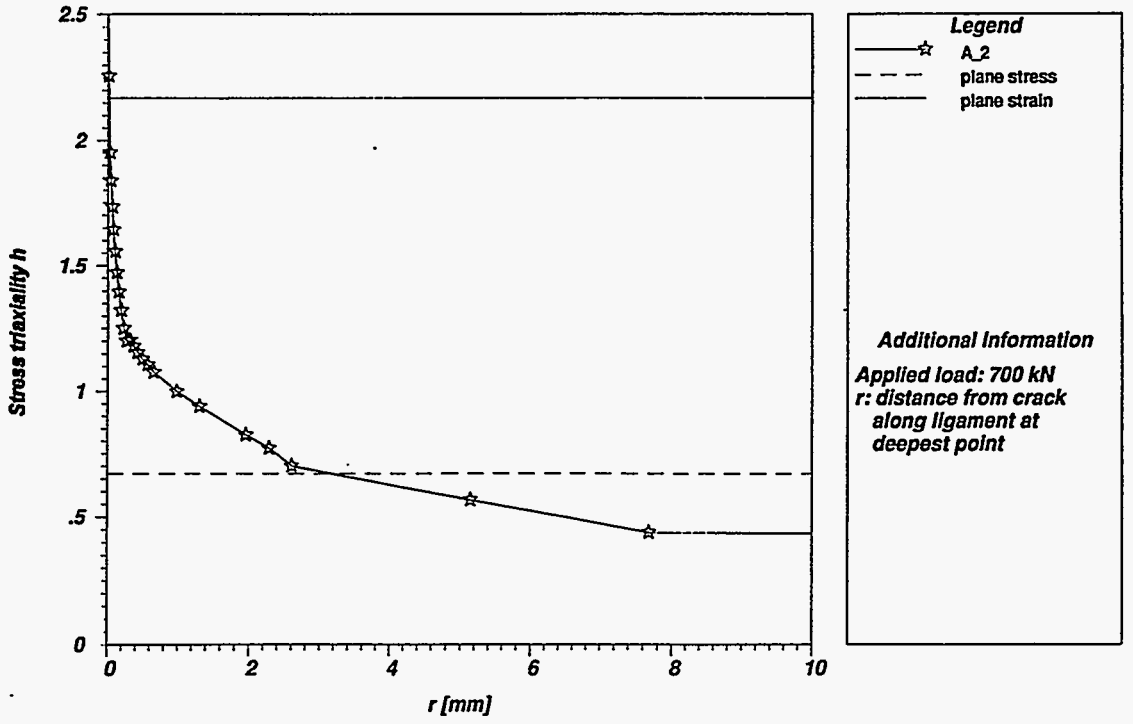

Figure 3.91 Triaxiality parameter h vs distance from crack along ligament at deepest point at applied load of 700 kN (DSR3 experiment)

LISAE was observed to be a contributor to low-stress brittle fractures. These situations were generally associated with as-welded structures, weld repairs, older steels, and old and new weld metals. The claim is made that any region of a welded joint is susceptible to strain-aging embrittlement, including the base metal adjacent to the HAZ up to several millimeters removed from the visibly transformed HAZ.

Locally intensified strain aging of material occurs at the tip of a preexisting flaw located adjacent to areas where further welding operations have been performed. Examples are flaws adjacent to weld repairs and flaws in areas influenced by the cladding process. The transient temperature distribution of the welding process causes high opening-mode tensile stresses to be generated at the flaw tip. These stresses occur at a time when local temperatures are sufficiently high for thermally activated carbon and nitrogen atoms to be available for diffusion to dislocations and to effectively lock them. An effect of this diffusion process is to restrict further plastic deformation of the flaw-tip material. It follows that the transition-range fracture toughness of material at the flaw tip is reduced by restricting its ability to yield and to blunt. Thus, in the context of the EdF clad beam experiments, the effect of LISAE could impact the material fracture toughness associated with preexisting subclad flaws.

Additional fracture toughness data for subclad flaws are included in the data base of an experimental program described by MacDonald et al.* and by Bass et al.[7] These data were generated from beam specimens machined from A 508 Class 2 pressure vessel steel and tested in four-point bending. The fabrication process for the beams involved the application of cladding over an existing surface flaw in the test section, followed by a postclad heat treatment at a temperature of 593°C. MacDonald et al.* performed statistical analyses of these data as part of a larger warm-prestressed (WPS) data set that included more than 100 unclad specimens of pressure vessel steel. Comparisons were made between fracture toughness values obtained from the unclad and subclad data sets, with temperature the only independent variable. The generally lower fracture toughness values that were observed in the subclad flaw data base are consistent with LISAE effects brought on by the cladding process.[7]

3.7 Biaxially Loaded Cruciform Beam Experiment BB-4

Structural and fracture assessments of the BB-4 cruciform beam experiment are summarized in Table 3.12. Calculated values of longitudinal load vs LLD are compared with measured data in Fig. 3.92. Figure 3.93 provides a comparison of measured and calculated values of longitudinal load vs CMOD at the midplane of the BB-4 cruciform specimen. With one exception (analysis A_10), the analytical results are tightly grouped and in reasonably good agreement with the measured data near the point of failure (814 kN). Deviations of the computed results from the experimental data at intermediate values of CMOD can be traced to the use of preliminary stress-strain data for these calculations. Updated material properties that became available during completion of the FALSIRE II analyses were used in a sensitivity study performed by participant A_17. The higher yield stress of ~450 MPa used in that study resulted in decreased values of LLD and CMOD for loads above 600 kN.

Crack-opening stress and effective stress vs distance along the ligament at the center of the crack for two applied loads (~650 and 800 kN) are compared in Figs. 3.94–3.97, respectively. Agreement among the calculations of crack-opening stress is good for both values of applied load. For the effective stress calculations, the scatter band is significantly greater near the measured load corresponding to cleavage fracture (Fig. 3.97). The level of plasticity in the specimen is large near the failure load, and relatively small differences in the material stress-strain representation have significant effects on the stress distribution.

In Fig. 3.98, the computed values of K_I vs applied longitudinal load at the center of the crack show a small scatter band up to the load at fracture. The calculated K_I values along the crack front in the cruciform specimen at an intermediate load and near the load at failure are shown in Figs. 3.99 and 3.100, respectively. Near the fracture load (Fig. 3.100), two analyses (A_10 and A_16) deviate from the other analyses in the group. Modeling of the slots in the cruciform specimen and differences concerning approximation of the stress-strain curve are the primary reasons for this variability in the analytical results. Maximum crack loading is reached at the crack center, where crack initiation took place. Therefore, a fracture toughness value of about 180 MPa$\sqrt{m}$ can be derived, which is twice the lower bound value of deeply notched standard specimens at the test temperature.

Evaluations of the constraint parameter Q at the midplane of the biaxially loaded BB-4 specimen (see Figs. 3.101 and 3.102) near the fracture load showed a strong loss of constraint of about Q = –0.8 on the ligament near the crack front. This result can be compared with the uniaxially loaded specimen BB-2, which showed a greater loss of constraint at failure of about Q = –1, which can be correlated with an increased fracture toughness value of about 210 MPa$\sqrt{m}$. In Fig. 3.103, variation of the stress

*B. D. MacDonald et al., "Analysis of Warm-Prestress Data," *Fracture Mechanics: 27th Volume, ASTM STP 1296* (American Society for Testing Materials, Philadelphia, to be published).

EFG 96-6638

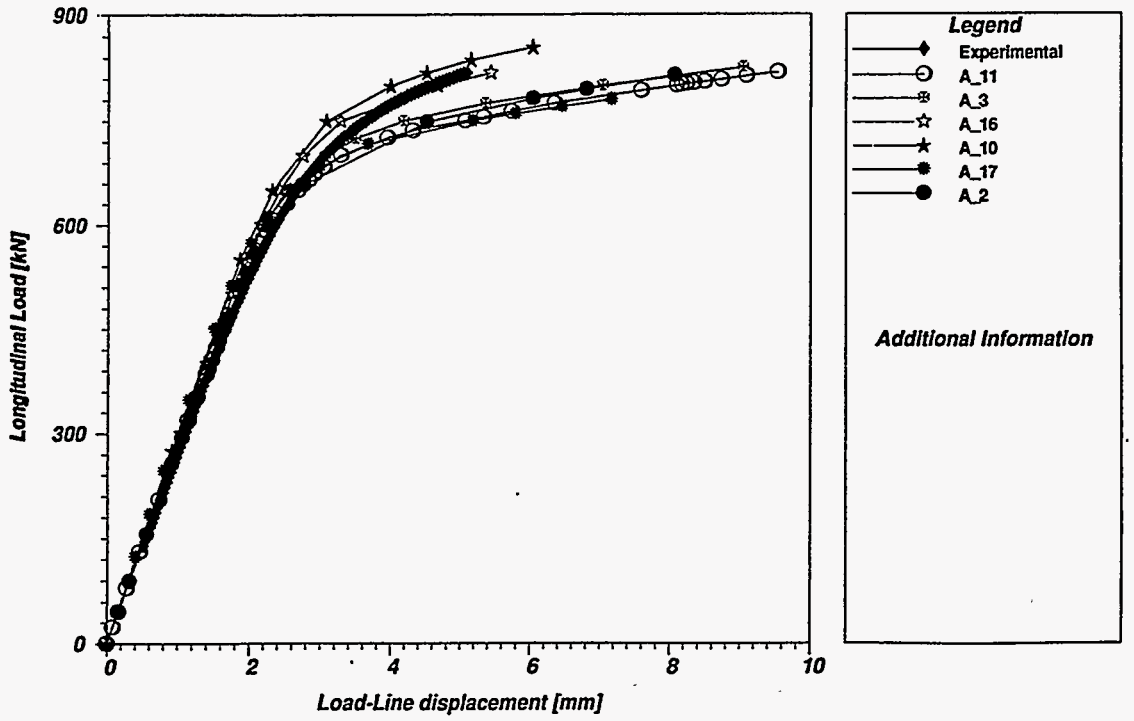

Figure 3.92 Longitudinal load vs LLD for cruciform beam in BB-4 experiment

EFG 96-6639

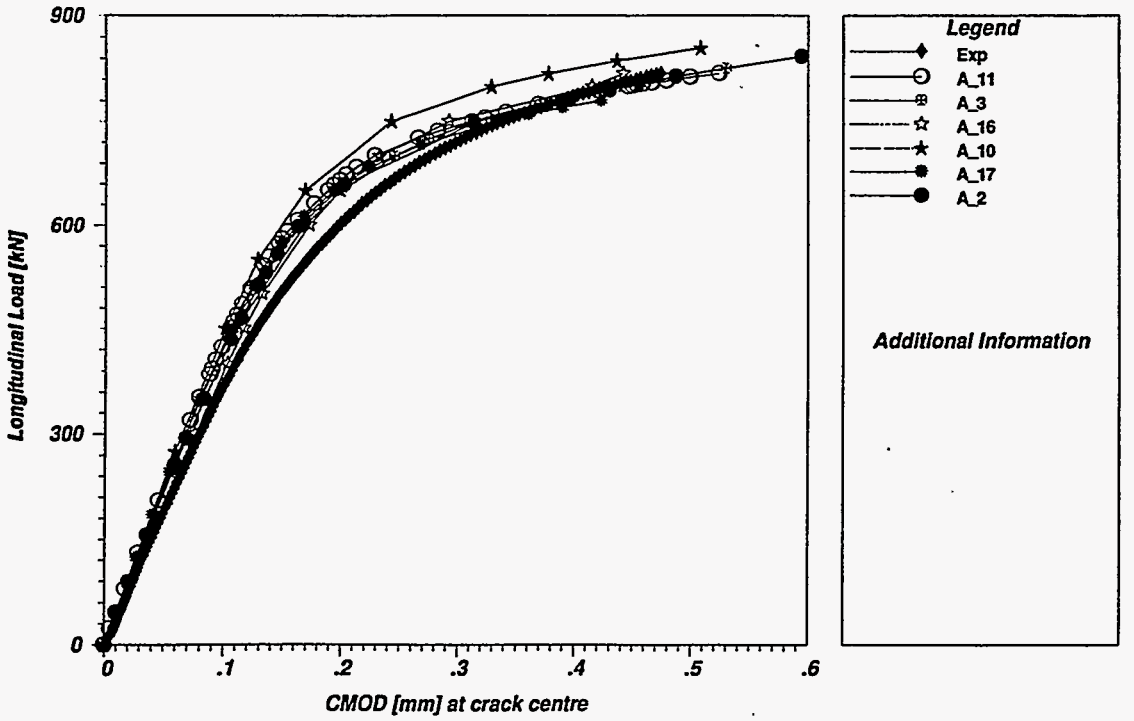

Figure 3.93 Longitudinal load vs CMOD for cruciform beam in BB-4 experiment

EFG 96-6640

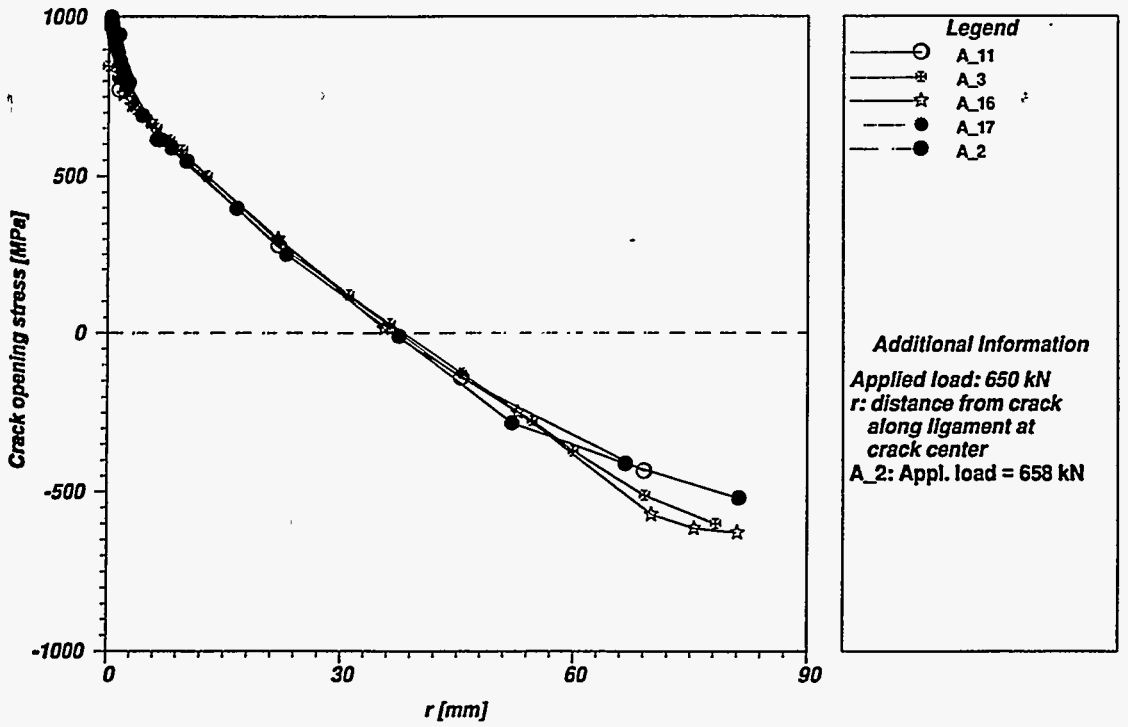

Figure 3.94 Crack-opening stress vs distance from crack along ligament at applied load of 650 kN in BB-4 experiment

EFG 96-6641

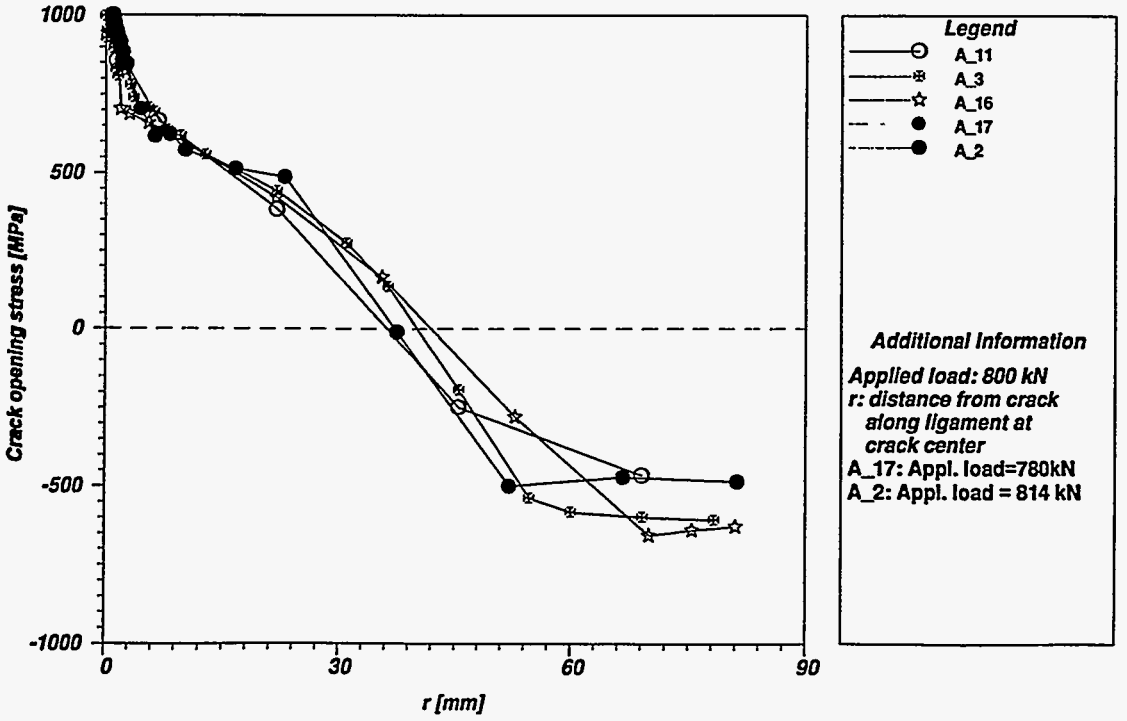

Figure 3.95 Crack-opening stress vs distance from crack along ligament at applied load of 800 kN in BB-4 experiment

EFG 96-6642

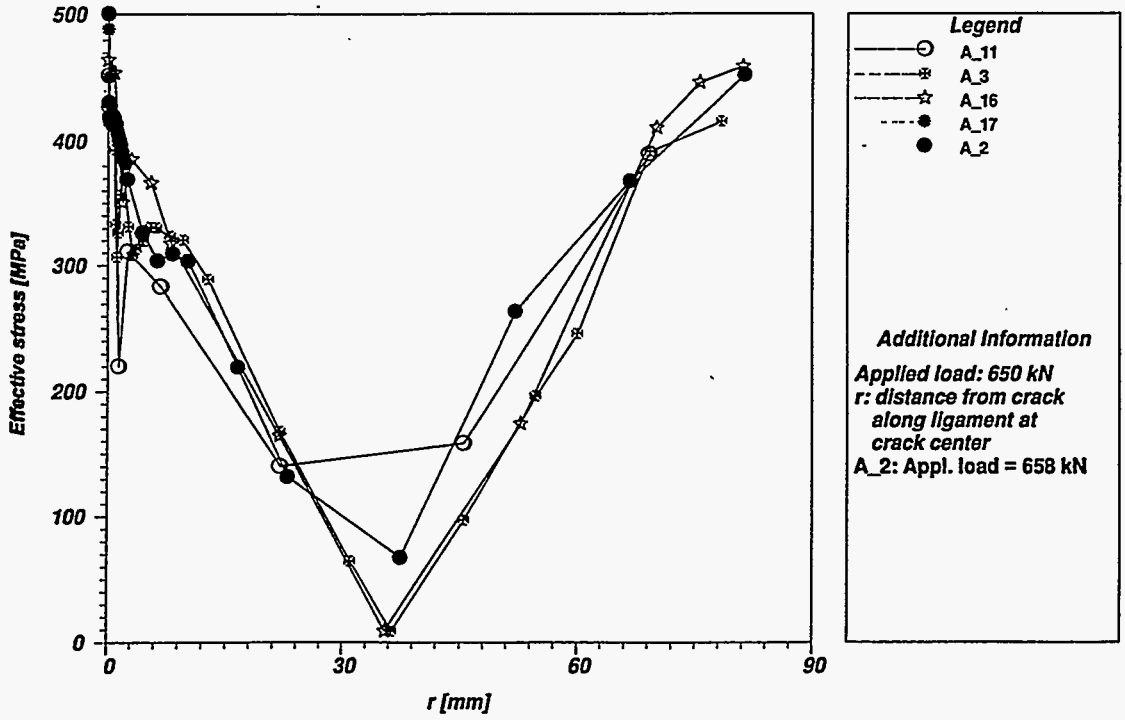

Figure 3.96 Effective stress vs distance from crack along ligament at applied load of 650 kN in BB-4 experiment

EFG 96-6643

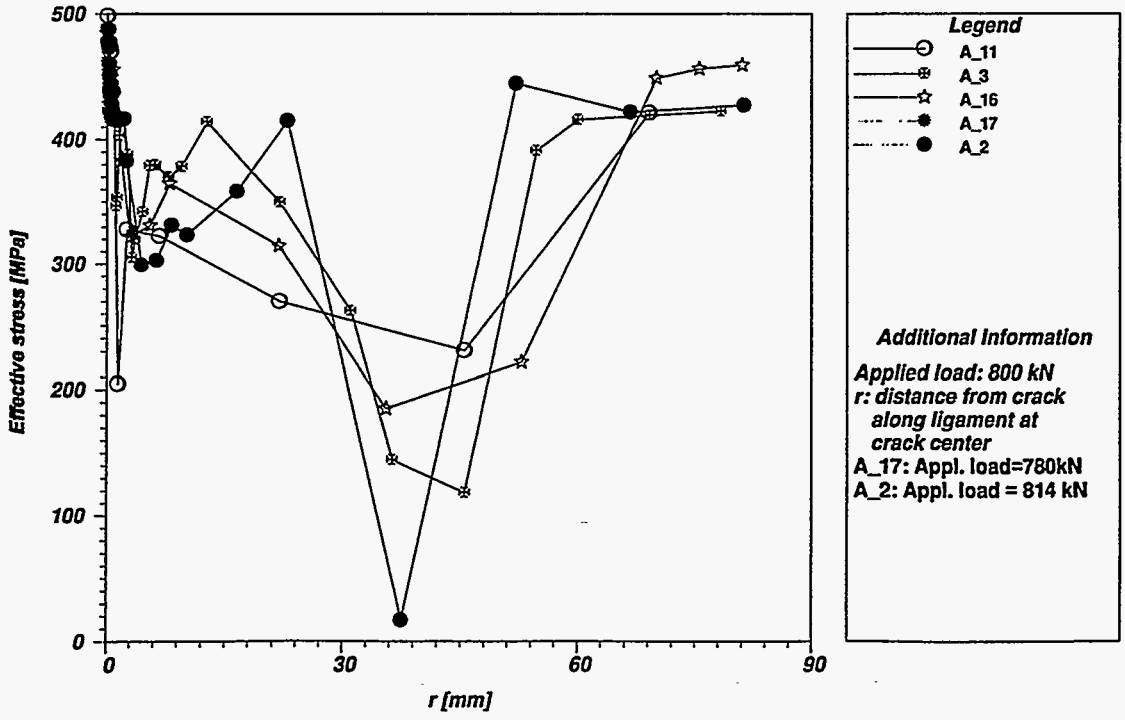

Figure 3.97 Effective stress vs distance from crack along ligament at applied load of 800 kN in BB-4 experiment

EFG 96-6644

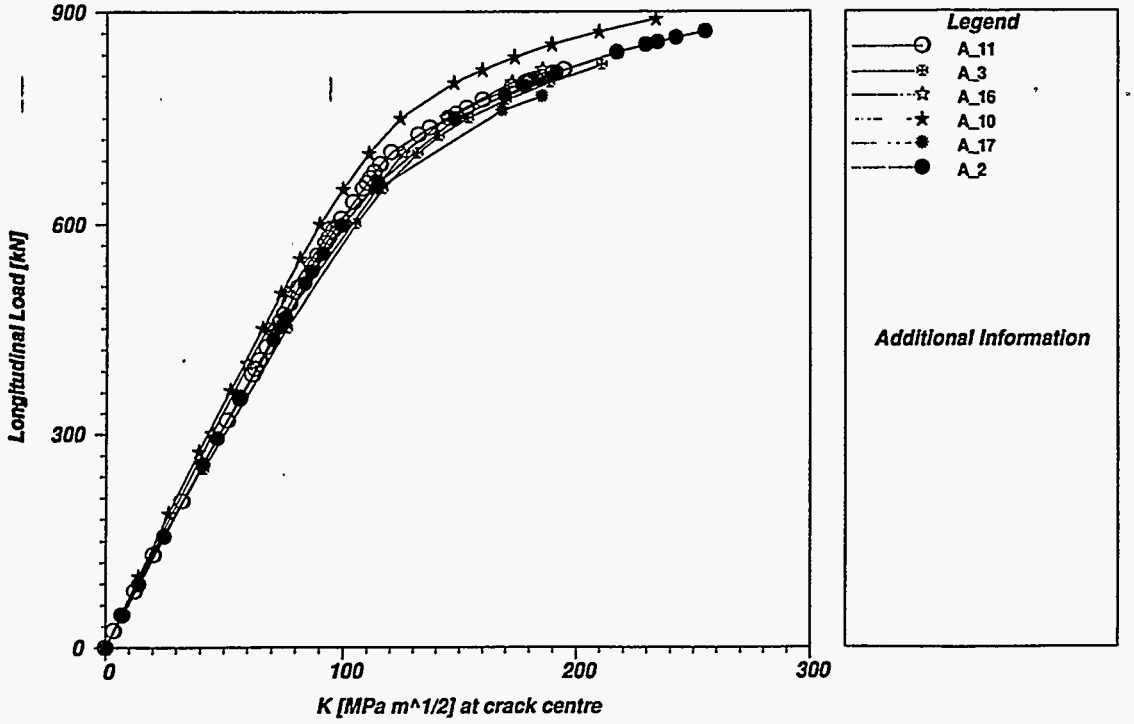

Figure 3.98 Longitudinal load vs applied K at crack center in BB-4 experiment

EFG 96-6645

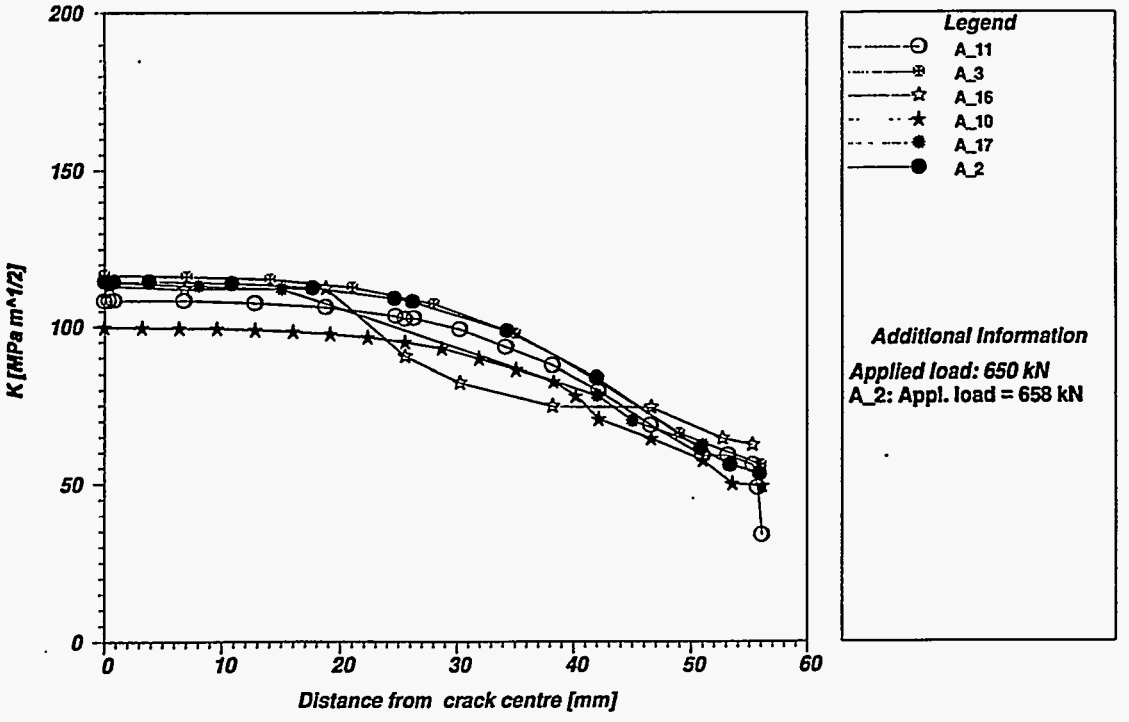

Figure 3.99 Applied K vs distance from crack center at applied load of 650 kN in BB-4 experiment

EFG 96-6646

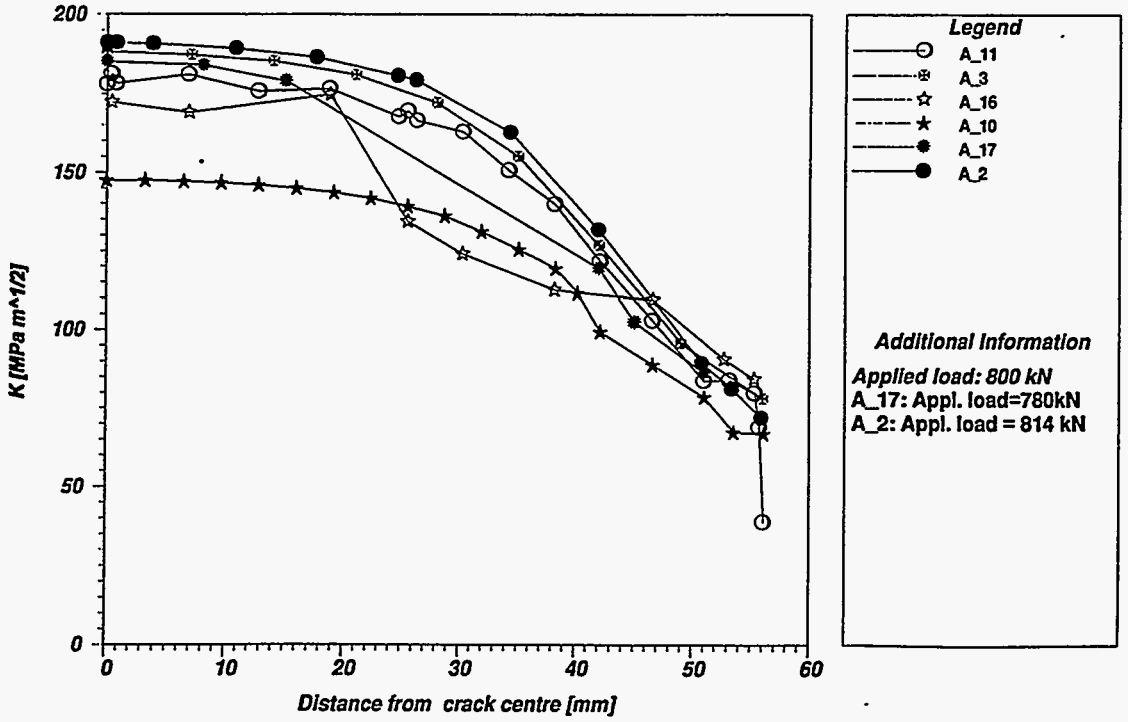

Figure 3.100 Applied K vs distance from crack center at applied load of 800 kN in BB-4 experiment

EFG 96-6647

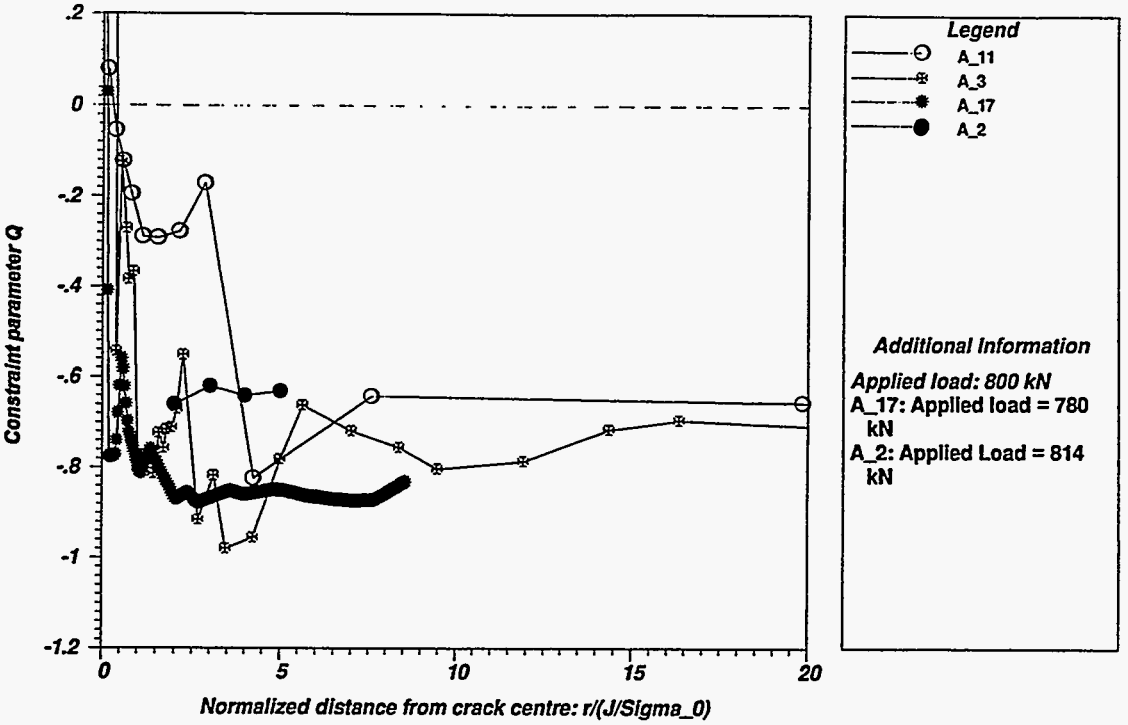

Figure 3.101 Constraint parameter Q vs normalized distance from crack along ligament at applied load of 800 kN in BB-4 experiment

EFG 96-6648

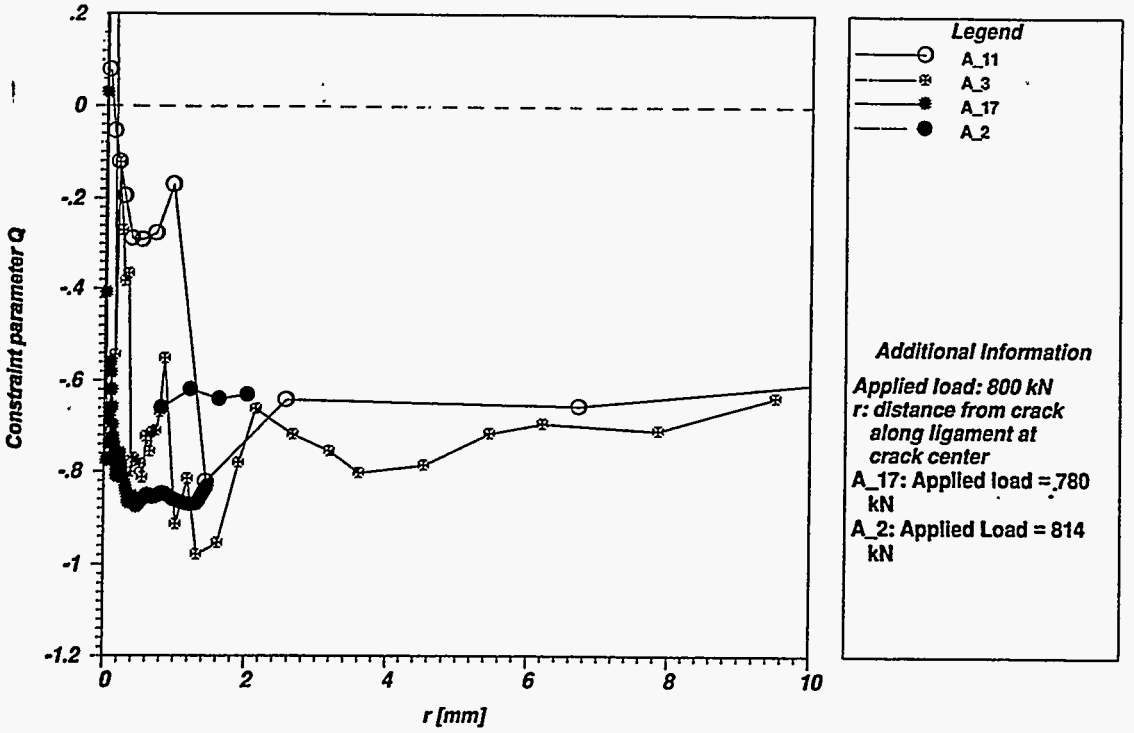

Figure 3.102 Constraint parameter Q vs distance from crack along ligament at applied load of 800 kN in BB-4 experiment

EFG 96-6649

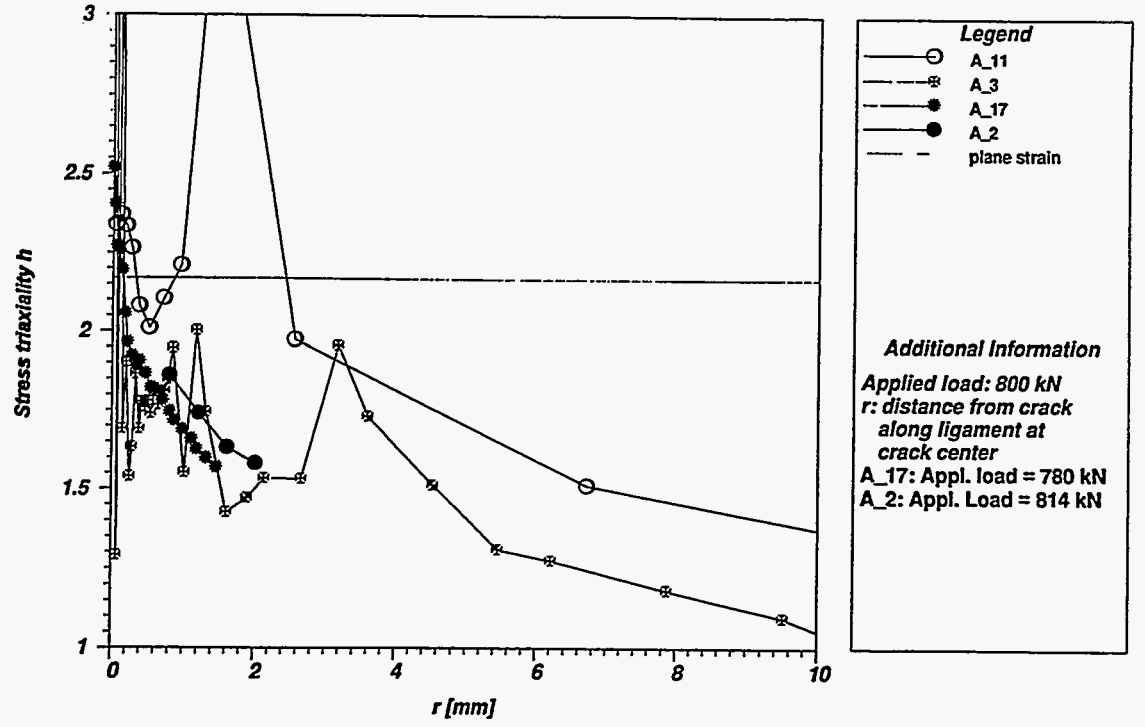

Figure 3.103 Stress triaxiality h vs distance from crack along ligament at applied load of 800 kN in BB-4 experiment

triaxiality parameter h along the ligament in front of the crack near the fracture load exhibited a pronounced departure from conditions of plane strain constraint.

The Q-stress approach of O'Dowd and Shih[2] represents one of several stress-based procedures for correlating constraint conditions at the crack tip. Others include the constraint correction procedure proposed by Dodds, Anderson, and Kirk.[9] Each of these approaches utilizes the effect of crack-tip constraint on the in-plane stresses at the crack tip to infer the effect of constraint on fracture toughness. These stress-based constraint methodologies have been applied successfully to correlate constraint conditions for in-plane (or uniaxial) loading conditions. However, investigations of biaxial loading effects have concluded that out-of-plane biaxial loading has little effect on in-plane stresses at the crack tip, but does influence the width of the crack-tip plastic zone in the direction of crack propagation.[10,11] Inconsistencies were observed in the calculated values of Q-stress in the region of normalized distance $r/(J/\sigma o) < 5$ for different biaxial loading ratios applied to the cruciform specimen.[10] (Similar inconsistencies can also be seen in Fig. 3.101 for BB-4.) More recent elastic-plastic finite element analyses of the biaxial cruciform specimen, using a model with a highly refined treatment of the crack-tip region, have confirmed these conclusions.[12] In Fig. 3.104, far-field stress biaxiality is seen to have little effect on the in-plane stresses near the crack tip of the ORNL cruciform specimen. The analyses confirm that the stress-based constraint procedures cannot predict the observed effects of out-of-plane biaxial loading on shallow-flaw fracture toughness.

Tetelman and McEvily[13] (T-M) and Wells*,[14] proposed that initiation of cleavage fracture is controlled by strains in the crack-tip region reaching a critical value. According to the T-M criterion, plastically induced fracture initiates in a ligament immediately adjacent to the blunted crack tip when the ligament strain reaches the fracture strain (ε_f) of the material. Wells argued that the conditions at fracture can be characterized by a critical crack-tip opening displacement (CTOD) (δ_c). As previously noted herein, a second (or dual) correlation parameter must also be introduced into the cleavage fracture model to quantify loss-of-constraint or departure from small-scale yielding conditions. Recent interpretations of the strain-based models by Pennell et al.[15] concluded that effects of constraint on fracture toughness can be quantified by determining the effects of ligament strain fields on crack-tip deformation. However, direct application of the latter strain-based

*A. A. Wells, "Unstable Crack Propagation in Metals—Cleavage and Fast Fracture," Cranfield Crack Propagation Symposium, 1, September 1961, p. 210.

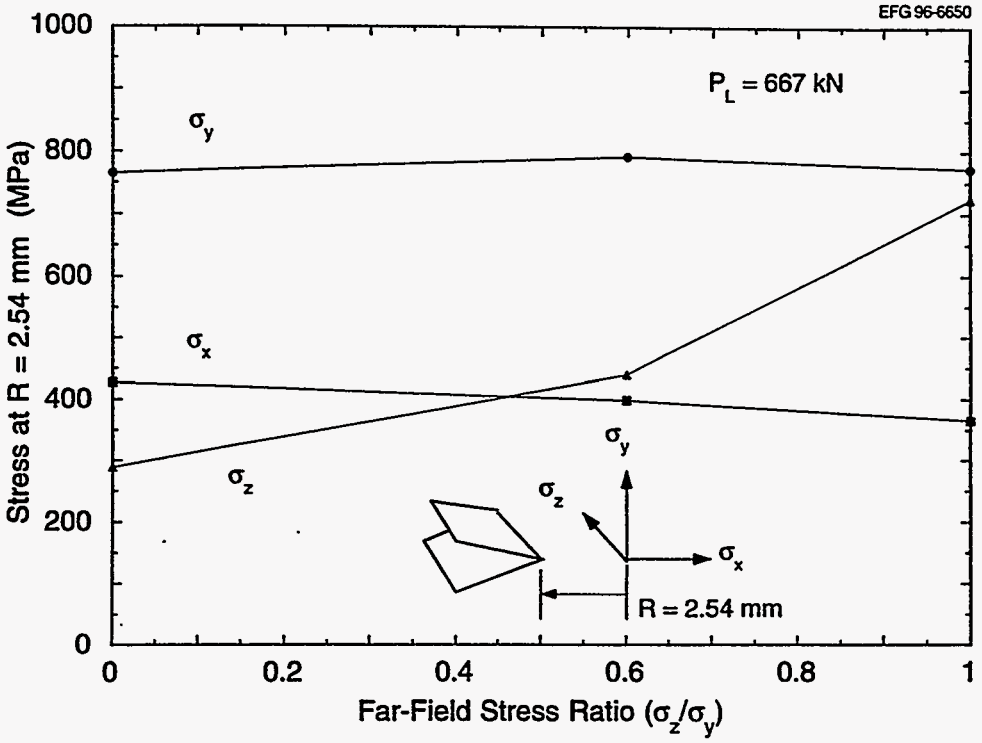

Figure 3.104 Dependence of in-plane and out-of-plane stresses near crack tip on far-field stress biaxiality for cruciform beam

approach would require a finite-strain, elastic-plastic, finite element analysis to determine the crack-tip deformation as a function of strain fields in the ligament. To circumvent this computationally intensive approach, an alternative methodology was proposed that utilizes R_{pl}, the plastic-zone width in the plane of the crack, as a second correlation parameter for fracture toughness.[15]

The case for using R_{pl} in a strain-based fracture-toughness correlation derives from the observation that the CTOD (δ) is a function of R_{pl} and that this relationship is constraint-dependent. Adopting a strip-yield model, Wells[14] studied the hypothesis that initiation of brittle fracture is uniquely determined by a critical value of δ. For plane stress conditions, he developed relationships between δ, R_{pl}, and overall plastic strain, for loading conditions that range from below to above general yielding. Beyond general yielding, he postulated that δ becomes proportional to the plastic strain taken over some gage length spanning the fully plastic area of the specimen.

The δ vs R_{pl} relationship has been studied by ORNL[16] for general beyond-plane-strain boundary conditions, for both contained and uncontained yielding, using test data from the biaxial cruciform testing program. A linear relationship between $\sqrt{\delta_c}$ and $\ln(R_{pl})$ was determined from 3-D finite element analysis of the biaxial test results at cleavage fracture initiation. These results are shown in Fig. 3.105, together with fracture-toughness data points obtained from the cruciform specimens. Also, in Fig. 3.105, the $\sqrt{\delta}$ vs $\ln(R_{pl})$ loading trajectories are depicted for three biaxial loading ratios (i.e., $P_T/P_L = 0$, 0.6, and 1.0) applied to the cruciform specimen. These loading trajectories were generated using a modified version of the Wells relation[15] for δ given by

$$\delta = \pi \bar{\varepsilon} R_{pl} \ , \tag{3.1}$$

where

$$\bar{\varepsilon} = \frac{1}{R_{pl}} \int_0^{R_{pl}} \varepsilon_{33} dr \ . \tag{3.2}$$

In Eq. (3.1), the integrated average of the opening-mode strain, $\bar{\varepsilon}$ taken over the plastic zone width, R_{pl}, replaces a quantity that Wells[15] defined as the overall tensile strain. In Fig. 3.106, variations of $\bar{\varepsilon}$ with longitudinal load, obtained from 3-D finite-element analysis of three biaxial loading cases, $P_T/P_L = 0$, 0.6, and 1, exhibit a pronounced dependence on biaxiality ratio. These $\bar{\varepsilon}$ vs load relations were used in Eq. (3.1), along with values of R_{pl} calculated from 3-D finite element analysis, to compute the predicted loading trajectories given in Fig. 3.105. These results confirm that a measure of the opening-mode strain field in the near-crack-tip ligament is capable of differentiating among the applied biaxial loading ratios to predict variations in biaxial loading trajectories.

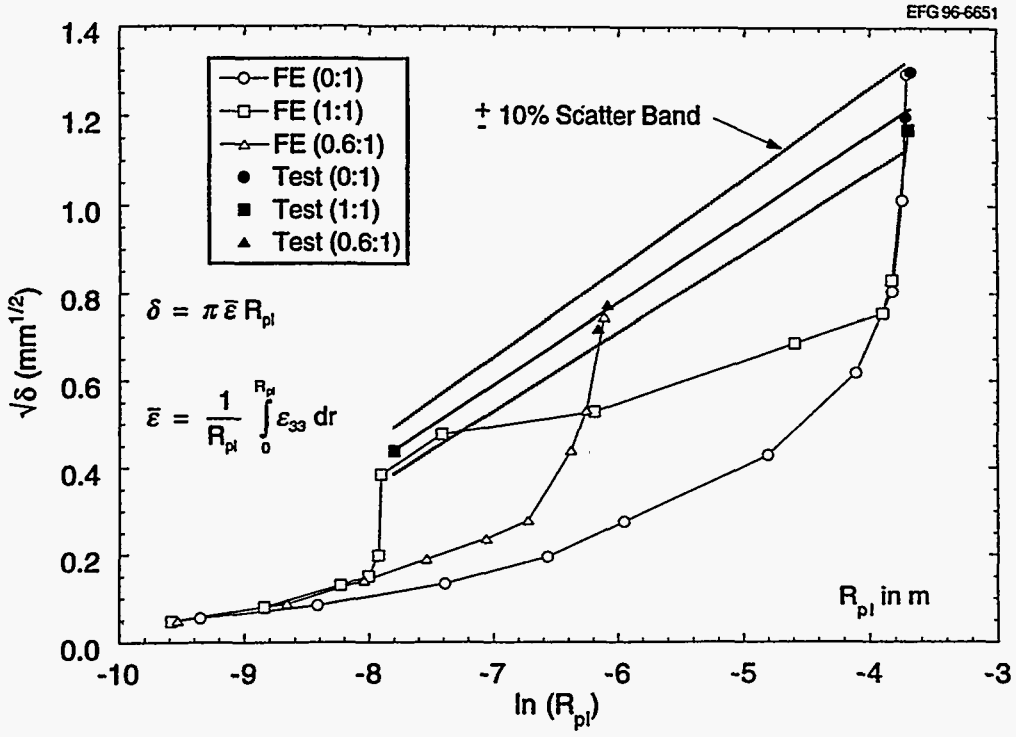

Figure 3.105 Dependence of CTOD on plastic zone width as function of biaxiality ratio in cruciform beam

Comparative

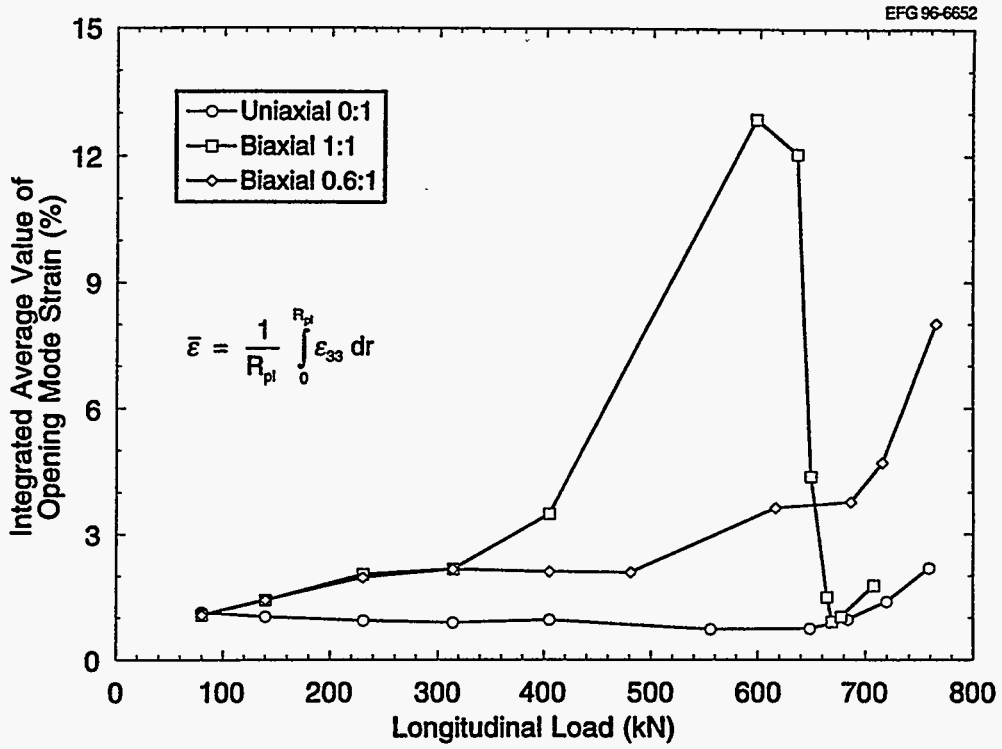

Figure 3.106 Variation of integrated average value of opening-mode strain with load shown as strongly dependent on biaxiality ratio for cruciform beams

In Fig. 3.105, the range of fracture toughness values possible at T – NDT = –10°C, for a given loading condition, is predicted by the intersection of the $\sqrt{\delta}$ vs $\ln(R_{pl})$ loading trajectories with the $\sqrt{\delta_c}$ vs $\ln(R_{pl})$ fracture toughness locus. Intersection of these nonlinear trajectories with the linear toughness locus is governed by the dependence of the trajectories on constraint as influenced by the biaxial loading ratio. Unique toughness values are predicted for the uniaxial ($P_T/P_L = 0$) and biaxial ($P_T/P_L = 0.6$) loading cases. The intersection of the trajectory for equibiaxial ($P_T/P_L = 1$) loading with the toughness locus predicts both low- and high-toughness values for this loading condition. In fact, these low- and high-toughness values were realized in tests of the biaxial ($P_T/P_L = 1$) loading case. Uncontained yielding that developed in two of the biaxial ($P_T/P_L = 1$) tests gave high-toughness values that were similar to those of the uniaxial loading tests. Analysis results[17] demonstrate that linearity of the K_J vs $\sqrt{\delta}$ relationship is preserved under the full range of biaxial loading ratios. Thus, the results in Fig. 3.105 can be restated in terms of equivalent K_J and K_{Jc} vs $\ln(R_{pl})$ relationships for the cruciform testing program.[16] Collectively, the results depicted in Figs. 3.105 and 3.106 confirm that $\ln(R_{pl})$ is a viable second parameter for characterizing strain-controlled fracture. This is an important observation because the parameter R_{pl} is relatively easy to calculate, making the resulting dual-parameter fracture-toughness correlation easy to use.

Other possible approaches (not considered here) include a modified version of the Dodds-Anderson scaling model,[17] in which the Weibull stress, σ_w, is adopted as a near-tip parameter to relate remote loading with a micromechanics model based on weakest-link statistics.[18]

References

1. D. J. Lacey et al., "Spinning Cylinder Test 4: An Investigation of Transition Fracture Behavior for Surface Breaking Defects in Thick-Section Steel Specimens," AEA Technology Report AEA TRS 4098, June 1991.

2. N. P. O'Dowd and C. F. Shih, "Family of Crack-Tip Fields Characterized by a Triaxiality Parameter: Part I—Structure of Fields," *J. Mech. Phys. Solids* 39(8), 989–1015, 1991.*

3. H. Kordisch, E. Sommer, and W. Schmitt, "The Influence of Triaxiality on Stable Crack Growth," *Nucl. Eng. Des.* 112, 27–35, 1989.*

4. H. Keinänen et al., "Pressurized Thermal Shock Tests with Model Pressure Vessels Made of VVER-40

Reactor Steel," pp. 275–88 in *Proceedings of IAEA Specialists' Meeting on Fracture Mechanics Verification by Large-Scale Testing, Oak Ridge, Tennessee, October 26–29, 1992.* USNRC Conference Proceeding NUREG/CP-0131 (ORNL/TM-12413), October 1993.‡

5. L. Stumpfrock et al., "Fracture mechanic investigations on cylindrical large-scale specimens under thermal-shock loading," *Nucl. Eng. Des.*, 144, 31–44 (1993).*

6. D. Moinereau et al., "Cleavage Fracture of Specimens Containing an Underclad Crack," *PVP* Vol. 233, *Pressure Vessel Fracture, Fatigue and Life Management* (American Society of Mechanical Engineers, 1992).*

7. B. R. Bass, T. L. Dickson, W. J. McAfee, and W. E. Pennell, Lockheed Martin Energy Research Corp., Oak Ridge Natl. Lab., "Assessment of the Influence of Clad Behavior on Reactor PressureVessel Integrity," ORNL/NRC/LTR-95/02, January 1996.†

8. M. G. Dawes, "Significance of Locally Intensified Strain Aging to the Fracture Toughness of Welded Steel Structures," *Fracture Mechanics: 26th Volume, ASTM STP 1256*, W. G. Reuter, J. H. Underwood, and J. C. Newman, Jr., Eds. (American Society for Testing Materials, Philadelphia, 1995).*

9. R. H. Dodds, Jr., T. L. Anderson, and M. T. Kirk, "A Framework to Correlate a/W Ratio Effects on Elastic-Plastic Fracture Toughness (J_c)," *Int. J. Fract.* 48, 1–22 (1991).

10. B. R. Bass, J. W. Bryson, T. J. Theiss, and M. C. Rao, Martin Marietta Energy Systems, Inc., Oak Ridge Natl. Lab., "Biaxial Loading and Shallow Flaw Effects on Crack-Tip Constraint and Fracture Toughness," USNRC Report NUREG/CR-6132 (ORNL/TM-12498), January 1994.‡

11. W. E. Pennell, "Heavy-Section Steel Technology Program: Recent Developments in Crack Initiation and Arrest Research," *Nucl. Eng. Des.* 255–66 (1993).*

12. W. J. McAfee, B. R. Bass, J. W. Bryson, and W. E. Pennell, Martin Marietta Energy Systems, Inc., Oak Ridge Natl. Lab., "Biaxial Loading Effects on Fracture Toughness of Reactor Pressure Vessel Steel," USNRC Report NUREG/CR-6273 (ORNL/TM-12866), May 1995.‡

13. A. S. Tetelman and A. J. McEvily, Jr., *Fracture of Structural Materials*, John Wiley & Sons, Inc., New York, 1967.

14. A. A. Wells, "Application of Fracture Mechanics at and Beyond General Yielding," Report M13/63, British Welding Research Association, *British Welding Journal*, 563–70 (November 1963).

15. W. E. Pennell and W. R. Corwin, "Reactor Pressure Vessel Structural Integrity Research," *Nucl. Eng. Des.* 157(1–2), 159–175 (1995).

16. W. E. Pennell et al., "Preliminary Assessment of the Effects of Biaxial Loading on Reactor Pressure Vessel Structural-Integrity-Assessment Technology," pp. 173–86 in *Proceedings of the ASME-JSME 4th International Conference on Nuclear Engineering, New Orleans, Louisiana, March 10–14, 1996,* Vol. 1—Part A (American Society of Mechanical Engineers, New York, 1996).*

17. R. H. Dodds, Jr., T. L. Anderson, and M. T. Kirk, "A Framework to Correlate a/W Ratio Effects on Elastic-Plastic Fracture Toughness (J_c)," *Int. J. Fract.* 48, 1-22 (1991).*

18. C. Ruggieri and R. H. Dodds, Jr., "Constraint and Ductile Tearing Effects in Statistical Analyses of Cleavage Fracture," Report UILU-ENG-95-2011, University of Illinois at Urbana-Champaign, October 1995.

*Available from public technical libraries.
†Available in NRC PDR for inspection and copying for a fee.
‡Available for purchase from the National Technical Information Service, Springfield, VA 22161.

4 Summary and Conclusions

Within FALSIRE II, comparative assessments have been performed for 7 reference fracture experiments based on 45 analyses received from 22 organizations representing 12 countries. The measured data and the analytical results from FALSIRE II have been made available in an electronic data base. Some conclusions from FALSIRE II follow:

- The temperature distributions in the specimens loaded by thermal shock generally were approximated with high accuracy and small scatter bands. Discrepancies appeared only for limited time periods during the transients and could be traced to different assumptions concerning the heat transfer coefficients.
- Structural response (i.e., CMOD, strains, etc.) of the test specimens was predicted reasonably well from best-estimate analyses. This outcome represents a significant change compared with some of the results achieved in FALSIRE I. In part, the change reflects a more widespread recognition that the assumptions adopted to ensure failure avoidance in safety assessments are inappropriate when attempting to predict actual failure.
- Discrepancies that appeared in the structural calculations could usually be traced to the assumed material models and to approximations of material properties (i.e., stress-strain data).
- Calculations of fracture parameters such as J or K_I and the parameter CMOD generally showed small scatter bands. Discrepancies could be traced to the differences between elastic and elastoplastic approaches or assumptions concerning material properties.
- The K_I vs temperature diagram combined with material data curves describing fracture toughness vs temperature were determined to be useful for fracture assessments of crack behavior. Crack initiation could be predicted from a single fracture parameter (K_I, J, etc.), reasonably well in tests where initiation was not significantly affected by constraint effects.
- When constraint effects become significant, a single parameter is not sufficient to characterize crack-tip conditions, and a second parameter must be introduced into the fracture model. Candidate constraint parameters employed by the participating analysts include Q-stress, stress triaxiality h, local approach of cleavage fracture, and a strain-based function of the plastic-zone width in the crack plane. In the SC-4 experiment, constraint effects were quantified using the Q-stress and, to a more limited degree, the triaxiality parameter h. In PTS-I/6 and NKS-5, the parameter h showed indications of loss-of-constraint, while the Q-stress was not evaluated. Finally, in BB-4, a shallow-crack effect was demonstrated by the computed Q-stress, which indicated a loss-of-constraint associated with the departure of in-plane stresses from reference small-scale yielding conditions.
- The Q-stress and other stress-based constraint methodologies have been applied successfully to correlate constraint conditions for in-plane (or uniaxial) loading conditions. However, prior studies have determined that stress-based constraint methodologies (such as the Q-stress) are not sensitive to changes in constraint conditions due to changes in out-of-plane biaxial loading. The plastic zone width was employed successfully to correlate changes in constraint conditions for shallow cracks subjected to changes in out-of-plane biaxial loading ratios. Further investigations are necessary to clarify whether one parameter can be recommended or a set of parameters should be computed to assess constraint effects.
- Additional toughness data measured in the transition temperature region using a range of specimen geometries and constraint conditions are required to validate the predictive capabilities of cleavage fracture methodologies that incorporate constraint effects.
- Simulations of crack growth and crack arrest events (e.g., in NKS-6) showed large uncertainties among the applied fracture methods.
- Additional data concerning the HAZ fracture toughness are necessary for further refinement of analyses of shallow subclad flaws.
- Almost all participants elected to use the finite-element method in addressing the problems of FALSIRE II. This represents a marked change from FALSIRE I, which included applications of a number of different estimation schemes. The detailed information that participants were asked to provide from the analyses in FALSIRE II encouraged the use of finite-element methods over estimation schemes (see the Special Requirements given in the appendix). It should not be inferred from the outcome of FALSIRE II that detailed finite-element analyses are always the preferred or necessary technique for structural integrity assessments.

5 Proposals for Future Work

An RPV Benchmark Analysis Project is being planned for the benefit of organizations concerned with evaluation of fracture methodologies used in RPV integrity assessments. This project is motivated in part by the strong interest expressed by participants in Phases I and II of FALSIRE to proceed with further evaluations of fracture mechanics analysis methods.

The RPV Benchmark Analysis Project will focus on a Western-type four-loop RPV with cladding on the inner surface. Primary emphasis of the project will be placed on the behavior of relatively shallow cracks (underclad and through-clad) at different locations in the vessel when subjected to PTS-type loading due to emergency core cooling. Cracks will be proposed at positions near core circumferential welds, near injection nozzle welds, and at the corner of an injection nozzle. Effects of cladding and constraint on cleavage fracture will be studied.

A detailed analysis matrix will be defined for the vessel that includes selected cases of transient thermomechanical loading associated with postulated loss-of-coolant accidents. Different assumptions will be made concerning the thermally shocked regions on the inner surface of the vessel. The number of cooling strips under the inlet nozzles will be varied, as well as the width of the cooled strips, so that comparisons can be made with the loading case due to axisymmetric cooling. Additional tasks will be proposed that can be addressed using thermohydraulic analysis techniques. Elements that will be of interest include calculations of fluid temperature and heat transfer to the vessel, with consideration given to fluid mixing as well as steam condensation.

The schedule for the RPV Benchmark Analysis Project calls for the OC to commence distribution of problem statements in mid-1996. Analysts participating in the Benchmark Project will be requested to submit analysis results to the OC by Spring 1997 in preparation for a workshop scheduled for Fall 1997 in the Eastern United States. A final report (included a NUREG report) will be issued after completion of the workshop.

GRS-Köln and ORNL will serve as co-organizers of all elements of the RPV Benchmark Analysis Project, which involves the following tasks: preparing the Call for Participation form; preparing the Benchmark Analysis Problem Statement package; soliciting candidate participants; monitoring progress of and providing assistance to participating analysts; developing an analysis results data base; and developing the technical program for a Specialists' Workshop to be held during Fall 1997, where all participating analysts will perform detailed evaluations of the benchmark analyses submitted to the OC. ORNL will be responsible for local arrangements and will serve as host of the Specialists' Workshop in an Eastern United States location yet to be determined. Also, ORNL will be responsible for preparation of a NUREG final report describing results and interpretations derived from the RPV Benchmark Analysis Project.

Appendix

Special Requirements for Comparative Analyses of Reference Experiments

Special Requirements Concerning Comparative Analyses Within FALSIRE Phase II

- **SC-IV**
  - temperature distribution in the wall for the times 0, 0.5, 1, 2, and 5 min
  - time history of outer surface axial strains (gages 6 and 8) and circumferential strains (gages 1 and 5; for locations see Fig. 5.2 of problem statements) without thermal part ($\alpha \Delta T$)
  - time history of crack-mouth-opening displacement at the middle of the 40-/60-mm crack
  - circumferential stress and effective stress in the wall without influence of the crack and on the ligament with influence of the crack at the deepest point and at a near-surface point of the crack front (about 4/7 mm in depth from the inner surface for the 40/-60-mm crack) for the times 0[10], 2, and 4 min
  - time history of J-integral at the deepest point and at a near-surface point of the crack front (about 4/7 mm in depth from the inner surface for the 40-/60-mm crack)
  - J-integral vs crack front angle (for definition see Fig. 15 of NKS-5 problem statement) for the times 0[10], 2, and 4 min
  - stress intensity factor vs crack-tip temperature at the deepest point and at a near-surface point of the crack front (about 4/7 mm in depth from the inner surface for the 40-/60-mm crack)
  - constraint/stress triaxiality parameters[11] on the ligament[12] at the deepest point and at a near-surface point of the crack front (about 4/7 mm in depth from the inner surface for the 40-/60-mm crack) for the times 0[10], 2, and 4 min

[10]Only mechanical loading occurs at t = 0.

[11]Recommended parameters are Q – stress, T – stress, and $h = \sigma_{hyd}/\sigma_{eff}$.

[12]For Q and h the evaluation region on the ligament should be about 10 mm from the crack front but also values on the order of (J_i/σ_{yield}) near the crack front (with J_i lower-bound physical ductile initiation value or calculated from K_{Ic} in case of cleavage) are desirable.

Special Requirements Concerning Comparative Analyses Within FALSIRE Phase II

- **PTS-1/6**

  - temperature distribution in the wall for the times 0, 0.5, 1, 2.5, and 5 min at the height 1000 mm from the vessel bottom

  - time history of outer surface circumferential strains without thermal part ($\alpha \Delta T$) at location S14 (740 mm from the vessel bottom, 360 mm from the crack line)

  - time history of crack-mouth-opening displacement at the middle of the crack and at the height of 1000 mm (location of gage S15)

  - hoop stress and effective stress in the wall without influence of the crack and on the ligament near positions 13, 9, and 21 (see page 14.4 of problem statements) with influence of the crack for the times 0[7], 0.5, 1, 2.5, and 5 min

  - time history of J-integral from 0[7] to 5 min near positions 13, 9, and 21 (see page 14.4 of problem statements)

  - stress intensity factor vs crack front angle (for definition see Fig. 15 of NKS-5 problem statement) for the times 0[7], 0.5, 1, and 2.5 min

  - stress intensity factor vs crack-tip temperature near positions 13, 9, and 21 (see page 14.4 of problem statements)

  - constraint/stress triaxiality parameters[8] on the ligament[9] near positions 13, 9, and 21 of the crack for the times 0[7], 0.5, 1, and 2.5 min

---

[7]Only mechanical loading occurs at t = 0.

[8]Recommended parameters are Q – stress, T – stress, and $h = \sigma_{hyd}/\sigma_{eff}$.

[9]For Q and h the evaluation region on the ligament should be about 10 mm from the crack front but also values on the order of (J_i/σ_{yield}) near the crack front (with J_i lower-bound physical ductile initiation value or calculated from K_{Ic} in case of cleavage) are desirable.

Special Requirements Concerning Comparative Analyses Within FALSIRE Phase II

- **NKS-5**
  - temperature distribution in the wall for the times 0, 1, 2, 5, 7.5, 10, 42, and 60 min
  - time history of inner surface axial and circumferential strains without thermal part ($\alpha \Delta T$) at location DL5/DU5 (366 mm below the crack ligament)
  - time history of crack-mouth-opening displacement at the middle of the crack
  - axial stress and effective stress in the wall without influence of the crack and on the ligament of the deepest point and surface point with influence of the crack for the times 0[1], 1, 2, 5, 7.5, 10, 42, and 60 min
  - time history of J-integral at the deepest point and at the surface point
  - J-integral vs crack front angle (for definition see Fig. 15 of the problem statement) for the times 0[1], 1, 2, 5, 7.5, 10, 42, and 60 min
  - stress intensity factor vs crack-tip temperature at the deepest point and at the surface point
  - constraint/stress triaxiality parameters[2] on the ligament[3] of the crack at the deepest point and at the surface point for the times 0[1], 1, 2, 5, 7.5, 10, 42, and 60 min

[1]Only mechanical loading occurs at t = 0.

[2]Recommended parameters are Q – stress, T – stress, and $h = \sigma_{hyd}/\sigma_{eff}$.

[3]For Q and h the evaluation region on the ligament should be about 10 mm from the crack front but also values on the order of (J_i/σ_{yield}) near the crack front (with J_i lower-bound physical ductile initiation value or calculated from K_{Ic} in case of cleavage) are desirable.

Special Requirements Concerning Comparative Analyses Within FALSIRE Phase II

- **NKS-6**
  - temperature distribution in the wall for the times 0, 0.5, 1, 1.5, 2, and 5 min
  - time history of inner surface axial and circumferential strains without thermal part ($\alpha \Delta T$) at location DL3/DU3 (184 mm above the crack ligament)
  - time history of crack-mouth-opening displacement at the middle of the crack
  - axial stress and effective stress in the wall without influence of the crack and on the ligament with influence of the crack for the times 0[4] ,0.5, 1, 1.5, 2, and 5 min
  - time history of J-integral
  - stress intensity factor vs crack-tip temperature
  - constraint/stress triaxiality parameters[5] on the ligament[6] of the crack for the times 0[4], 0.5, 1, 1.5, 2, and 5 min

[4]Only mechanical loading occurs at t = 0.

[5]Recommended parameters are Q – stress, T – stress, and $h = \sigma_{hyd}/\sigma_{eff}$.

[6]For Q and h the evaluation region on the ligament should be about 10 mm from the crack front but also values on the order of (J_i/σ_{yield}) near the crack front (with J_i lower-bound physical ductile initiation value or calculated from K_{Ic} in case of cleavage) are desirable.

Special Requirements Concerning Comparative Analyses Within FALSIRE Phase II

- **DD2/DSR3**

– load vs load line displacement

– crack-opening displacement vs distance from cladding at the position of the crack symmetry line for the loads 300, 600, and 900 kN (for DD2) and 300, 600, and 700 kN (for DSR3)

– load vs maximum crack-mouth opening (with factor of 2 due to symmetry)

– load vs strain at positions of gages J3, J7, and J8

– crack-opening stress and effective stress vs ligament at the deepest point for the loads 300, 600, and 900 kN (for DD2) and 300, 600, and 700 kN (for DSR3)

– load vs stress intensity factor at the deepest point of the crack

– stress intensity factor vs crack front angle (for definition see Fig. 15 of NKS-5 problem statement) for the loads 300, 600, and 900 kN (for DD2) and 300, 600, and 700 kN (for DSR3)

– constraint/stress triaxiality parameters[15] on the ligament[16] at the deepest point of the crack and at the point of cleavage initiation for the loads 300, 600, and 900 kN (for DD2) and 300, 600, and 700 kN (for DSR3)

– fracture toughness value based on the information about the point of cleavage initiation and the measured failure loads (890 kN for DD2 and 695 kN for DSR3)

[15]Recommended parameters are Q – stress, T – stress, and $h = \sigma_{hyd}/\sigma_{eff}$.

[16]For Q and h the evaluation region on the ligament should be about 10 mm from the crack front but also values on the order of (J_i/σ_{yield}) near the crack front (with J_i lower-bound physical ductile initiation value or calculated from K_{Ic} in case of cleavage) are desirable.

Special Requirements Concerning Comparative Analyses Within FALSIRE Phase II

- **BB-4**
  - longitudinal load (both arms) vs load line displacement
  - longitudinal load (both arms) vs crack-mouth-opening displacement at the middle of the crack
  - crack-opening stress component and von Mises effective stress on the ligament at the middle of the crack for the longitudinal load 450, 650, and 800 kN
  - longitudinal load (both arms) vs stress intensity factor at the middle of the crack
  - stress intensity factor vs distance from specimen center for the longitudinal load 450, 650, and 800 kN
  - constraint/stress triaxiality parameters[13] on the ligament[14] at the middle of the crack for the longitudinal loads 450, 650, and 800 kN

[13]Recommended parameters are Q – stress, T – stress, and $h = \sigma_{hyd}/\sigma_{eff}$.

[14]For Q and h the evaluation region on the ligament should be about 10 mm from the crack front but also values on the order of (J_i/σ_{yield}) near the crack front (with J_i lower-bound physical ductile initiation value or calculated from K_{Ic} in case of cleavage) are desirable.

INTERNAL DISTRIBUTION

1-5. B. R. Bass
6. J. W. Bryson
7. W. R. Corwin
8. W. G. Craddick
9. R. G. Gilliland
10. D. M. Hetrick
11. S. K. Iskander
12. J. A. Keeney
13. M. A. Kuliasha
14. W. J. McAfee
15. D. E. McCabe
16. J. G. Merkle
17. R. K. Nanstad
18 J. V. Pace, III
19. W. E. Pennell
20-24. C. E. Pugh
25-27. S. J. Ranney
28. J. Sheffield
29. J. O. Stiegler
30. ORNL Patent Section
31. Central Research Library
32. Document Reference Section
33-34. Laboratory Records
35. Laboratory Records (RC)

EXTERNAL DISTRIBUTION

36-40. A. Miller, OECD Nuclear Energy Agency, Le Seine Saint Germain, 12 Boulevard des Iles, 92130 Issy-les-Moulineaux, France
41-45. H. Schulz, Head, Structural Mechanics Department, Gesellschaft fur Anlagen-und Reaktorsicherheit, Schwertnergasse 1, D-50667, Koln, Germany
46-50. J. Sievers, Gesellschaft fur Anlagen-und Reaktorsicherheit, Schwertnergasse 1, D-50667, Koln, Germany
51-53. M. G. Vassilaros, U.S. Nuclear Regulatory Commission, Office of Nuclear Regulatory Research, Division of Engineering Technology, Electrical, Materials, and Mechanical Engineering Branch, Mail Stop T10 E10, Washington, D.C. 20555-0001
54. M. E. Mayfield, U.S. Nuclear Regulatory Commission, Office of Nuclear Regulatory Research, Division of Engineering Technology, Electrical, Materials, and Mechanical Engineering Branch, Mail Stop T10 E10, Washington, D.C. 20555-0001
55. M. Vagins, U.S. Nuclear Regulatory Commission, Office of Nuclear Regulatory Research, Division of Engineering Technology, Mail Stop T10 E10, Washington, D.C. 20555-0001
56. L. C. Shao, U.S. Nuclear Regulatory Commission, Office of Nuclear Regulatory Research, Division of Engineering Technology, Mail Stop T10 D20, Washington, D.C. 20555-0001
57. J. R. Strosnider, U.S. Nuclear Regulatory Commission, Office of Nuclear Reactor Regulation, Division of Engineering, Mail Stop O7 D4, Washington, D.C. 20555-0001
58. S. N. M. Malik, U.S. Nuclear Regulatory Commission, Office of Nuclear Regulatory Research, Division of Engineering Technology, Electrical, Materials, and Mechanical Engineering Branch, Mail Stop T10 E10, Washington, D.C. 20555-0001
59-89. IAEA/IWG/LMNPP Members
90. B. Gueorguiev, International Atomic Energy Agency, Division of Nuclear Power, Wagramerstrasse 5, P. O. Box 100, A-1400 Vienna, Austria
91. V. Lyssakov, International Atomic Energy Agency, Division of Nuclear Power, Wagramerstrasse 5, P. O. Box 100, A-1400 Vienna, Austria
92. J. Pachner, International Atomic Energy Agency, Division of Nuclear Safety, Wagramerstrasse 5, P. O. Box 100, A-1400 Vienna, Austria

93. R. Havel, International Atomic Energy Agency, Division of Nuclear Safety, Wagramerstrassse 5, P. O. Box 100, A-1400 Vienna, Austria
94. L. Myrddin Davies, 176 Cumnor Hill, Oxford, GB-OX2 9PJ, United Kingdom
95. Y. Kurakov, Staromonetny 26, Minatom, 109180 Moscow, Russia
96. G. P. Karzov, Prometey, Central Research Institute for Structural Materials, Monastyrka River Quay 1, 192167 St. Petersburg, Russia
97. U. Von Estorff, European Commission, Joint Research Centre, NL 1755 ZG Petten, P. O. Box 2, The Netherlands
98. S. Crutzen, European Commission, Joint Research Centre, NL 1755 ZG Petten, P. O. Box 2, The Netherlands
99. K. Torronen, EC DGJRC/IAM, European Commission, Joint Research Centre, NL 1755 ZG Petten, P. O. Box 2, The Netherlands
100. P. Mignot, Branch Head, Nuclear Safety Analysis Department, AIB-Vincoue Nuclear, Av. Du Roi. 157, B-1060 Bruxelles, Belgium
101. K. Pereira, ABCB, 280 Slater Street, P. O. Box 1046, Station B, Ottawa, Ontario K1P SS9, Canada
102. C. Ottosson, STUK, Department of Reactor Safety, P. O. Box 14, FIN-00881 Helsinki, Finland
103. K. Kussmaul, Director, MPA Stuttgart, Universitat Stuttgart, Pfaffenwaldring 32, D70569 Stuttgart, Germany
104. L. Brusa, ENEL/ATN, Viale Regina Margherita, 137, I-00198 Roma, Italy
105. K. Shibata, Head, Reactor Cpt. Rel. Lab., Nuclear Safety Research Center, JAERI Tokai Research Establishment, Tokai-Mura, Naka-gun, Ibaraki-ken 319-11, Japan
106. Y-W. Park, Korea Institute of Nuclear Safety (KINS), P. O. Box 114, Yuscong, Taejon, Korea
107. J. M. Figueras, Consejo de Seguridad Nuclear, Subdirection de Analysis, y Evaluacion, C/Justo Dorado 11, E-28040, Madrid, Spain
108. G. Frescura, Head, Nuclear Safety Division, OECD Nuclear Energy Agency, Le Seine St-Germain, 12 Boulevard des Iles, F-92130 Issy-les-Moulineaux, France
109. H. Keinanen, VTT Manufacturing Technology, Tekniikantie 12, Espoo, P. O. Box 17041, FIN-02044, Finland
110. J. Brochard, Centre D-Etudes de Saclay, 91191 GIF sur Yvette Cedex, Saclay, France
111. C. Faidy, EDF Septen, 12 Av. Dutrievoz, 69628 Villeurbanne, France
112. D. Moinereau, Electricite de France, Les Renardieres, route de Sens, B.P.1-Eculles, 77250 Moret sur Loing, Paris, France
113. E. Keim, Siemens, KWU AG Abt. NT13, Freyeslebenstr. 1, D-91058 Erlangen, Germany
114. L. Stumpfrock, MPA Stuttgart, Pfaffenwaldring 32, D-70569, Stuttgart, Germany
115. M. Beghini, DCMN-U. of Pisa, Via Diotisalvi, 2 Pisa 56126, Italy
116. S. McAllister, European Commission, Joint Research Centre, Structural Component Integrity Unit, Postbus 2, 1755ZG Petten, The Netherlands
117. A. Kiselev, RRC Kurchatov Institute, Pl. Kurchatov-1, Moscow 123182, Russia
118. V. Kostylev, Prometey, Central Research Institute for Structural Materials, Monastyrka River Quay 1, 192167 St. Petersburg, Russia
119. L. Anderson, Onsala Ingenjorsbyra, Tulla lagom 11, Onsala 43930, Sweden
120. M. Niffenegger, PSI Switzerland, PSI-Ost, CH-5232 Villigen, Switzerland
121. V. V. Pokrovsky, Institute for Problems of Strength, National Academy of Science of Ukraine, 2 Timiryazovskaya Str. Kiev 252014, Ukraine
122. A. H. Sherry, AEA Technology, Risley, Warrington, WA3 6AT, United Kingdom
123. R. Sillitoe, Nuclear Electric PLC, Berkeley Technology Centre, Berkeley, Gloucestershire, GL13 9PB, United Kingdom
124. W. Lee, FMC, 1205 Coleman Avenue, Santa Clara, CA 95052
125. C. W. Schwartz, University of Maryland, Department of Civil Engineering, College Park, MD 20742

126. S. Sheng, U.S. Nuclear Regulatory Commission, Office of Nuclear Reactor Regulation, Mail Stop OWFN 7D4, Washington, D.C. 20555-0001
127. K. Wichman, U.S. Nuclear Regulatory Commission, Office of Nuclear Reactor Regulation, Mail Stop OWFN 7D4, Washington, D.C. 20555-0001
128. J. Wintle, AEA Technology, Risley Warrington, Cheshire W A3 6AT, United Kingdom
129. S. Bhandari, Framatome, Tour Framatome, F-92084 Paris la Defense, CEDEX 16, France
130. D. Aker, BMT, Bat. 454, CEA, CEN Saclay, 91191 Gif Sur Yvette, France
131. F. Boydon, HSE, NII, St. Peter's House, Balliol Road, Bootle, Merseyside L20 3LZ, United Kingdom
132. D. Lidbury, AEA Technology, Risley Warrington, Cheshire W A3 6AT, United Kingdom
133. M. C. Smith, Nuclear Electric plc, Berkeley Technology Centre, Gloucestershire GL13 9PB, England
134. G. Airey, Nuclear Electric plc, Barnett Way, Barnwood, Gloucester GL4 7RS, England
135. B. Crossland, Queen's University Belfast, Belfast BT7 1NN, Northern Ireland
136. S. Finzi, EC DGXI/C2, Rue de la Loi 200, BU 56/121, B1049 Brussels, Belgium
137. B. Hemsworth, B. Hemsworth Associates, Engineering Safety Consultants, Maple House, Carin Lane, Appleton, Warrington W A4 5NF, United Kingdom
138. R. C. Hurst, EC DGJRC/IAM, P. O. Box 2, NL-1755 ZG Petten, The Netherlands
139. R. Nichols, Nichols Consultancies, Squirrels 3, Cockney Hill, Tilehurst, Reading RG30 4HF, United Kingdom
140. A. Pellissier-Tanon, Framatome, Tour Framatome, F-92084 Paris-la-Defense CEDEX 16, France
141. R. Rintamaa, VTT-Technical Rsearch Centre, P.B. 1704, FIN-02044 VTT, Espoo, Finland
142. D. P. Miannay, ISPN/DES/SAMS, CEA, B.P. No. 6, F-92265 Fontenay-Aux-Roses, France
143. F. Nilsson, Department of Solid Mechanics, Royal Institute of Technology, S-10044 Stockholm, Sweden
144. G. Bart, Head, Lab Material Behavior, Paul Scherrer Institute, CH-5232 Villigen PSI, Switzerland
145. S. Brosi, Paul Sherrer Institute, CH-5232 Villigen PSI, Switzerland
146. R. Palframan, RR&A, P. O. Box 31, Derby DE2 8BJ, United Kingdom

NRC FORM 335 (2-89) NRCM 1102, 3201, 3202

U.S. NUCLEAR REGULATORY COMMISSION

BIBLIOGRAPHIC DATA SHEET

(See instructions on the reverse)

1. REPORT NUMBER (Assigned by NRC, Add Vol., Supp., Rev., and Addendum Numbers, if any.)

NUREG/CR-6460
ORNL/TM-13207

2. TITLE AND SUBTITLE

CSNI Project for Fracture Analyses of Large-Scale International Reference Experiments (FALSIRE II)

3. DATE REPORT PUBLISHED

MONTH: November | YEAR: 1996

4. FIN OR GRANT NUMBER

W6631

5. AUTHOR(S)

B. R. Bass, C. E. Pugh, J. Keeney/ORNL
H. Schulz, J. Sievers/GAR

6. TYPE OF REPORT

Technical

7. PERIOD COVERED *(Inclusive Dates)*

8. PERFORMING ORGANIZATION – NAME AND ADDRESS *(If NRC, provide Division, Office or Region, U.S. Nuclear Regulatory Commission, and mailing address; if contractor, provide name and mailing address.)*

Oak Ridge National Laboratory
Oak Ridge, TN 37831-6285

Gesellschaft für Anlagen-und Reaktorsicherheit
Department of Component Integrity (GRS)
Köln, Germany

9. SPONSORING ORGANIZATION – NAME AND ADDRESS *(If NRC, type "Same as above"; if contractor, provide NRC Division, Office or Region, U.S. Nuclear Regulatory Commission, and mailing address.)*

Division of Engineering Technology
Office of Nuclear Regulatory Research
U.S. Nuclear Regulatory Commission
Washington, DC 20555 -0001

10. SUPPLEMENTARY NOTES

M. Vassilaros, NRC Project Manager

11. ABSTRACT *(200 words or less)*

A summary of Phase II of the Project for Fracture Analysis of Large-Scale International Reference Experiments (FALSIRE) is presented. Project FALSIRE was created by the Fracture Assessment Group (FAG) of the Organization for Economic Cooperation and Development/Nuclear Energy Agency's (OECD/NEA's) Committee on the Safety of Nuclear Installations (CSNI) Principal Working Group No. 3 (PWG-3). The CSNI/FAG was formed to evaluate fracture prediction capabilities currently used in safety assessments of nuclear components. Members were from laboratories and research organizations in Western Europe, Japan, and the United States. The CSNI/FAG initiated an international project (FALSIRE I) in 1988 to assess various fracture methodologies through interpretive analyses of six large-scale fracture experiments. These experiments were conducted by research organizations in Europe, Japan, and the United States. Following the successful completion of FALSIRE I in 1992, several participating organizations indicated a desire to proceed with further evaluation of fracture analysis methods in a Phase II program. FALSIRE II included seven reference cleavage fracture experiments that focused primarily on behavior of relatively shallow cracks in the transition temperature region.

12. KEY WORDS/DESCRIPTORS *(List words or phrases that will assist researchers in locating the report.)*

fracture mechanics
reactor pressure vessels
brittle fracture toughness
ductile fracture
reference experiments

13. AVAILABILITY STATEMENT

Unlimited

14. SECURITY CLASSIFICATION

(This Page) Unclassified

(This Report) Unclassified

15. NUMBER OF PAGES

16. PRICE